Influence of Photospheric Back-Scatter on Flare Hard X-Ray Diagnostics.

Robert Calum Alexander

Presented for the degree of
Doctor of Philosophy
The University of Glasgow
2010

This thesis is my own composition except where indicated in the text.

March 20, 2010

Acknowledgements

I would like to acknowledge the help, guidance, and useful discussions from J.C. Brown, A.L. MacKinnon, E.P. Kontar and M. Hendry.
I would also like to thank Juri Poutanen (University of Oulu, Finland) for kindly giving his permission for his work to be used as a basis for the radiative transfer solution presented within this thesis.

Abstract

In this thesis I present the results of studies on the influence of solar photospheric back–scatter on Hard X–Ray (HXR) flare diagnostics. Specifically the thesis presented is concerned with the effect of back–scatter photons upon the morphology of the Hard X–Ray photon spectrum and its effect on the inferred parent electron spectrum.

I present a theoretical investigation into Compton reflected HXR photons, known as the photospheric Albedo, and explore the effect of photospheric albedo on observations of global flare hard X-ray spectra for isotropic emission. I examine, for the Kramers cross-section, the consequences of ignoring the albedo correction in using observed spectra to infer flare source electron spectra for thin and thick target interpretations and show that the effects are very significant in terms of inferred spectral shape, especially for hard spectra.

I extend this investigation to consider the effect of the photospheric albedo on observations of global flare hard X-ray spectra for anisotropic primary photon emission by examining, for the Kramers cross-section, the consequences of ignoring the albedo correction in using observed spectra to infer flare source electron spectra for thin and thick target interpretations. For an energy dependent multiplier α I find that the results for anisotropic emission are similar in shape to isotropic emission when I assume a linear model for the anisotropy.

I then explore two complementary techniques for determining the Compton back-scattered component of the observed photon spectrum using a model independent Greens function approach. The first is a matrix based technique developed by Kontar & Brown (2006) which I extend to include anisotropic primary photon emission using an Eddington hemispheric approach along with an empirical fit to published data. The second is a full radiative transfer Greens function approach developed by Poutanen et al. (1996) which I also extend to include anisotropic primary photon emission again using an empirical fit to published data.

In both cases I investigate how anisotropic primary photon emission effects the observed photon spectrum by studying the differences in the size and shape of the albedo.

In the final chapter I use the results from the anisotropic Eddington hemispheric Greens function approach and the anisotropic full radiative transfer Greens function approach to investigate the findings published in Kontar & Brown (2006) using the Stereoscopic electron spectroscopy technique.

I conclude from the results of this comparison that doing a full anisotropic scattering properly does not fundamentally change the findings Kontar and Brown which are specifically that the electron distribution ($\bar{F}(E, \mu)$) is nearly isotropic to such a degree of confidence that it casts doubt on models which are based upon beaming such as the collisional thick target (Brown 1971).

Contents

List of Figures

List of Tables

List of Abbreviations

RHESSI	Reuven Ramaty High Energy Solar Spectroscopic Imager
SOHO	Solar and Heliospheric Observatory
OSO	Orbiting Solar Observatory
IDL	Interactive Data Language
HXR	Hard X-Ray
SXR	Soft X-Ray
EUV	Extreme Ultra-Violet
ADS	The SAO/NASA Astrophysics Data System
EM	Electromagnetic (Spectrum)
CME	Coronal mass ejection
ESA	European Space Agency

Chapter 1

Solar Flare Activity and Diagnostics - An Overview

1.1 An Overview of the Sun

As our local star, the Sun is the only star close enough to be studied in great detail. At an estimated age of 4.6 billion years it is approximately half way through its lifespan and it affects all activity within the solar system from the edge of its atmosphere to the outer most reaches of the solar system. It is a yellowish looking star (it peaks more towards the green part of the spectrum) and, with an effective surface temperature of 5770K, is classified as a type G2V star.

It has an approximate equatorial radius of 6.955 x 10^8 m ($\simeq$109 earth radii (Woan 2000)), and a mass of 1.989 x 10^{30} kg (3.33 x 10^5 earth masses), and it comprises approximately 99.85% of all the mass within the solar system. It is mainly composed of hydrogen (71% by mass) with helium the next most abundant element (27% by mass). The heavier elements, which are commonly referred to as the *metals*, account for the remaining (2%) of the solar mass. Its luminosity is 3.85 x 10^{26} Watts which means that it's losing 4.3 x 10^9 kg of its mass every second as radiation.

1.1.1 The Solar Structure

The solar interior

The energy source of the Sun is the fusion of hydrogen into helium which happens in the solar *core* (a region of radius $\approx$175,000 km) at temperatures up to 15 million K. Surrounding the core is the *radiative zone* so called because radiative transfer

is the dominant energy transport mechanism within this region. The energy generated as part of the fusion process within the core, although travelling at the speed of light, is scattered a countless number of times within this region such that a photon generated within the core takes $10^5 - 10^6$ years to reach the outer most regions of the radiative zone. Figure 1.1 gives an indication of typical temperature and density variation within the solar interior. The interface between the radiative and convective zones is called the *tachocline* and it is here where the changes in fluid (shear) flow velocities are thought to result in a stretching of magnetic field lines which gives rise to a magnetic dynamo, thought to be the source of the solar magnetic field and thus solar flares and other types of activity on the solar surface. The *convection zone* is the outermost layer of the solar interior named to reflect the most energetic efficient transport mechanism there. It extends from 200,000km to the visible surface and within this zone the plasma fluid has cooled from an estimated 2 million K to the surface temperature of 5700K. This convective motion can be seen at the solar surface as granulation and supergranulation.

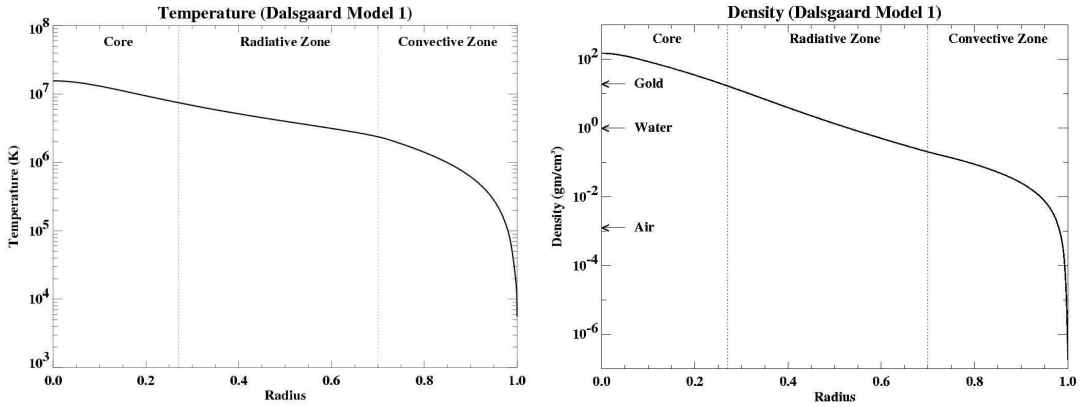

a. *temperature* b. *density*

Figure 1.1: Temperature and density variations with solar radius in the solar interior. After Christensen-Dalsgaard et al. (1996). Source: http://solarscience.msfc.nasa.gov/interior.shtml

The Outer Sun

The *photosphere* is the visible surface of the Sun at optical wavelengths. It is actually a very thin (optical depth units) layer approximately 100km thick and most of the familiar features observed on the solar surface such as sunspots, faculae and granulation occur in this layer. The *chromosphere* is the layer above

the photosphere where the temperature fall counter-intuitively reverses (from 4000-6000K to over 20000K) - this is the coolest region of the Sun. The solar activity within this layer is dominated by magnetic phenomena such as spots, active regions, coronal holes, loops, flares and post flare loops. The layer between the chromosphere and the corona is called the *transition region*, a thin layer where the temperature within the plasma rises rapidly from 20000K to between 1 & 3 million K. Figure 1.2 shows the sharp transition from chromospheric to coronal temperatures (n_e indicates the electron density, n_{H_0} the neutral hydrogen density and T_e the temperature).

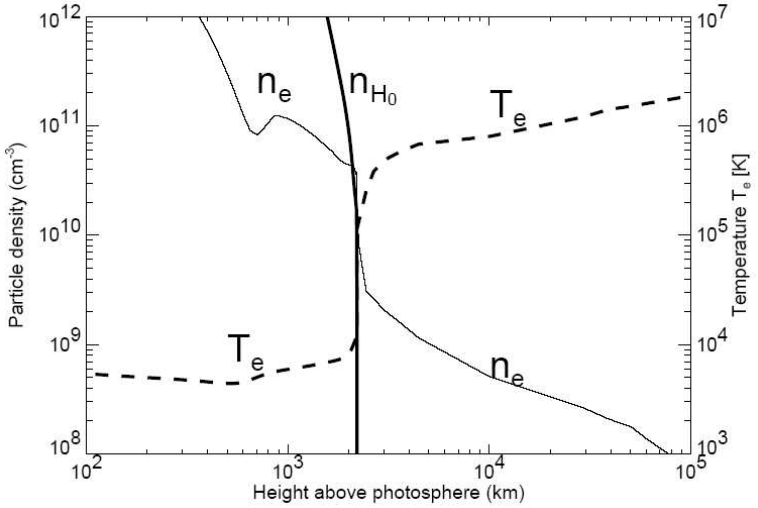

Figure 1.2: Electron density and temperature model of the chromosphere. Source: Aschwanden (2005)

The outer layer of the Sun is the solar *corona*. Emission in the corona is so washed out by the emission from the solar disk that it can only generally be observed by blocking the disk emission during an eclipse or using a coronagraph. It had long been thought of as a hot placid plasma until the launch of satellites such as OSO (Orbiting Solar Observatory), SOHO (Solar Heliospheric Observatory) and recently RHESSI (Ramaty High Energy Solar Spectroscopic Imager). The insights gained from these missions allowed the true nature of the corona to be appreciated (Golub & Pasachoff (2001)), namely that the corona is not only very hot ($> 1MK$), and very tenuous plasma, but also a very dynamic region of the Sun. The corona extends to several solar radii before it becomes the *solar wind*. This stream of charged particles (such as electrons, protons and helium ions)

interacts with planetary systems throughout the solar system. We notice these effects from their interactions with the earth's magnetic field as auroral light in the polar regions. The reach of the solar wind is called the *heliosphere* and is thought to be about 100 AU (Ridpath 1997). At this distance interstellar gas pressure becomes sufficient to slow the solar wind at a boundary known as the *heliopause*, which defines the limit of our solar system and thus the limits of our Sun's influence.

1.1.2 The Solar Cycle

The solar magnetic cycle is about 11 years, during which the magnetic polarity of the global solar magnetic field is alternately reversed. Output in many wavelength regions of the spectrum follow this variation of the magnetic field. This cycle was observed because of the increase and decrease of sunspot numbers and which as part of active regions, migrate from high latitudes towards lower latitudes near the equator during a cycle. This can be illustrated by the butterfly diagram of sunspots, when their latitudinal position is plotted as a function of time (figure 1.3)

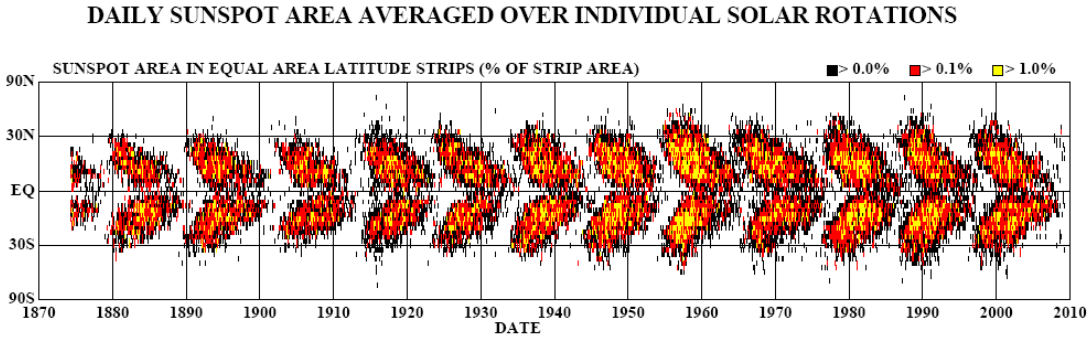

Figure 1.3: Observations of sunspots with solar lattitude - the butterfly diagram. Source: http://solarscience.msfc.nasa.gov/SunspotCycle.shtml

A full cycle of 22 years, after which the original magnetic configuration is restored, is called a Hale cycle. The total magnetic flux reaches a maximum during the peak of a cycle and drops to a low level during the minimum of the cycle. Since many radiation mechanisms are directly coupled to the release of magnetic energy (*i.e.* solar flares) and related plasma heating, the radiation output in these wavelengths (e.g., in soft X-rays, hard X-rays, and radio wavelengths) follows the

peaks and troughs of the solar cycle.

1.2 Solar Flares

Solar flares are amongst the most energetic events in our solar system, releasing up to 10^{25}J of energy within a period of several minutes (Emslie 1996) and can last up to a few hours or exceptionally up to a 24 hour period. To give some context to this figure, this energy could power the human race for centuries. They are part of a class of magnetic phenomena (with solar flares at one end and magnetars at the cosmic extreme) which all involve a reconfiguration of stressed magnetic field lines to a lower energy state which results in a release of energy across the whole EM spectrum (Tandberg-Hanssen & Emslie 1988).

Although we are approximately 150 million km from the solar surface we still feel the effects of flare and CME activity in the emission of light in polar aurorae and disruption to communication satellites. This disruption was first experienced during World War II when disruption from solar flares led the British military to believe that the Germans had found a way to jam radar which had just entered service at that time. More recently solar cycle activity has caused a power grid failure in Canada (1989) where a transformer in a power station was effectively destroyed by the current induced in the grid's power lines by a solar driven geomagnetic storm.

A more precient worry is the potential for flare activity to damage the *GPS* (global positioning system) communication satellite network in the next solar maximum due in $2011-2$ (Hecht (2006)). These satellites provide the worldwide infrastructure for navigation from GPS-enabled equipment like mobile phones to in-car navigation and are fundamental to modern shipping and commercial aircraft navigation. GPS satellites provide a navigational fix via timing signals transmitted from each of a series of satellite. Receivers use these timing signals to determine their location - the more satellites that are within view of the receiver the more accurately the location will be determined. Clearly the loss of a satellite and the resulting degradation in locational information may not be problematic for a car driver but the loss of a navigational fix for an airliner using GPS to assist landing in poor visibility may result in loss of life. Indeed as we build ever more sophisticated and sensitive communication equipment within commercial satellites we expose ourselves more to the effects of solar flare and space weather disruption than ever before.

Flares are found generally in the Sun's activity belts at low latitudes below and above the equator and are closely associated with sunspots. Sunspots are regions of the photosphere that are cooler (4000K) and thus dimmer than the surrounding material. The low sunspot temperatures result from stronger magnetic fields that inhibit convection of hotter material from deeper regions and conduction of heat from surrounding regions. Strong magnetic fields form a central role in flare theories. The magnetic fields originating in sunspots are of one polarity or the other with field lines leaving one sunspot, rising into the corona, and eventually returning to the photosphere via another nearby sunspot of the opposite polarity or via magnetic network fields where there are no sunspots. There can be many such sunspot pairs in a local group of sunspots and a line can always be drawn between them - dividing the photosphere in regions of +ve and -ve magnetic field lines. This line known as a neutral line, (vertical component of magnetic field = 0 or neutral). It is along these magnetic divisions that flares are most commonly seen (Tandberg-Hanssen & Emslie 1988).

It is generally accepted that the origin of the energy in the coronal magnetic field is the solar dynamo which is generated by the magnetic shearing of fluid within the tachocline. Generally the plasma and magnetic fields are frozen together - the plasma follows the magnetic field or vice versa depending upon which type of pressure (magnetic or gas) dominates. In the tachocline the plasma will rise due to convective buoyancy carrying the magnetic field lines with it through the convective region eventually pushing through the photosphere as the familiar coronal loops. Since β (which is the ratio of the thermal to magnetic pressure $P_{thermal}/P_{magnetic}$) $\gg 1$ at the photosphere the magnetic field lines effectively follow the plasma flows. This leads to the kinetic energy in the plasma flows being converted into magnetic energy in the twisted/stressed fields in the corona where $\beta \ll 1$. The plasma flows originate where the plasma fluid become convectively unstable and a bulk movement of the plasma occurs. This manifests itself visibly in the photosphere as granulation. Where these twisted field lines become sufficiently close such that they are effectively "touching" - or more accurately within close proximity - reconnection occurs - the Flare. The process of reconnection is a local process (Tandberg-Hanssen & Emslie 1988) but with global effects and releases energy as particle acceleration, specifically electrons and fast-ions, heat, flare mass motion[1] and radiation. It also allows the non-potential energy stored

[1]Craig & McClymont (1976) emphasised that strong temperature and pressure gradients established in the flare atmosphere would result in significant mass motion

within a stressed magnetic field to be released and allows the magnetic field to relax to a lower energy state (Tandberg-Hanssen & Emslie 1988).

1.2.1 Flare Morphology

Figure 1.4 shows the typical radiative energy release spectrum in a solar flare versus time for various frequencies and illustrates the pre-flare, impulsive, flash, and gradual phases.

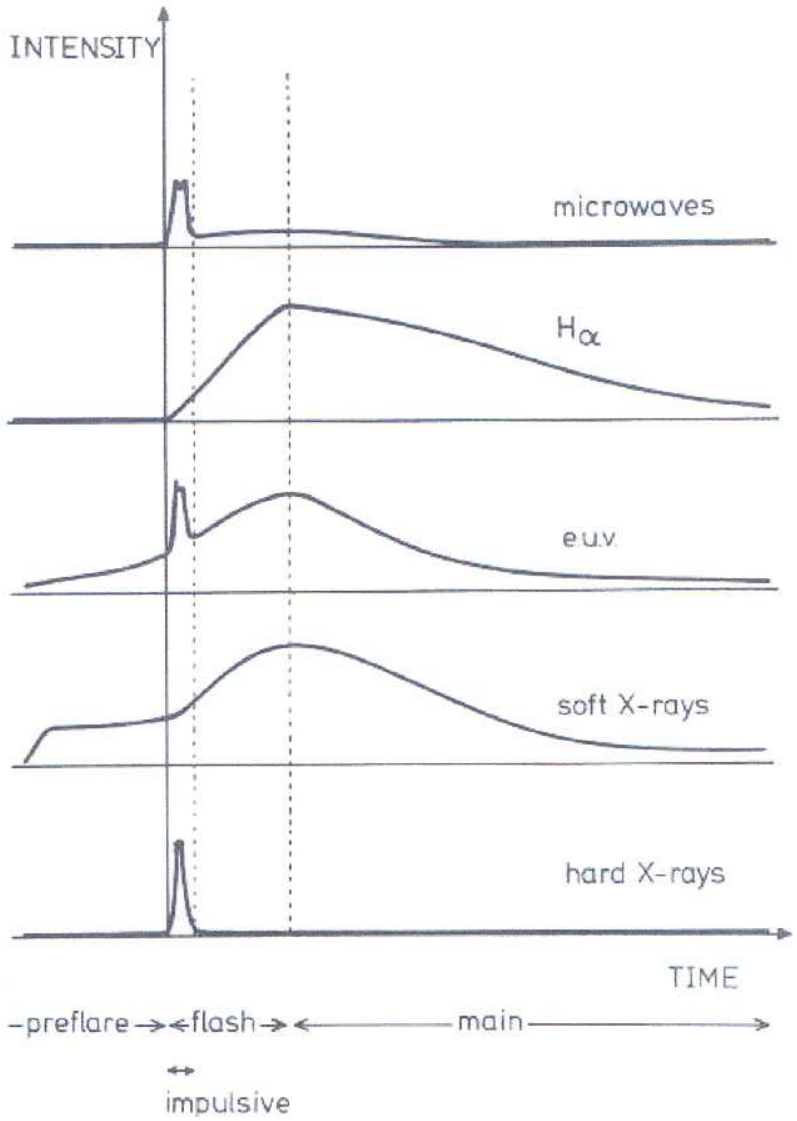

Figure 1.4: Energy release in a flare with time. Source: Priest (1984)

A solar flare often begins with a pre-flare phase, indicated by a gradual rise in SXR and EUV in the region of the eventual flare, and is followed by an impulsive phase. Much of the emission within this phase is related to acceleration of particle to very high energies resulting in short lived HXR emission, (sometimes) gamma rays and emission across a broad range of frequencies. An extended slower release phase or equilibrium phase follows the impulsive phase. Although the HXR emission has died away by the gradual phase, the SXR and EUV (*i.e.* thermal emission) initially continues to rise and decays over the space of a few hours.

1.2.2 Flare Spectroscopy

Modern satellites allow the study of flare spectra across the full range of the EM spectrum. Figure 1.5 (Aschwanden 2004) shows the wavelength bands studied by spacecraft. It can be seen that the HXR/EUV band all benefitted from spacecraft missions from the 1960s onwards - EM ranges which cannot be studied from ground based observatories.

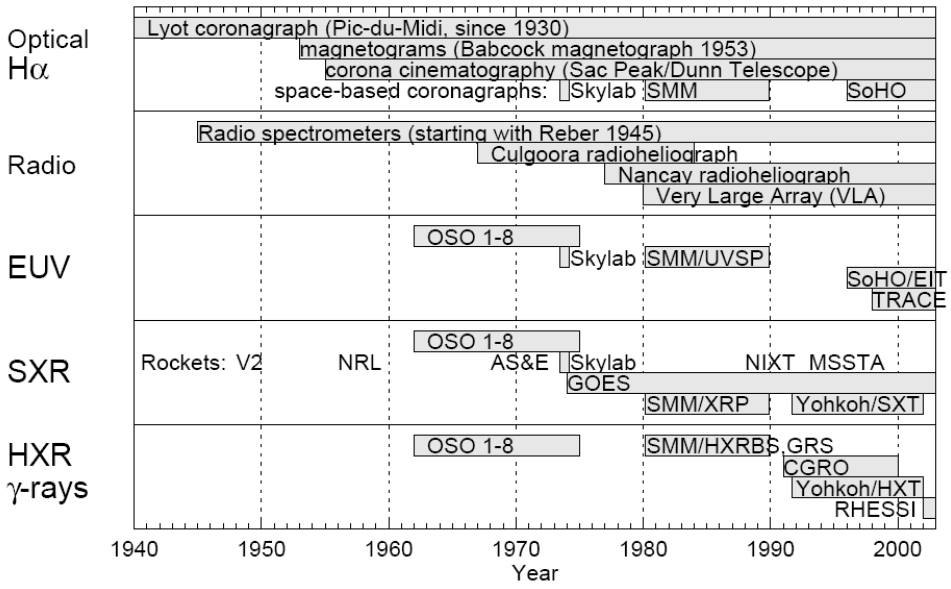

Figure 1.5: Spacecraft missions and their energy range of study. Source: Aschwanden (2004)

Flare observations have been taken in most of the parts of the EM spectrum from radio waves to energies exceeding 10MeV (HXR and γ rays).With each new mission we gain a step improvement in spatial and temporal resolution such that

it is now possible to follow super-heated plasma flows and directly calculate the energies involved.

The analysis of spectra in order to gain insight into the physical conditions is a crucial diagnostic in studying solar flares. From the shapes and strengths and magnetic splitting of spectral lines we gain an idea of the physical conditions in the magnetized plasma at the point the light is emitted. Traditional observation focussed on the visible part of the spectrum and indeed the most energetic flare emit in the visible continuum (white light flares - Carrington (1859)). Equally important is the information derived from the X-ray and γ ray regions of the spectrum. This was only realised with the more recent space missions such as RHESSI. This thesis is devoted to using the energy spectra or count spectra from spacecraft such as RHESSI.

Flare spectra result from a variety of emission mechanisms. Prior to the 70's the free free and free bound electrons transitions in atoms and ions in non-relativistic conditions (which dominate the visible EM emission) were studied in great detail. Later research has concentrated on X, γ ray and radio emissions initially by SMM later Hinotobi and Yohkoh or more recently RHESSI.

Higher energy photons in flares are mainly generated by Bremsstrahlung and by nuclear reactions, following electron and ion acceleration. Most relevant to the work presented in this thesis is the Bremsstrahlung emission modified by Compton Scattering which dominates observations in the deka-keV (10keV-100keV) energy range.

1.2.3 Radiative Processes Resulting in HXR Emission

Radiation is not only an important diagnostic of conditions within flares but it accounts for a significant component of the overall energy budget (Tandberg-Hanssen & Emslie 1988). One of the main tools for analyzing this radiation or emission is the photon (flux) spectrum illustrated by Figure 1.6. The analysis of the photon spectrum is the main diagnostic that will be used in chapters 4 and 5. Figure 1.6 below shows the composite high energy photon spectrum of a large flare, extending from soft X-rays (1-10 keV), hard X-rays (10 keV-1 MeV), to gamma rays (1 MeV-10 GeV), mostly produced by thermal, and nonthermal or highly-energetic electrons. Gamma-ray line emission and parts of the gamma-ray continuum are produced by interactions of accelerated protons, neutrons, ions, and by pion decay (Ramaty 1987).

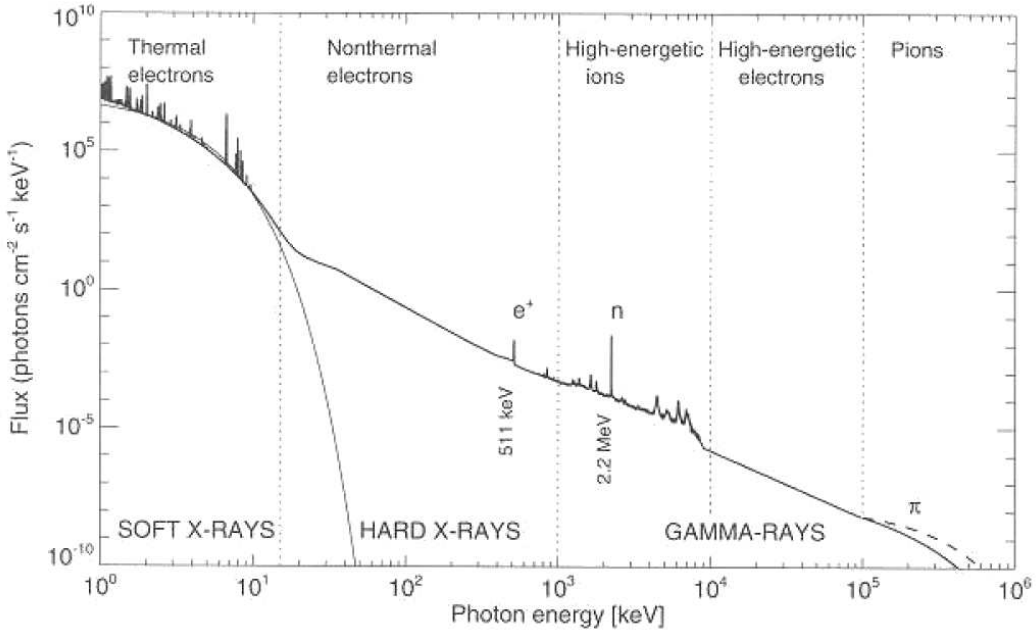

Figure 1.6: Composite photon spectrum. Source: Aschwanden 2002

As most of the flaring plasma is highly ionised this means that more than one half of the particles present are free electrons. Thus electrons play a dominant role in many radiative processes, and they are also more easily accelerated than ions. At reconnection sites particles (electrons and ion species) are accelerated up to a fraction of the speed of light along the magnetic field lines. These particles collide (or interact) and thus lose energy within the surrounding (atmospheric) plasma. Different radiative mechanisms are important for different parts of the electromagnetic spectrum and in different atmospheric regions. Here we consider radiation from Coulomb interactions of electron with heavier particles and the scattering of the resulting photons on coronal electrons.

1.2.4 Bremsstrahlung

This is the most common HXR emission mechanism in flares in the 10-100keV (deka-keV) energy range. In this energy range it can be described classically but at higher energies, approaching $\epsilon \approx m_e c^2$ relativistic corrections apply. It is also known as free-free emission since the electron remains free after its interaction with an ion.

Classical electromagnetism predicts that an accelerated electron will emit radiation throughout its acceleration (Kramers 1923) derived an expression, used

in chapters 2 and 3, for the radiation rate in free free transitions as a function of the acceleration of the electron. In quantum physics, we describe this radiation as being composed of discrete quanta of energy (photons) whose characteristics depend on the size and direction of the perturbing force.

For distant encounters the force is small thus the photon energy is small which means that the photons are not HXR photons. But close binary collisions between electrons and heavier particles (or between electrons) result in HXR photons. For such close interactions a quantum mechanical description is really required for precise results but in chapters 2 and 3 we use an approximation to this analysis, as commonly done in the literature.

In general we describe Bremsstrahlung interactions in terms of differential cross sections $\frac{d^2\sigma}{dEd\Omega}$ (per unit energy and solid angle) for which Koch & Motz (1959) tabulated many cross sections. At higher energies relativistic corrections apply and for high values of photon energy ϵ to Electron energy E, the cross section is highly anisotropic. The effects of anisotropic emission is studied in chapters 3 to 6. However for the deka-keV energy range the Bethe Heitler (1.1 and chapter 2) cross-section formula applies reasonably well

$$\sigma_B(\epsilon, E) = \frac{7.9 \times 10^{-25} \bar{Z}^2}{\epsilon E} ln \left(\frac{1 + (1 - \frac{\epsilon}{E})^{\frac{1}{2}}}{1 - (1 - \frac{\epsilon}{E})^{\frac{1}{2}}} \right) cm^2 keV^{-1} \tag{1.1}$$

where

- $\sigma_B(\epsilon, E)$ is the cross section which is differential in photon energy ϵ but includes all possible directions of the outgoing and all possible directions and polarization of the outgoing photon (Tandberg-Hanssen & Emslie 1988).
- E the energy of the electron.
- Z is the atomic number of the scattering ion.
- $\bar{Z}^2$ is the abundance-weighted value of the atomic number of the scattering ion. $\bar{Z}^2 \approx 1.4$ for solar abundances.

1.2.5 Bremsstrahlung as a Flare Diagnostic - The Photon Spectrum

To use bremsstrahlung flux as a diagnostic of the processes within a solar flare we must make a further assumption : whether the electrons are thermal or non-thermal (Figure 1.6). Electrons are thermalised if their energy is similar to the

energy of the background plasma. We are interested here in the non thermal regime where $\epsilon, E \gg kT$ of the background plasma - the electron population that has been accelerated in the impulsive phase of the flare. We must also consider the nature of the conditions in the flaring target which determines the photon flux spectrum $I(\epsilon)$ as being produced by a *thin* or *thick* target.

What we actually observe is the HXR bremsstrahlung flux $I(\epsilon)$ (photons $cm^{-2}s^{-1}keV^{-1}$) at the earth resulting from the injection of a beam of suprathermal energetic electrons with a differential energy spectrum $F(E_o)$ (electrons $cm^{-2}s^{-1}keV^{-1}$) over flare area S.

In a thin target electrons are injected through a 'thin' tenuous region such as the corona where the electron loses only part of its energy. In a thick target the electrons are stopped: this applies to electrons emitted downwards into the dense chromospheric plasma. In the latter case the important thing is the injection rate spectrum $F_o(E_o)$ and we must modify $F(E)$ as it evolves through the target.

For a thin target Brown (1971) (chapter 2 and 3) $I(\epsilon)$ can be described as

$$I(\epsilon) = \frac{S\Delta N}{4\pi R^2} \int_{\epsilon}^{\infty} F(E_o)\sigma_B(\epsilon, E)dE \tag{1.2}$$

where $\Delta N = \int n_p(s)ds$ - the column density of the source, $n_p(s)$ is the proton density which is a function of distance along the injected electron path, S is the flare area, and R is 1 astronomical unit (AU).

For the thick target $F(E)$ is not the injected spectrum but the target averaged flux spectrum (Brown 1971). However, in order to gain an insight into the particle acceleration mechanisms it is more meaningful to have information on the actual injected spectrum $F_o(E_o)$. The relationship between the target averaged $F(E)$ and the injected $F_o(E_o)$ is obtained by considering the energy losses suffered by the bremsstrahlung producing electron in the target. For simple energy loss processes such as coulomb collisions on ambient particle the energy loss rate can be described in terms of the energy loss cross section $\sigma_E(E)$. The number of photons emitted per unit energy, centered on ϵ, by an electron of initial energy E_o is (Brown 1971)

$$m(\epsilon, E_o) = \int_{\epsilon}^{E_o} \frac{\sigma_B(\epsilon, E)}{E\sigma_E(E)}dE \tag{1.3}$$

The Bremsstrahlung flux spectrum (observed at Earth at distance R) is obtained by integrating $m(\epsilon, E_o)$ over the injected spectral rate $F_o(E_o)$ and over the flare area S

$$I(\epsilon) = \frac{S}{4\pi R^2} \int_{E_o=\epsilon}^{\infty} F(E_o) \int_{\epsilon}^{E_o} \frac{\sigma_B(\epsilon, E) dE}{E \sigma_E(E)} dE_o \tag{1.4}$$

which for Coulomb losses give the following for the thick target (Emslie 1978).

$$I(\epsilon) = \frac{S}{4\pi R^2} \left(2\pi e^4 ln\Lambda\right)^{-1} \int_{E_o=\epsilon}^{\infty} F(E_o) \int_{\epsilon}^{E_o} E \sigma_B(\epsilon, E) dE dE_o \tag{1.5}$$

where $ln\Lambda$ is known as the Coulomb logarithm. This is the factor by which small-angle collisions are more effective than large-angle collisions in Coulomb losses (typically 10 to 20 for a warm plasma (Woan 2000)).

Brown (1971) developed an analytic solution to the recovery of the mean electron spectrum $\bar{F}(E)$ from the Bremsstrahlung emission where the electron spectrum is not locally Maxwellian (non-thermal) for the Kramer's and non-relativistic Bethe–Heitler cross sections. It was found that the problem can be expressed in terms of an Abel equation and thus an analytic solution can be found for the $F(E)$ and $F_o(E_o)$ needed for any photon spectrum. In chapters 2 and 3 we use approximations to Equations (1.2) and (1.5) in this analytic approach to investigate the inferred error in the electron spectrum for an assumed form of the photospheric backscattering (see next section).

1.3 Photospheric Backscatter - Compton Reflection

Emission observed from flares at the Earth is composed of both the directly emitted photons (upwards from the solar surface) and those emitted towards the photosphere then backscattered. These bremsstrahlung photons undergo Compton scattering within the dense plasma and those which are scattered back into the direction of the observer at earth are said to have undergone Compton reflection and become part of the observed photon flux. At a few keV Thomson scattering results in coherent or elastic scattering but at deka–keV energies scattering is dominated by Compton scattering. Compton scattering involves a change in wavelength of a photon when it collides with an electron resulting in some of the photon's energy being transferred to the particle and the photon being re-radiated at a longer wavelength.

If the direction of the photon changes by θ it can be shown that

$$\lambda_2 = \lambda_1 + \frac{h}{mc}(1 - cos\theta) \tag{1.6}$$

where $\Delta\lambda = \lambda_2 - \lambda_1$ is the Compton shift (in Angstroms, $\mathring{A}$)[2] and $cos\theta$ is the angle through which the photon momentum vector changes. When expressed in terms of energy this shows that Compton scattering reduces the energy of the scattered photon - energy degradation (chapter 2-4) which is the cause of the physical characteristic of the albedo "bump" in $I(\epsilon)$ discussed at length in this thesis.

In Tomblin (1972), it was first stated that, in the few keV region of the spectrum, the Compton backscattering effects manifest themselves as a wavelength shift of X-Ray emission lines such as the Fe K line at 6.6keV. At energies near 1 keV the Compton process is less than 4 percent of the photoabsorption cross-section but at a few deka-keV photoabsorption is negligible compared to Compton scattering. This shift generates a tail on the long wavelength side of the emission lines. Also, since the strength of Compton backscattering intensity is a function of the photo-absorption processes (which are strongly dependent), it will itself be strongly energy dependent - this is readily seen in the results presented in the subsequent chapters in this thesis.

Compton backscatter of solar flare emission has several interesting effects on solar X-Ray spectra on the solar disk. The rapid decrease in the photoelectric cross-section causes the Compton backscattering contribution to increase from 5 to 50 percent in the 30-50keV range which implies that a substantial correction to primary photon spectra obtained from HXR solar events must be made to compensate for the reflected component of the spectrum.

The ratio of the backscattered intensity to the incident intensity is referred by Tomblin as the 'Compton reflectivity' ($R(\epsilon)$) however we use the alternative term 'photospheric albedo' ($A(\epsilon)$) in chapters 2 and 3. Compton reflectivity is thus dependent on both the scattering and the absorption properties of the atmosphere.

The Compton reflectivity is defined as

$$R(\epsilon) = A(\epsilon) = \frac{I_{obs}}{I_o} \tag{1.7}$$

[2]The ratio $\frac{h}{mc} \equiv \lambda_c$ is referred to as the *Compton wavelength*, which for electrons is $\frac{h}{m_e c} = 0.024\mathring{A}$

where I_{obs} is the observed photon spectrum and I_o is the primary photon spectrum.

The total 'reflectivity' R at all energies obtained by summing the various contributions of the Thomson and Compton scatterings and the photoelectric absorption from the Sun was calculated by Tomblin (1972), extended to higher energies in Santangelo et al. (1973), and extended to include polarisation later by Bai (1978) (chapter 2). Magdziarz & Zdziarski (1995) and Poutanen et al. (1996) have also calculated Compton reflectivity in cosmic disks which we apply here within a solar context. Kontar et al. (2006) later built upon the work in Magdziarz & Zdziarski (1995) to develop a model independent matrix Green's function approach to the albedo problem. These papers show that the albedo problem does not simply involve a coloured reflection $A(\epsilon)$ but rather a convolution/transfer function.

The effect of this is that a power law photon spectrum in the region 10-50keV (especially if the flare is at the disk centre) would be hardened due to Compton scattering.

1.4 “Stereoscopic” Electron Spectroscopy and Photospheric Backscatter

In Kontar & Brown (2006) the authors emphasise that the albedo spectral component within the observed photon spectrum offers valuable insight into the anisotropy of the flare fast electron distribution. They maintain that, given that the primary emission and albedo bump have very distinct signatures, the strength of the albedo bump (introduced in chapter 2) in the observed spectrum will be an indicator of the degree of downward beaming of the electron distribution. This is indeed the premise of the work presented in this thesis.

This insight in turn can be used to constrain the directivity of the flare electrons so strongly that the conventional models such as the collisional thick target (CTT) (Brown 1972) with downward beaming or collimated beaming may be excluded. We investigate this further in chapter 6.

1.5 Structure of Thesis

In Chapter 2 we explore the effect of the photospheric albedo on observations of global flare hard X-ray spectra and derive an expression to allow approximate

correction for this in the case of primary power-law photon spectra. We also examine, for the Kramers cross-section, the consequences of ignoring the albedo correction in using observed spectra to infer flare source electron spectra for thin and thick target interpretations and show that the effects are very significant in terms of inferred spectral shape, especially for hard spectra.

In Chapter 3 we extend the work in chapter 2 to investigate the influence of anisotropy on the inferred electron spectrum. Again we examine, for the Kramers cross section, the consequences of ignoring the albedo correction in using observed spectra to infer flare source electron spectra for thin and thick target interpretations by introducing a simple hemispheric (Eddington approximation), energy dependent, anisotropic approach.

In Chapter 4 we discuss in more detail the influence of the albedo on the Hard X–Ray photon spectrum in terms of a convolution from input to output energies. We demonstrate a model independent approach for studying the effect of the albedo on the primary photon spectrum $I_o(\epsilon)$ using the Green's operator approach initially developed by Kontar et al. (2006). We extend Kontar's approach to include anisotropy by using an energy dependent empirical fit to published data. We also demonstrate that one of the dominant influences on the photospheric albedo is simply a geometric effect - a consequence of the photospheric area that an observer can see.

In Chapter 5 we introduce a full anisotropic radiative transfer approach initially developed by Poutanen et al. (1996) for studying Compton scattering in the accretion disks of AGNs. We initially compare Poutanen's approach against the Eddington approximation approach developed by Kontar et al and then extend the radiative transfer approach to investigate the effects of anisotropic emission by using a simple empirical anisotropic form in the primary photon spectrum. Finally we use an empirical fit to published data to examine the effects of a more realistic anisotropic form on the primary photon spectrum.

In Chapter 6 we combine the work in chapters 4 and 5 to test whether using a full radiative transfer approach alters the findings published in Kontar & Brown (2006) using the Stereoscopic electron spectroscopy technique. Specifically we test whether by using a proper anisotropic scattering approach we confirm as claimed by Kontar and Brown that the electron distribution $\bar{F}(E,\mu)$ ($\mu = cos\theta$ is the angle of primary photon emission) is nearly isotropic to such a degree of confidence that it casts doubt on models which are based upon beaming such as the collisional thick target (Brown 1972).

Chapter 2

An Empirical Albedo Correction of RHESSI Spectra for Photospheric Albedo and its Effect on Inferred Electron Spectra

2.1 Introduction

As detailed in Chapter 1, one of the main aims in studying solar flare spectroscopy is not only to understand the origin of observed spectroscopic features but also to use these observed features to infer conditions within the flare plasma itself (which can't be directly observed) and in particular the electron acceleration mechanism.

Radiation emitted from accelerated electrons in the electrostatic field of ions is an important source of X-Ray emission from astronomical plasmas (Craig & Brown 1986). This emission, known as *Bremsstrahlung*, or braking radiation, is produced in collisions between electrons and ambient plasma ion species (mainly protons) and specifically within flare emitting regions, viz electron-ion collisional bremstrahlung, this is the dominant emission mechanism in the 20-100keV Hard X-Rays (HXR) energy range. The HXR energy spectrum that results thus provides a test of the available models of solar flares and since the observed HXR photon spectrum can be coupled to its *parent* electron spectrum, a powerful diagnostic has been developed to allow the interpretation of the ambient conditions within the plasma acceleration region from observed spectroscopic features.

This is particularly relevant with the launch of the spacecraft RHESSI which is

capable of high HXR spectral resolution. This has created the chance for precise study of source electron spectra provided the observed spectra are well corrected for non–primary effects at the Sun including albedo, directivity, polarisation, source ionisation variations and the like. However a general treatment of all of these is theoretically complex and computationally intensive for each source model one wants to try.

2.1.1 Photospheric Compton Backscatter

It was initially noted by Tomblin's investigation into the effects of Compton scattering on solar X-Ray photons (Tomblin 1972) (primarily for line emission $\lessapprox 20keV$)) and later by Santangelo et al. (1973) which extended the energy range of this investigation to include up to the 100keV energy, that photons emitted towards the photosphere in the deka-keV energy range in the optically thin solar atmosphere have a high probability of being Compton scattered back from the photosphere (termed albedo). These albedo photons come from an extended area and arrive with a spread of delay times, depending on the primary source height. Indeed, it has been suggested (Brown, McClymont and van Beek 1975) that careful imaging or time delay (Bai 1978) studies could help infer source heights. Recently researchers such as Schmahl & Hurford (Schmahl et al. 2004) have used source profiles to identify albedo patches from RHESSI image data by forward fitting.

These backscattered photons add to the primary photons emitted upwards in the observed signal and thus the immediate consequence of this backscattering of photons is that the observed hard X-ray photon spectra are in fact a combination of photons directly emitted into the observers direction and those which have been backscattered from the solar photosphere via Compton scattering. As noted by many authors (Santangelo et al 1973, Bai & Ramaty 1978, Johns & Linn 1992 and Alexander & Brown 2002) the photospheric Compton backscatter makes a significant contribution to observed hard X-Ray (HXR) spectral fluxes over the RHESSI energy range and should be allowed for in spatially integrated HXR spectral interpretation.

As previously stated the albedo as a spectral feature of the HXR photon spectrum can be used as a powerful diagnostic of the intrinsic conditions within the plasma emitting region. Specifically removing the effects of the albedo from the observed photon spectra, leaving the primary photon spectrum, can be used

to recover the parent electron spectrum and give the true nature of the conditions within the flare plasma.

Other authors have developed general techniques for calculating the fully angularly dependent Compton scattering (Poutanen Nagendra & Svensson (1996)) and their work will be addressed within chapter 5 of this thesis.

2.1.2 Characteristics of Compton Backscatter

The simulations of Bai & Ramaty (1978) show that the reflectivity of the photospheric albedo can be characterised by the following (section 1.3):

1. Absorption due to the photoelectric effect. At lower energies as noted in Tomblin (1972) the Compton reflectivity is greatly reduced by absorption; however, as stated in Bai & Ramaty (1978), even at $\epsilon = 100keV$ one-third of the incident photons are absorbed.

2. Energy degradation *i.e.* the reduction in energy of Compton scattered photons due to electron recoil. Bai and Ramaty state that this reduces the reflectivity mainly at higher energies and, because of energy degradation, at these energies, the reflectivity is larger for flatter spectra.

3. Compression in energy space. This results from the fact that the energy degradation becomes larger with increasing energy. This accentuates the 'bump' (peak albedo) around the 30-50keV energy range arising from (1) and (2).

These properties are evident in figure 2.1 which shows the characteristic form of the photospheric albedo for a power law HXR photon spectra, resulting from the Bai and Ramaty 1978 simulations (shown for a primary photon spectral index (γ) of 2,3,4 and 5). The reflectivity axis is a measure of the Compton reflection from the photosphere; the energy axis is the photon energy in keV.

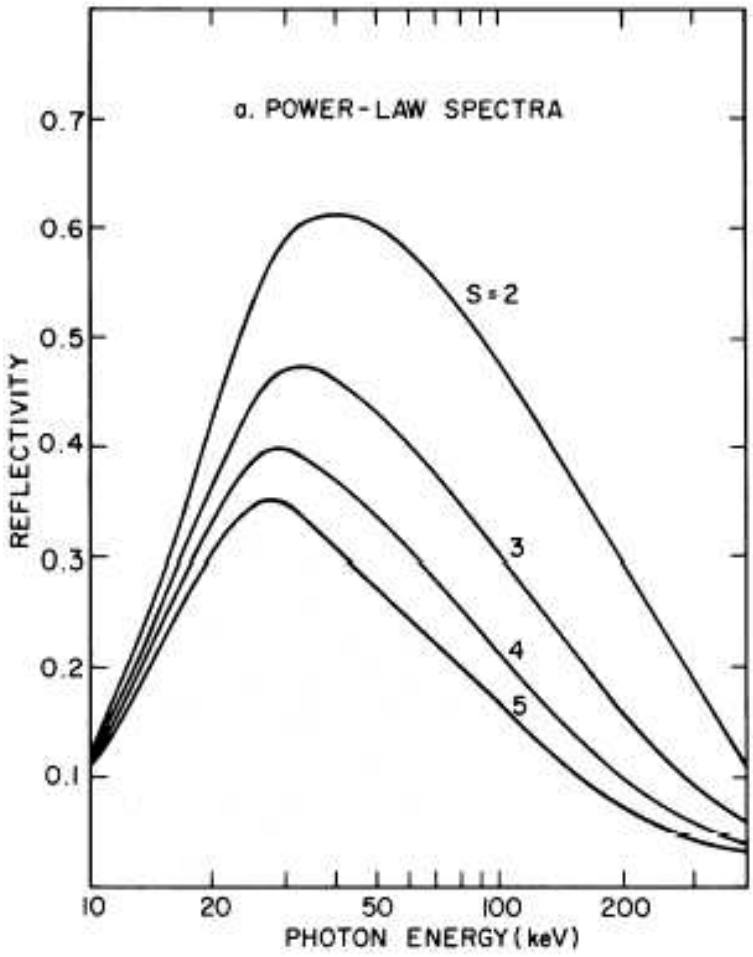

Figure 2.1: Photospheric albedo as simulated by Bai & Ramaty 1978 for a photon spectral index (γ) range of 2 to 5

2.2 A Simplified Approach for Empirically Correcting Photospheric Albedo

The main need for empirical simplification is the fact that albedo correction is not just a spectral correction *factor* (like a 'coloured' mirror) but strictly speaking a convolution. That is, the fractional albedo addition A(ϵ) at photon energy ϵ to the primary photon spectrum $I_o(\epsilon)$ itself depends on the functional form of $I_o(\epsilon)$, since Compton scattering shifts photons in energy *i.e.* the photon-electron Compton interaction produces a number of HXR photons 'smeared' across a range of lower energies.

Thus recovery of $I_o(\epsilon)$ from the total observed spectrum $I(\epsilon)$ involves inversion

of a convolution of $I_o(\epsilon)$ with the scattering and absorption processes.

Indeed if we recognise that electron-ion collisional Brehmstrahlung is both directional and polarised (Elwert & Haug (1970), Brown (1972), Leach & Petrosian (1983), Magdziarz & Zdziarski (1995), Poutanen et al. (1996)), then it becomes apparent that the full correction problem is nonlinear and messy. Here we offer a simple approximate first order correction procedure for global HXR spectra based on empirical fits to published albedo simulations. We do so primarily to illustrate the impact of this correction on inferred electron spectra for the thin and thick target models, never previously recognised prior to our work.

In this chapter we present the effects of the albedo contribution on the spectrum of the HXR source as a whole, based on function fits to the Bai & Ramaty (1978) results given in Figure 2.1. The spectral distribution of the albedo contribution was studied in detail by Bai & Ramaty (1978) via Monte Carlo Compton scattering simulation allowing for photon absorption, bremsstrahlung directivity and polarization.

A general treatment of the impact of albedo on electron spectrum inference should be an eventual goal for the work presented in this chapter and such treatments are now being developed by Kontar inspired by our work. Here we present our simpler basic first order correction of spectral data (after optimal removal of the already complex instrumental effects). In this chapter we implement such an approach for correction of the photospheric albedo.

2.3 Empirical Correction of RHESSI Spectra for Photospheric Albedo

Suppose the primary HXR source emission rate is $I_o(\epsilon)$ (photons $\mathrm{cm}^{-2}\mathrm{s}^{-1}$ per unit ϵ) as seen at the Earth. The total observed rate $I_{tot}(\epsilon)$ can be written approximately as

$$I_{tot}(\epsilon) = I_o(\epsilon)(1 + A_{I_o}(\epsilon)) \tag{2.1}$$

where $A_{I_o}(\epsilon)$ is the fractional albedo contribution at energy ϵ. In general, because of effects (2) and (3) above this depends on $I_o(\epsilon)$ itself as well as on ϵ explicitly. In fact A_{I_o} also depends somewhat on the source geometry; specif-

ically on the source height above the photosphere and the heliocentric–angle[1] of the source, since Compton backscatter is angle and energy dependent. Since variation across the disk is not large and is more of a scale factor than a spectral distortion, here we ignore it and use angle–averaged results for A_{I_o} from Bai & Ramaty (1978), though our approach could be extended to apply to each flare heliocentric angle separately by fitting of our empirical form to the appropriate Bai & Ramaty results for that angle.

Bai & Ramaty computed $A_{I_o}(\epsilon)$ for the specific forward problem of a simple power–law input $I_o(\epsilon) \sim \epsilon^{-\gamma}$ (given in figure 2.1) and for these cases we can write

$$A_{I_o}(\epsilon) = A_\gamma(\epsilon) \tag{2.2}$$

As a simplified procedure to estimate $I_o(\epsilon)$ from $I(\epsilon)$ allowing for the influence of $A(\epsilon)$ we do the following

1. Since A, while significant, is never large or rapidly varying, obtain a first approximation to the primary $I_o(\epsilon)$ as a power–law $\sim \epsilon^{-\gamma}$ by best fitting the total data $I_{tot}(\epsilon)$ to a power–law index γ (essentially taking A = constant to zeroth order).

2. Use the best fit γ from 1 with the Bai & Ramaty results on $A_\gamma(\epsilon)$ for that power law $I_o(\epsilon)$ to obtain a first order estimate of $A_{I_o}(\epsilon)$ using Eq. 2.2.

3. Adopt this $A_\gamma(\epsilon)$ in Eq. 2.1 to derive a first order albedo–corrected $I_o(\epsilon) = I_{tot}(\epsilon)/(1 + A_\gamma(\epsilon))$.

To make this easy to do in practice we have explored convenient parameterized forms of $A_\gamma(\epsilon)$ and best fit the (γ dependent) parameters to the Bai & Ramaty results for each of the four different γ values which they simulated. We found a convenient form was

$$A_\gamma(\epsilon) = A_o(\gamma)\,(\epsilon)^{a(\gamma)}\,e^{-b(\gamma)(\epsilon)} \tag{2.3}$$

where ϵ is in units of $10keV$ and the best fit values for of A_0, a, and b are given in Table 2.3. In figure (2.2) (a)–(d) we show the Bai & Ramaty $A_\gamma(\epsilon)$ results with our best fit superimposed.

[1]The heliocentric angle is the angle between the solar surface normal and the line of sight to the observer.

γ	A_o	a	b
2	0.0077	1.53	0.31
3	0.0088	1.46	0.34
4	0.0098	1.41	0.37
5	0.0111	1.34	0.38

Table 2.1: Best fit parameters to the Bai & Ramaty data

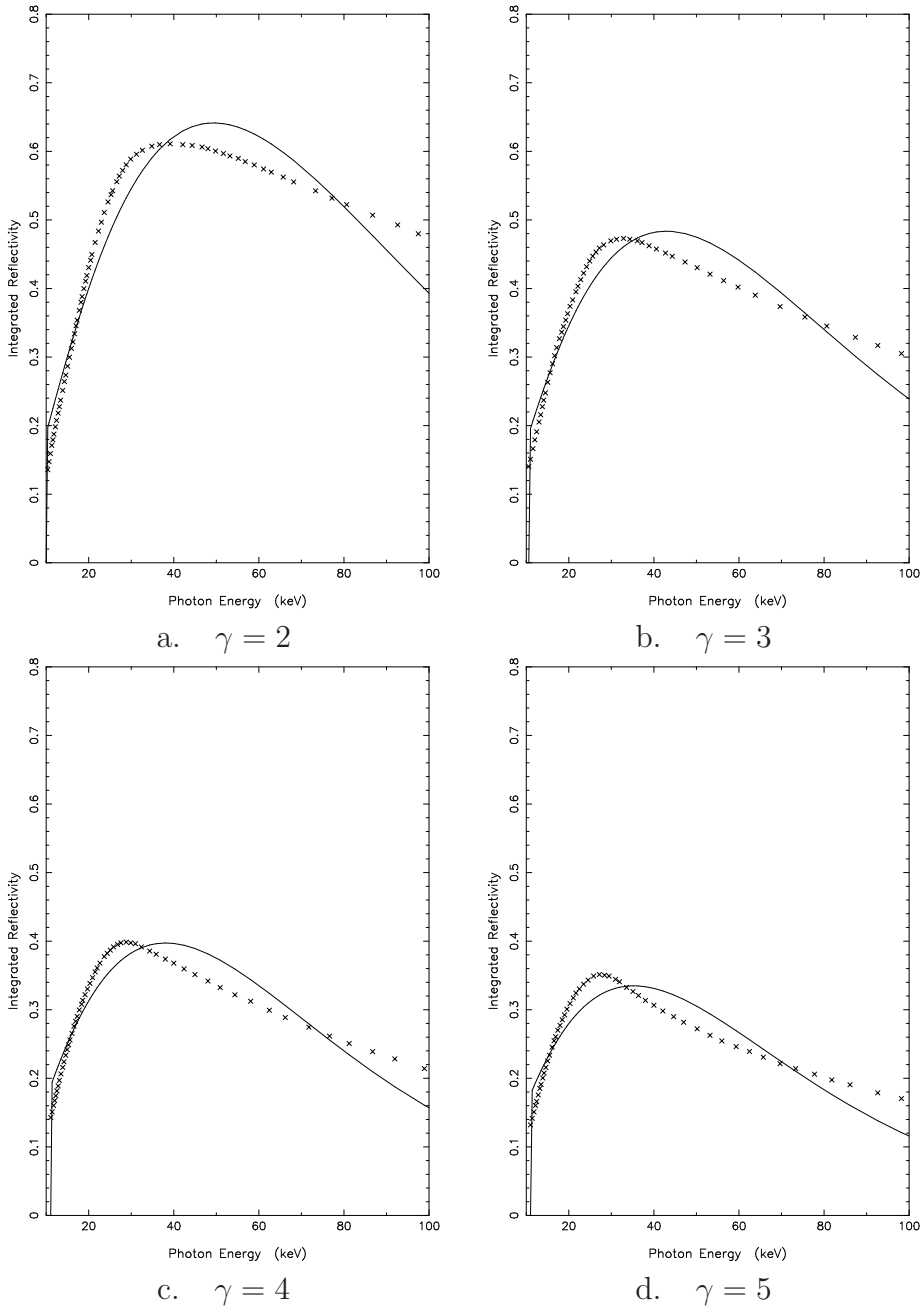

a. $\gamma = 2$ b. $\gamma = 3$

c. $\gamma = 4$ d. $\gamma = 5$

Figure 2.2: Plots of best fit parameters, along with the Bai & Ramaty data.

Figures 2.2.a.–2.2.d. show the plots of the best–fit parameters given in Table 2.3 for $A_o(\gamma)$, a(γ), & b(γ) substituted into (2.3) (*full line*) compared with the Bai & Ramaty data plots for the four values of γ studied (*crosses*).

Bai & Ramaty only computed 4 cases of γ. To extend these fits empirically to general γ we show in Figures 2.3.(a).–2.3.(c). plots of $A_o(\gamma)$, a(γ), & b(γ) versus γ with smooth fits through these 4 points.

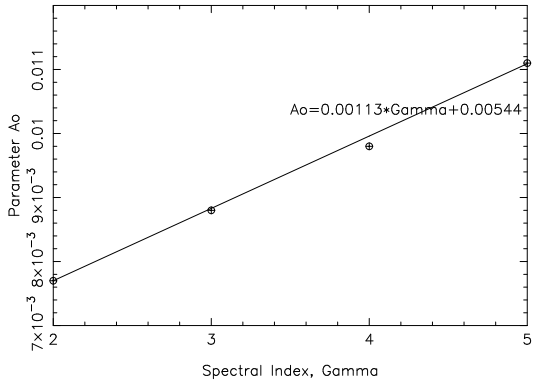

a. Linear fit for parameter A_o versus γ

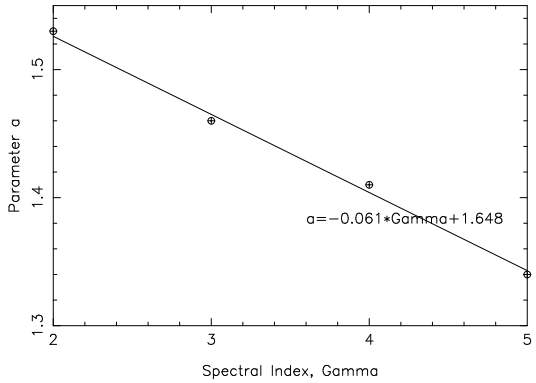

b. Linear fit for parameter a versus γ

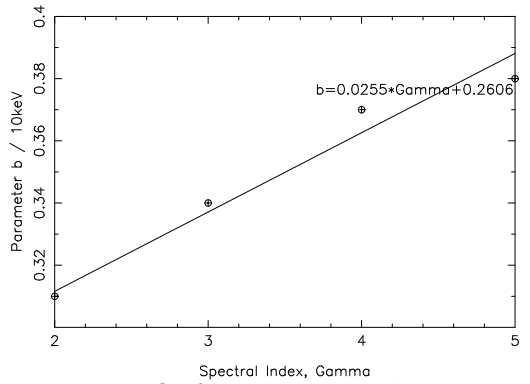

c. Linear fit for parameter b versus γ

Figure 2.3: Plots of linear fits for the parameters $A_o(\gamma)$, a(γ), & b(γ)

Figures 2.3.a.– 2.3.c. show the plots of the best–fit parameters given in Table 2.3 for $A_o(\gamma)$, a(γ), & b(γ). A smooth fit *straight line* through the data points is shown for each parameter.

2.4 Effect of Albedo Correction on Inferred Electron Spectra

2.4.1 Formulation

Given $I_o(\epsilon)$, one can derive the source mean electron spectrum $\bar{F}(E)$ ("thin–target") and the collisional thick target electron injection spectrum $\mathcal{F}_o(E_o)$ by inversion of the bremstrahlung spectral integral. This was shown analytically by Brown (1971) for the Bethe–Heitler cross section and by Brown and Emslie (1988) for the Kramers Cross–Section. Here we use the Kramer's analytic case to demonstrate how large the effect of $A(\epsilon)$ can be on the inference of source electron spectra. Specifically we:

- (a) consider cases where the primary electron spectra are in fact power–law (thin target $E^{-\delta}$ or thick target $E_o^{-\delta}$), resulting in power–law $\epsilon^{-\gamma}$ in both cases (with $\gamma = \delta + 1, \delta - 1$ respectively)

- (b) generate the total $I_{tot}(\epsilon) = I_o(\epsilon)(1 + A(\epsilon))$ that would be observed using equation (2.3).

- (c) Use the analytic inversion formulae to find out what $\bar{F}(E)$, $\mathcal{F}_o(E_o)$ would be derived from that $I_{tot}(\epsilon)$ if albedo were ignored, i.e. if it were assumed that $I_o = I_{tot}$.

The Kramers approximation to the bremstrahlung cross–section is

$$Q(\epsilon, E) = \frac{Q_o}{\epsilon E}$$

where Q_o is a constant.

2.4.2 Thin Target Inversion

For this case the solution for the mean (thin target) electron spectrum $\bar{F}(E)$ in a source of mean density $\bar{n}_p$, volume V is (Brown & Emslie 1988)

$$\bar{F}(E) = \frac{1}{\bar{n}_p V Q_o} E \left[-\frac{d}{d\epsilon}(\epsilon I_{tot}(\epsilon)) \right]_{\epsilon=E} \tag{2.4}$$

We can evaluate the expression within the brackets as follows

$$\left[\frac{d}{d\epsilon}(\epsilon I_o(\epsilon)) \right] = I_o(\epsilon) + \epsilon I_o^{'}(\epsilon) \tag{2.5}$$

which in the case of a power law

$$I_o(\epsilon) = C\epsilon^{-\gamma} \tag{2.6}$$

where

$$I_o^{'}(\epsilon) = -\gamma C \epsilon^{-\gamma-1} = -\frac{\gamma}{\epsilon} C\epsilon^{-\gamma} = -\frac{\gamma}{\epsilon} I_o(\epsilon) \tag{2.7}$$

gives

$$\frac{d}{d\epsilon}(\epsilon I_o(\epsilon)) = (1-\gamma) I_o(\epsilon) \tag{2.8}$$

and substituting (2.8) into (2.5) and then in turn (2.5) into (2.4) yields

$$\bar{F}(E) \equiv \bar{F}_o(E) = \frac{(\gamma-1)C}{\bar{n}_p V Q_o} E^{-\gamma+1} \tag{2.9}$$

However, in reality we observe as the true solution $I_{tot} = I_o(1 + A(\epsilon))$ rather than I_o so that

$$\left[\frac{d}{d\epsilon}(\epsilon I_{tot}(\epsilon)) \right] = \frac{d}{d\epsilon} \left[\epsilon I_o(\epsilon) \left(1 + A(\epsilon)\right) \right] \tag{2.10}$$

$$= \frac{d}{d\epsilon} \left[\epsilon I_o(\epsilon) \right] \left(1 + A(\epsilon)\right) + \epsilon I_o(\epsilon) \frac{d}{d\epsilon} \left(1 + A(\epsilon)\right) \tag{2.11}$$

$$= \left[I_o(\epsilon) + \epsilon I_o^{'}(\epsilon) \right] \left(1 + A(\epsilon)\right) + \epsilon I_o(\epsilon) A^{'}(\epsilon) \tag{2.12}$$

The derivative of our form (2.3) for A gives

$$A^{'}(\epsilon) = a A_o \epsilon^{a-1} e^{-b\epsilon} + (-b) A_o \epsilon^a e^{-b\epsilon} \tag{2.13}$$

$$A^{'}(\epsilon) = A_o \epsilon^a e^{-b\epsilon} \left(\frac{a}{\epsilon} - b \right) \tag{2.14}$$

$$A^{'}(\epsilon) = A(\epsilon)\left(\frac{a}{\epsilon} - b\right) \tag{2.15}$$

Substituting (2.15) and (2.7) into (2.12) gives

$$\left(I_o(\epsilon) - \gamma I_o(\epsilon)\right)\left(1 + A(\epsilon)\right) + \epsilon I_o(\epsilon)A(\epsilon)(\frac{a}{\epsilon} - b) \tag{2.16}$$

and grouping by $I_o(\epsilon)$ terms gives

$$\left[\frac{d}{d\epsilon}(\epsilon I_{tot}(\epsilon))\right] = I_o(\epsilon)\left[(1-\gamma)(1+A(\epsilon)) + \epsilon A(\epsilon)(\frac{a}{\epsilon} - b)\right] \tag{2.17}$$

simplifying (2.17) gives

$$I_o(\epsilon)\left[1 - \gamma + A(\epsilon)\left(1 + a - (\gamma + b\epsilon)\right)\right] \tag{2.18}$$

inserting (2.18) into (2.4) gives

$$\bar{F}(E) = -\frac{1}{\bar{n}_p V Q_o} E\left[I_o(\epsilon)\left[1 - \gamma + A(\epsilon)\left(1 + a - (\gamma + b\epsilon)\right)\right]\right]_{\epsilon=E} \tag{2.19}$$

and evaluating (2.19) gives

$$\bar{F}(E) = -\frac{1}{\bar{n}_p V Q_o} E\left[I_o(E)\left[1 - \gamma + A(E)\left(1 + a - (\gamma + bE)\right)\right]\right] \tag{2.20}$$

We can now see that if we ignore the albedo correction by misidentifying I_{tot} ((2.1) & (2.6)) with I_o then by (2.4), we would infer

$$\bar{F}(E) = \frac{(\gamma-1)C}{\bar{n}_p V Q_o} E^{-\gamma+1}\left[1 - A_o E^a e^{-bE}\frac{\left(1 + a - (\gamma + bE)\right)}{\gamma - 1}\right] \tag{2.21}$$

which is shown in Figures 2.4.(a).– 2.4.(d). or equivalently a mean electron spectrum wrong by a fractional error

$$f_{thin}(\gamma) = \frac{\Delta\bar{F}(E)}{\bar{F}_o(E)} = \frac{\bar{F}(E) - \bar{F}_o(E)}{\bar{F}_o(E)} = \frac{A_o E^a e^{-bE}\left[(\gamma + bE) - (a+1)\right]}{\gamma - 1} \tag{2.22}$$

which is shown in Figure 2.5.

2.4.3 Thick Target

Here the relevant electron spectrum is the total thick target electron injection rate $\mathcal{F}_o(E_o)$ electrons per s^{-1} per unit E_o and for the Kramers Q_B is given from the photon spectrum by Brown & Emslie (1988) (with $K = 2\pi e^4 \Lambda$ and Λ is the coulomb logarithm)

$$\mathcal{F}_o(E_o) = \frac{K}{Q_o}\left[\frac{d^2}{d\epsilon^2}(\epsilon I_o(\epsilon))\right]_{\epsilon=E_o} \tag{2.23}$$

Now for a primary power law $I_o(\epsilon)$, (2.6), when the albedo is neglected then the differentiation gives

$$\left[\frac{d^2}{d\epsilon^2}(\epsilon I_o(\epsilon))\right] = \frac{d}{d\epsilon}\left[\frac{d}{d\epsilon}(\epsilon I_o(\epsilon))\right] = \frac{d}{d\epsilon}\left[(1-\gamma)I_o(\epsilon)\right] = \frac{\gamma(\gamma+1)}{\epsilon}I_o(\epsilon) \tag{2.24}$$

therefore for a primary power law $I_o(\epsilon)$ this leads to

$$\mathcal{F}_o(E_o) = \frac{K}{Q_o}C(\gamma-1)E_o^{-\gamma-1} \tag{2.25}$$

while if the albedo correction is added to I_o we must evaluate the expression within the brackets as follows. We can differentiate (2.10) as follows

$$\frac{d^2}{d\epsilon^2}\left[\epsilon I(\epsilon)\right] = \frac{d}{d\epsilon}\left[\frac{d}{d\epsilon}(\epsilon I(\epsilon))\right] = \frac{d}{d\epsilon}\left[(I_o(\epsilon)+\epsilon I_o^{'}(\epsilon))(1+A(\epsilon)) + \epsilon I_o(\epsilon)A^{'}(\epsilon)\right] \tag{2.26}$$

If we express (2.26) as

$$\frac{d}{d\epsilon}\left[(I_o(\epsilon)+\epsilon I_o^{'}(\epsilon))(1+A(\epsilon))\right] + \frac{d}{d\epsilon}\left[\epsilon I_o(\epsilon)A^{'}(\epsilon)\right] \tag{2.27}$$

we can evaluate the first part of equation (2.27) as follows

$$\begin{aligned}\frac{d}{d\epsilon}\left[(I_o(\epsilon)+\epsilon I_o^{'}(\epsilon))(1+A(\epsilon))\right] &= \frac{d}{d\epsilon}\left((I_o(\epsilon)+\epsilon I_o^{'}(\epsilon))(1+A(\epsilon))\right) \\ &+ \left[(I_o(\epsilon)+\epsilon I_o^{'}(\epsilon)\right]\frac{d}{d\epsilon}\left(1+A(\epsilon)\right)\end{aligned} \tag{2.28}$$

which gives

$$\left(2I_o^{'}(\epsilon)+\epsilon I_o^{''}(\epsilon)\right)\left(1+A(\epsilon)\right) + \left(I_o(\epsilon)+\epsilon I_o^{'}(\epsilon)\right)A^{'}(\epsilon) \tag{2.29}$$

We can also evaluate the second part of equation (2.27) to give

$$\frac{d}{d\epsilon}\left[\epsilon I_o(\epsilon)A^{'}(\epsilon)\right] = \left(I_o(\epsilon) + \epsilon I_o^{'}(\epsilon)\right)A^{'}(\epsilon) + (\epsilon I_o(\epsilon)A^{''}(\epsilon)) \tag{2.30}$$

Finally combining (2.29) and (2.30) gives

$$\begin{aligned}\frac{d^2}{d\epsilon^2}\left[\epsilon I(\epsilon)\right] = (2I_o^{'}(\epsilon) + \epsilon I_o^{''}(\epsilon))(1 + A(\epsilon)) + (I_o(\epsilon) + \epsilon I_o^{'}(\epsilon))A^{'}(\epsilon) + \\ (I_o(\epsilon) + \epsilon I_o^{'}(\epsilon))A^{'}(\epsilon) + \epsilon I_o(\epsilon)A^{''}(\epsilon)\end{aligned} \tag{2.31}$$

Using the derivatives of $A^{'}(\epsilon)$ (2.15) and $I^{'}(\epsilon)$ (2.7) which are given by

$$A^{''}(\epsilon) = A(\epsilon)\left[(\frac{a}{\epsilon} - b)^2 - \frac{a}{\epsilon^2}\right] \tag{2.32}$$

and

$$I_o^{''}(\epsilon) = \frac{d}{d\epsilon}\left[-\frac{\gamma}{\epsilon}I_o(\epsilon)\right] = \frac{\gamma(\gamma+1)}{\epsilon^2}I_o(\epsilon) \tag{2.33}$$

we can substitute (2.33),(2.32), (2.15) and (2.7) into (2.31) to give

$$\begin{aligned}\frac{d^2}{d\epsilon^2}\left[\epsilon I(\epsilon)\right] = (-2\frac{\gamma}{\epsilon}I_o(\epsilon) + \epsilon\frac{\gamma(\gamma+1)}{\epsilon^2}I_o(\epsilon))(1 + A(\epsilon)) + \\ (-\frac{\gamma}{\epsilon}I_o(\epsilon) + \epsilon(-\frac{\gamma}{\epsilon}I_o(\epsilon)))A(\epsilon)\left(\frac{a}{\epsilon} - b\right) + \\ (I_o(\epsilon) + \epsilon - \frac{\gamma}{\epsilon}I_o(\epsilon))A(\epsilon)\left(\frac{a}{\epsilon} - b\right) + \epsilon I_o(\epsilon)A(\epsilon)\left[(\frac{a}{\epsilon} - b)^2 - \frac{a}{\epsilon^2}\right]\end{aligned} \tag{2.34}$$

and grouping together like terms and inserting into (2.23) gives $\mathcal{F}_o(E_o)$ if I_{tot} is misinterpreted as I_o, namely

$$\begin{aligned}\mathcal{F}(E_o) = \frac{K}{Q_o}CE_o^{-\gamma} \times \left[\frac{\gamma}{E_o}(\gamma - 1) + A_o\epsilon^a e^{-b\epsilon}\left((\gamma-1)(\frac{\gamma}{E_o} - 2(\frac{a}{E_o} - b)) + \right.\right. \\ \left.\left. E_o\left((\frac{a}{E_o} - b)^2 - \frac{a}{E_o^2}\right)\right)\right]\end{aligned} \tag{2.35}$$

which is incorrect by a fractional amount

$$\begin{aligned}f_{thick}(\gamma) = \frac{\mathcal{F}(E_o) - \mathcal{F}_o(E_o)}{\mathcal{F}_o(E_o)} &= \frac{A_o\epsilon^a e^{-b\epsilon}E_o}{\gamma(\gamma-1)} \times \left[(\gamma-1)(\frac{\gamma}{E_o} - 2(\frac{a}{E_o} - b)) + \right. \\ &\left. E_o\left((\frac{a}{E_o} - b)^2 - \frac{a}{E_o^2}\right)\right]\end{aligned} \tag{2.36}$$

which is shown in Fig. 2.7

2.4.4 Resulting Correction for the Kramers Cross Section

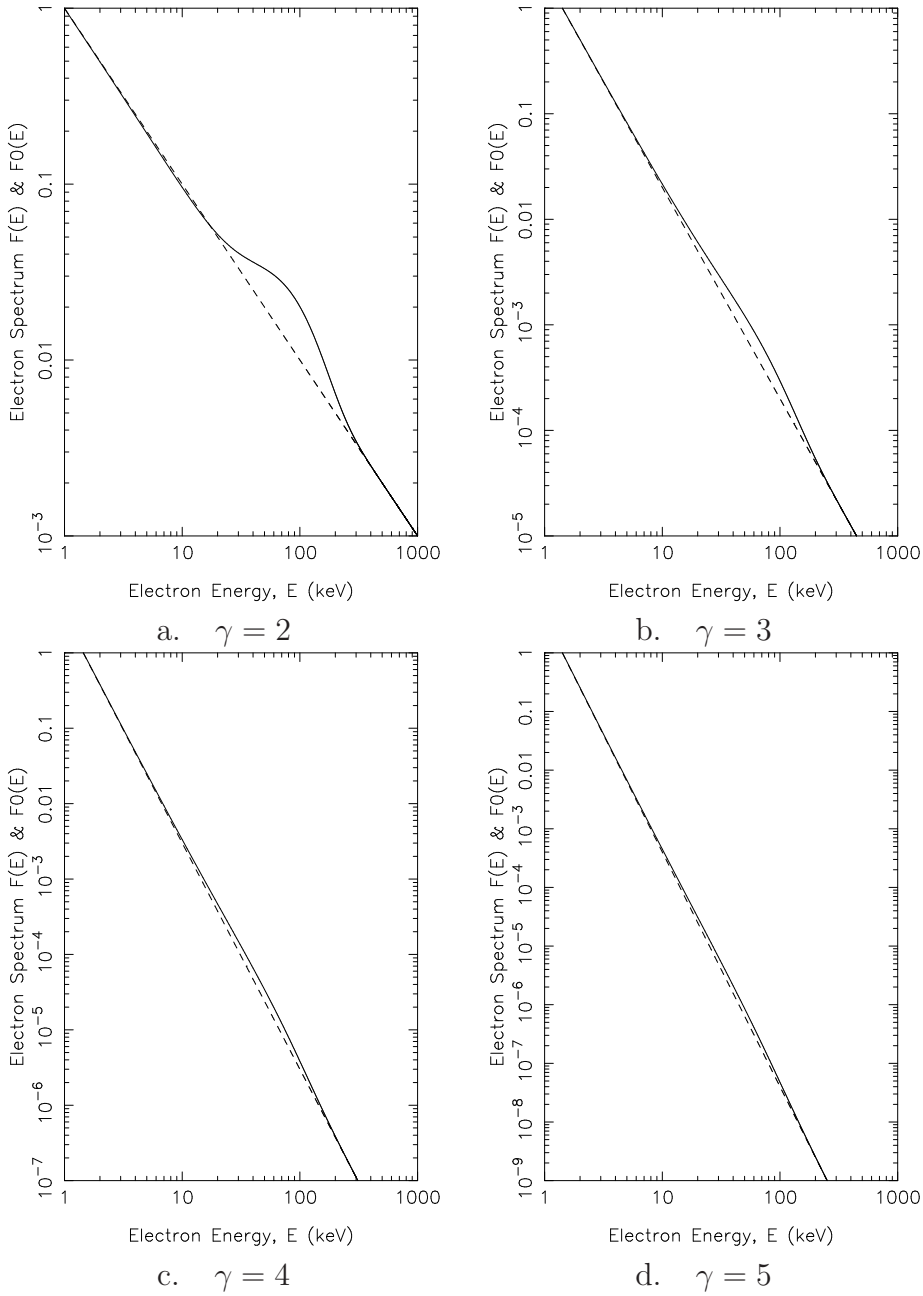

Figure 2.4: Plots of the Kramers recovered thin target electron spectra

Figures 2.4.(a).–2.4.(d). show the plots of the Kramers recovered thin target electron spectra (*full lines*) along with their respective primary electron spectrum (*broken lines*) for the four values of γ studied. The error in the recovered spectrum can be observed as a 'bump' in the spectrum.

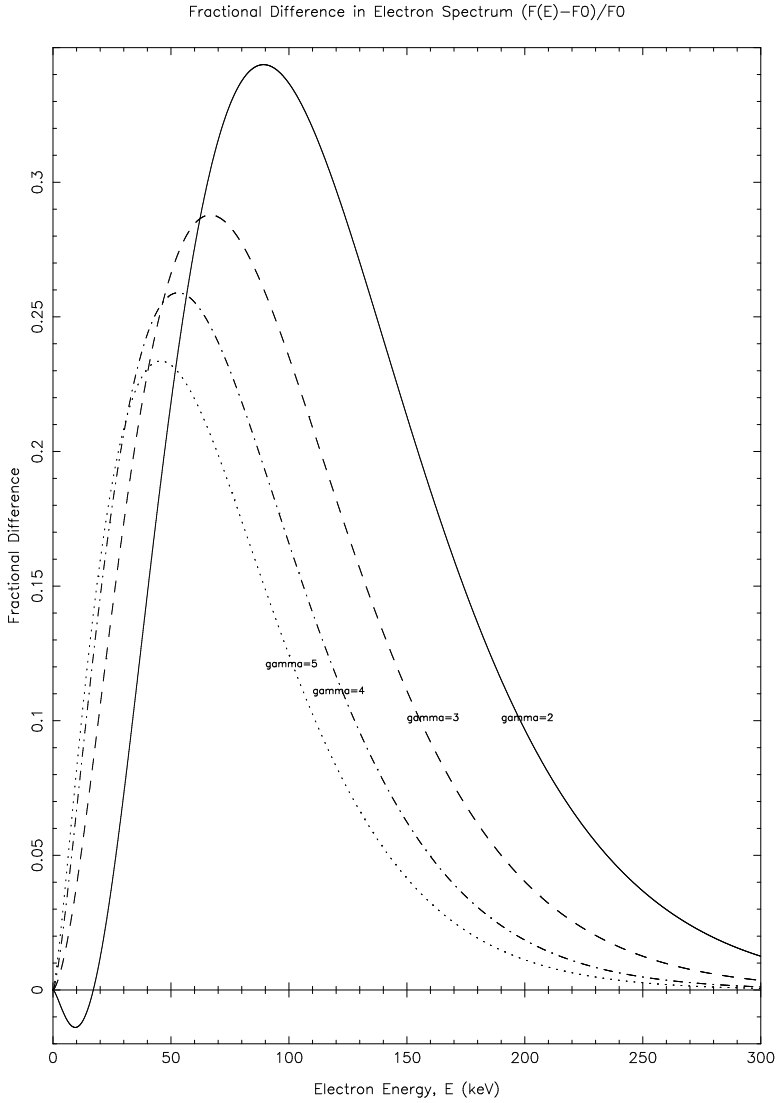

Figure 2.5: Fractional difference between the observed and primary thin target (Kramer's) electron spectrum showing the fractional difference decreasing with increasing γ

Figure 2.5 shows the fractional difference decreasing as γ increases. It also shows that the inferred electron flux at 'X' keV will be *greater* by 'Y' percent when the effect of an albedo has been included. This percentage also varies with energy. For example, at 100 keV, an error of approximately 35 percent is obtained for $\gamma = 2$.

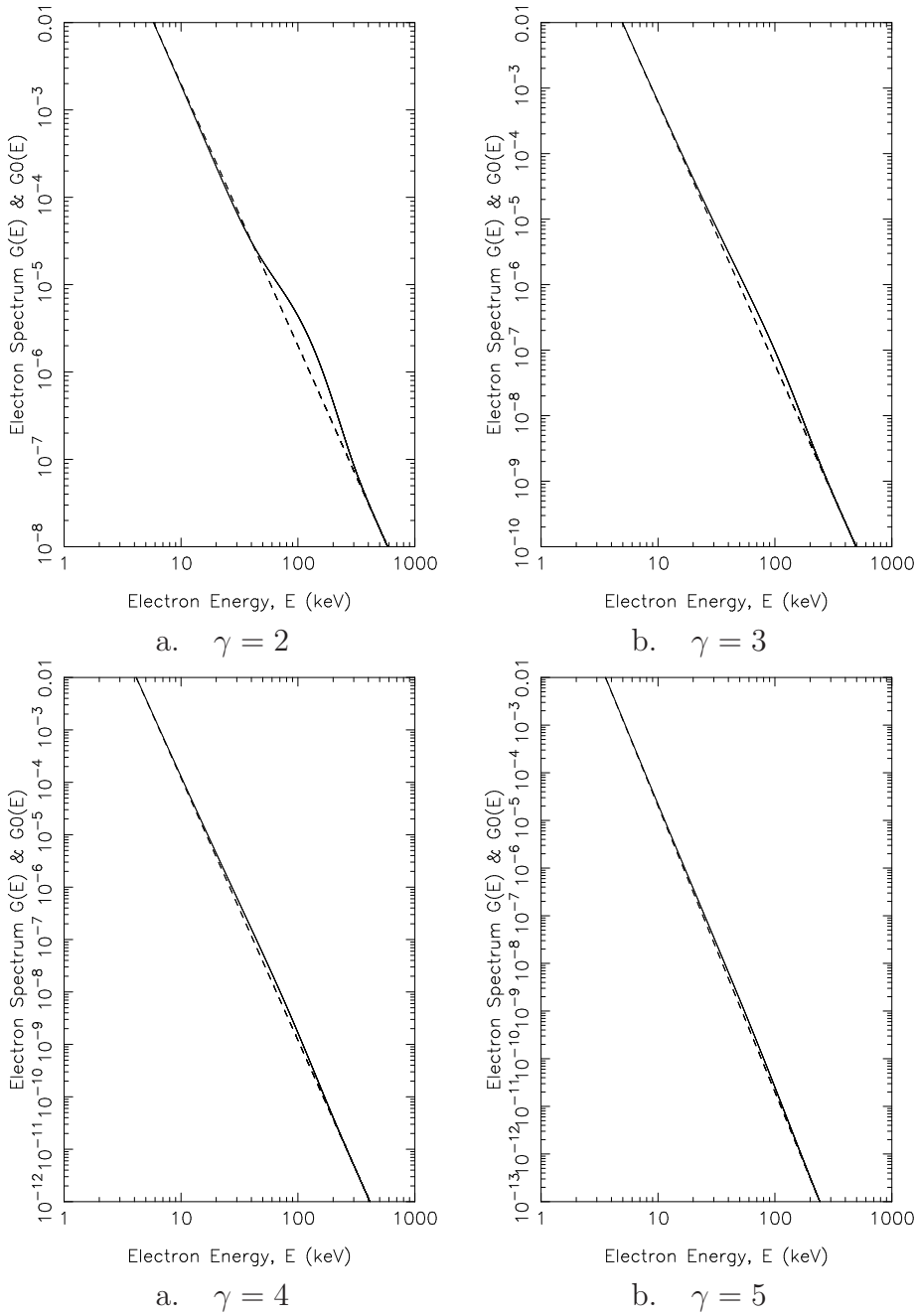

Figure 2.6: Plots of the Kramers recovered thick target electron spectra

Figures 2.6.(a).–2.6.(d). show the log plots of the Kramers recovered thick target electron spectra $\mathcal{F}(E_o)$ (*full lines*) along with their respective primary electron spectra $\mathcal{F}_o(E_o)$ (*broken lines*) for the four values of γ studied.

Figure 2.7 shows the fractional difference decreasing as γ increases. As previously mentioned for the thin target case, there is an energy dependent difference in the

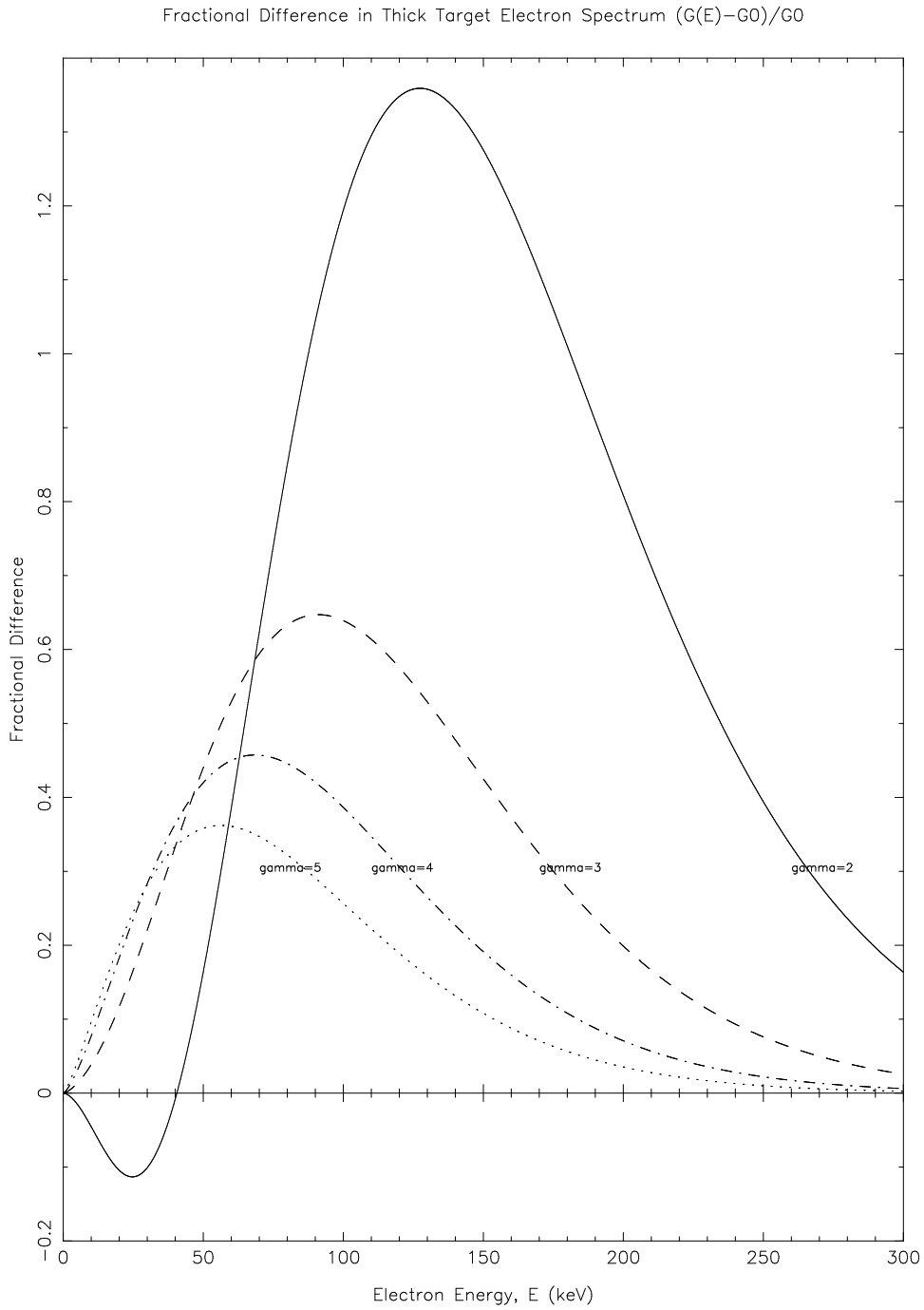

Figure 2.7: Fractional difference between the observed and primary thick target electron spectrum

inferred electron flux where the effect of an albedo has been included. It is also apparent from Figure 2.7 that the error in the thick target is significantly greater than in the thin target case.

2.5 Discussion

RHESSI spectra have not been reported as exhibiting evident spectral bulges like those shown in Figures 2.4.(a)–2.4.(d) and 2.6.(a)–2.6.(d).

In order to redress this apparent discrepancy the following explanations might be offered:

1. The primary spectrum $I_o(\epsilon)$ has a dip where $A(\epsilon)$ has a bulge, the two offsetting one another. This seems too much of a coincidence to be plausible.

2. The bulges are present but have not been specifically noticed or reported as such since they are usually rather small on a log plot. Subsequent to our present work on this, Kontar and others have claimed that the feature may be present in data and the 'unphysical dips' exhibited in some RHESSI electron spectra can be accounted for by including the albedo.

3. In fact, the lower energy end of the bulge is down around 10keV which may be lost in the thermal emission component. The middle and upper end energy range of the bulge looks somewhat like a downward knee in the deka-keV range. Such features are regularly seen in data - cf. discussion in Kontar, Brown and McArthur (2002) Albedo may thus be a partial explanation of these.

4. There are other corrections - especially that for non-uniform target ionisation in the case of thick target primary sources discussed by Kontar, Brown and McArthur (2002) which have been ignored in this chapter. Depending on the depth ('energy') of the transition region , this correction might tend to either augment or hide the effect of albedo on the spectrum.

5. The assumption of an isotropic, point source (Bai & Ramaty 1978) which provided our source data for $A(\epsilon)$ may require modification.

2.6 Conclusion

In this chapter we have explored the effect of photospheric albedo on observations of global flare hard X-ray spectra and derived an expression to allow approximate correction for this in the case of primary power-law photon spectra. We have also examined, for the Kramers cross-section, the consequences of ignoring the albedo

correction in using observed spectra to infer flare source electron spectra for thin and thick target interpretations and shown that the effects are very significant in terms of inferred spectral shape, especially for hard spectra. We have not extended the analysis to other cross sections but we note that the effects of albedo on deriving electron spectra will be even larger for more realistic smoother cross-section approximations, such as the Bethe Heitler, than for Kramers because they filter the electron spectral features even more. This is confirmed by our preliminary results for the Bethe Heitler case, to be presented in future work. We also note that the effects of albedo should be considered alongside other corrections such as that of nonuniform target ionisation in the case of the thick target beam model as discussed by Kontar, Brown and McArthur (2002).

In the following chapters some of the assumptions will be revised such as anisotropic source emission (directivity) and by using more sophisticated inversion techniques such as those developed by Kontar and Poutanen to be able to approximate more closely actual solar conditions.

Chapter 3

An Empirical Albedo Correction of Anisotropic Power Law Primary Photon Emission and its Effects on Recovered Electron Spectra

3.1 Introduction

In chapter 2 we studied the effects of ignoring the albedo on the inferred parent electron spectrum from an isotropically emitted photon spectrum. We argued that as we observed $I_{tot} = I_o(1 + A(\epsilon))$ rather than I_o then ignoring albedo would lead to an incorrect electron spectrum and found that both the form and magnitude of this error was dependent on the cross section assumed in the inversion (Kramers or Bethe–Heitler). In order to investigate this effect analytically we adopted a simplified, empirical approach. Here we extend that approach to the case of an anisotropic primary photon source, for the case of Kramers cross-section (chapter 2).

3.2 Anisotropic Emission - The Eddington Hemispheric Approximation

We use a simple method to approximate anisotropic emission in this chapter based upon the *Eddington approximation* (equation 3.1). The Eddington approximation originates from the study of radiative transfer and is the assumption that the ratio of the second moment of the radiation field to the mean intensity is equal

everywhere, to the value of the ratio for an isotropic field (Tandberg-Hanssen & Emslie 1988).

Here we use the Eddington approximation to simulate anisotropy within the primary photon emission. We do this as follows:

1. We can treat the emission as two separate hemispheres - the upwards and the downwards hemisphere (relative to the surface of the photosphere) - I_o^{up} and I_o^{down} respectively. We assume that the emission within each hemisphere is isotropic *i.e.* averaged in θ (and ϕ - the emission is azimuthally symmetric).

2. The amount of emission into each hemisphere can be varied to simulate the degree to which the emission is anisotropic.

We can express the primary photon spectrum mathematically as

$$I_o(\epsilon, \mu) = \begin{cases} I_o^{up}(\epsilon) & 0 \leq \mu < 1 \\ I_o^{down}(\epsilon) & -1 \leq \mu < 0 \end{cases} \tag{3.1}$$

where $\mu = cos(\theta)$ the angle at which primary HXR photons are emitted[1].
We can illustrate the Eddington hemispheric approach to anisotropy by using a surface area analogy. This is illustrated in Figure 3.1 below.

[1] μ is measured relative to the normal to the solar surface with $\mu = -1$ representing the downwards direction.

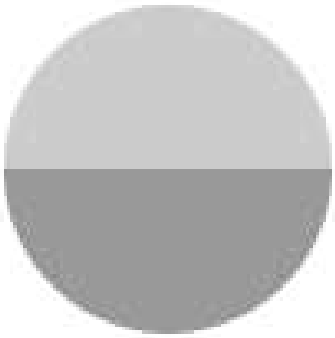

a. Isotropic emission

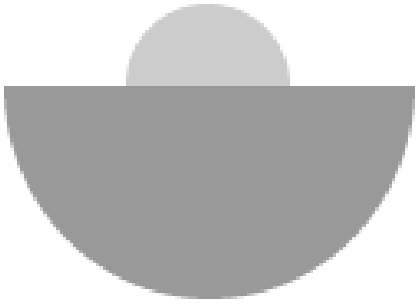

b. Slightly anisotropic emission

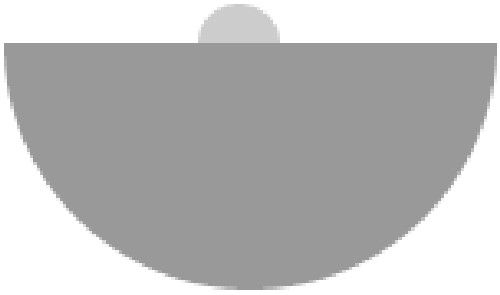

c. Highly anisotropic emission

Figure 3.1: Polar diagram or surface area represention of the anisotropic HXR photon spectrum using the Eddington approximation. The size of each hemisphere represents the fraction of emission emitted into the respective hemisphere but it is important to note that total emission remains the same.

We introduce the idea of a simple model of anisotropic emission into (3.1) by the use of a multiplier $\alpha(\epsilon)_{down}$ which represents the fraction of the total primary photon spectrum emission which is emitted into the downward hemisphere at energy ϵ[2].

Clearly to conserve emission then

$$\alpha(\epsilon)_{up} = 1 - \alpha(\epsilon)_{down} \tag{3.2}$$

where $\alpha(\epsilon)_{up}$ represents the fraction of the total primary photon spectrum emission which is emitted into the upward hemisphere at energy ϵ.
We now express the primary emission in an anisotropic form using an α however we need to ensure that our anisotropic model is compatible with the isotropic model of Alexander & Brown (2002). We do this by considering the following reasoning.

Suppose I_o is the same for all μ and the primary source at some specific energy ϵ has specific intensity $I_o(\mu)$. For the isotropic case, the total source power $L = \int I_o d\Omega$ at energy ϵ is $4\pi I_o$.

The resulting observed isotropic photon spectrum $I(\epsilon)$ in that case is thus

$$I(\epsilon) = I_o(\epsilon) + A(\epsilon)I_o(\epsilon) = I_o(\epsilon)\left[1 + A(\epsilon)\right] \tag{3.3}$$

note that $I = 2I_o(\epsilon)$ if $A(\epsilon) = 1$. For Eddington anisotropy, using (3.2), we can express (3.3) as

$$I(\epsilon) = 2\left[(1-\alpha)I_o(\epsilon) + A(\epsilon)\alpha I_o(\epsilon)\right] \tag{3.4}$$

We note that in the isotropic case ($\alpha = \frac{1}{2}$) equation (3.4) reduces to (3.3) and conserves

$$L = 2\pi I_{up} + 2\pi I_{down} = 4\pi\left[(1-\alpha)I_o + \alpha I_o\right] = 4\pi I_o \tag{3.5}$$

A second issue when extending Alexander & Brown 02 to include anisotropy is what to keep constant when looking at the error in the inferred $\bar{F}(E)$ and $\mathcal{F}(E_o)$ when ignoring the albedo.

If we take L and I_o as constant and use equations (3.3) to (3.4) for I to find F then there are two sources of error - the first is assuming isotropy and the other is neglecting albedo. Even if $A(\epsilon) = 0$ we would get the wrong $F(\epsilon)$ because $I(\epsilon)$

[2]This is only a convenient definition used to simplify the mathematical calculation.

is not equal to $I_o(\epsilon)$. What is actually fixed is what the observer sees, namely $I_{up} = 2(1-\alpha)I_o(\epsilon)$ in the absence of albedo.

We can now use the formulation to infer how large an albedo error occurs in $\bar{F}(E)$, $\mathcal{F}_o(E_o)$ by applying the Brown and Emslie inversion expression to $I_{obs}(\epsilon)$ ignoring the fact that this is not the primary $I_o(\epsilon)$ but modified by albedo and anisotropy.

3.2.1 Effect in Inferred $\bar{F}(E)$

Brown & Emslie (1988) find (for Kramers cross section, Q)

$$\bar{F}(E) = \frac{1}{\bar{n}_p V Q_o} E \left[-\frac{d}{d\epsilon}(\epsilon I(\epsilon)) \right]_{\epsilon=E} \tag{3.6}$$

which gives, using equation 3.4

$$\bar{F}(E) = \frac{2E}{\bar{n}_p V Q_o} \left[-\frac{d}{d\epsilon} \left[\epsilon \left(I_o(\epsilon)[(1-\alpha) + A(\epsilon)\alpha] \right) \right] \right]_{\epsilon=E} \tag{3.7}$$

We now refer to α_{down}[3] as simply α and assume that $I(\epsilon)$ and $I_o(\epsilon)$ refer to the anisotropic case unless otherwise stated.
Differentiating the expression within the brackets in (3.7) gives

$$\frac{d}{d\epsilon}\left[\epsilon I(\epsilon)\right] = I(\epsilon) + \epsilon I^{'}(\epsilon) \tag{3.8}$$

and differentiating (3.8) in turn gives

$$I^{'}(\epsilon) = \frac{d}{d\epsilon}\left[2I_o\left[(1-\alpha) + A\alpha\right]\right] \tag{3.9}$$

Substituting (3.9) and (3.8) into (3.8) gives

$$\frac{d}{d\epsilon}\left[\epsilon I(\epsilon)\right] = 2I_o^{'}(\epsilon)\left[(1-\alpha) + 2A\alpha\right] + I_o(\epsilon)(\alpha A^{'}(\epsilon)) \tag{3.10}$$

At this point (3.10) makes no assumptions about the form of $I(\epsilon)$, $A(\epsilon)$. We now evaluate (3.10) using the functional forms detailed in chapter (2)

$$I_o^{'}(\epsilon) = -\frac{\gamma}{\epsilon} C \epsilon^{-\gamma} = -\frac{\gamma}{\epsilon} I_o(\epsilon) \tag{3.11}$$

and

$$A^{'}(\epsilon) = \frac{d}{d\epsilon}\left[A(\epsilon)\right] = \frac{d}{d\epsilon}\left[A_o \epsilon^a e^{-b\epsilon}\right] = \frac{A(\epsilon)}{\epsilon}(a - b\epsilon) \tag{3.12}$$

[3] α_{up} can be expressed as α_{up}.

and substituting (3.11) and (3.12) into (3.10) we can express $I^{'}(\epsilon)$ as

$$I^{'}(\epsilon) = -\frac{\gamma}{\epsilon} I_o(\epsilon) \left[(1-\alpha) + A\alpha\right] + \alpha I_o(\epsilon) \left(\frac{A(\epsilon)}{\epsilon}\right) (a - b\epsilon) \tag{3.13}$$

and substituting (3.13) and (3.4) into (3.8) gives

$$\frac{d}{d\epsilon}\left[\epsilon I(\epsilon)\right] = I_o(\epsilon) \left[\left((1-\alpha) + A(\epsilon)\alpha\right)(1-\gamma) + \alpha A(\epsilon)(a - b\epsilon)\right] \tag{3.14}$$

Finally inserting (3.14) into (3.6) we obtain the mean anisotropic thin–target electron spectrum as

$$\bar{F}(E) = \frac{2E}{\bar{n}_p V Q_o} \left[I_o(E) \left[\left((1-\alpha) + A(E)\alpha\right)(\gamma - 1) - \alpha A(E)(a - bE)\right]\right] \tag{3.15}$$

From Alexander & Brown (2002) we see that if we actually observe an isotropic spectrum (3.11) then we would infer a mean thin–target electron spectrum of

$$\bar{F}(E) \equiv \bar{F}_o(E) = \frac{(\gamma - 1)C}{\bar{n}_p V Q_o} [E^{-\gamma+1}] \tag{3.16}$$

while for the anisotropic case we would get

$$\bar{F}(E) \equiv \bar{F}_o(E) = \frac{2(\gamma - 1)(1-\alpha)C}{\bar{n}_p V Q_o} [E^{-\gamma+1}] \tag{3.17}$$

Thus we would infer an anisotropic mean electron spectrum wrong by a fractional error of

$$\frac{\Delta\bar{F}(E)}{\bar{F}_o(E)} = \frac{\bar{F}(E) - \bar{F}_o(E)}{\bar{F}_o(E)} \tag{3.18}$$

which substituting (3.15) and (3.17) into (3.18) above gives

$$\frac{\Delta\bar{F}(E)}{\bar{F}_o(E)} = \frac{\left[\left((1-\alpha) + A(E)\alpha\right)(\gamma - 1) - \alpha A(E)(a - bE)\right]}{(\gamma - 1)(1-\alpha)} - 1 \tag{3.19}$$

Results are shown in Figures 3.2 to 3.9 for values of α =0.0625, 0.125, 0.25, 0.5, 0.75, 0.875, 0.95, 0.99.

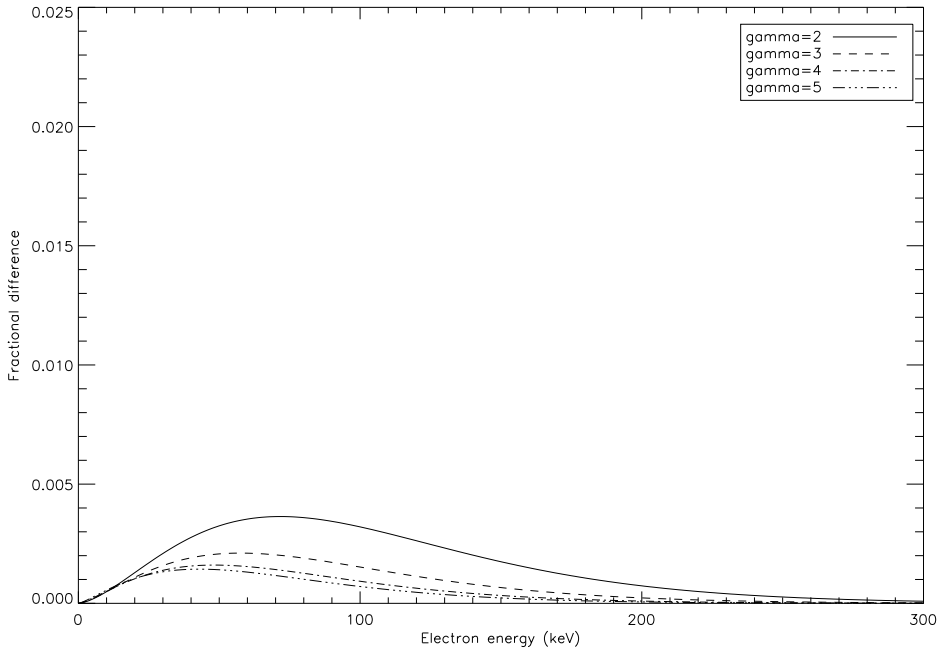

Figure 3.2: Fractional difference between the true and albedo corrupted thin target electron spectra $\bar{F}(E)$ for spectral indexes (γ) of 2-5 ($\alpha = 0.0625$ - *mostly emitted upwards*)

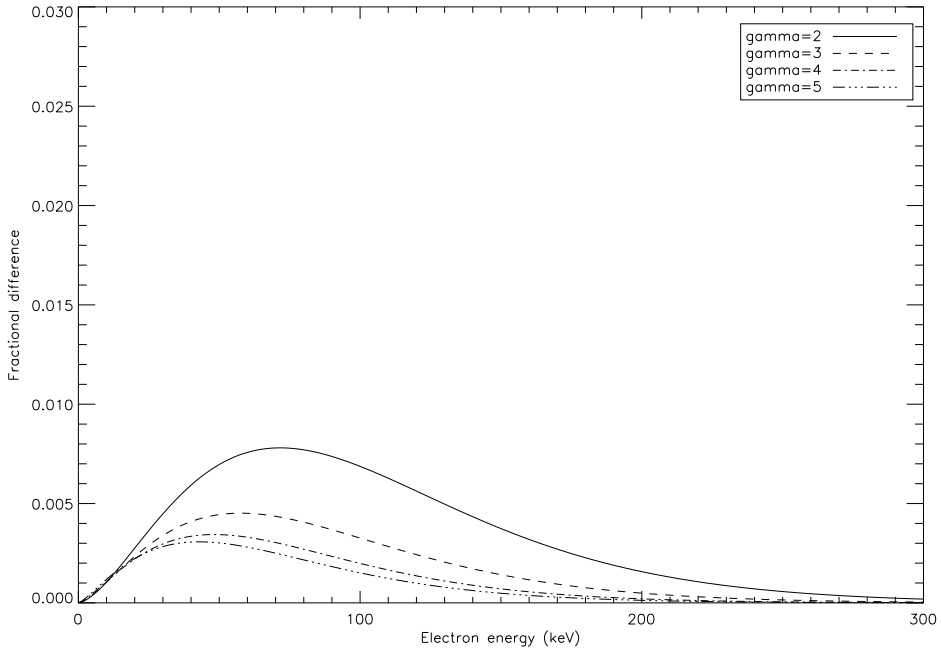

Figure 3.3: Fractional difference between the true and albedo corrupted thin target electron spectra $\bar{F}(E)$ for spectral indexes (γ) of 2-5 ($\alpha = 0.125$)

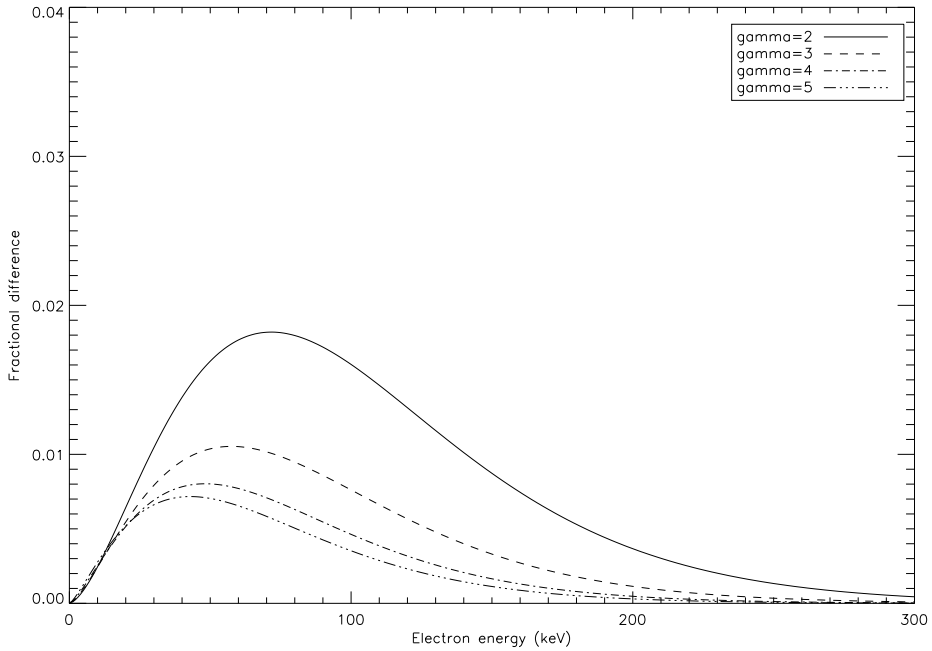

Figure 3.4: Fractional difference between the true and albedo corrupted thin target electron spectra $\bar{F}(E)$ for spectral indexes (γ) of 2-5 ($\alpha = 0.25$)

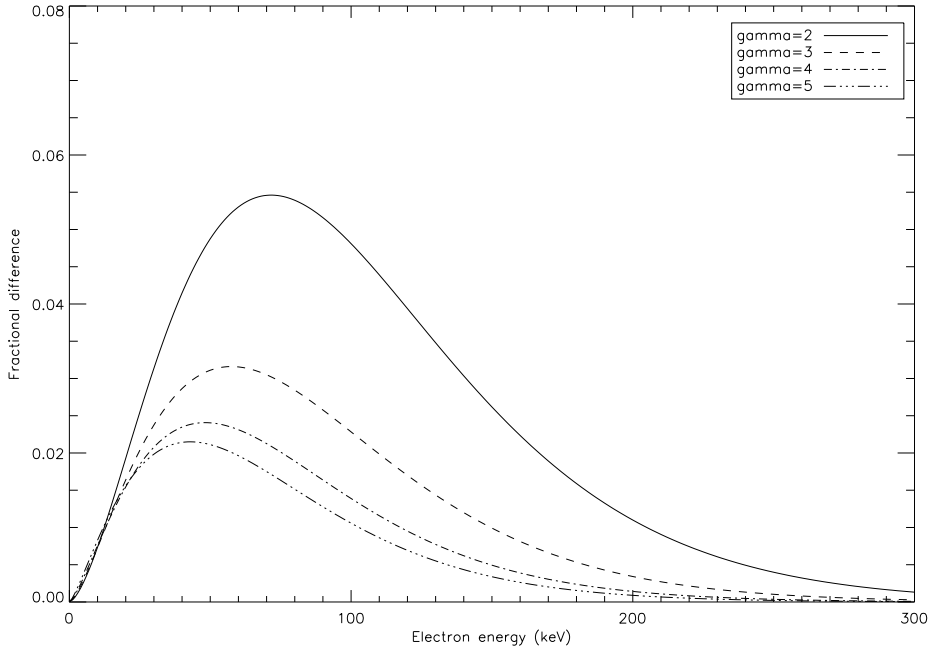

Figure 3.5: Fractional difference between the true and albedo corrupted thin target electron spectra $\bar{F}(E)$ for spectral indexes (γ) of 2-5 ($\alpha = 0.5$)

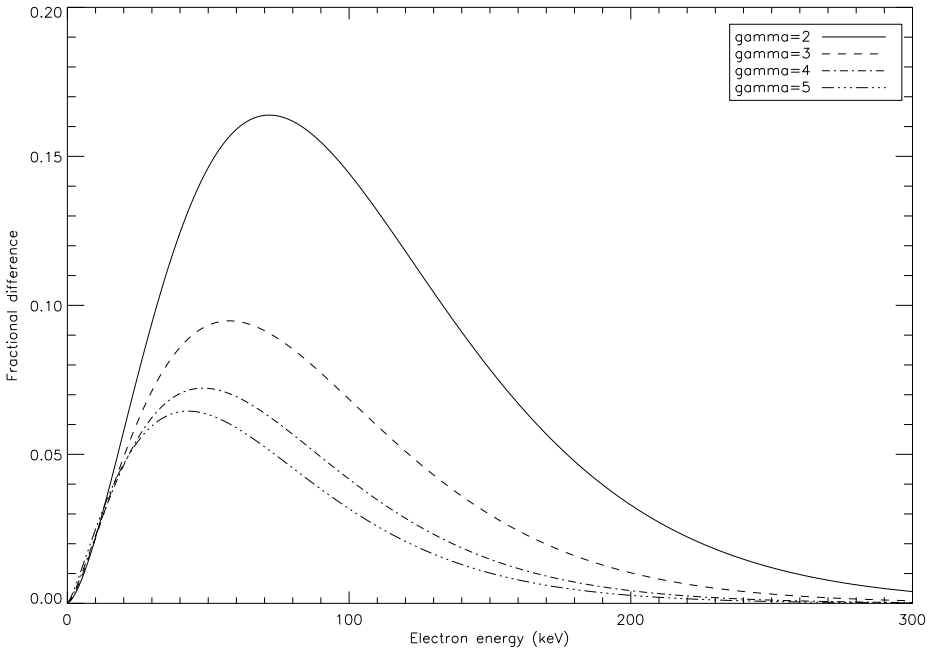

Figure 3.6: Fractional difference between the true and albedo corrupted thin target electron spectra $\bar{F}(E)$ for spectral indexes (γ) of 2-5 ($\alpha = 0.75$)

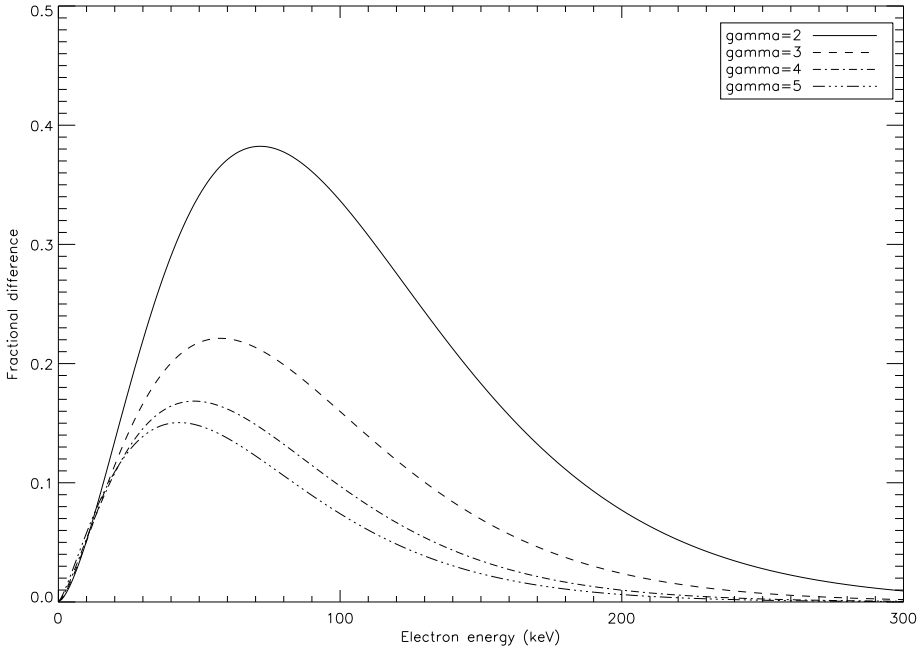

Figure 3.7: Fractional difference between the true and albedo corrupted thin target electron spectra $\bar{F}(E)$ for spectral indexes (γ) of 2-5 ($\alpha = 0.875$)

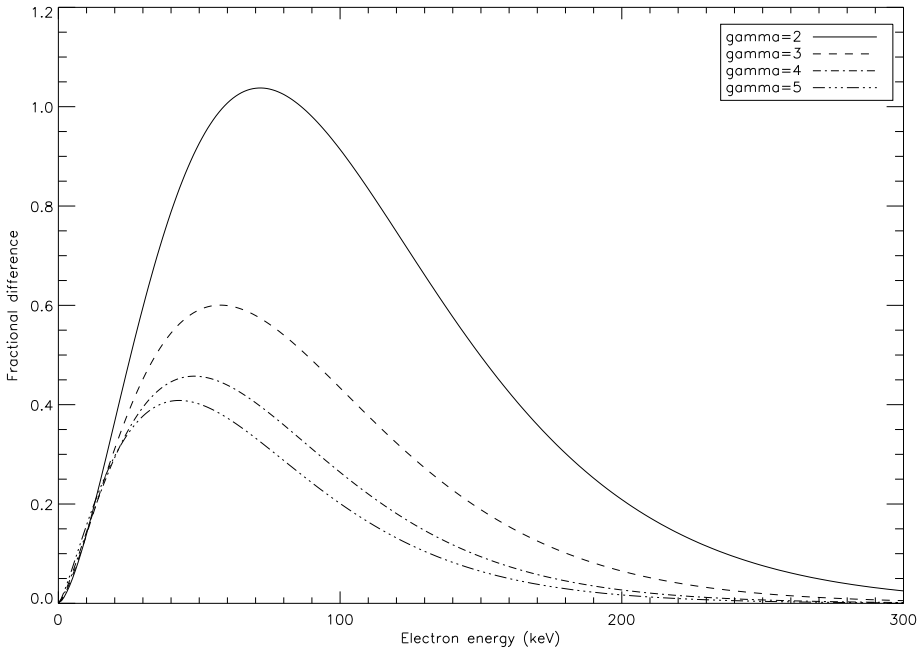

Figure 3.8: Fractional difference between the true and albedo corrupted thin target electron spectra $\bar{F}(E)$ for spectral indexes (γ) of 2-5 ($\alpha = 0.95$)

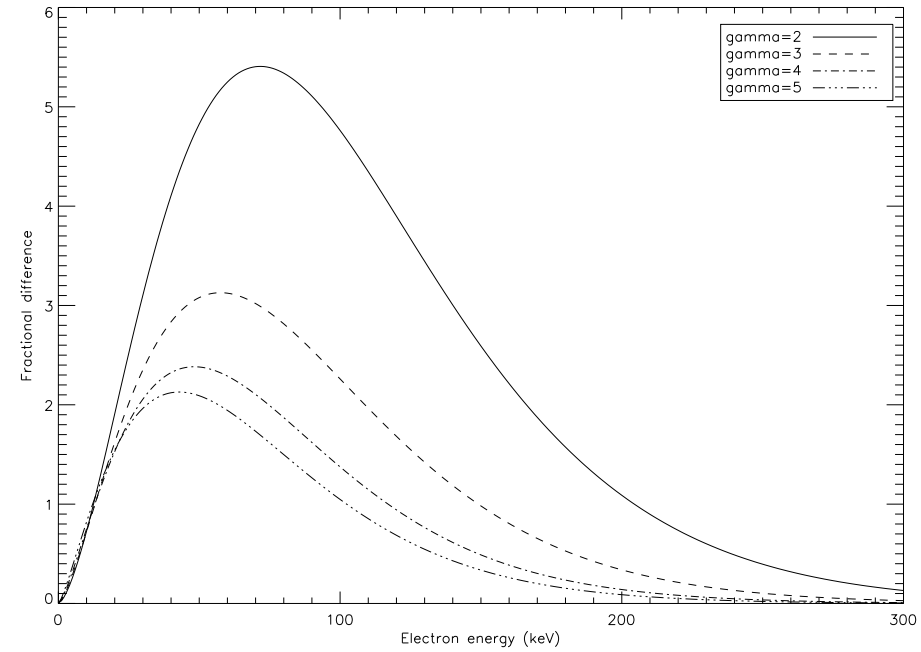

Figure 3.9: Fractional difference between the true and albedo corrupted thin target electron spectra $\bar{F}(E)$ for spectral indexes (γ) of 2-5 ($\alpha = 0.99$ - *mostly emitted downwards*)

The fractional differences inferred using the Kramer cross section, in the electron spectra given in Figures (3.2) to (3.9) are immediately recognizable as generating the bumps in the electron spectra errors given in chapter (2) figures 2.4.a to 2.4.d.

In Figures (3.2) to (3.9) as α increases (representing the degree of downward beaming towards the solar photosphere) the effect is to increase the fractional error inferred in the electron spectrum by a scalar constant in this case. Note that the fractional difference becomes infinite at $\alpha = 1$ since all the emission is in the downwards direction.

3.3 Energy Dependent Anisotropy - $\alpha(\epsilon)$ for a Thin Target

We now extend the energy independent anisotropy error analysis to investigate the error in the inferred thin-target electron spectrum ($\bar{F}(E)$) if the fraction of the primary photon emission emitted into the downward hemisphere is energy dependent - ($\alpha = \alpha(\epsilon)$), again treating the albedo as a multiplier not a convolution. In reality, however, the Compton scattering of incoming photons results in a spread of scattered photons at lower energies. Using this approach we can therefore generalise the fraction representing the anisotropic emission between the two hemispheres, using an Eddington approximation approach, as $\alpha(\epsilon)$ rather than α. The Eddington approach used here is described more comprehensively in section 3.2 of Chapter 4.

We rewrite (3.1) in terms of $\alpha(\epsilon)$ as

$$I(\epsilon) = 2I_o(\epsilon)\left[(1-\alpha(\epsilon)) + A(\epsilon)\alpha(\epsilon)\right] \tag{3.20}$$

which we can substitute into (3.6) to give the inferred mean thin target electron spectrum to give

$$\bar{F}(E) = \frac{2E}{\bar{n}_p V Q_o}\left[-\frac{d}{d\epsilon}\left[\epsilon I_o(\epsilon)\left[(1-\alpha(\epsilon)) + A(\epsilon)\alpha(\epsilon)\right]\right]\right]_{\epsilon=E} \tag{3.21}$$

We can therefore differentiate the expression within the brackets of (3.7) using (3.8) and express (3.6) in terms of an anisotropic $I(\epsilon)$ as

$$\begin{aligned}\frac{d}{d\epsilon}\left[\epsilon I(\epsilon)\right] &= I(\epsilon)+\epsilon I^{'}(\epsilon)\\ &= I_o(\epsilon)((1-\alpha(\epsilon))+\alpha(\epsilon)A(\epsilon))\\ &\quad +\epsilon\frac{d}{d\epsilon}\left[I_o(\epsilon)((1-\alpha(\epsilon))+\alpha(\epsilon)A(\epsilon))\right] \qquad (3.22)\end{aligned}$$

Differentiating $I(\epsilon)$ in (3.22) for a power law photon spectrum gives

$$\begin{aligned}I^{'}(\epsilon) &= I_o(\epsilon)\Bigg[-\frac{\gamma}{\epsilon}\Bigg((1-\alpha(\epsilon))\\ &\quad +\alpha(\epsilon)A(\epsilon)\Bigg)\\ &\quad +\epsilon\alpha^{'}(\epsilon)(a-b\epsilon)+\alpha(\epsilon)\left(\frac{A(\epsilon)}{\epsilon}\right)(a-b\epsilon)\Bigg] \qquad (3.23)\end{aligned}$$

substituting (3.22) into (3.23) gives

$$\begin{aligned}\frac{d}{d\epsilon}\left[\epsilon I(\epsilon)\right] &= I_o(\epsilon)\left((1-\alpha(\epsilon))+\alpha(\epsilon)A(\epsilon)\right)\\ &\quad +\epsilon\Big(I_o^{'}(\epsilon)\left[(1-\alpha(\epsilon))+\alpha(\epsilon)A(\epsilon)\right]\\ &\quad +I_o(\epsilon)\left[\alpha^{'}(\epsilon)(A(\epsilon)-1)+\alpha(\epsilon)A^{'}(\epsilon)\right]\Big) \qquad (3.24)\\ &= I_o(\epsilon)\left[\left((1-\alpha(\epsilon))+\alpha(\epsilon)A(\epsilon)\right)(1-\gamma)\right.\\ &\quad \left.+\alpha(\epsilon)A(\epsilon)(a-b\epsilon)+\epsilon\alpha^{'}(\epsilon)(A(\epsilon)-1)\right] \qquad (3.25)\end{aligned}$$

and substituting (3.25) into (3.21) gives the electron spectrum that would be inferred for an anisotropic photon spectrum ($I(\epsilon)$) as

$$\begin{aligned}\bar{F}(E) &= \frac{2E}{\bar{n}_p V Q_o}I_o(E)\left[\left((1-\alpha(E))+\alpha(E)A(E)\right)(\gamma-1)\right.\\ &\quad \left.-\alpha(E)A(E)(a-bE)-E\alpha^{'}(E)(A(E)-1)\right] \qquad (3.26)\end{aligned}$$

Now if we misidentify $I(\epsilon)$ for $I_o(\epsilon)$ (3.26) and thus observe the photon spectrum as

$$I(\epsilon)=2(1-\alpha(\epsilon))I_o(\epsilon) \qquad (3.27)$$

which can be differentiated to give

$$I^{'}(\epsilon) = 2(-\alpha^{'}(\epsilon))I_o(\epsilon) + 2(1-\alpha(\epsilon))I_o^{'}(\epsilon) \quad (3.28)$$

$$= 2I_o(\epsilon)\left[-\frac{\gamma}{\epsilon}(1-\alpha(\epsilon)) - \alpha^{'}(\epsilon)\right] \quad (3.29)$$

now substituting (3.28) and (3.29) into (3.8) gives

$$\frac{d}{d\epsilon}\left[\epsilon((1-\alpha(\epsilon))I_o(\epsilon))\right] = 2I_o(\epsilon)\left[(1-\alpha(\epsilon))\left(1-\frac{\gamma}{\epsilon}\right) - \alpha^{'}(\epsilon)\right] \quad (3.30)$$

which we can substitute into (3.6) to give the mean thin target electron spectrum as

$$\bar{F}_o(E) = \frac{2E}{\bar{n}_p V Q_o}\left[I_o(\epsilon)\left[(1-\alpha(\epsilon))\left(1-\frac{\gamma}{\epsilon}\right) - \alpha^{'}(\epsilon)\right]\right]_{\epsilon=E} \quad (3.31)$$

therefore given (3.31) then we would infer a fractional error in the electron spectrum as

$$\frac{\Delta\bar{F}(E)}{\bar{F}_o(E)} = \left(\frac{1}{(\gamma-1)(1-\alpha(\epsilon))} \times \left[((1-\alpha(\epsilon)) + \alpha(\epsilon)A(\epsilon))(\gamma-1)\right.\right.$$
$$\left.\left. -\alpha(\epsilon)A(\epsilon)(a-b\epsilon) - \epsilon\alpha^{'}(\epsilon)(A(\epsilon)-1)\right]\right) - 1 \quad (3.32)$$

3.3.1 The Functional Form of $\alpha(\epsilon)$

In equation (3.32) a general functional form for $\alpha(\epsilon)$ was assumed in order to estimate the effect of anisotropic emission under real flare conditions. We here introduce a simple linear fit[1] for the anisotropy data published by Leach & Petrosian (1983).

In Leach & Petrosian (1983, Figure 1) the magnetic field structure of a flare is modelled as a semi circular loop in the corona with a vertical component in the transition layer and chromosphere. Each model is parameterized in terms of the spectral index of the electron spectrum δ, the mean magnetic field direction $\mathbf{B}$ at depth τ and the pitch angle of the electrons α_o. The model parameters are summarized in Leach & Petrosian (1983, Table 1). Leach and Petrosian give their results in the form of a X-Ray directivity which is given in Figure 3.10.

[1] A linear fit was used as a more complicated interpolation in energy would not yield additional benefits

We use the ADS data plot extraction application, Dexter (Demleitner et al. 2001) to extract the data points given in Figure 3.10 and this data is given in Table 3.1 below. The full angular digitised data can be found in table 5.1 but in this chapter we convert the data into a hemispherical average - $\alpha(\epsilon)$.

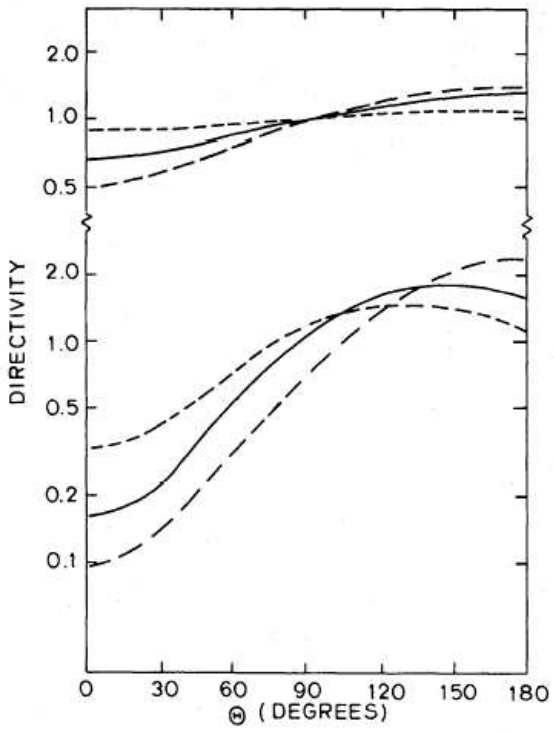

Figure 3.10: X-Ray directivity as a function of the polar angle θ (taken from Leach and Petrosian (1983), Figure 4. Zero degrees is the vertical direction away from the photosphere. The dashed line shown (model 5 within LP83) is given for photon energies of 22 keV (upper set), and 210keV (lower set).

We can determine a simple functional form for $\alpha(\epsilon)$ as follows:

1. Using (Leach & Petrosian 1983, Table 1) we choose model 5 (long dashed line) shown in figure 3.10 as this has the closest morphological match for our purposes. As the effects of the albedo can easily be seen in *hard* photon spectra (small values of γ) we choose the model which will produce X-Ray photon spectrum that is relatively hard ($\gamma \approx 3$ for model 5) and has a small pitch angle α_o suggesting high directivity.

2. The emission is modelled using the Leach and Petrosian directivity values

emitted at $\theta = 0^o$ and $\theta = 180^o$ in order to be compatible with the Eddington approach detailed in section 3.2 where the emission occurs within the two separate hemispheres.

3. We then obtain a value for the ratio of the emission into the upward and downward hemispheres at $\theta = 0^o$ and $\theta = 180^o$ at the 22 keV and 210 keV energies.

4. Using the ratios, we obtain the fractions of the emission emitted into each hemisphere. This subsequently yields values of α_{22keV} and α_{210keV} for these two energies.

5. Finally we use a simple linear interpolation between the two energy data points to arrive at a linear relationship for $\alpha(\epsilon)$.

$\frac{\epsilon}{(keV)}$	$\theta = 0^o$	$\theta = 180^o$
22	0.5	1.5
210	0.1	2.25

Table 3.1: Directivity of the emission at 22keV and 210keV

As we are interested in the directivity of the emission and the fraction α emitted into each hemisphere, we can convert the values given in table 3.1 into emission fractions into each hemisphere give using the ratio of the $emission_{up}$: $emission_{down}$ which is reflected in table (3.2) below

$\frac{\epsilon}{(keV)}$	θ_0	θ_{180}
22	$\frac{1}{4}$	$\frac{3}{4}$
210	$\frac{2}{47}$	$\frac{45}{47}$

Table 3.2: Fraction of the emission into the upward and downward hemisphere at 22keV and 210keV

From table (3.2) we can obtain two data points in the form $(\epsilon, \alpha(\epsilon))$. Interpolating between the points provides a crude functional form for $\alpha(\epsilon)$ and we can express this in the form of a straight line as

$$\alpha(\epsilon) = G\epsilon + H \tag{3.33}$$

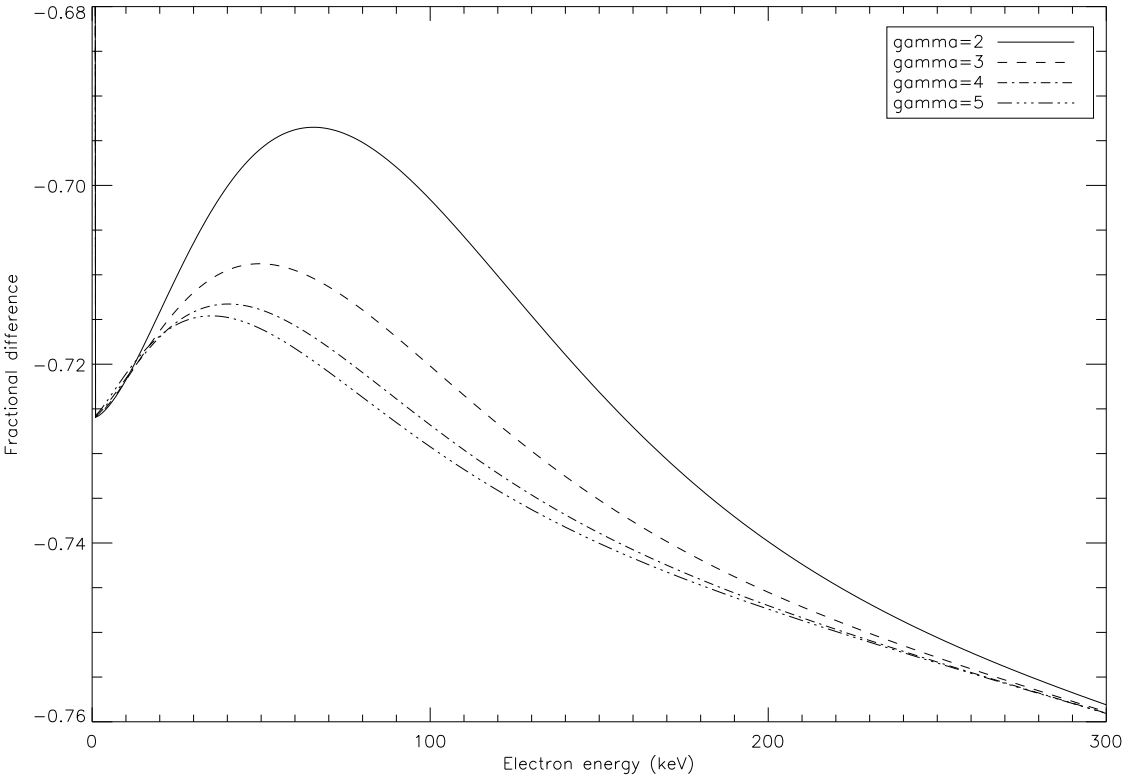

Figure 3.11: The fractional differences inferred within the Kramers electon spectrum are given in Figure (3.11) for a range of spectral indexes ($\gamma = 2$ to 5), for our empirically derived $\alpha(\epsilon)$

and then evaluating the values of G and H we can express the functional form of $\alpha(\epsilon)$ as

$$\alpha(\epsilon) = \left(\frac{39}{35344}\right)\epsilon + 0.726 \tag{3.34}$$

Finally we substitute (3.34) into (3.32) to obtain the fractional difference in the inferred electron spectrum for the empirically fitted form for $\alpha(\epsilon)$.

3.3.2 Resulting Error Inferred for an Energy Dependent Anisotropic Correction - $\alpha(\epsilon)$

A comparison of figure (3.11) with (3.2) to (3.9) shows that the main effect of an energy dependent anisotropy within the inferred fractional difference is in the shape of the fractional difference. Whilst the energy independent anisotropic correction resulted in a simple 'scaling factor' of $\frac{\Delta\bar{F}(E)}{\bar{F}_o(E)}$, the energy dependent anisotropic case results in an increase in the negative value of $\frac{\Delta\bar{F}(E)}{\bar{F}_o(E)}$ as energy

increases. This physically represents the photon emission becoming more beamed in the downward direction at higher energies.

The energy range in Figure 3.11 has been restricted due to the approximate nature of the empirical fit which causes $\alpha(\epsilon)$ to become unphysical (greater than 1) above 250keV. We can again use the energy range over which $\alpha(\epsilon)$ *is* physically valid to calculate the fractional difference in $\bar{F}(E)$.

3.4 Thick–target

From Brown & Emslie (1988) the thick–target electron spectrum $\mathcal{F}(E_o)$, (total injection rate of electrons per second per unit E_o) is given for an isotropic primary photon spectrum $I(\epsilon)$ by

$$\mathcal{F}_o(E_o) = \frac{\mathcal{K}}{Q_o}\left[\frac{d^2}{d\epsilon^2}\Big(\epsilon I(\epsilon)\Big)\right]_{\epsilon=E_o} \tag{3.35}$$

where $\mathcal{K} = 2\pi e^4\Lambda$ and Λ is the coulomb logarithm (section 1.2.5), and

$$\frac{d^2}{d\epsilon^2}\left[\epsilon I(\epsilon)\right] = 2I^{'}(\epsilon) + \epsilon I^{''}(\epsilon) \tag{3.36}$$

which allows us to determine the inferred error in the parent thick target electron spectrum given an anisotropic observed photon spectrum assuming either an energy-dependent or eergy-independent α.

3.4.1 Energy Independent Eddington Anisotropy - α

Differentiating the energy independent anisotropic $I^{'}(\epsilon)$ (3.13) (given in section 3.3) for a power law photon spectrum gives

$$\begin{aligned}
I^{''}(\epsilon) &= \frac{d}{d\epsilon}\left[I_o(\epsilon)\left(-\frac{\gamma}{\epsilon}\left((1-\alpha)+\alpha A(\epsilon)\right)+\alpha A^{'}(\epsilon)\right)\right] && (3.37)\\
&= I_o(\epsilon)\frac{d}{d\epsilon}\left[-\frac{\gamma}{\epsilon}\left((1-\alpha)+\alpha A(\epsilon)\right)+\alpha A^{'}(\epsilon)\right]\\
&\quad + I_o^{'}(\epsilon)\left(-\frac{\gamma}{\epsilon}\left((1-\alpha)+\alpha A(\epsilon)\right)+\alpha A^{'}(\epsilon)\right) && (3.38)\\
&= I_o(\epsilon)\left[\frac{\gamma}{\epsilon^2}\left((1-\alpha)+\alpha A(\epsilon)\right)-\frac{\gamma}{\epsilon}\alpha A^{'}(\epsilon)\right.\\
&\quad \left.+\alpha A^{''}(\epsilon)+\frac{\gamma}{\epsilon}\left[\frac{\gamma}{\epsilon}\left((1-\alpha)+\alpha A(\epsilon)\right)-\alpha A^{''}(\epsilon)\right]\right] && (3.39)
\end{aligned}$$

Differentiating (3.12), the energy independent $A^{'}(\epsilon)$, gives

$$\begin{aligned} A^{''}(\epsilon) &= -\frac{A(\epsilon)}{\epsilon}b + (a-b\epsilon)\left[\frac{A^{'}(\epsilon)}{\epsilon} - \frac{A(\epsilon)}{\epsilon^2}\right] \\ &= -\frac{A(\epsilon)}{\epsilon}b + (a-b\epsilon)\left[\frac{A(\epsilon)}{\epsilon^2}(a-b\epsilon) - \frac{A(\epsilon)}{\epsilon^2}\right] \\ &= \frac{A(\epsilon)}{\epsilon^2}\Big[(a-b\epsilon)^2 - (a-b\epsilon) - b\epsilon\Big] \end{aligned} \tag{3.40}$$

and substituting (3.13), (3.39), (3.12) and (3.40) into (3.36) gives

$$\begin{aligned} \frac{d^2}{d\epsilon^2}\Big[\epsilon I(\epsilon)\Big] &= I_o(\epsilon)\Big[\Big[\frac{\gamma}{\epsilon^2}\left((1-\alpha)+\alpha A(\epsilon)\right) \\ &\quad -\frac{\gamma}{\epsilon}\alpha\frac{A(\epsilon)}{\epsilon}(a-b\epsilon) + \alpha\frac{A(\epsilon)}{\epsilon^2}\left[(a-b\epsilon)^2 - a\right] \\ &\quad +\frac{\gamma}{\epsilon}\Big[\frac{\gamma}{\epsilon}\Big((1-\alpha)+\alpha A(\epsilon)\Big) - \alpha\frac{A(\epsilon)}{\epsilon^2}\left[(a-b\epsilon)^2 - a\right]\Big] \end{aligned} \tag{3.41}$$

Finally, substituting (3.41) into (3.35) gives

$$\begin{aligned} \mathcal{F}_o(E_o) &= \frac{\mathcal{K}}{Q_o}\Big[I_o(\epsilon)\Big[\Big[\frac{\gamma}{\epsilon^2}\left((1-\alpha)+\alpha A(\epsilon)\right) \\ &\quad -\frac{\gamma}{\epsilon}\alpha\frac{A(\epsilon)}{\epsilon}(a-b\epsilon) + \alpha\frac{A(\epsilon)}{\epsilon^2}\left[(a-b\epsilon)^2 - a\right] \\ &\quad +\frac{\gamma}{\epsilon}\Big[\frac{\gamma}{\epsilon}\Big((1-\alpha)+\alpha A(\epsilon)\Big) - \alpha\frac{A(\epsilon)}{\epsilon^2}\left[(a-b\epsilon)^2 - a\right]\Big]\Big] \end{aligned} \tag{3.42}$$

Now if we misidentify $I(\epsilon)$ for $I_o(\epsilon)$ in (3.35) and differentiate (3.11) evaluating each component in turn and substituting them into (3.36) gives

$$\begin{aligned} \frac{d^2}{d\epsilon^2}\left[\epsilon I(\epsilon)\right] &= 2I^{'}(\epsilon) + \epsilon I^{''}(\epsilon) \\ &= -4\left(\frac{\gamma}{\epsilon}\right)(1-\alpha)I_o(\epsilon) + 2\epsilon\frac{\gamma}{\epsilon^2}(1-\alpha)(1+\gamma)I_o(\epsilon) \\ &= 2\left(\frac{\gamma}{\epsilon}\right)(1-\alpha)(\gamma-1)I_o(\epsilon) \end{aligned} \tag{3.43}$$

given that

$$
\begin{aligned}
I(\epsilon) &= 2(1-\alpha)I_o(\epsilon) \\
I^{'}(\epsilon) &= 2(1-\alpha)I_o^{'}(\epsilon) \\
&= -2\left(\frac{\gamma}{\epsilon}\right)(1-\alpha)I_o(\epsilon) \qquad (3.44) \\
I^{''}(\epsilon) &= 2\left(\frac{\gamma}{\epsilon^2}\right)(1-\alpha)I_o(\epsilon) + 2\left(\frac{\gamma}{\epsilon}\right)^2(1-\alpha)I_o(\epsilon) \\
&= 2\left(\frac{\gamma}{\epsilon^2}\right)(1-\alpha)(1+\gamma)I_o(\epsilon) \qquad (3.45)
\end{aligned}
$$

for

$$
\begin{aligned}
I_o^{''}(\epsilon) &= \frac{d}{d\epsilon}\left[-\frac{\gamma}{\epsilon}I_o(\epsilon)\right] \\
&= \frac{\gamma}{\epsilon^2}I_o(\epsilon) - \frac{\gamma}{\epsilon}I_o^{'}(\epsilon) \\
&= \frac{\gamma}{\epsilon^2}(\gamma+1)I_o(\epsilon) \qquad (3.46)
\end{aligned}
$$

and finally substituting (3.43) into (3.35) for $I_o(\epsilon)$ gives

$$
\mathcal{F}_o(E_o) = \frac{\mathcal{K}}{Q_o}\left[2\left(\frac{\gamma}{\epsilon}\right)(1-\alpha)(\gamma-1)I_o(\epsilon)\right]_{\epsilon=E_o} \qquad (3.47)
$$

which gives a fractional error in the thick target electron spectrum as

$$
\begin{aligned}
\frac{\Delta\bar{F}(E)}{\bar{F}_o(E)} &= \left(\left(\frac{\gamma}{\epsilon}\right)(1-\alpha)(\gamma-1)\right)^{-1}\left[\left(\frac{\gamma}{\epsilon}\right)(1-\alpha)(\gamma-1) + \alpha A(\epsilon)\times\right. \\
&\quad \left.\left((\gamma-1)(\gamma-2\alpha(a-b\epsilon)) + ((a-b\epsilon)^2 - (a-b\epsilon) - b\epsilon)\right)\right] \\
&\quad -1 \qquad (3.48)
\end{aligned}
$$

3.4.2 Resulting Thick–target Errors for Energy Independent Anisotropic Correction - α

The fractional differences inferred (using the Kramers cross section) for electron spectra given in Figures (3.12) to (3.19) are immediately recognizable as being similar to bumps in the electron spectra given in chapter (2) figures 2.6.(a).–2.6.(d). In figures (3.2) to (3.5) as α increases this has the effect of increasing the fractional error inferred in the electron spectrum by a scaling factor (a scalar constant in this case). As in the thin–target case, the fractional difference becomes infinite at $\alpha = 1$ since all emission is into the downwards direction.

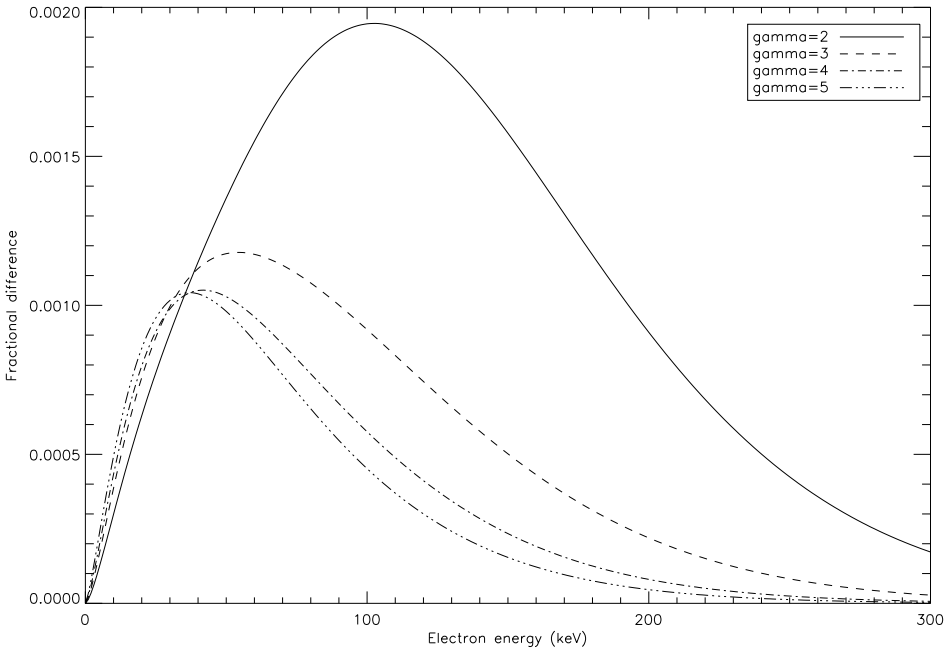

Figure 3.12: Fractional difference between the true and inferred thick target (Kramer's) electron spectrum $\bar{F}(E)$ for spectral indexes (γ) of 2-5 ($\alpha = 0.0625$ - *mostly emitted upwards*)

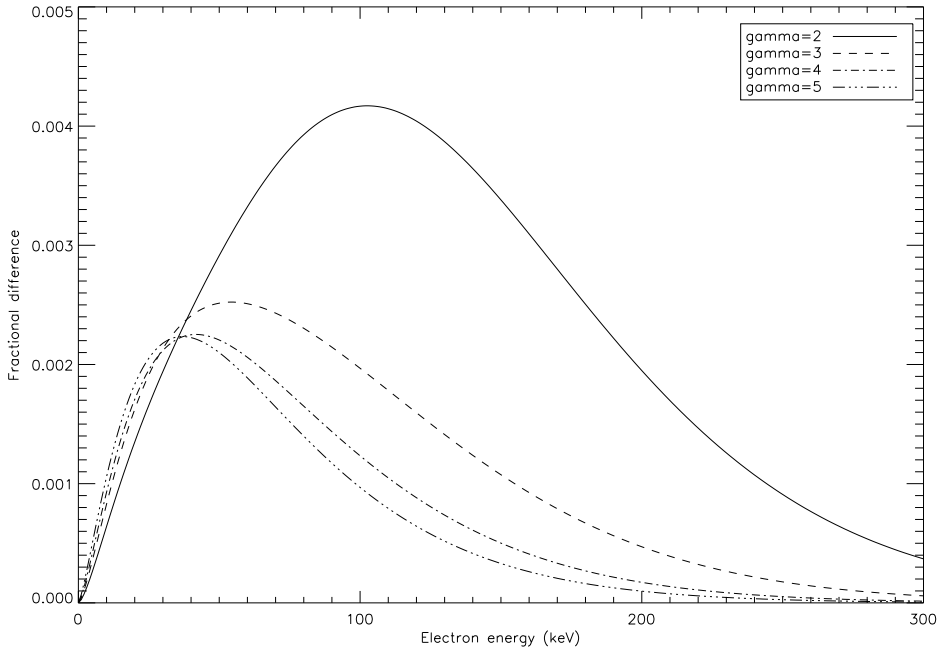

Figure 3.13: Fractional difference between the true and inferred thick target (Kramer's) electron spectrum $\bar{F}(E)$ for spectral indexes (γ) of 2-5 ($\alpha = 0.125$)

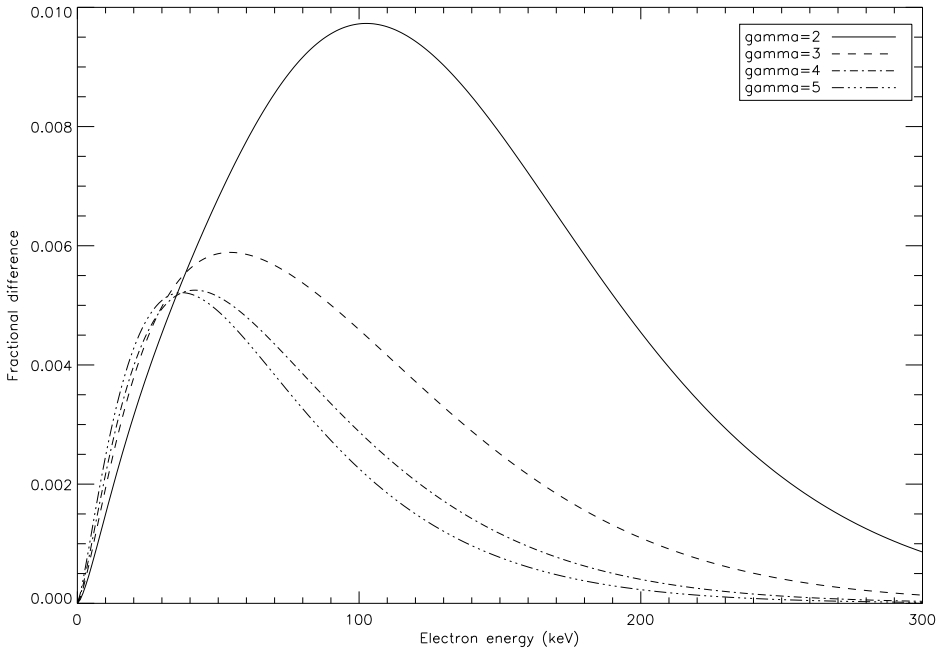

Figure 3.14: Fractional difference between the true and inferred thick target (Kramer's) electron spectrum $\bar{F}(E)$ for spectral indexes (γ) of 2-5 ($\alpha = 0.25$)

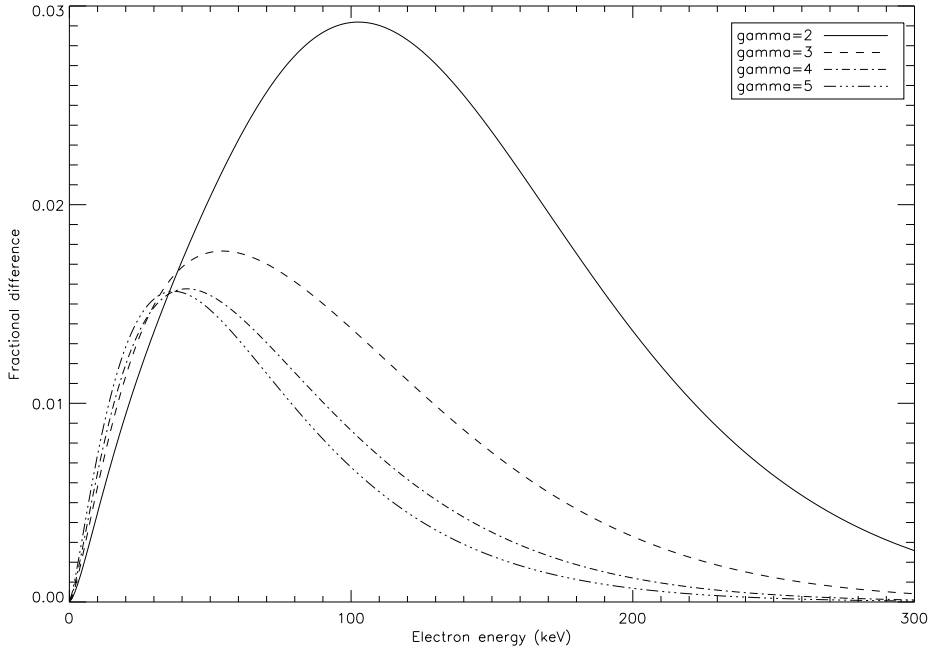

Figure 3.15: Fractional difference between the true and inferred thick target (Kramer's) electron spectrum $\bar{F}(E)$ for spectral indexes (γ) of 2-5 ($\alpha = 0.5$)

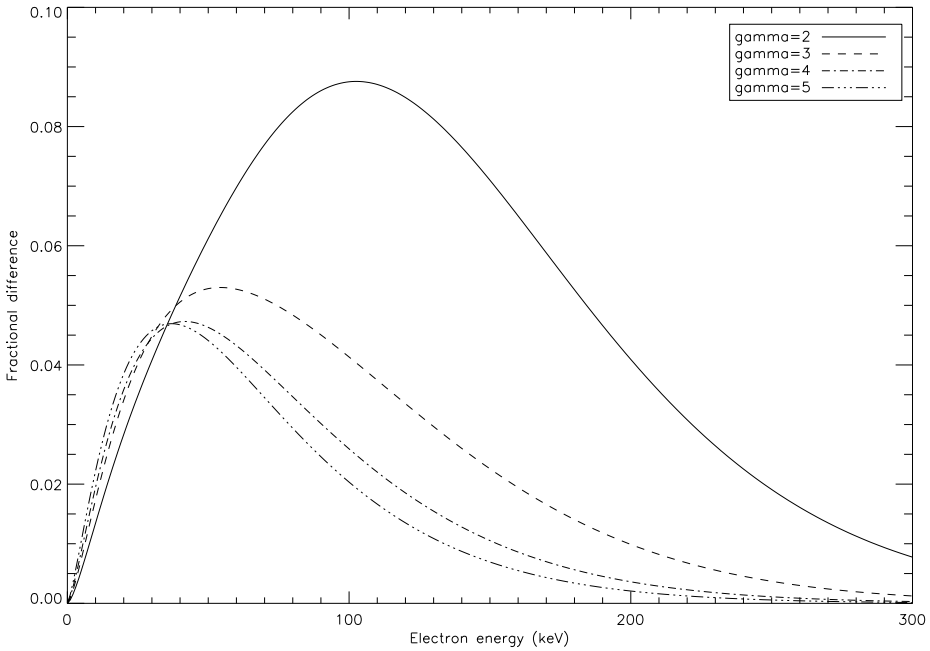

Figure 3.16: Fractional difference between the true and inferred thick target (Kramer's) electron spectrum $\bar{F}(E)$ for spectral indexes (γ) of 2-5 ($\alpha = 0.75$)

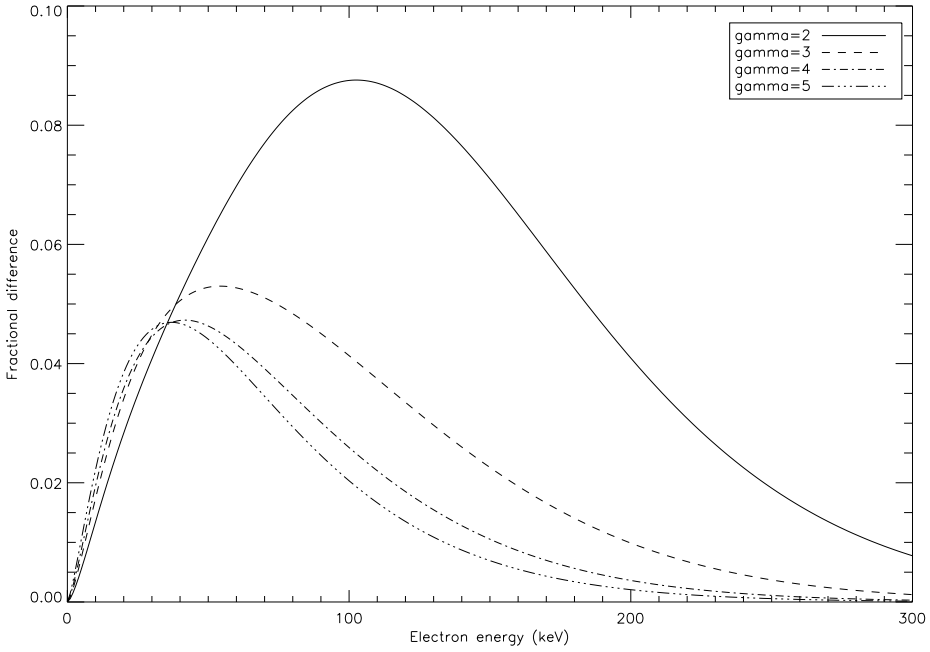

Figure 3.17: Fractional difference between the true and inferred thick target (Kramer's) electron spectrum $\bar{F}(E)$ for spectral indexes (γ) of 2-5 ($\alpha = 0.75$)

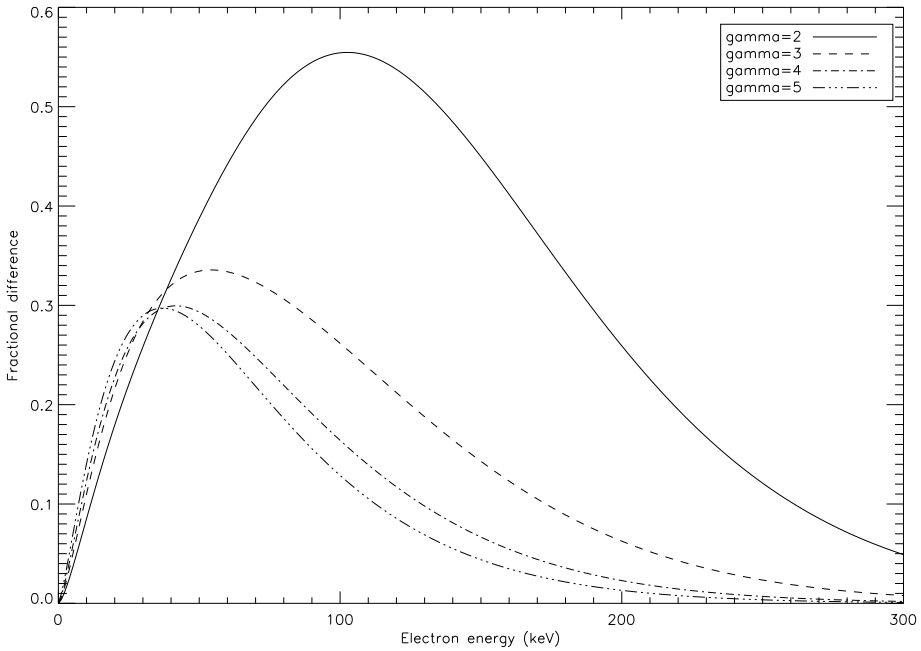

Figure 3.18: Fractional difference between the true and inferred thick target (Kramer's) electron spectrum $\bar{F}(E)$ for spectral indexes (γ) of 2-5 ($\alpha = 0.5$)

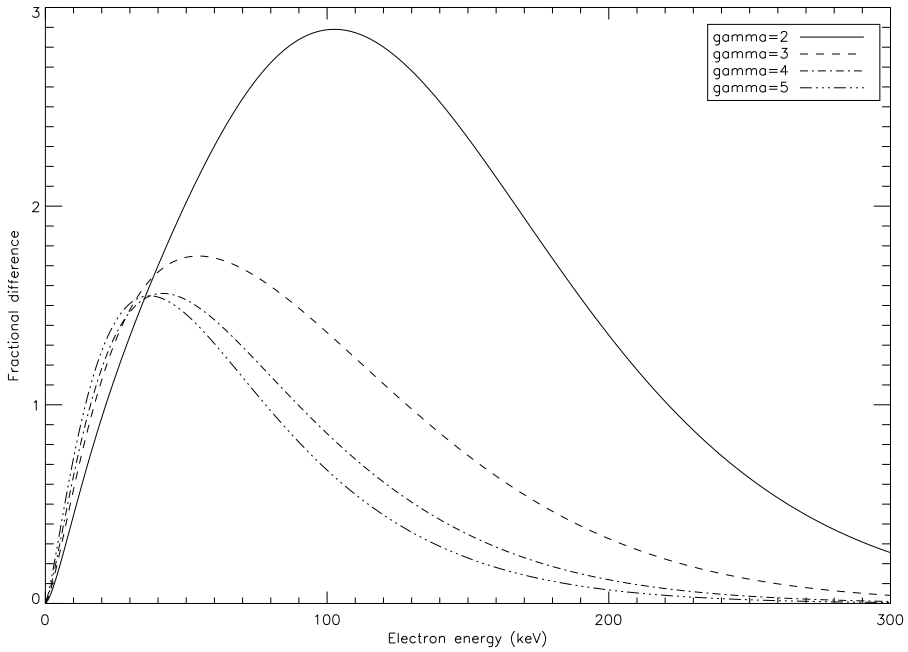

Figure 3.19: Fractional difference between the true and inferred thick target (Kramer's) electron spectrum $\bar{F}(E)$ for spectral indexes (γ) of 2-5 ($\alpha = 0.99$ - *mostly emitted upwards*)

3.5 Energy Dependent Anisotropy - $\alpha(\epsilon)$ for a Thick–target

Again we extend the energy independent correction to calculate the inferred fractional difference in the thick–target electron spectrum $\mathcal{F}(E_o)$ if the photon spectrum we observed was produced in a thick target where the emission of the photons was beamed into the forward direction but the extent of this beaming was energy dependent. As before this energy dependent anisotropy is represented by an energy dependent multiplier $\alpha(\epsilon)$. We do this using the same approach as we used for the energy independent thick target.

Given (3.35), the thick target electron spectrum, we can differentiate the expression within the brackets using (3.36) for an energy dependent anisotropy.

For an observed photon spectrum as given from (3.20)

$$I(\epsilon) = 2I_o(\epsilon)\left[(1-\alpha(\epsilon)) + \alpha(\epsilon)A(\epsilon)\right] \tag{3.49}$$

We need to derive expressions for the first and second order derivatives of this as follows:

$$\begin{aligned} I^{'}(\epsilon) &= 2\Bigg[I_o^{'}(\epsilon)\left((1-\alpha(\epsilon)) + \alpha(\epsilon)A(\epsilon)\right) \\ &\quad + I_o(\epsilon)\left(-\alpha^{'}(\epsilon) + \alpha^{'}(\epsilon)A(\epsilon) + \alpha(\epsilon)A(\epsilon)\right)\Bigg] \end{aligned} \tag{3.50}$$

and for a power law photon spectrum of the form $I_o(\epsilon) = C\epsilon^{-\gamma}$ we can express (3.50) in term of $I_o(\epsilon)$ as

$$\begin{aligned} I^{'}(\epsilon) &= 2\Bigg[-\left(\frac{\gamma}{\epsilon}\right) I_o(\epsilon)\left((1-\alpha(\epsilon)) + \alpha(\epsilon)A(\epsilon)\right) \\ &\quad + I_o(\epsilon)\left(-\alpha^{'}(\epsilon) + \alpha^{'}(\epsilon)A(\epsilon) + \alpha(\epsilon)A(\epsilon)\right)\Bigg] \end{aligned} \tag{3.51}$$

which can be simplified to give the first order derivative of the observed photon spectrum $I(\epsilon)$ as

$$I^{'}(\epsilon) = -\left(\frac{\gamma}{\epsilon}\right) I(\epsilon) + 2I_o(\epsilon)\left[\alpha^{'}(\epsilon)(A(\epsilon)-1) + \alpha(\epsilon)A^{'}(\epsilon)\right] \tag{3.52}$$

We can subsequently differentiate (3.52) as follows

$$I^{''}(\epsilon) = \frac{d}{d\epsilon}\left[-\left(\frac{\gamma}{\epsilon}\right) I(\epsilon)\right] + \frac{d}{d\epsilon}\left[2I_o(\epsilon)\left[\alpha^{'}(\epsilon)(A(\epsilon)-1) + \alpha(\epsilon)A^{'}(\epsilon)\right]\right] \quad (3.53)$$

$$I^{''}(\epsilon) = \frac{\gamma}{\epsilon^2} I(\epsilon) - \frac{\gamma}{\epsilon} I^{'}(\epsilon) + \frac{d}{d\epsilon}\left[2I_o(\epsilon)\left[\alpha^{'}(\epsilon)(A(\epsilon)-1) + \alpha(\epsilon)A^{'}(\epsilon)\right]\right] \quad (3.54)$$

Now

$$\begin{aligned} & \frac{d}{d\epsilon}\left[2I_o(\epsilon)\left(\alpha^{'}(\epsilon)(A(\epsilon)-1) + \alpha(\epsilon)A^{'}(\epsilon)\right)\right] \\ = \; & 2\left[I_o^{'}(\epsilon)\left(\alpha^{'}(A(\epsilon)-1) + \alpha(\epsilon)A^{'}(\epsilon)\right)\right. \\ & \left. + I_o(\epsilon)\left(\alpha^{''}(\epsilon)(A(\epsilon)-1) + 2\alpha^{'}(\epsilon)A^{'}(\epsilon) + \alpha(\epsilon)A^{''}(\epsilon)\right)\right] \end{aligned} \quad (3.55)$$

which can be shown to give

$$2I_o(\epsilon)\left[(A(\epsilon)-1)\left(\alpha^{''}(\epsilon) - \frac{\gamma}{\epsilon}\alpha^{'}(\epsilon)\right) + A^{'}(\epsilon)\left(2\alpha^{'}(\epsilon) - \frac{\gamma}{\epsilon}\right) + \alpha A^{''}(\epsilon)\right] \quad (3.56)$$

substituting (3.56) into (3.54) gives

$$\begin{aligned} I^{''}(\epsilon) \; = \; & \frac{\gamma}{\epsilon^2} I(\epsilon) - \frac{\gamma}{\epsilon} I^{'}(\epsilon) \\ & + \; 2I_o(\epsilon)\left[(A(\epsilon)-1)\left(\alpha^{''}(\epsilon) - \frac{\gamma}{\epsilon}\alpha^{'}(\epsilon)\right)\right. \\ & + \; \left. A^{'}(\epsilon)\left(2\alpha^{'}(\epsilon) - \frac{\gamma}{\epsilon}\right) + \alpha A^{''}(\epsilon)\right] \end{aligned} \quad (3.57)$$

and substituting (3.50) into (3.57) gives

$$\begin{aligned} I^{''}(\epsilon) \; = \; & \frac{\gamma}{\epsilon^2} I(\epsilon) + \left(\frac{\gamma}{\epsilon}\right)^2 I(\epsilon) \\ & - \frac{2\gamma}{\epsilon} I_o(\epsilon)\left[\alpha^{'}(\epsilon)(A(\epsilon)-1) + \alpha(\epsilon)A^{'}(\epsilon)\right] \\ & + 2I_o(\epsilon)\left[(A(\epsilon)-1)\left(\alpha^{''}(\epsilon) - \frac{\gamma}{\epsilon}\alpha^{'}(\epsilon)\right)\right. \\ & \left. + A^{'}(\epsilon)\left(2\alpha^{'}(\epsilon) - \frac{\gamma}{\epsilon}\right) + \alpha A^{''}(\epsilon)\right] \end{aligned} \quad (3.58)$$

and grouping like terms gives

$$I^{''}(\epsilon) = \frac{\gamma}{\epsilon^2} I(\epsilon)(\gamma+1) + 2I_o(\epsilon)\left[(A(\epsilon)-1)\left(\alpha^{''}(\epsilon) - \frac{2\gamma}{\epsilon}\alpha^{'}(\epsilon)\right)\right.$$
$$\left. + A^{'}(\epsilon)\left(2\alpha^{'}(\epsilon) - \frac{2\gamma}{\epsilon}\alpha(\epsilon)\right) + \alpha(\epsilon)A^{''}(\epsilon)\right] \quad (3.59)$$

Now substituting (3.59) and (3.50) into (3.36) gives

$$\frac{d^2}{d\epsilon^2}\left[\epsilon I(\epsilon)\right] = -\frac{2\gamma}{\epsilon} I(\epsilon) + 4I_o(\epsilon)\left(\alpha^{'}(\epsilon)\left(A(\epsilon)-1\right) + \alpha(\epsilon)A^{'}(\epsilon)\right)$$
$$+\frac{\gamma}{\epsilon} I(\epsilon)\left(\gamma+1\right) + 2\epsilon I_o(\epsilon)\left[(A(\epsilon)-1)\left(\alpha^{''}(\epsilon) - \frac{2\gamma}{\epsilon}\alpha^{'}(\epsilon)\right)\right.$$
$$\left. + A^{'}(\epsilon)\left(2\alpha^{'}(\epsilon) - \frac{2\gamma}{\epsilon}\alpha(\epsilon)\right) + \alpha(\epsilon)A^{''}(\epsilon)\right] \quad (3.60)$$

which can be shown to give

$$\frac{d^2}{d\epsilon^2}\left[\epsilon I(\epsilon)\right] = \frac{\gamma}{\epsilon} I(\epsilon)\left(\gamma-1\right)$$
$$+2I_o(\epsilon)\left[(A(\epsilon)-1)\left(\epsilon\alpha^{''}(\epsilon) + 2\alpha^{'}(\epsilon)(1-\gamma)\right)\right.$$
$$\left. + A^{'}(\epsilon)\left(2\epsilon\alpha^{'}(\epsilon) + 2\alpha(\epsilon)(1-\gamma)\right) + \epsilon\alpha(\epsilon)A^{''}(\epsilon)\right] \quad (3.61)$$

finally substituting (3.61) into (3.35) gives

$$\mathcal{F}_o(E_o) = \frac{\mathcal{K}}{Q_o}\left[\frac{\gamma}{\epsilon} I(\epsilon)\left(\gamma-1\right)\right.$$
$$+2I_o(\epsilon)\left[(A(\epsilon)-1)\left(\epsilon\alpha^{''}(\epsilon) + 2\alpha^{'}(\epsilon)(1-\gamma)\right)\right.$$
$$\left.\left. + A^{'}(\epsilon)\left(2\epsilon\alpha^{'}(\epsilon) + 2\alpha(\epsilon)(1-\gamma)\right) + \epsilon\alpha(\epsilon)A^{''}(\epsilon)\right]\right]_{\epsilon=E_o} \quad (3.62)$$

which we can simplify to give

$$\mathcal{F}_o(E_o) = \frac{2\mathcal{K}}{Q_o}\left[I_o(\epsilon)\left(\left(\gamma-1\right)\left[\frac{\gamma}{\epsilon}((1-\alpha(\epsilon)) + \alpha(\epsilon)A(\epsilon)) - 2(\alpha^{'}(\epsilon)(A(\epsilon)-1) + \alpha(\epsilon)A^{'}(\epsilon))\right]\right.\right.$$
$$\left.\left. +\epsilon\left[\alpha^{''}(\epsilon)(A(\epsilon)-1) + 2\alpha^{'}(\epsilon)A^{'}(\epsilon) + \alpha(\epsilon)A^{''}(\epsilon)\right]\right)\right]_{\epsilon=E_o} \quad (3.63)$$

If we were to mistake $I_o(\epsilon)$ for $I(\epsilon)$ in (3.35) then using (3.36) we would infer a thick target electron spectrum as follow:

Given the observed photon spectrum, $I(\epsilon)$, as

$$I(\epsilon) = (1 - \alpha(\epsilon))I_o(\epsilon) \tag{3.64}$$

which we can differentiate to give the first order derivative as follows

$$\begin{aligned} I^{'}(\epsilon) = & -\alpha^{'} I_o(\epsilon) + (1 - \alpha(\epsilon))I_o^{'}(\epsilon) \\ & -\alpha^{'} I_o(\epsilon) - \frac{\gamma}{\epsilon}(1 - \alpha(\epsilon))I_o(\epsilon) \\ & - \left[\alpha^{'} + -\frac{\gamma}{\epsilon}(1 - \alpha(\epsilon))\right] I_o(\epsilon) \end{aligned} \tag{3.65}$$

again differentiating each part in turn we obtain the second order derivative as

$$\begin{aligned} I^{''}(\epsilon) &= -\alpha^{''}(\epsilon)I_o(\epsilon) - \alpha^{'}(\epsilon)I_o^{'}(\epsilon) - \alpha^{'} I_o^{'}(\epsilon) + (1 - \alpha(\epsilon))I_o^{''}(\epsilon) \\ &= -\alpha^{''} I_o(\epsilon) - 2\alpha^{'} I_o^{'}(\epsilon) + (1 - \alpha(\epsilon))I_o^{''}(\epsilon) \end{aligned} \tag{3.66}$$

Now inserting (3.65) and (3.66) into (3.36) gives

$$\begin{aligned} \frac{d^2}{d\epsilon^2}\left[\epsilon I(\epsilon)\right] &= 2I^{'}(\epsilon) + \epsilon I^{''}(\epsilon) \\ &= 2\left[-\left[\alpha^{'}(\epsilon) + -\frac{\gamma}{\epsilon}(1 - \alpha(\epsilon))\right] I_o(\epsilon)\right] \\ &\quad +\epsilon\left[-\alpha^{''} I_o(\epsilon) - 2\alpha^{'}\left(\frac{-\gamma}{\epsilon}\right) I_o(\epsilon) + (1 - \alpha(\epsilon))\left(\frac{\gamma}{\epsilon}\right)^2 I_o(\epsilon)\right] \end{aligned} \tag{3.67}$$

which can be shown to give

$$\begin{aligned} \frac{d^2}{d\epsilon^2}\left[\epsilon I(\epsilon)\right] &= I_o(\epsilon) \times \\ &\quad \left[-(1 - \alpha(\epsilon))\left(\frac{\gamma}{\epsilon}\right)(\gamma - 2) + 2\alpha^{'}(\epsilon)(\gamma - 1) - \epsilon\alpha^{''}(\epsilon)\right] \end{aligned} \tag{3.68}$$

and thus inserting into (3.35) gives

$$\mathcal{F}_o(E_o) = \frac{2\mathcal{K}}{Q_o}\left[I_o(\epsilon)\left(\left((1 - \alpha(\epsilon))\left(\frac{\gamma}{\epsilon}\right) + 2\alpha^{'}(\epsilon)\right)(\gamma - 1) - \epsilon\alpha^{''}(\epsilon)\right)\right]_{\epsilon = E_o} \tag{3.69}$$

and thus using (3.63) and (3.69) we obtain a fractional error of

$$\frac{\Delta\bar{F}(E)}{\bar{F}_o(E)} = \left[\left(\left((1-\alpha(\epsilon))\left(\frac{\gamma}{\epsilon}\right)+2\alpha^{'}(\epsilon)\right)(\gamma-1)-\epsilon\alpha^{''}(\epsilon)\right)^{-1}\times \left((\gamma-1)\left[\frac{\gamma}{\epsilon}((1-\alpha(\epsilon))+\alpha(\epsilon)A(\epsilon))-2(\alpha^{'}(\epsilon)(A(\epsilon)-1)+\alpha(\epsilon)A^{'}(\epsilon))\right] +\epsilon\left[\alpha^{''}(\epsilon)(A(\epsilon)-1)+2\alpha^{'}(\epsilon)A^{'}(\epsilon)+\alpha(\epsilon)A^{''}(\epsilon)\right]\right)\right]-1 \quad (3.70)$$

The fractional difference inferred within the Kramers electron spectrum and described by equation (3.70) is shown in figure 3.20 below.

3.5.1 Resulting Error Inferred for an Energy Dependent Anisotropic Correction - $\alpha(\epsilon)$

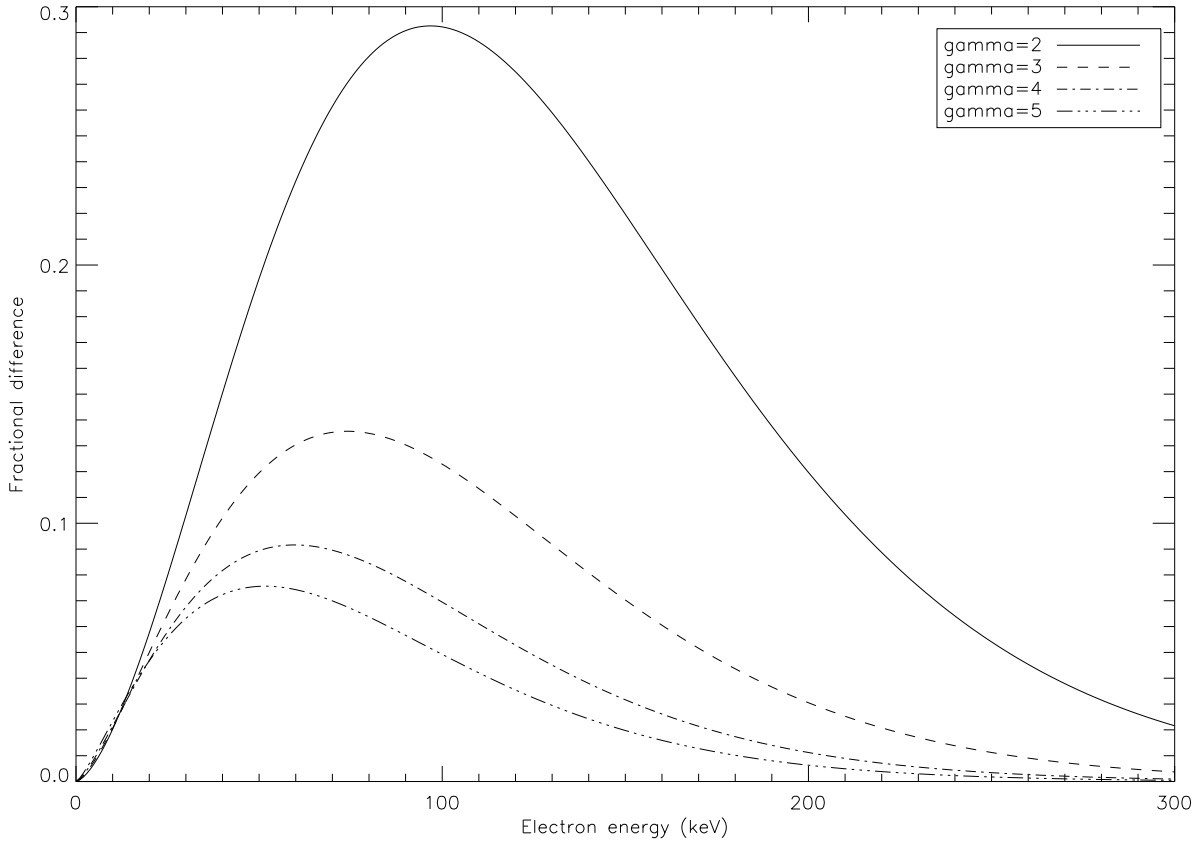

Figure 3.20: The fractional difference inferred within the Kramers electron spectrum are given in Figure (3.20) for a range of spectral indexes ($\gamma = 2$ to 5), given an empirically derived $\alpha(\epsilon)$

A closer examination of figure 3.20 indicates that it is similar in shape to its thin target counterpart. As a consequence of the assumed functional form of $\alpha(\epsilon)$, which was chosen to be a linear, second order terms in (3.70) were zero and thus the shape is dominated by the first order terms. Thus it will look similar to the thin-target case.

However it should be noted that if we were able to use a more complex form for $\alpha(\epsilon)$ based on more complete data being available then this would result in a more complex fractional difference in (3.70) and thus a more complex form in figure 3.20.

Chapter 4

A Hemispheric Eddington Green's Function Approach to the Albedo and the Influence on the Hard X-Ray Photon Spectrum

4.1 Introduction

In Chapters 2 and 3 we studied the effects of ignoring the albedo and the effect on the inferred parent electron spectrum. This was done for a specific functional form of the observed photon spectrum which was chosen to have a power law primary photon spectrum with an albedo feature which has a power law rise and an exponential decay. These properties along with an empirical fit to Bai and Ramaty results (Bai & Ramaty 1978) allowed the use of an analytic approach. However it is apparent that this technique would not be useful as a more general technique applied to a real observed photon spectrum which would require a numerical approach. In this chapter we study the effects of the albedo present within the observed photon spectrum, $I(\epsilon)$ by forward modelling. We adopt a generic, model independent, approach which uses Green's functions to calculate the Compton backscattered component within the observed photon spectrum using the work presented in Kontar et al. (2006).

4.1.1 Inversion Techniques

The production of the photon spectrum from a mean electron spectrum is a forward modelling problem (chapter 4) where we start with an assumed form of the electron spectrum, we predict using a model for the emission process (bremstrahlung) and end with a photon spectrum that would be produced for that assumed electron spectrum.

However, what we have in reality is the reverse of the forward fit - we start with the observed photon spectrum (the data function) and have to use the process of inversion to recover the electron spectrum (the source function) and possibly its anisotropy that would produce the observed photon spectrum.

Inversion is extremely important in flare spectroscopy as it allows us to investigate the physical conditions at the acceleration sites and given its importance it is worthwhile to provide a brief overview of the process of inversion (and regularisation) which forms the basis of the "Stereoscopic" electron spectroscopy technique Kontar & Brown (2006).

4.1.2 Forward Modelling

The scientific method is based upon the premise of hypothesis testing. This can be summarised as the development of a model and testing if the model compares to the data or observation. Mathematically, this is a form of convolution where the model and method of testing it are in essence, convolved (Craig & Brown 1986). This form of convolution is known as forward modelling. It is demonstrated extensively in previous chapters (2) – (5) where the observed photon spectrum $I(\epsilon)$ is a combination of the primary (or *true*) photon spectrum $I_p(\epsilon)$ emitted towards the observer and the reflected photon spectrum from the solar atmosphere.

The general mathematical form of the convolutions studied in previous chapters is given in Craig & Brown (1986) where the mapping properties for an integral equation are described as

$$\mathcal{K}[f(y); x] = g(x) \tag{4.1}$$

where $f(y)$ is the source function and $g(x)$ is the data function and $\mathcal{K}$ is the operator associated with the kernel k of the equation and the relevant limits.

Within this thesis, depending on the context, we use $g(x)$ to represent the observed photon spectrum $I(\epsilon)$, $f(y)$ represents the primary photon spectrum $I_p(\epsilon)$ with the kernel $\mathcal{K}$ encapsulating all the physical processes acting on the

source emission or $g(x)$ to represent the primary photon spectrum $I_p(\epsilon)$, $f(y)$ represents the mean electron spectrum $\bar{F}(E)$ with the kernel $\mathcal{K}$ encapsulating all the physical processes acting on the source emission

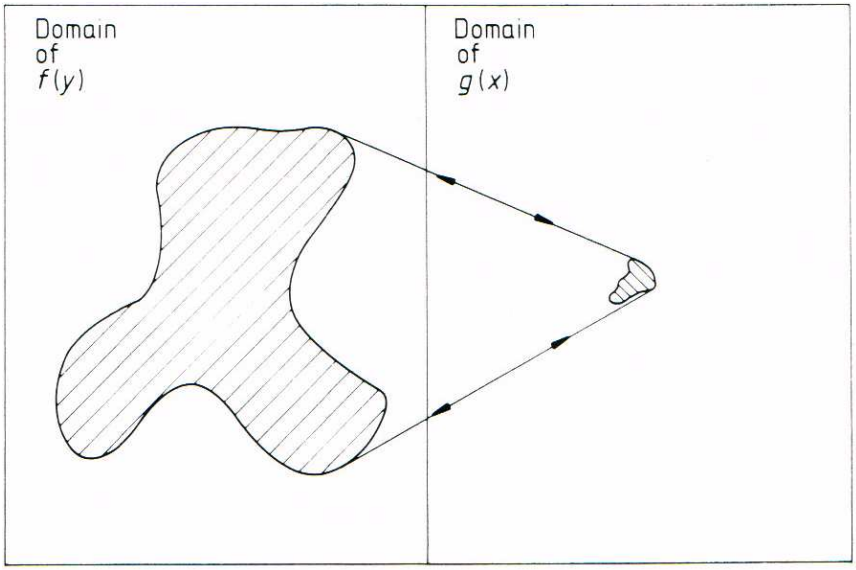

Figure 4.1: Illustration of the mapping properties of a typical integral equation (taken from Craig & Brown (1986), Figure 1.3)

Figure 4.1 illustrates that for the forward direction a wide range of $\bar{F}(E)$ or $\bar{F}(E,\mu)$ can be mapped to a narrow range of $I_p(\epsilon)$. This is not a problem for the forward direction as in chapters (2) – (5) we are specifying our starting conditions by defining a specific form for $I_p(\epsilon)$ and we have calculated the kernel from the known physics of the scattering processes present at the source.

Conversely Figure 4.1 also demonstrates that no matter how well $I(\epsilon)$ or $I(\epsilon,\mu)$ is determined (or measured) and we can therefore determine $I_p(\epsilon,\mu)$, many $\bar{F}(E,\mu)$ may be obtained when working backwards. Specifically the deconvolution here refers to the recovery of a primary photon spectrum $I_p(\epsilon)$ from data – $I(\epsilon)$.

This ultimately limits what can be concluded from work that naively uses the deconvolution process but Craig & Brown (1986) discuss several techniques for dealing with deconvolutions – the most relevant to the work presented in this thesis are discussed later in this chapter.

4.1.3 Deconvolving - The Inverse Problem

In reality we observe photon counts from satellites such as RHESSI and these counts, binned by energy, give us the familiar observed photon spectra - $I(\epsilon)$. However $I(\epsilon)$ does not represent the data function $g(x)$ because the integral equation $\mathcal{K}f = g$ (4.1) describes an idealised problem.

Unfortunately in all practical applications of (4.1) we have to take into account systematic errors such as rounding errors in the computer hardware or measurement errors in the recording of the data (Craig & Brown 1986). We can therefore rewrite (4.1) as

$$\mathcal{K}(f + \delta f) = g + \delta g \tag{4.2}$$

which we can write in a shorthand notation as

$$\mathcal{K}\hat{f} = \hat{g} \tag{4.3}$$

where $\hat{f}$ and $\hat{g}$ are known as the actualisation of f and g. In the context of the work presented in this thesis $\hat{g}$ in equation (4.3) actually represents the observed photon spectrum $I(\epsilon)$ along with all its errors. Unfortunately no matter how exacting the measurement process of $I(\epsilon)$ within the RHESSI spacecraft the nature of the noise processes present in $I(\epsilon)$ (and thus the realisation of the data function δg) will only ever be partially known.

It is apparent that, as a consequence of equation (4.2), a whole family of solutions of $\hat{f}(y)$ is defined by (4.1). Some of these solutions will be close to the true solution of $\mathcal{K}f = g$. However others will be entirely spurious as illustrated by Figure 4.1.

4.1.4 Regularisation

Regularisation is used to force which solutions are close to the true source function from those that are spurious according to some subjective criterion such as smoothness. The classical solution $\hat{f} = \mathcal{K}^{-1}\hat{g}$ to (4.1) is not strong enough to eliminate all the bad solutions. In fact $\|f - \hat{f}\|$ may be arbitrarily large (Craig & Brown 1986).

This is illustrated in figure 4.2 which highlights that two functions that differ by a small high frequency ripple in data space can be arbitrarily far apart in

function space (derivative space) and indicates that the backward solution is unstable to high frequency components within the data (Craig & Brown 1986).

Regularisation introduces a smoothness condition on the source function, in effect adding the extra information required to stabilise the inversion or to complete the definition of the problem.

A solution is thus obtained by solving

$$\|\mathcal{K}\hat{f} - \hat{g}\|^2 + \lambda\|\mathcal{K}f\|^2 = min \tag{4.4}$$

where λ is the regularisation parameter.

Alternatively the condition is arrived at by minimising the function $\mathcal{K}f$ and bounding the residuals though it is generally convenient to associate the regularisation parameter with the smoothness parameter (Kontar & Brown (2006) used in chapter 6).

This means in practice that by varying the smoothness parameter we can vary the constraint on the regularized solution. But this is ultimately a trade off as too much smoothing leads to a source function which has lost all of information that we are interested in studying. Alternatively too little smoothing and the source function becomes oscillatory *i.e.* unphysical.

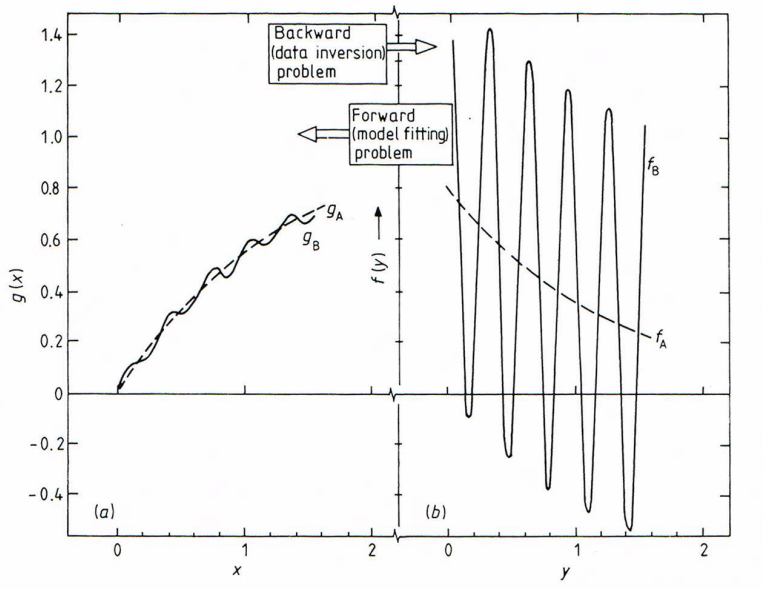

Figure 4.2: Illustration that the data functions g_i which are close to the extract data can result in unphysical source function upon inversion (taken from Craig & Brown (1986), Figure 3).

Ideally, as discussed within Craig & Brown (1986) the aim is to use different sources of data or observations to provide an independent verification of the model by the additional information on the source that this data will provide. In this way the source function and the kernel can be constrained. But this is not easily done as it depends not only upon the different, independent sources of data used along with the nuances that these add to the problem.

Craig & Brown (1986) provide an in depth discussion of the underlying theory of forward fitting and the inverse problem, and their implications in astronomy.

4.2 A Green's Operator Approach to Compton Reflection

Green's functions have been obtained for Compton scattering from Monte Carlo studies in Galactic Black holes and Active Galactic Nuclei (AGNs) by authors such as White et al. (1988), Poutanen et al. (1996) and others. These were determined by making specific assumptions about the angular distribution of the incident radiation field and were not a full anisotropic angular Compton reflection Green's function.

They consider radiation reflected from a semi infinite slab and averaged over all viewing angles, and resulted in an angle averaged Green's function $\hat{G}(\epsilon, \epsilon^{'})$ which describes the relationship between inbound photons $\epsilon^{'}$ and outbound scattered photons ϵ. Although these studies were extended in some cases to yield solutions for specific viewing angles, a general angular dependent treatment was not developed until the work published by Magdziarz & Zdziarski (1995). Their work was also based on a Monte Carlo approach but resulted in an angular dependent Compton Green's function for spatially integrated reflected flux $\bar{\mathbf{G}}(\mu, \epsilon, \epsilon^{'})$ such that we can express the reflected photon spectrum from a semi infinite slab as an integral over the Green's function and the downward emitted, primary photon spectrum (for any specific observer direction)

$$I_r(\epsilon) = \int_{-1}^{1} \int_{\epsilon}^{\infty} \bar{\mathbf{G}}(\mu, \epsilon, \epsilon^{'}) I_o(\epsilon^{'}) d\epsilon^{'} d\mu \tag{4.5}$$

Magdziarz & Zdziarski derived approximations to Green's function $G(\mu, \epsilon, \epsilon^{'})$ for the Compton scattering of X-rays and γ-rays by electrons for an isotropic incident flux on a semi infinite slab of matter, specifically for accretion disks surrounding Active Galactic Nuclei and Galactic Black holes but a semi infinite

slab also applies to the solar photosphere.

In practice the Compton scattered (or albedo) component presented by Magdziarz & Zdziarski 1995 is implemented as a set of analytic functional forms, fitted to data which combine to represent a Compton reflection Green's operator which extends over an energy range from a few keV to several MeV. Although the Green's function obtained in this way is angle dependent, Magdziarz & Zdziarski, precalculated the Green's function at pre-defined angular intervals. As such it was referred to as a semi angular Compton Green's function in Poutanen et al. (1996) in which a general, fully angular, Green's function was published for Compton scattering. This Green's function was later applied within the context of solar flare plasmas by Kontar et al. (2006) for the case of isotropic primary photon emission $I_o(\epsilon)_{isotropic}$.

In this Chapter we extend the work of Kontar et al. (2006) to include anisotropic emission (Appendix A.1). Kontar's algorithm was implemented in Interactive Data Language (IDL) which is a computer programming language used to develop software for visualisation of complex data sets and was used to develop the data analysis software for the RHESSI mission (Lin et al. 2002).

Here we use that environment to investigate the effects of an anisotropic emission model on the albedo using a Green's function approach as given in equation (4.5). Specifically we build upon the isotropic model by extending it to include anisotropic emission in the form of an energy independent multiplier (Appendix A.2) and an energy dependent multiplier (A.3) empirically fitted to published data.

Studying the effects of an energy dependent anisotropy upon the albedo will allow us to determine what physical effects such as aberration or beaming influence the observed spectrum. Aberration will cause the photon emission to become preferentially beamed into the forward direction and thus causes the emission to be anisotropic. As such this is very important in the study of models such as the *Collisional Thick target* (CTT) model of Brown (1971) where the emission of photons is beamed into the forward direction and this anisotropic emission is itself a function of energy.

4.3 An Angular Dependent Green's Function

The HXR photon spectrum as seen by an observer at Earth $I(\epsilon)$ is a combination of the primary photon energy spectrum $I_o(\epsilon)$ emitted directly towards the observer and that which has been emitted towards the solar photosphere and (Compton) backscattered in the direction of the observer $I_r(\epsilon)$.

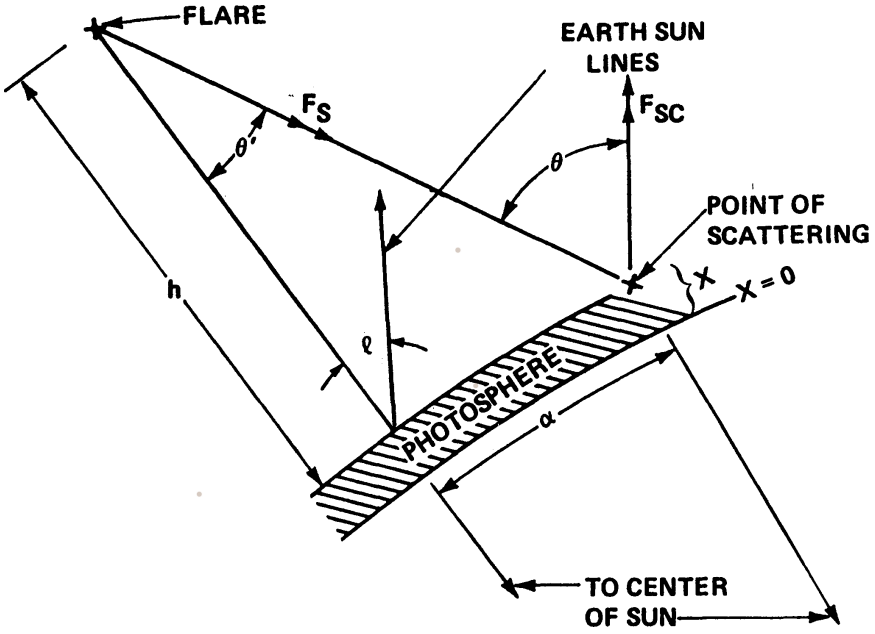

Figure 4.3: Flare source geometry (taken from Tomblin 1972)

Figure 4.3[1] illustrates diagrammatically the flare source geometry (Tomblin 1972). Figure 4.3 does not show the component of the emission that is directly emitted towards the observer.
We can express the observed photon spectrum as seen by an observer at earth as

$$I_{obs}(\epsilon) = I_o(\epsilon) + I_r(\epsilon) \tag{4.6}$$

In (4.6) the reflected component $I_r(\epsilon)$ represents, the physical scattering response of the photospheric plasma to those incident primary photons emitted downward towards the photosphere. This can be represented as a (mathematical) convolution of the primary photon spectrum $I_o(\epsilon)$ with an *albedo function* $A(\epsilon)$ as

[1]Note that α here refers to the heliocentric angle.

$$I_r(\epsilon) = A(\epsilon) I_o(\epsilon) \tag{4.7}$$

Substituting (4.7) into (4.6) we can express the observed photon spectrum in terms of the primary photon spectrum gives

$$I_{obs}(\epsilon) = I_o(\epsilon) + A(\epsilon) I_o(\epsilon) \tag{4.8}$$

which is just a more general form of equation (2.1) given in Chapter 2.

In equation (4.8) the function $A(\epsilon)$ is a specific instance of the Green's function operator $\hat{G}$ for Compton scattering as given in (4.5) (studied in Chapters 2 and 3). We can therefore use the more general form of the operator, instead in expressions (4.7) to (4.8) to describe the Compton reflection of HXR photons.

4.4 The Discrete Compton Green's Function

Kontar et al. (2006) developed a discrete version of the Green's function which was produced in the form of a Matrix G_{ij} which could more readily be used within IDL simulations.

Using this discrete form of G_{ij} we can express (4.5) as a matrix equation and obtain an expression for the observed photon spectrum in terms of the discrete Green's function as

$$(I_{obs})_\mu = (I_o)_\mu + \int d\mu \int_\epsilon^\infty \bar{\mathbf{G}}(\mu, \epsilon, \epsilon^{'}) I(\epsilon^{'}) d\epsilon^{'} \tag{4.9}$$

we can re-write (4.9) in the form of a matrix equation as

$$\mathbf{I_{obs}} = \mathbf{I_p} + \hat{\mathbf{G}}\mathbf{I_p} \tag{4.10}$$

and the ith element I_i^{obs} of I_{obs} (for an observed angle μ) can be written as

$$(\mathbf{I_{obs}})_i = (\mathbf{I_p})_\mathbf{i} + \mathbf{\Sigma_j} \hat{\mathbf{G}}^\mu_\mathbf{ij} (\mathbf{I_p})_\mathbf{j} \tag{4.11}$$

4.4.1 Isotropic Green's Correction to a Power Law Primary Photon Spectrum

We initially use an isotropic primary photon spectrum I_o given by

$$I_o(\epsilon) = \frac{(\gamma - 1)}{4\pi\epsilon_o} \left(\frac{\epsilon}{\epsilon_o} \right)^{\gamma} \tag{4.12}$$

Substituting (4.12) into (4.11) we get the observed photon spectrum $I_{obs}(\epsilon)$ using the Green's function.

In previous chapters we used the albedo to investigate the error inferred in the parent electron spectrum for both isotropic and anisotropic primary photons emission. However here we are interested in studying how the isotropic and anisotropic primary photon emission effects the size and shape of the Compton reflected spectrum (or albedo) itself and not the abolute value of the observed photon spectrum. Therefore in order to allow a comparison between the isotropic and anisotropic results it is more meaningful to use the albedo (spectrum) $R(\epsilon)$ defined as

$$R(\epsilon) = \frac{I_r(\epsilon)}{I_o(\epsilon)} \tag{4.13}$$

where $R(\epsilon)$ is the albedo spectrum, $I_o(\epsilon)$ is the primary and $I_r(\epsilon)$ represents the observed spectrum in equation (4.13).

By studying the size and shape of $R(\epsilon)$ rather than the absolute value of the primary photon spectrum I_o and the observed photon spectrum I_{obs} the differences between isotropic and anisotropic emission will be apparent later in this chapter.

Results - Isotropic Green's correction

Figure 4.4.(a) shows the results of $R(\epsilon)$ as given in expression (4.13). It is the albedo for a power–law primary spectrum of $\gamma = 4$ (chosen to represent a reasonably soft spectrum) and scaled to a photon energy ϵ_o of 30keV. It shows the characteristic albedo features as a peak reflectivity around 30keV. The lower part, 4.4.(b), shows the effect of the albedo upon the photon spectrum as seen by an observer at earth for a primary power–law photon spectrum emitted isotropically into the downward hemisphere or towards the photosphere.

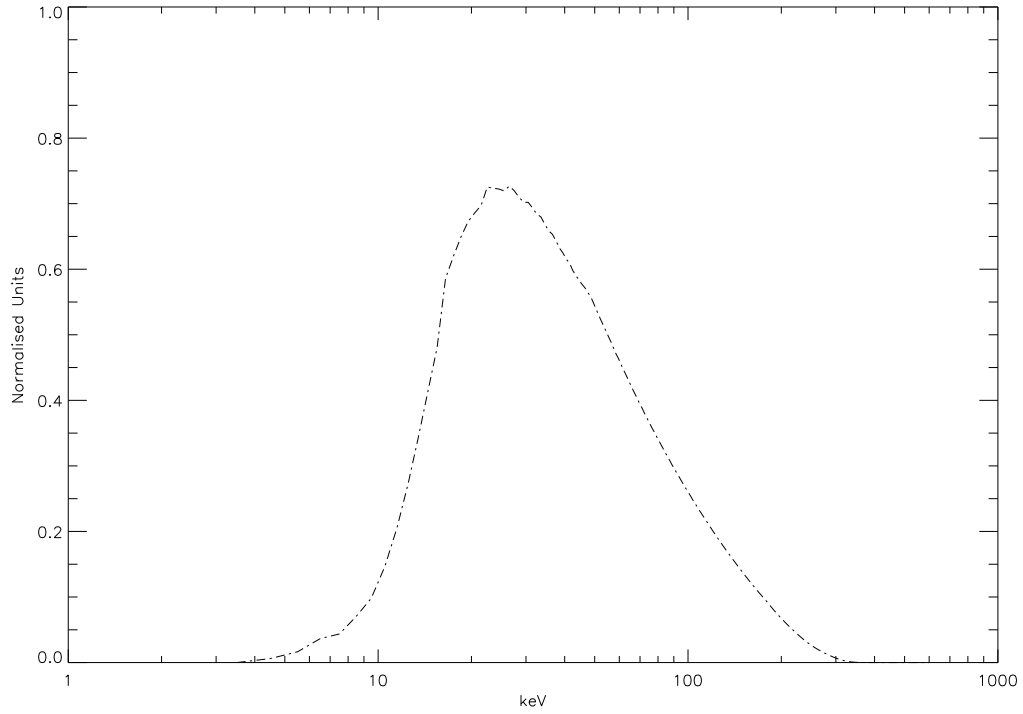

a. Reflection albedo spectrum $R(\epsilon)$

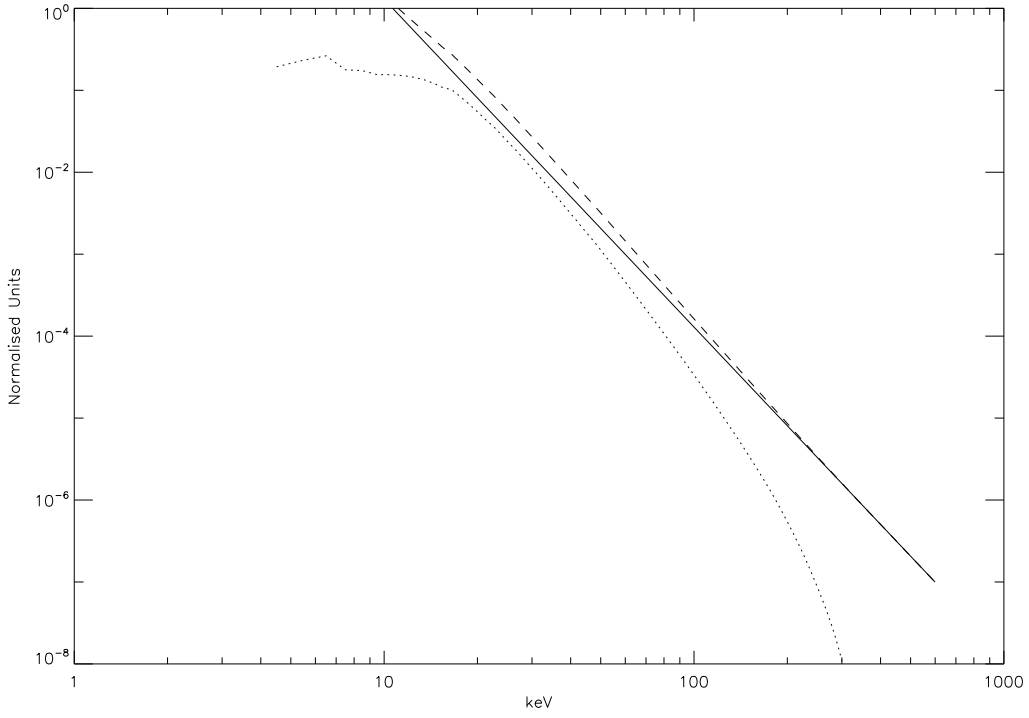

b. Primary (solid line) , total (dashed line), and albedo (dotted line) spectra

Figure 4.4: Isotropic Greens correction for primary photon spectrum $I_o(\epsilon)$ with $\gamma = 4$

4.5 Anisotropic Emission - The Eddington Hemispheric Approximation

In section 3.2 we introduced the Eddington hemispheric approximation for anisotropic emission which represents anisotropic emission as a fraction emitted into an upward and downward hemisphere.

In reality each hemisphere represents the integration of $I_o(\epsilon, \mu)$ over μ ($\mu = cos(\theta)$) in that hemisphere ($\int_{-1}^{1} I_o(\epsilon, \mu) d\mu$) and we will use this in a later chapter to compare the differences between the anisotropic Eddington hemispheric approach and a full anisotropic radiative transfer approach.
We can express the primary emission in an anisotropic form using an α as

$$I(\epsilon) = 2I_o(\epsilon)((1-\alpha) + \alpha A(\epsilon)) \tag{4.14}$$

Expression (4.14) gives the photon spectrum emitted from a photospheric source with $A(\epsilon)$ as the Compton reflection or albedo component and is really an approximation to the Green's operator. Therefore, given equations (4.5) and (4.6), we can express $I(\epsilon)$ in terms of $\alpha(\epsilon)$ and a Green's function analogous to (4.9) as

$$I(\epsilon, \mu) = I_o(\epsilon, \mu)(1 - \alpha(\epsilon)) + \int_{\epsilon}^{\infty} \bar{G}(\mu, \epsilon, \epsilon^{'}) \alpha(\epsilon^{'}) I(\epsilon^{'}, \mu^{'}) d\epsilon^{'} \tag{4.15}$$

We can write (4.15) in term of an Eddington hemispheric approximation as

$$I(\epsilon) = I_o(\epsilon)_{up}(1 - \alpha(\epsilon)) + \int_{\epsilon}^{\infty} \bar{G}(\mu, \epsilon, \epsilon^{'}) \alpha(\epsilon^{'}) I(\epsilon^{'})_{down} d\epsilon^{'} \tag{4.16}$$

which we can write in its discrete form as an energy independent anisotropic Green's correction.

Thus the i^{th} element of I_{obs}, I_i^{obs} for an observer angle of μ can be written as

$$I_i^{\mu} = (I_p^{up})_i (1 - \alpha) + \Sigma_j \hat{G}_{ij}^{\mu} \alpha (I_{p,i}^{down})_j \tag{4.17}$$

4.6 Results - Eddington Hemispheric Anisotropic Multiplier

The following plots detail the reflection (albedo) spectrum $R(\epsilon)$ for different values of α.

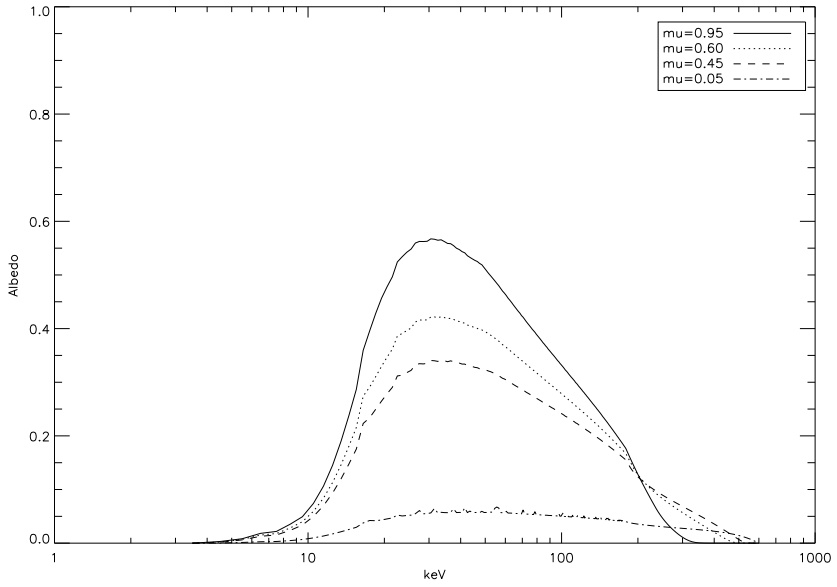

a. Albedo spectrum - alpha=0.5 (isotropic)

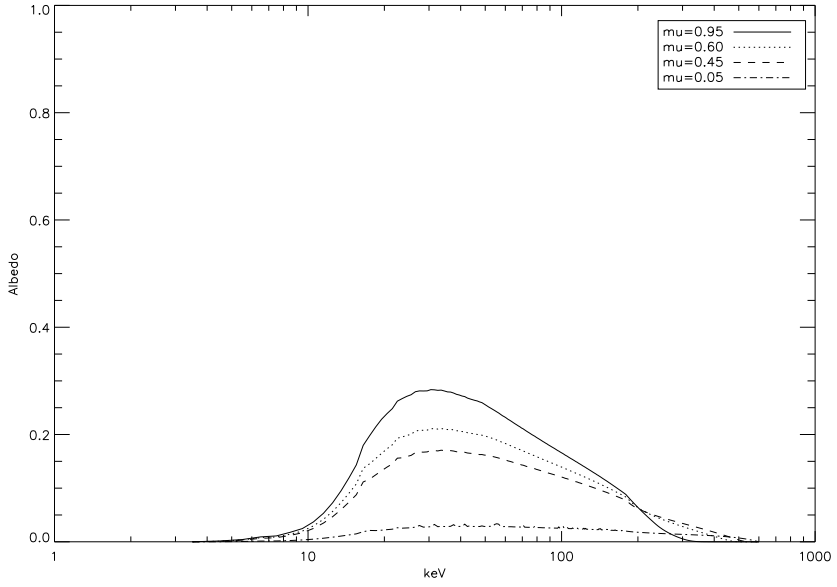

b. Albedo spectrum - alpha=0.25

Figure 4.5: Anisotropic Green's hemispheric correction for a $\gamma = 3$

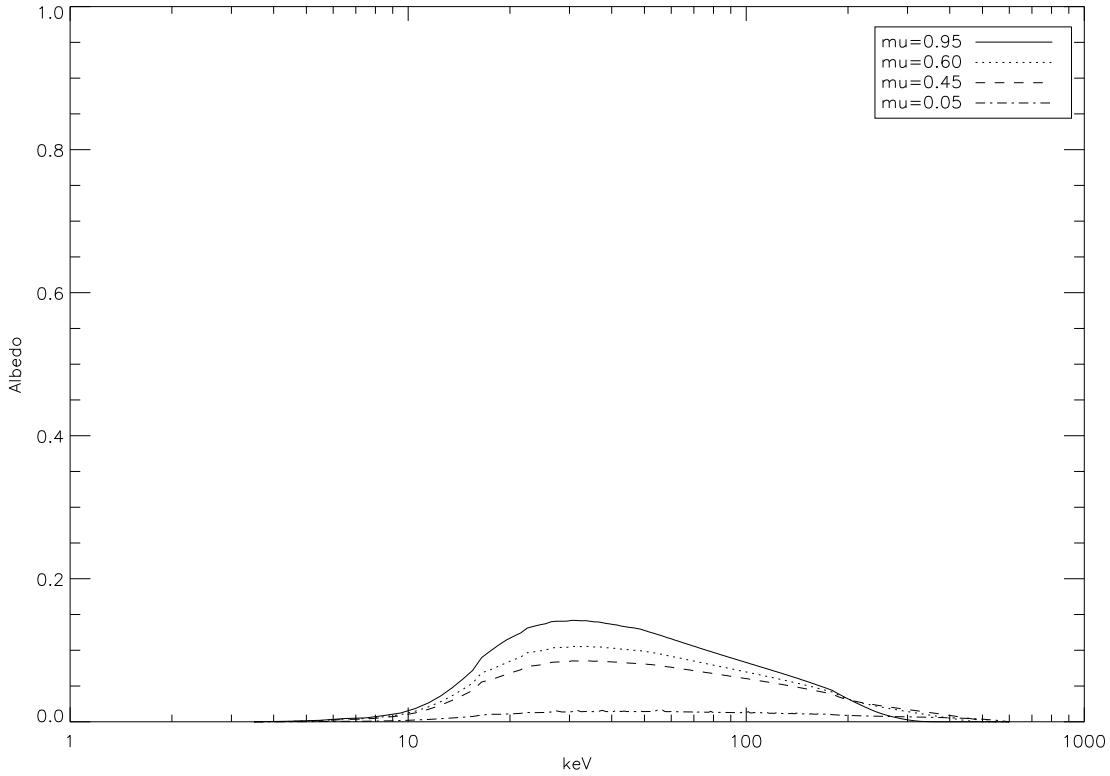

c. Albedo spectrum - alpha=0.125

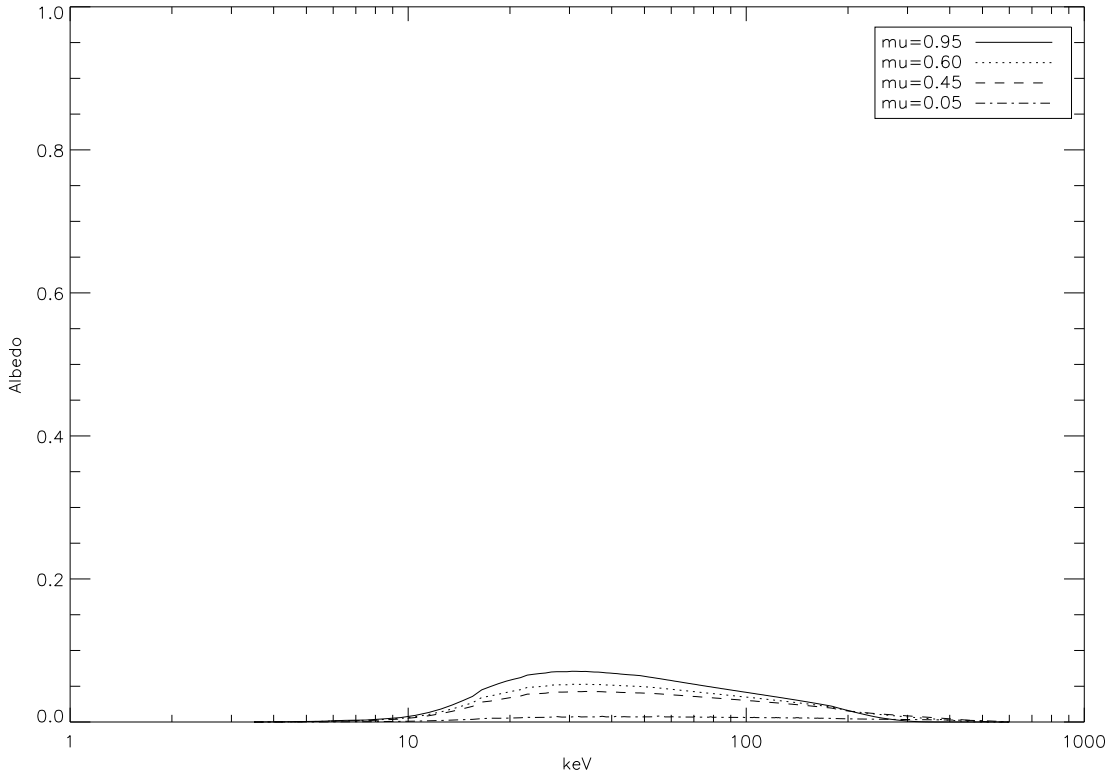

d. Albedo spectrum - alpha=0.0625

Figure 4.6: Anisotropic Green's hemispheric correction for a $\gamma = 3$

Given (4.17) we would expect that an energy independent α will simply result in the peak value of $R(\epsilon)$ being scaled with the value of α and this can be clearly seen in Figures (4.5) and (4.6)[2].

We now extend this approach to the more interesting case of an energy dependent α, $\alpha(\epsilon)$ which we will use to model the energy dependent beaming suggested by the Collisional Thick Target model (Brown 72).

4.7 An Angular Dependent, Energy Dependent Green's Function Approach

In this section we extend the discrete form of the Compton Green's function to be anisotropic (Appendix A.3), where the anisotropy itself is a function of energy.

Until now we have introduced anisotropy into our models using a simple multiplier or energy dependent multiplier. However care must be taken in the introduction of an energy dependent anisotropy into the Green's function approach as the Green's function as given in equation (4.9) also depends upon the inbound energy and is within an integral *i.e.* the introduction of an additional energy dependent $\alpha(\epsilon)$ into (4.9) has the effect of changing $\bar{\mathbf{G}}(\mu, \epsilon, \epsilon^{'})$ and this will invalidate the pre-calculated values of the discrete form of the Green's function G_{ij} as used within (4.11) which we use in the IDL routines.

Clearly we cannot introduce $\alpha(\epsilon)$ into (4.9). However we can circumvent this by considering the primary photon spectrum as being composed of a sum of discrete pulses of photons each emitted at energy ϵ and apply the anisotropy as a simple multiplier α_ϵ which has a value dependent upon each different energy[3].

If we express equation 4.6 in terms of anisotropic emission as

$$I(\epsilon, \mu) = I_o(\epsilon, \mu) + I_r(\epsilon, \mu) \tag{4.18}$$

Where $\mu = cos(\theta)$ here is the angle between the observer and the plane of emission[4].

We can now express the Compton reflected spectrum (equation 4.5) in an anisotropic form as

[2]An analogous scaling effect can be seen in the energy independent anisotropic fractional difference ($\frac{\Delta F(E)}{F_o(E)}$) of recovered electron spectra given in Figures (3.2) to (3.9).

[3]As X-Ray photon emission at energy ϵ is independent of emission at other energies then it is valid to consider the total X-Ray photon emission as consisting of a sum of the emission from each individual energy ϵ in this way.

[4]the plane of emission here is assumed to be normal to the photosphere.

$$I_r(\epsilon,\mu) = \int d\mu^{'} \int G(\mu,\mu^{'},\epsilon,\epsilon^{'}) I_o(\epsilon^{'},\mu^{'}) d\epsilon^{'} \tag{4.19}$$

Therefore we can re-write (4.9) in an isotropic form as

$$I(\epsilon,\mu) = I_o(\epsilon,\mu) + \int d\mu^{'} \int G(\mu,\mu^{'},\epsilon,\epsilon^{'}) I_o(\epsilon^{'},\mu^{'}) d\epsilon^{'} \tag{4.20}$$

where $\mu^{'} = cos(theta)$ in this instance is the angle of photon emission.
we can write equation 4.20 in a discrete form as a matrix equation as

$$I_{\epsilon,\mu} = \Sigma_{\epsilon'} \left[(\mathbf{I_o})_{\epsilon',\mu} + \mathbf{\Sigma}_{\mu'} \left(\alpha_\epsilon \hat{\mathbf{G}}_{\epsilon,\epsilon',\mu,\mu'} (\mathbf{I_o})_{\epsilon',\mu} \right) \right] \tag{4.21}$$

or, in its discrete form the ith energy element I_i of the observed photon spectrum at observer angle μ, as

$$(\mathbf{I}_i^{\mu}) = \Sigma_k \left[(\mathbf{I_o})_{\mathbf{i}}^{\mu} + \mathbf{\Sigma_j} \alpha_{\mathbf{i}} \hat{\mathbf{G}}_{\mathbf{ijk}}^{\mu} (\mathbf{I_o})_{\mathbf{j}}^{\mu} \right] \tag{4.22}$$

which we can sum to give the anisotropic, angular and energy dependent observed photon spectrum $\mathbf{I}(\epsilon)$.

To complete the energy and angle dependent Green's function approach we now apply this to a particular form of I_o. We do this using the empirical fit which was introduced in Chapter 2.

4.7.1 Empirical Fit to Leach & Petrosian Data (Eddington Hemispheric Approach)

In this section we develop a discrete version of the empirical fit, given in Section 3.3.1)[5]. The fit is based on data taken from Figure 3.10 which gives the directivity D of the X-Ray photon emission as a function of polar angle θ for flare models at two photon energies $22keV$ and $210keV$.

We include an Eddington Hemispheric approach in the empirical fit by converting the directivity D into an equivalent value which represent the emission in that hemisphere (α) by assuming that the value of the directivity D at $\theta = 0$ (upwards) and $\theta = 180$ (downwards) applies isotropically within that hemisphere. This hemispheric equivalent directivity (α) is shown in equation 4.24 below.

[5]This results in a more convenient expression that was used in the IDL simulation

Given section 3.3.1 we now express table 3.1 in terms of the directivity D. These are given in table 4.1 below

$\epsilon(keV)$	$D_{\theta=0^\circ}$	$D_{\theta=180^\circ}$
22	1	3
210	1	22

Table 4.1: Empirical fit - ratio of emission into each hemisphere.

Using the values given in Table 4.1 we extend the directivity to be energy dependent by applying a linear interpolation between the two data points which gives

$$D(\epsilon) = \frac{19.0}{188}\epsilon(keV) + 0.78 \tag{4.23}$$

We then express the relationship for directivity (4.23) in terms of an energy dependent $\alpha(\epsilon)$ as

$$\alpha(\epsilon) = \frac{1}{D(\epsilon) + 1} \tag{4.24}$$

or, in its discrete form the jth element (or energy) α_j of the directivity, as

$$\alpha_i = \frac{1}{D_i + 1} \tag{4.25}$$

where ϵ ranges from 1keV to 300keV.

Finally substituting (4.25) into (4.22) gives

$$(\mathbf{I}_i^\mu) = \Sigma_k \left[(\mathbf{I_o})_\mathbf{i}^\mu + \mathbf{\Sigma_j} \left(\frac{\mathbf{1}}{\mathbf{D_i + 1}} \right) \hat{\mathbf{G}}_\mathbf{ijk}^\mu (\mathbf{I_o})_\mathbf{j}^\mu \right] \tag{4.26}$$

Equation (4.26) describes an empirically fitted expression for the discrete, energy and angular dependent hemispheric Green's observed photon spectrum.

4.7.2 Results - The Anisotropic, Angular Dependent Green's Function

Using the albedo spectrum $R(\epsilon)$ we now show the influence of an energy dependent anisotropic emission on the albedo component of the spectrum for the angular hemispheric Green's function approach.

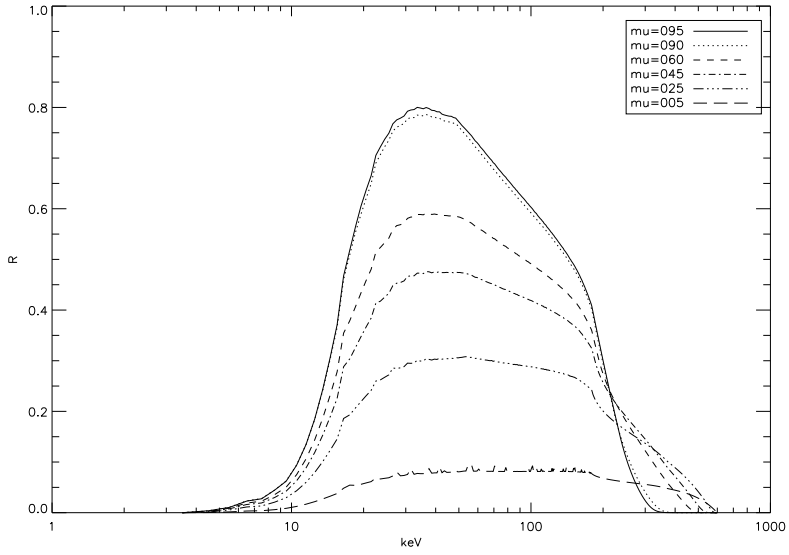

a. Albedo spectrum - $\gamma = 2$

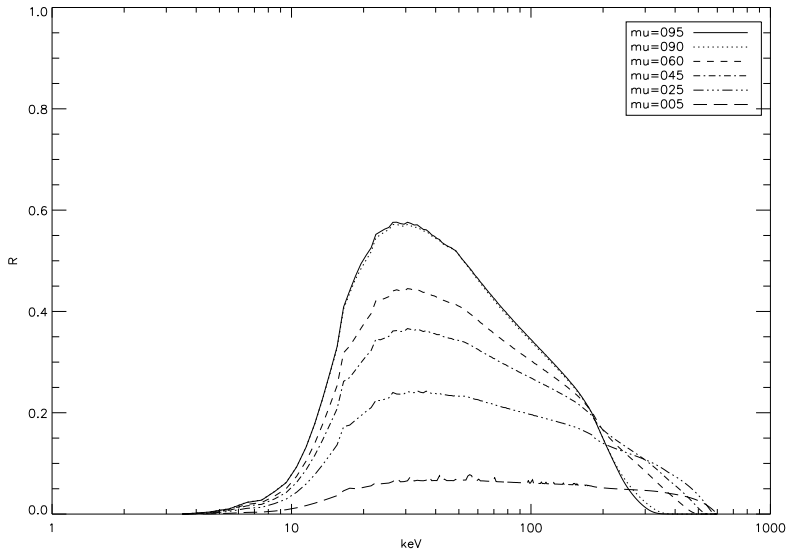

b. Albedo spectrum - $\gamma = 3$

Figure 4.7: Anisotropic Green's correction

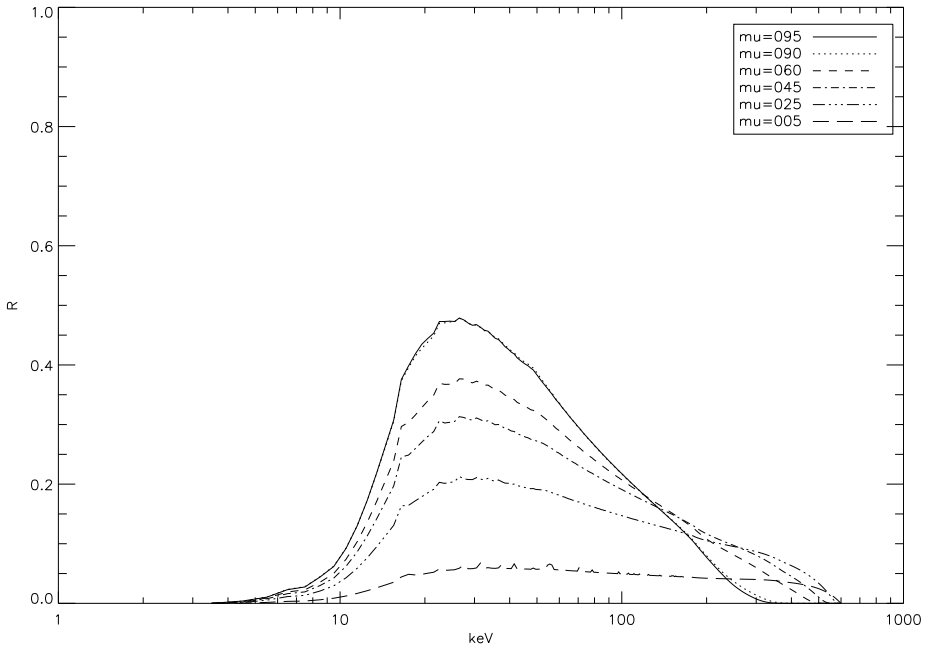

a. Albedo spectrum - $\gamma = 4$

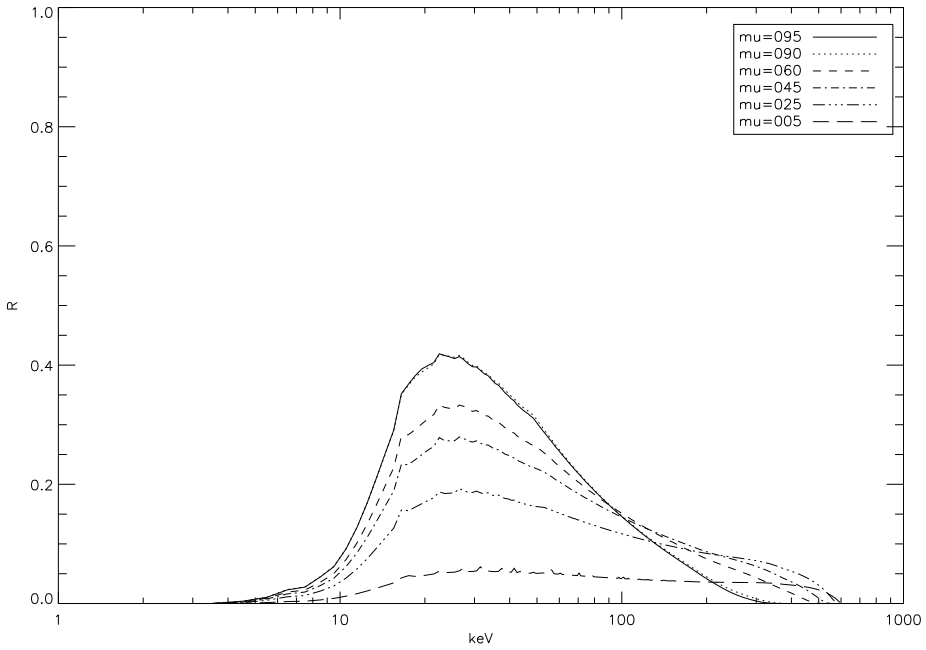

b. Albedo spectrum - $\gamma = 5$

Figure 4.8: Anisotropic Green's correction

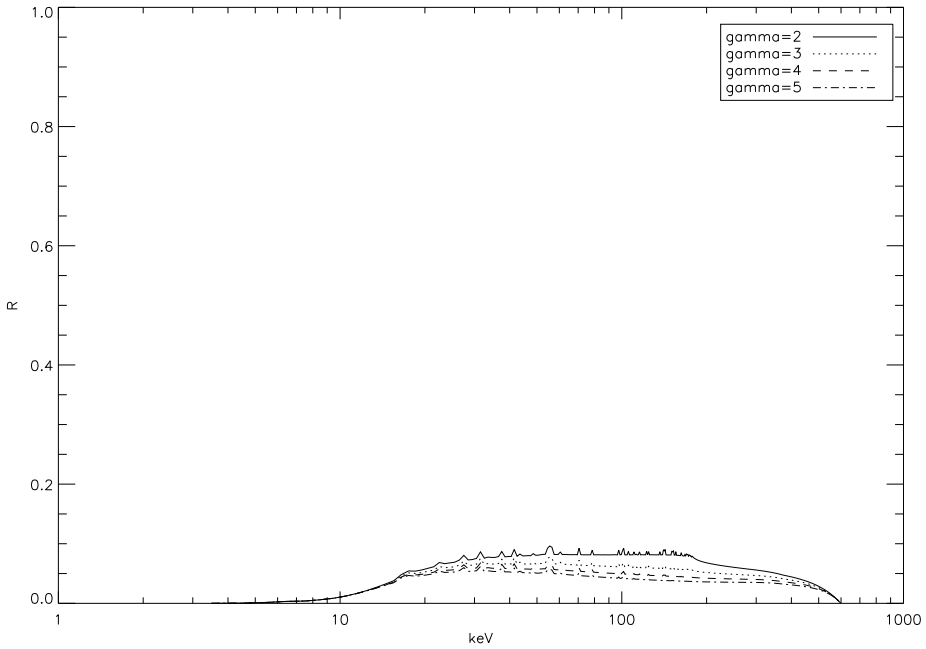

a. Albedo spectrum - $\mu = 0.05$ (limb)

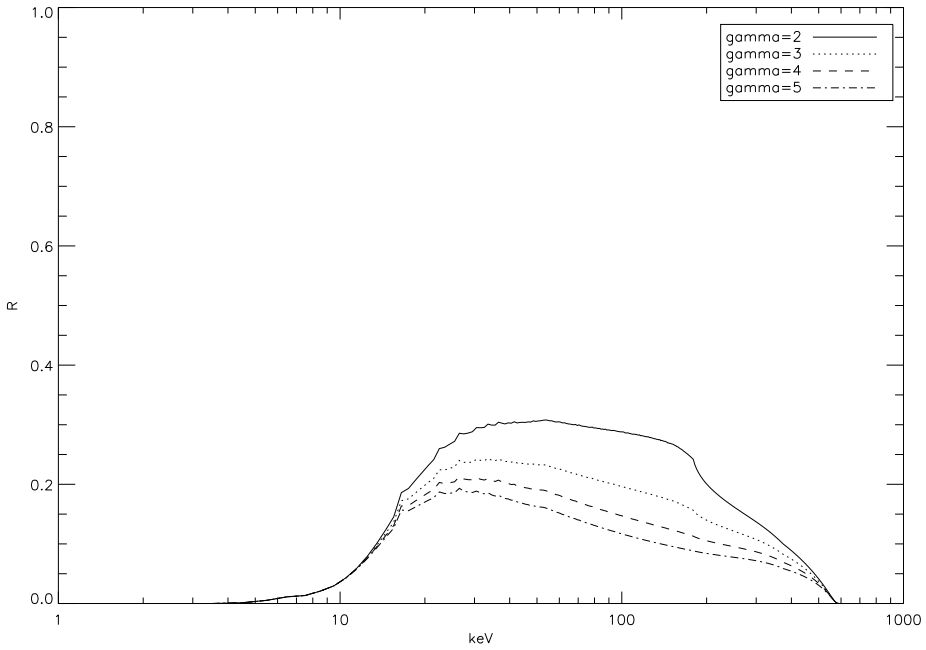

b. Albedo spectrum - $\mu = 0.25$

Figure 4.9: Anisotropic Green's correction

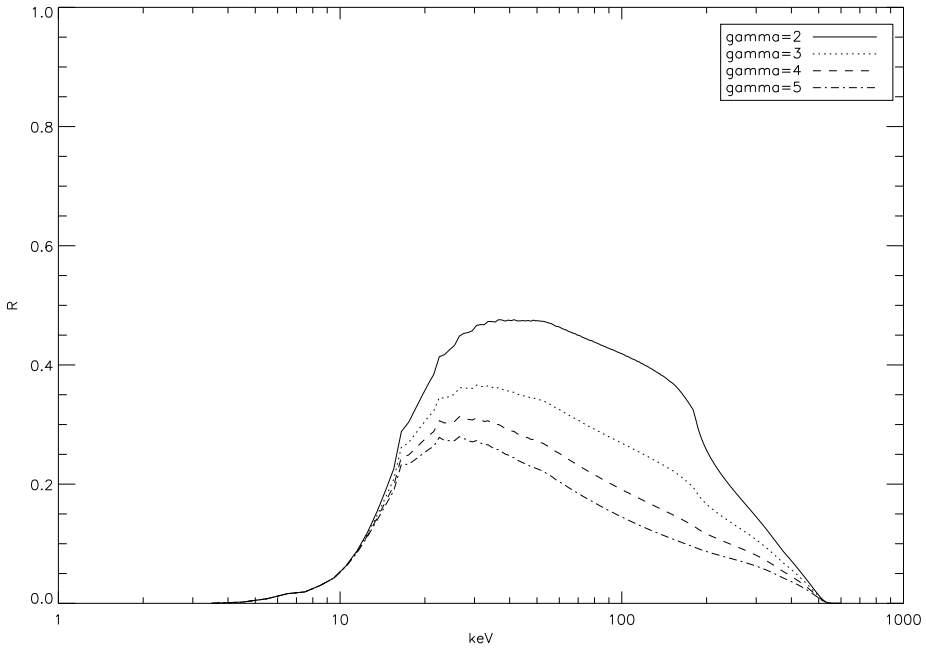

a. Albedo spectrum - $\mu = 0.45$

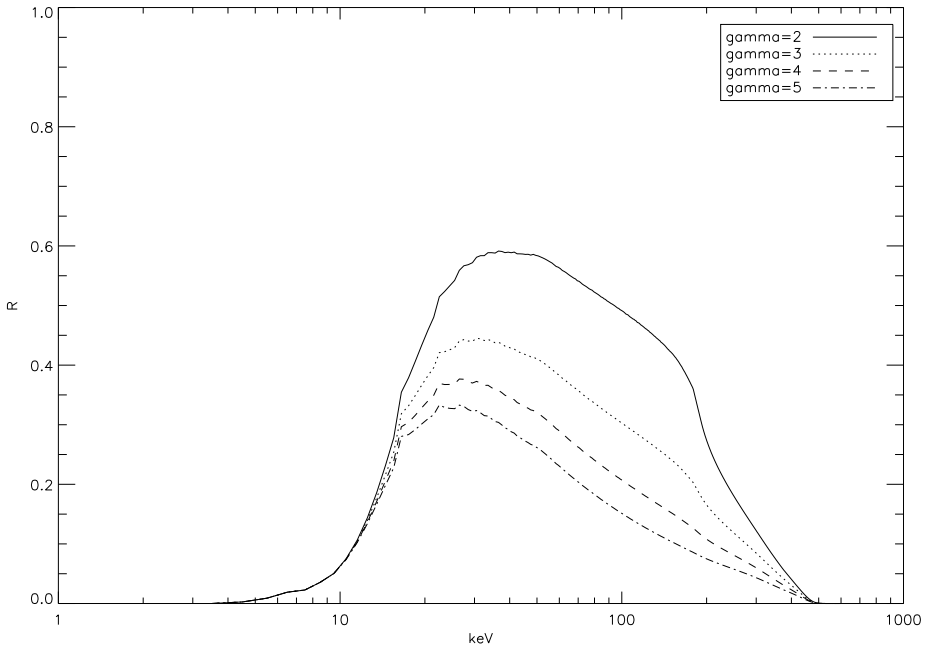

b. Albedo spectrum - $\mu = 0.60$

Figure 4.10: Anisotropic Green's correction

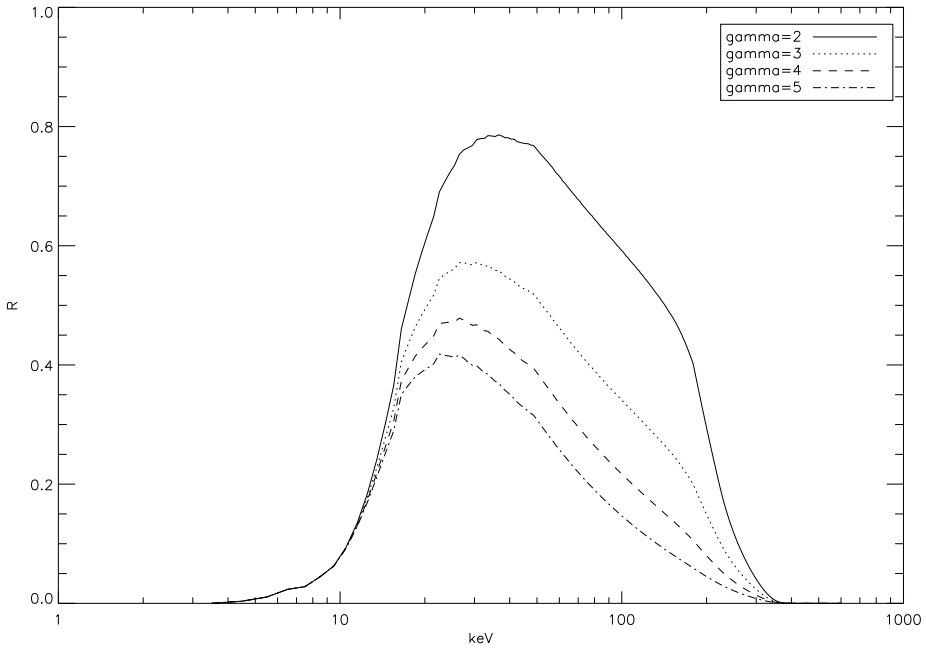

a. Albedo spectrum - $\mu = 0.90$

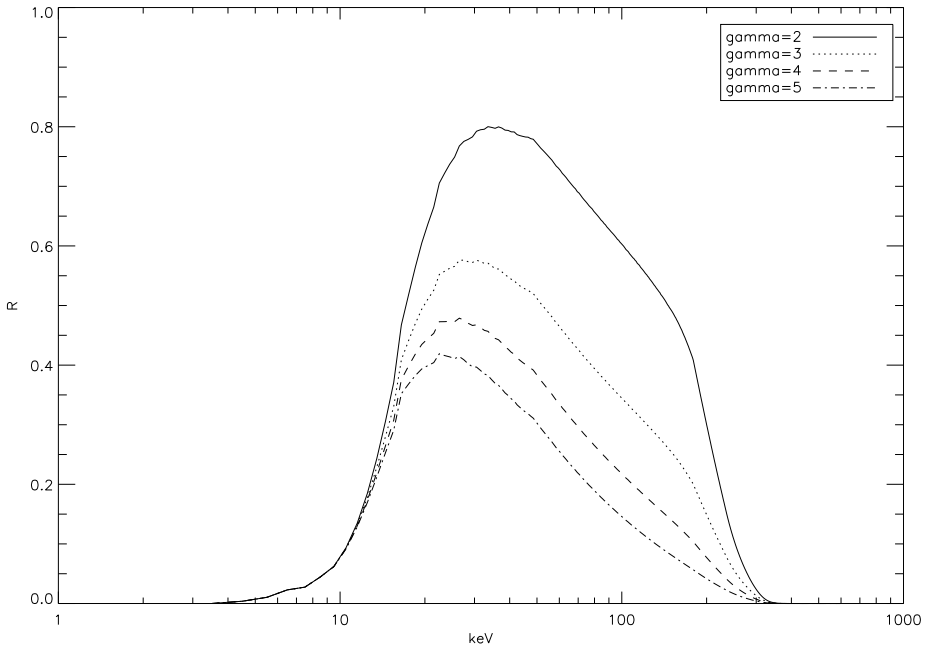

b. Albedo spectrum - $\mu = 0.95$

Figure 4.11: Anisotropic Green's correction

Figures 4.7 and 4.8 shows the variation of the albedo spectrum for $\gamma = 2$ to $\gamma = 5$ for various viewing angles μ. Figures 4.9 and 4.11 shows the variation of the albedo spectrum with viewing angles for spectral indices $\gamma = 2$ to $\gamma = 5$. The

peak at 7keV is due to Iron (K-edge) line absorption. This results in an increase in the Compton-backscattered radiation at energies slightly less than 7keV.

It is apparent from these Figures that the shape of the reflection spectrum itself has been modified from the isotropic case between the 30 and 200 keV photon energies. The effect of the empirical fit to the Leach and Petrosian data is particularly apparent for hard photon spectra ($\gamma = 2, 3$). The direct consequence of this is that in assuming a power law photon spectrum with a simple isotropic reflection component will underestimate the resulting observed photon spectrum within the 30keV to 200keV energy range.

4.8 Discussion

We demonstrated a model independent approach for studying the effect of the albedo upon the primary photon spectrum $I_o(\epsilon)$. We use *model independent* here to reflect that this approach does not require us to make specific assumptions about the form of the primary photon emission[6] and the form of the albedo which would be required for an analytic approach. The Green's operator approach initially developed by Kontar was extended to include anisotropic effects using an energy independent factor α.

We extended the energy independent approach to study the effects of energy dependent anisotropy on the photon spectrum using an empirical fit to Leach and Petrosian data. We note that using such an empirical fit is simplistic, specifically that

1. The empirical fit was based upon two data points (Leach and Petrosian 1983). This allows only a linear fit to the data points below 250 keV - the fit above this energy becomes unphysical.

2. The excess introduced into the reflected spectrum is only valid for energies below 250 keV.

3. Ideally as and when further data points become available then this will allow a more complex empirical fit to be introduced into our models and allow the model to be refined.

[6]To be physically realistic the primary photon emission must remain approximately power-law.

Finally, using the energy dependent anisotropic Green's hemispheric approach, we found that in assuming an isotropic power law primary photon spectrum we underestimate the reflection spectrum $R(\epsilon)$ and therefore the primary spectrum is the overestimated within the 30keV to 250 keV energy range.

Chapter 5

A Full Radiative Transfer Approach with Anisotropy

5.1 Introduction

Current research directed at using recovered electron spectra as a diagnostic of the electron emission processes within flare plasmas is dependent upon the observed photon spectrum ($I(\epsilon)$) being corrected for the effects of the photospheric backscattering of X-ray photons which are present within the observed signal to give the primary photon spectrum ($I_p(\epsilon)$). However this was predominantly done for photon spectra that were produced by isotropic X-Ray radiation field which we refer to as an isotropic photon spectrum.

However models such as the thick target (Brown 1973) within which electron emission is (forward) beamed would require that the primary radiation field is in fact anisotropic and thus the primary photon spectrum in anisotropic. This was investigated in the previous chapter using a hemisphere averaged, semi angular dependent, Green's function approach of Kontar et al. (2006). These authors developed a data based, Green's operator, technique for removing the reflection component from a photon spectrum thus allowing $I_p(\epsilon)$ to be recovered from an arbitrary $I(\epsilon)$. This technique was applied from Magdziarz & Zdziarski (1995) in which Green's function operators were developed primarily for the study of AGN and galactic black holes candidates.

Prior to this, the existing treatment of Green's functions only produced angle integrated Green's functions. The results of Magdziarz and Zdziarski's monte carlo method produced angle dependent approximations to green's functions $\mathbf{G}$ for the Compton reflection of X-Ray and γ-Rays by cold electrons that were dependent upon the viewing angle of the reflecting slab. Crucially this work does

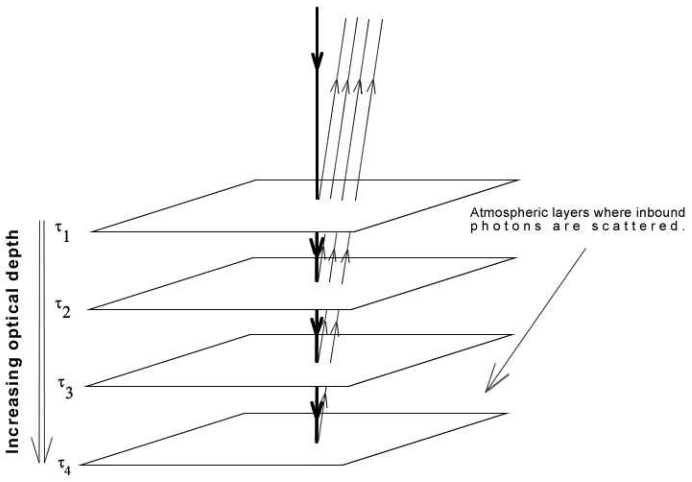

Figure 5.1: Poutanen model layer geometry

not account for anisotropic emission or is able to calculate Green's functions for an arbitrary (viewing) angle. Thus the fully angular, Green's operator radiative transfer method developed by Poutanen should be thought of as the 'gold standard' for the production of the Green's Compton spectrum as it does not make any averaging assumptions that the methods make.

Poutanen uses a discrete ordinate finite difference method (Grant & Hunt (1969a) and Grant & Hunt (1969b)) for numerically solving the polarized radiative transfer equation derived within Poutanen et al. (1996) for radiation incident on an optically thick planar slab of neutral matter accounting for both angle and polarization properties as seen in figure 5.1 below.

Figure 5.1 shows the diagramatic representation of the flare slab geometry (taken from Poutanen et al. (1996))[1].

This results in a general Green's matrix able to correct an arbitrary (power-law like) photon spectrum at any viewing angle in the forward direction.

[1]Note that using this model each slab only reflects photons or allow photons to pass through - no part of the emission originates in the slab itself.

5.2 A Radiative Transfer Green's Function Algorithm

5.2.1 An Overview

The work presented in Poutanen et al. (1996) was implemented in the form of a programming language algorithm (specifically, in Fortran 77).

Here we use the Fortran 77 version of the algorithm but in order to preserve the integrity of the science implemented in it and to ensure we do not add errors, we use the algorithm as a 'black box'. This is achieved by arranging the code in such a way that all of the code that is required to define the photon spectra that we are trying to study is provided within externally supplied routines, distinct from the main algorithm. This in practice means that we provide a primary photon spectrum to it (the input) and it gives the observed photon spectrum (the output) and crucially we are not concerned with the internal workings of the algorithm which we assume to be correct.

The full listing of the Poutanen algorithm is extensive and it is not necessary or feasible to list it in its entirety. However our aim in this section is to describe the points relevant to the work presented in this thesis.

The physical program can be broken into 3 parts: the 'black box' calculation of the reflection spectrum, the externally supplied definition of the outgoing photon spectrum ($I(\epsilon, \mu)$) and a 'driver' routine within which the energy and angular values are setup and subsequently used within the call to the Compton reflection calculation part.

5.2.2 The Driver Routine

The driver routine (Appendix C.1) manages the file input and output for the results of the Compton spectrum calculation. It also allocates the memory and sets up the arrays of variables - the (μ), (ϵ) values, the escaping flux ($I(\epsilon, \mu)$) and the incoming primary photon spectrum ($I_o(\epsilon^{'}, \mu^{'})$) for the main part of the program.

The driver routine computes the following:

1. The cosine of angles (μ) where reflected spectrum is computed.

2. The photon energies (in units of $m_e c^2$) where the reflected spectrum is computed (ϵ).

3. Call the external library to provide the following:

   (a) The total escaping flux in a given direction; generally this can be a function of energy, angle and anisotropy.

   (b) The specific intensity of the incoming photon spectrum as a function of photon energy and angles photon energies in $m_e c^2$ - $I(\epsilon', \mu')$.

4. The Compton spectrum, $R(\epsilon, \mu)$, is calculated at each output angle for the provided primary photon spectrum[2].

5.2.3 The Externally Supplied Models

The input spectrum $I_o(\epsilon, \mu)$ is supplied in the form of specific intensity as a function of both energy ϵ and angle μ. This is done in the form of an externally supplied routine written in the 'C' programming language[3].

This external routine takes a value for ϵ and μ and the spectral index γ and returns a value for $I(\epsilon, \mu)$ to the main algorithm[4].

5.2.4 Limits on the Techniques

The fully angular Green's method assumes that the input photon spectrum is power law like. Whilst an arbitrary form did cause the algorithm to break - indicated by an incomplete or infinite solution, in practice, it was found that some departure from the power law photon spectrum was tolerated by the algorithm, enough to allow a thermal component and a high energy cut off. In reality this is sufficent to handle most of the flare models in the other parts of this thesis.

5.3 Compton Reflection from an Isotropic Source

Here we use the radiative transfer method to obtain the Compton reflection spectrum for a power law photon spectrum. By applying this technique in the isotropic limit we will be able to verify the results that were suggested in Poutanen et al.

[2]This part of the calculation is treated as a 'black box' as we are only concerned with providing the input parameters to the function and reading the output values returned to the driver routine.

[3]C was chosen for convenience as any 3rd generation programming language would be suitable

[4]This allows the models to be changed without changing the main routine and thus to preserve it as a black box.

(1996, section 4.2.3), specifically that Poutanen found that the results for fully radiative transfer method agreed with those of Magdziarz & Zdziarski (1995) to $\approx 6\%$ for an unpolarized isotropic power law spectrum.

This is an important point - as Magdziarz & Zdziarski (1995) is the underlying basis for both Poutanen et al. (1996) and Kontar et al. (2006) discretized Green's method; both methods should be similar in the isotropic limit. Furthermore we now have an independent method for verifying the work done using the hemisphere averaged Green's operator approach albeit in its isotropic limit but it does provide confidence in the anisotropic extension.

This provides a powerful technique which allows the comparison between the fully radiative transfer (Green's) method and the Green's method of Kontar et al, which as stated previously is based on the results in Magdziarz & Zdziarski (1995) and is a result of functions empirically fitted to energy ranges in the spectrum. Therefore the results that we obtained using the Kontar et al. Green's method should be within 10 percent of our results obtained from using the radiative transfer technique. This will be explored in more detail later in this chapter.

As the Poutanen et al. approach is a radiative transfer solution to Compton reflection and not an empirical fit, we consider it as a 'gold standard'. The two approaches are different in that one is empirical and the other is a radiative transfer solution, it is expected that there will be small differences due to the different assumptions - the approximations introduced by empirical fitting to data, and the theoretical simplifications made to arrive at a valid model and allow integration of the model.

5.3.1 Results - Simple Isotropic Radiative Transfer Solution

Figures 5.2.a, 5.2.b, 5.3.a and 5.3.b give the reflection (albedo) spectrum $R(\epsilon) = I(\epsilon)/I_o(\epsilon)$ for $\gamma = 2 - 5$ for various values of μ. Figures 5.4 (a)-(h), 5.5 (a)-(h), 5.6 (a)-(c) show the plots of the albedo spectrum for $\gamma = 2-5$ for various viewing angles μ. The peak at 7keV which is visible in all of the results given here is due to Iron (K-edge) absorption.

5.3.2 Comparison of the Two Approaches

The figure below (5.7) shows the results for the two methods for $\gamma = 2$ and an observing angle $\mu = 0.95$ - effectively on the disk centre.

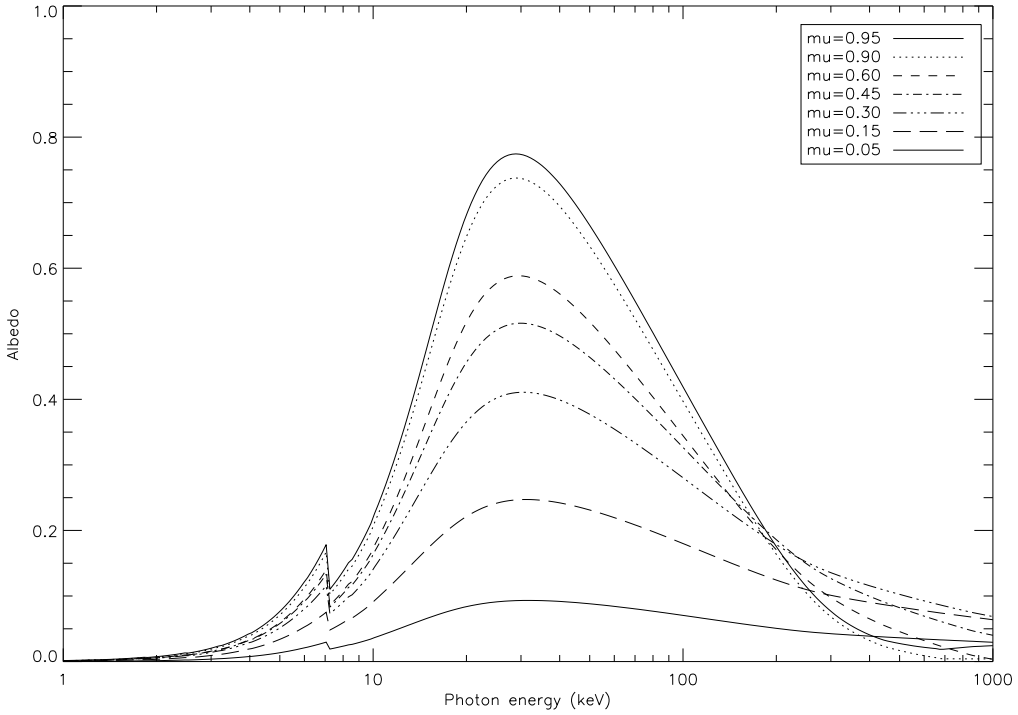

a. Reflection spectrum for $\gamma = 2$ (isotropic)

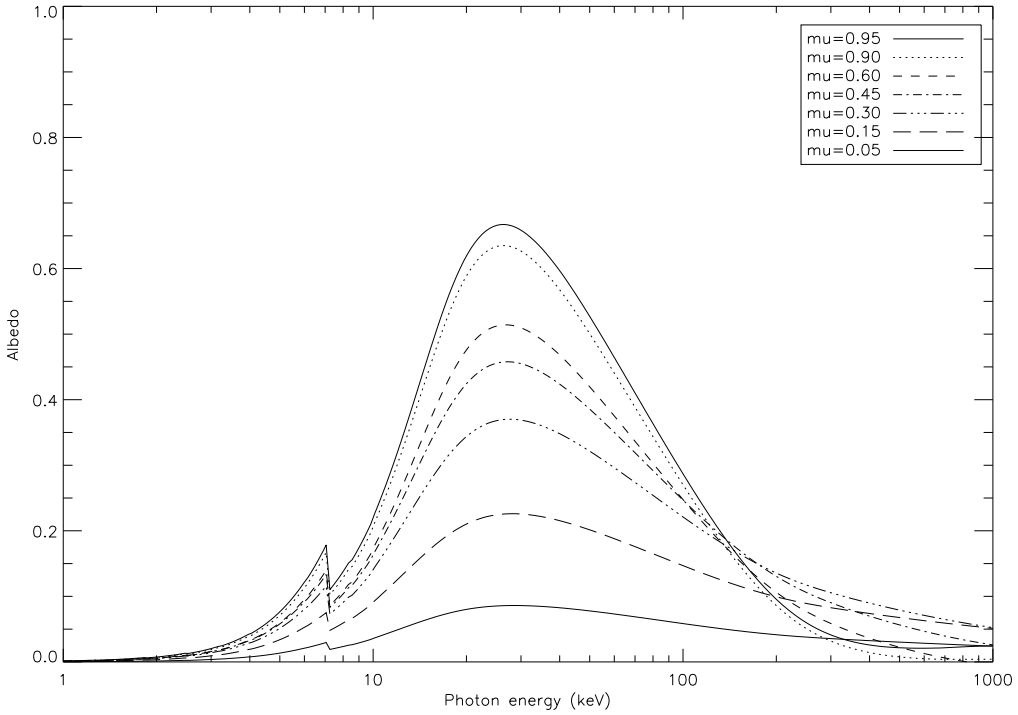

b. Reflection spectrum for $\gamma = 3$ (isotropic)

Figure 5.2: Isotropic albedo using a radiative solution

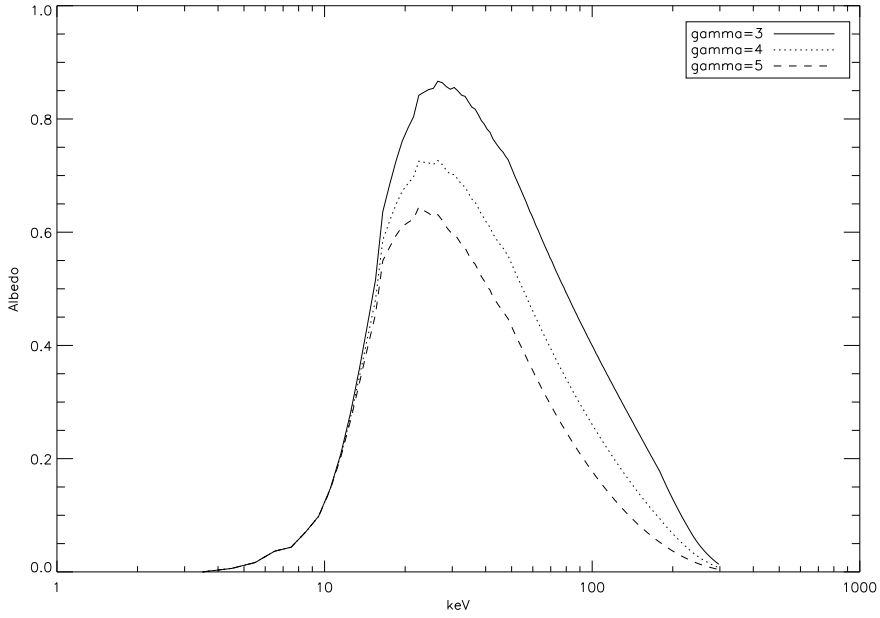

a. Intrinsic reflection spectrum Hemisphere averaged

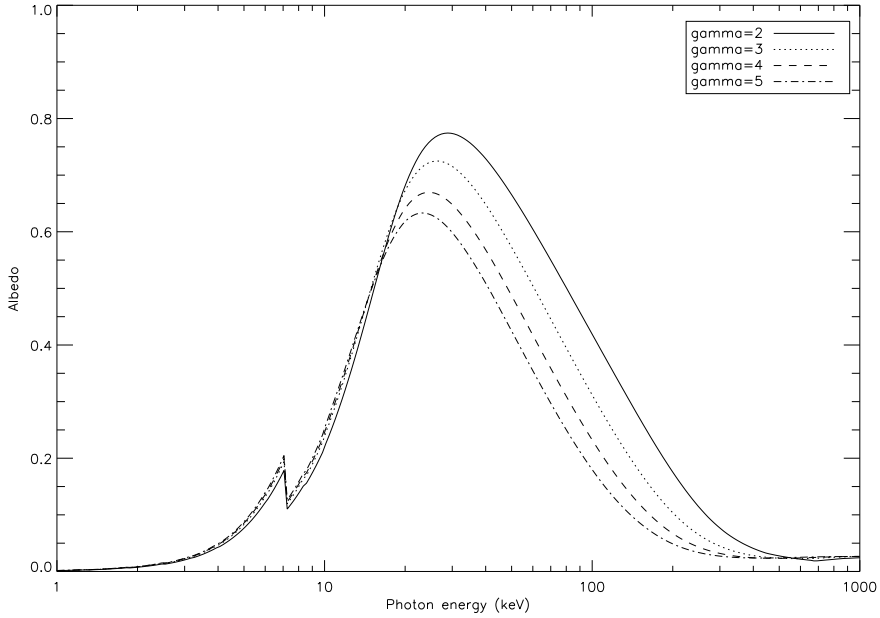

b. Intrinsic reflection spectrum Full angular greens

Figure 5.7: Isotropic Green's correction for $\mu = 0.95$

Figure 5.7.(a) shows the reflection spectrum $R(\epsilon)$ in the hemisphere average approach for $\gamma = 3 - 5$ whilst figure 5.7.(b) shows the reflection spectrum $R(\epsilon)$ for the full radiative transfer approach for $\gamma = 2 - 5$, both for a viewing angle of $\mu = 0.95$. It can be seen that both techniques agree well for spectra at the disk

centre $\mu > 0.90$ in both scale and shape. However as we demonstrate later in this thesis even small differences between the photon spectra may be amplified when the photon spectrum is inverted into electron space.

As stated earlier in this section a difference of $\approx 6\%$ was found between the results obtained by Poutanen et al. (1996) and those of Magdziarz & Zdziarski (1995) (used in Kontar et al. (2006) and thus in chapter 4) for unpolarised isotropic power law incident flux and intensity. The difference between the two approaches given in Figure 5.7 at their peak values is $\approx 10\%$ and is therefore consistent with the difference indicated in Poutanen et al. (1996, Section 4.2.3)[5].

5.4 Compton Reflection from an Anisotropic Source

As previously stated both the semi angular Green's function developed by Kontar et al. (2006) and the fully angular method developed by Poutanen et al. (1996) are based upon an empirical fit Green's function presented in Magdziarz & Zdziarski (1995).

The semi angular Green's function of Magdziarz & Zdziarski (1995) and consequently the implementation of it by Kontar et al. (2006) assumes a primary radiation field (prior to scattering) that has been averaged.

Kontar precalculates the Green's function as a matrix array at preset angles (implemented as an IDL routine). Critically, this method does not allow an energy dependent anisotropic emission in $I_p(\epsilon)$[6]. Although this is due to limitations intrinsic to the way the precalculated matrix is made, we circumvented this limitation by introducing an energy dependent anisotropy as a series of primary spectrum input $I_p(\epsilon)$ at each energy ϵ, calculating the reflection, and effectively constructing $I(\epsilon)$ by repeating the calculation for each photon energy value in turn. On the other hand the Poutanen method allows an energy dependent anisotropic primary photon spectrum - $I_p(\epsilon, \mu)$.

One question which can be investigated with a fully angular Green's function is: does the averaging of the source emission affect the resulting observed photon spectrum in the situation where the source emission is anisotropic such as in the thick target where the emission would be forward beamed. In this section we will investigate the effects of an anistropic primary photon spectrum on the

[5]Given that the two approaches agree in the limit of isotropic photon emission we can therefore make a meaningful comparison between both approaches for anisotropic photon emission.

[6]We found in the previous chapter (4) that energy independent anisotropy simply introduces a scaling factor in $R(\epsilon)$

albedo using the fully angular Green's function approach (Poutanen). Initially we introduce this using a simple functional form which will model the anisotropy within the polar angle θ' which is illustrated in Figure 5.8 below.

Figures 5.8.a.–5.8.d. show, diagramatically, the anisotropic HXR photon spectrum for a fully angular anisotropic primary radiation field - the primary photon spectrum. Specifically figure 5.8.a.–5.8.d. represents the emission profile that would be expected with increasing photon energies [7].

5.4.1 Anisotropic Photon Spectrum Assuming a Simple Functional Form for Anisotropy

Here we take the model described in Figure 5.8 and assume a simple functional form for the anisotropic emission as

$$I(\epsilon, \theta) = A_o \epsilon^{-\gamma} (\cos(\theta))^n \tag{5.1}$$

where A_o is a normalisation constant, and n is even[8].

In section 5.3.1 we defined the albedo as $R(\epsilon) = \frac{I_r(\epsilon)}{I_p(\epsilon)}$

In the fully anisotropic case we have a primary emission of $I_p(\epsilon, \mu)$ thus it is clear that we must integrate the primary emission over μ to get the primary spectrum that will be reflected at that energy.

We can rewrite the albedo as

$$R(\epsilon) = \frac{I(\epsilon)}{\int_{-1}^{0} I_p(\epsilon, \mu) d\mu} \tag{5.2}$$

Although equation 5.1 is separable in ϵ and θ, this property of the functional form is not important for this model as we are investigating the effect of the anisotropy on the Compton reflection spectrum here[9].

[7] it should be noted that in practice photons of energy ϵ will have been emitted from electrons at energies $< 2\epsilon$. This is an important consideration for the albedo as the photon emission at the albedo peak (around 30keV) will mainly come from electrons which have energies of 60keV or less.

[8] This is to ensure that the emission remains non negative at all θ.

[9] However our ultimate aim is to use an empirical fit to published data to provide a physically realistic model with energy dependent anisotropy.

5.4.2 Results - Simple Anisotropic Radiative Transfer Solution

The following Figures 5.9.a, 5.9.b, 5.10.a and 5.10.b give the intrinsic reflection spectrum $R(\epsilon)$ for $\gamma = 2 - 5$ for various values of μ.

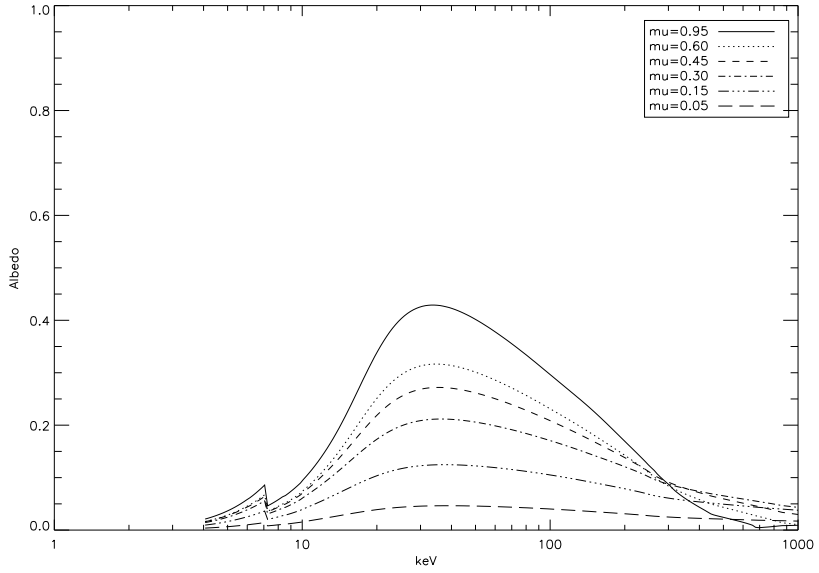

a. Reflection spectrum for $\gamma = 2$ (anisotropic)

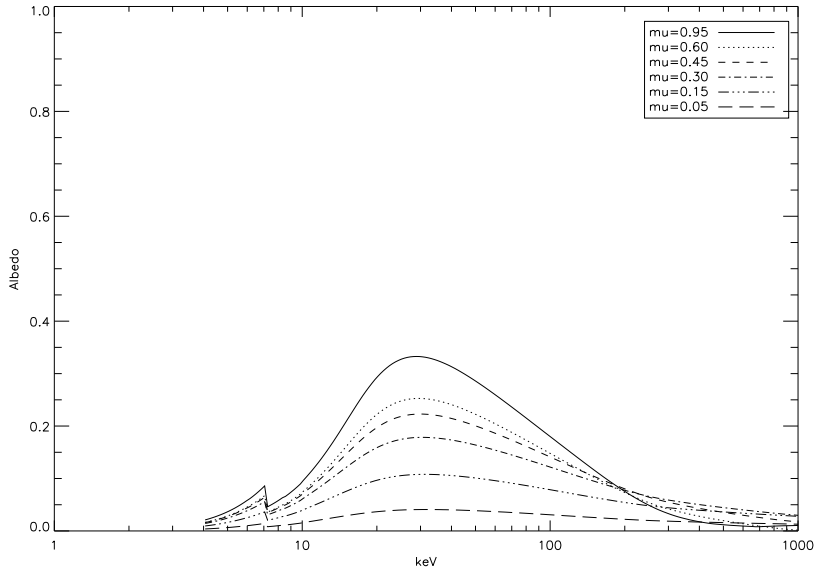

b. Reflection spectrum for $\gamma = 3$ (anisotropic)

Figure 5.9: Anisotropic albedo using a radiative transfer solution at spectral indexes $\gamma = 2, 3$ for various observer angles μ (n=0 - isotropic)

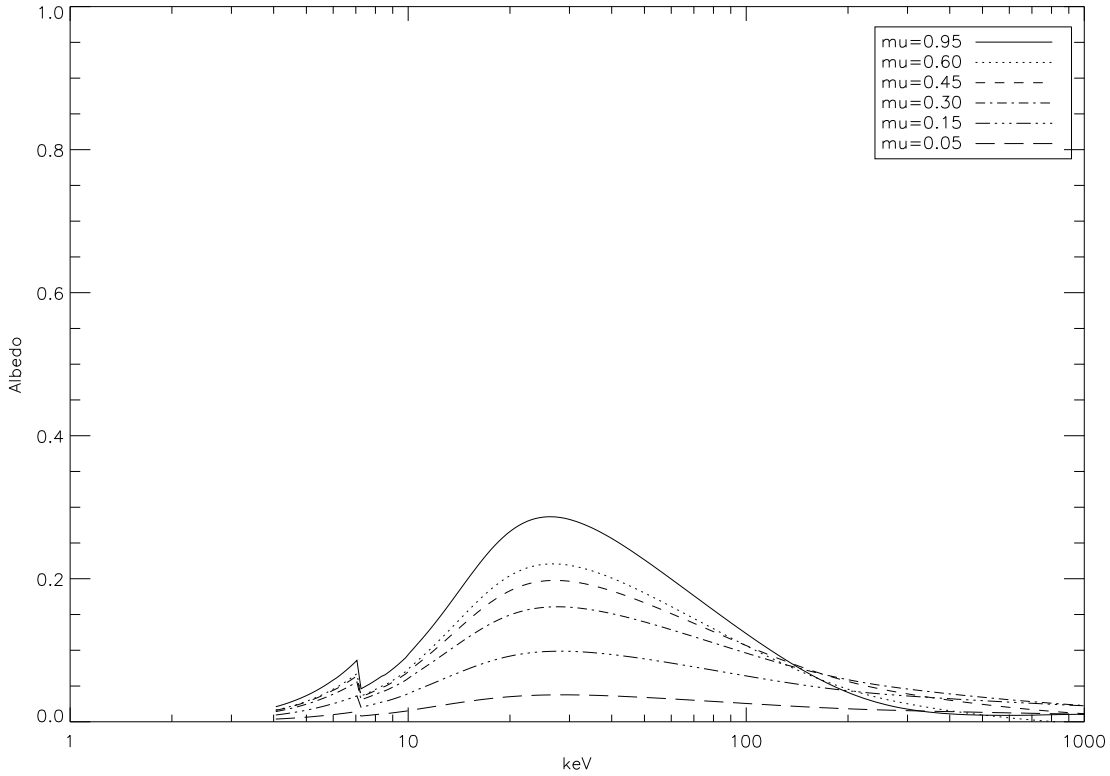

c. Reflection spectrum for $\gamma = 4$ (anisotropic)

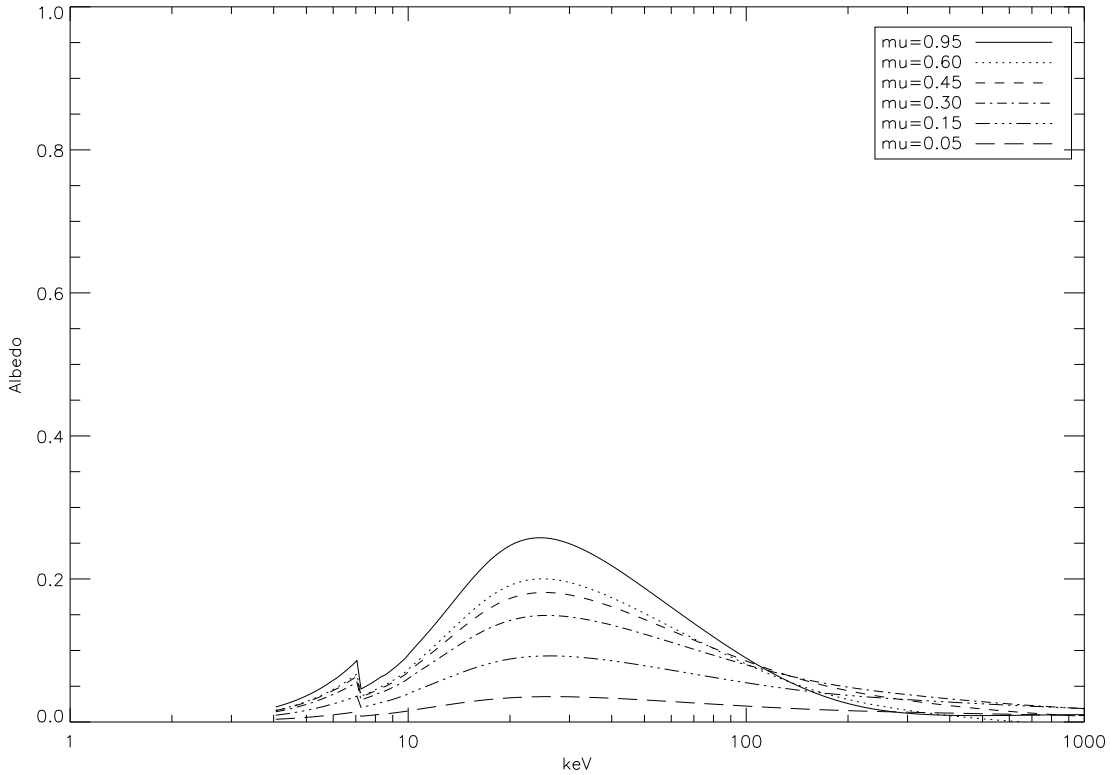

d. Reflection spectrum for $\gamma = 5$ (anisotropic)

Figure 5.10: Anisotropic albedo using a radiative transfer solution at spectral indexes $\gamma = 4, 5$ for various observer angles μ (n=0 - isotropic)

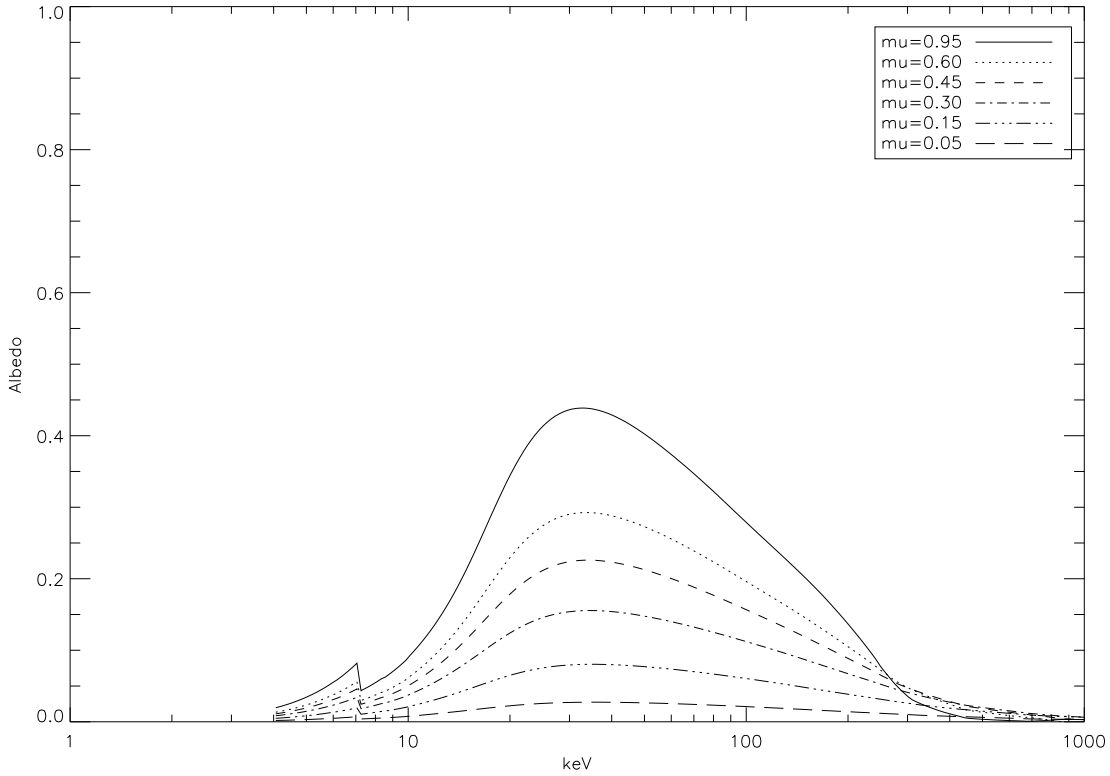

a. Reflection spectrum for $\gamma = 2$ (anisotropic)

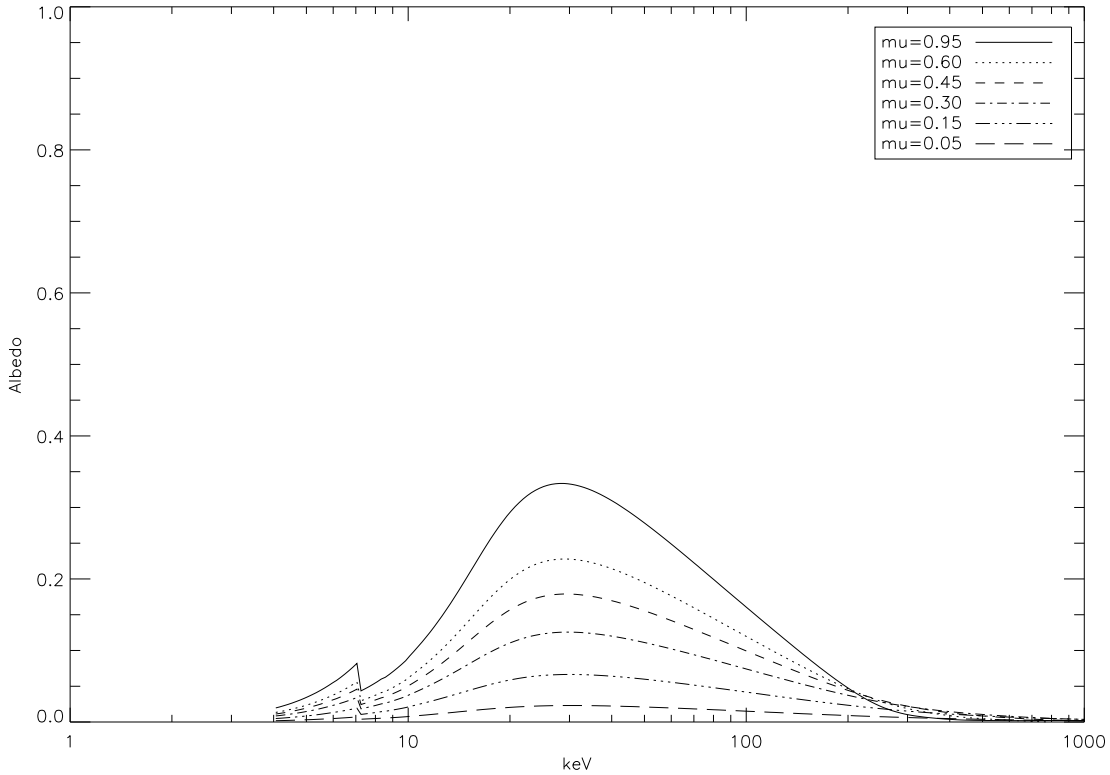

b. Reflection spectrum for $\gamma = 3$ (anisotropic)

Figure 5.11: Anisotropic albedo using a radiative transfer solution at spectral indexes $\gamma = 2, 3$ for various observer angles μ (n=2)

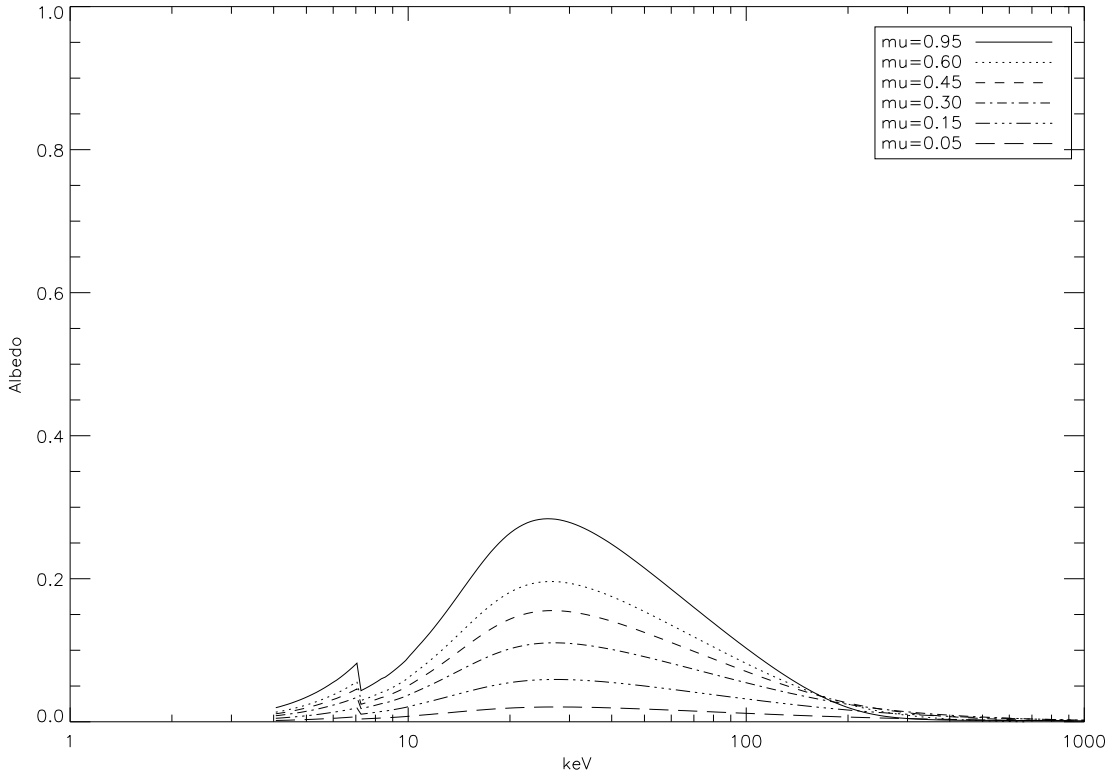

c. Reflection spectrum for $\gamma = 4$ (anisotropic)

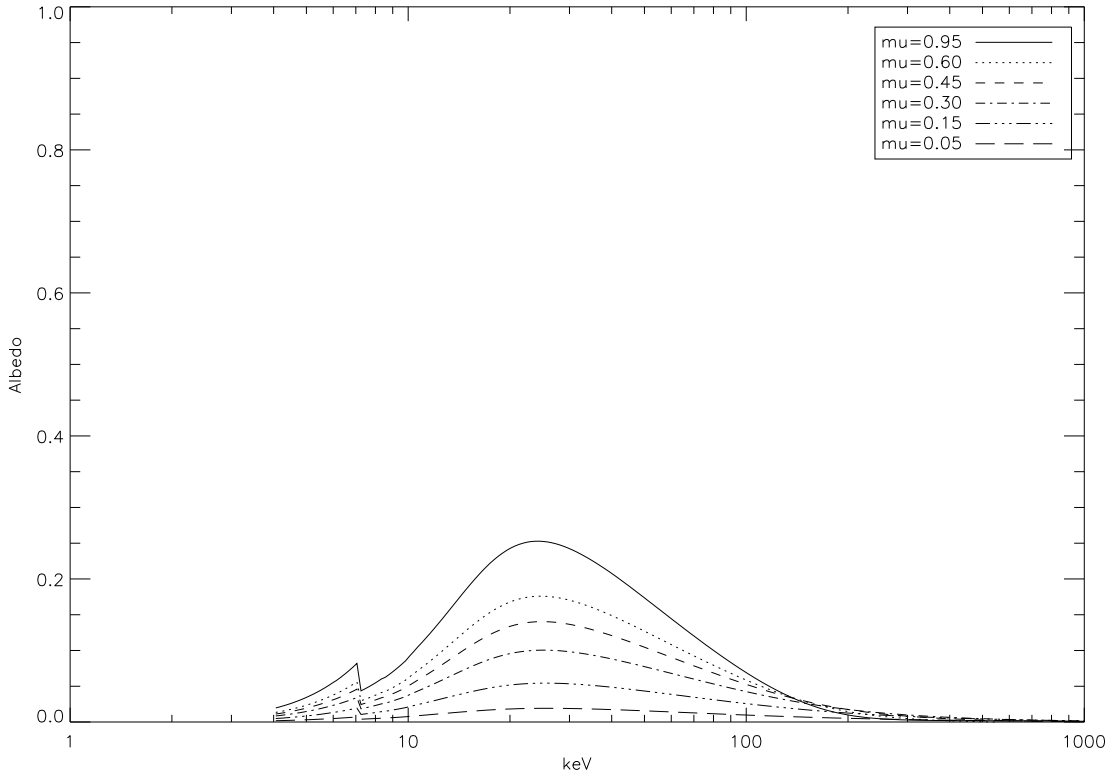

d. Reflection spectrum for $\gamma = 5$ (anisotropic)

Figure 5.12: Anisotropic albedo using a radiative transfer solution at spectral indexes $\gamma = 4, 5$ for various observer angles μ (n=2)

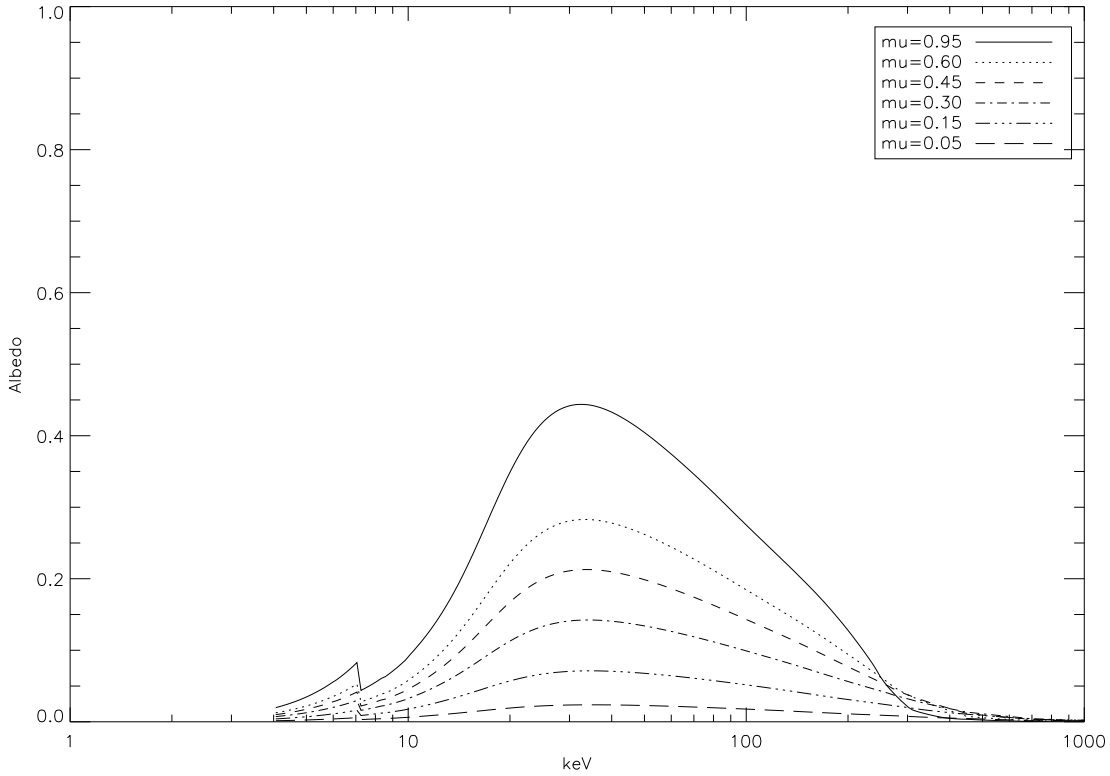

a. Reflection spectrum for $\gamma = 2$ (anisotropic)

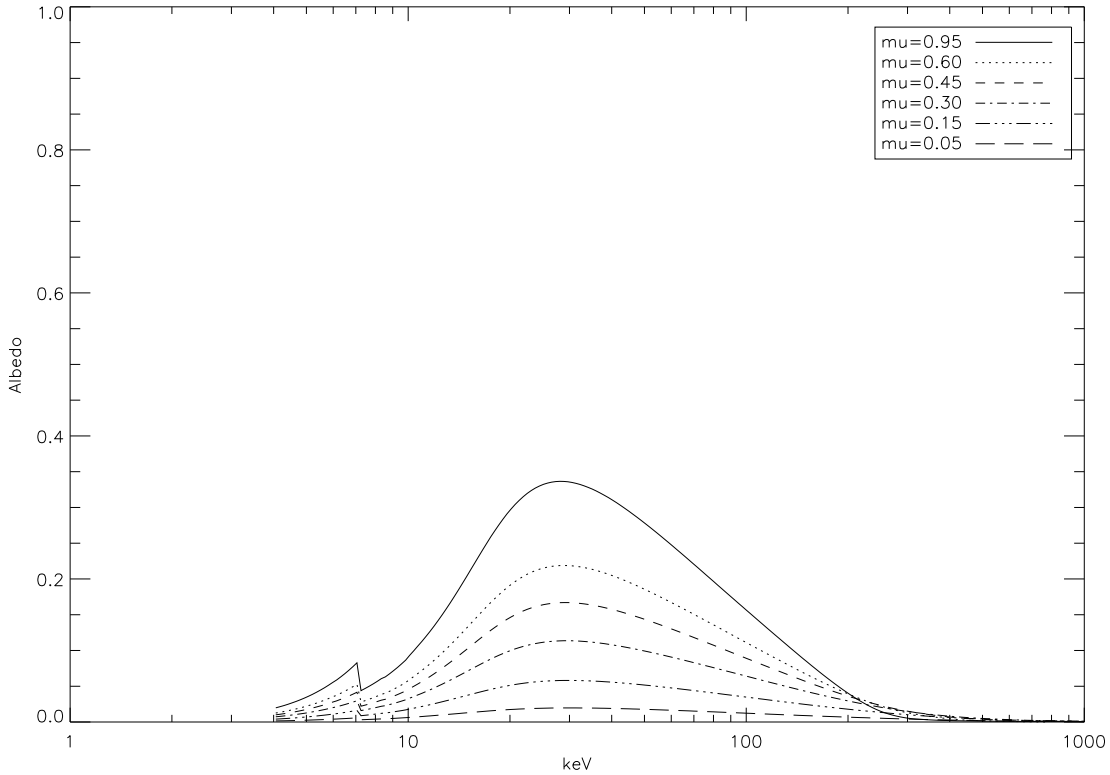

b. Reflection spectrum for $\gamma = 3$ (anisotropic)

Figure 5.13: Anisotropic albedo using a radiative transfer solution at spectral indexes $\gamma = 2, 3$ for various observer angles μ (n=4)

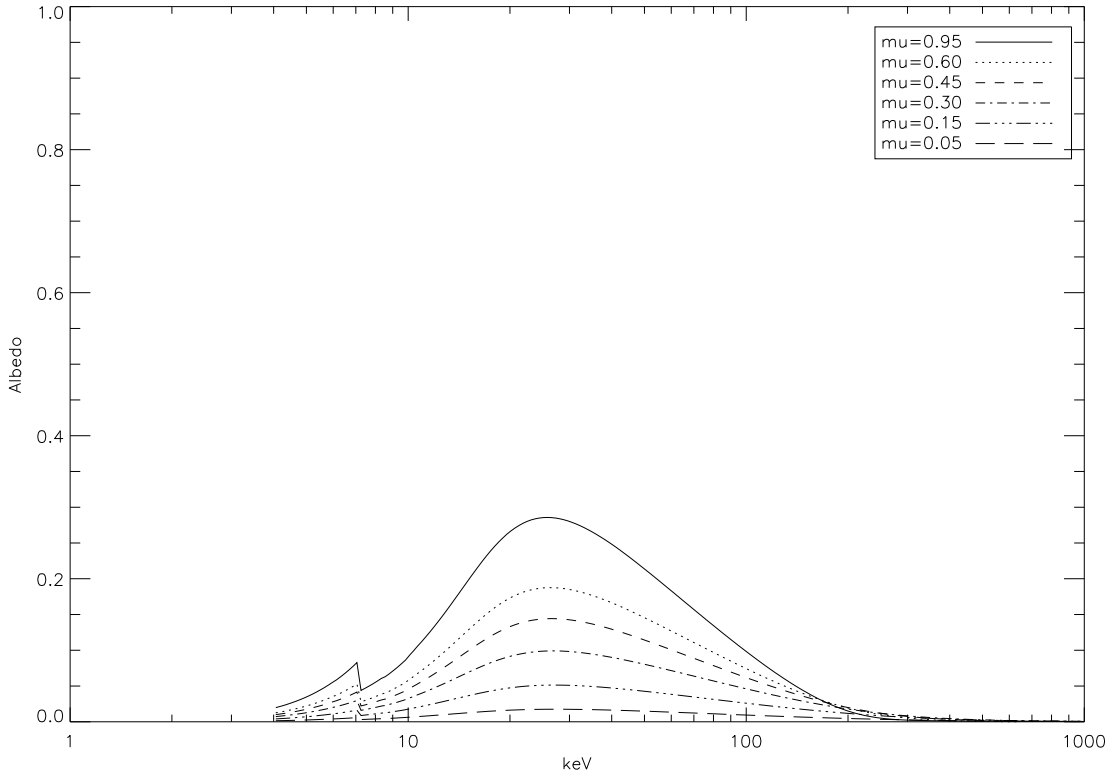

a. Reflection spectrum for $\gamma = 4$ (anisotropic)

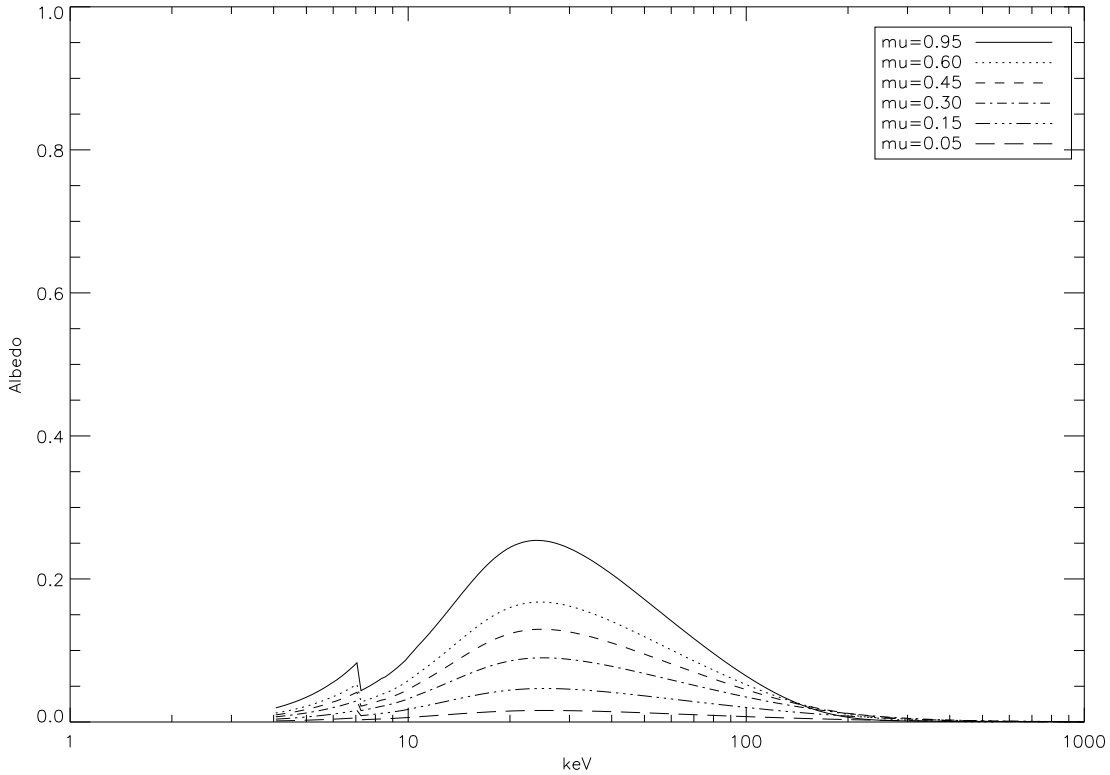

b. Reflection spectrum for $\gamma = 5$ (anisotropic)

Figure 5.14: Anisotropic albedo using a radiative transfer solution at spectral indexes $\gamma = 4, 5$ for various observer angles μ (n=4)

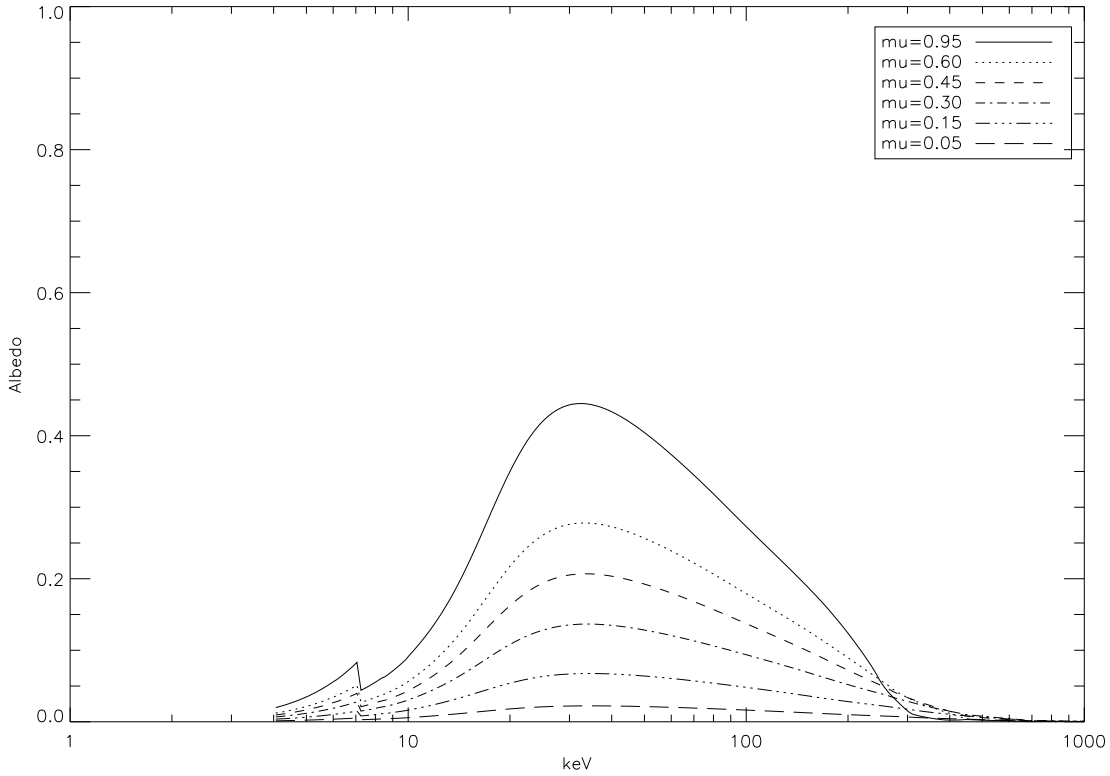

a. Reflection spectrum for $\gamma = 2$ (anisotropic)

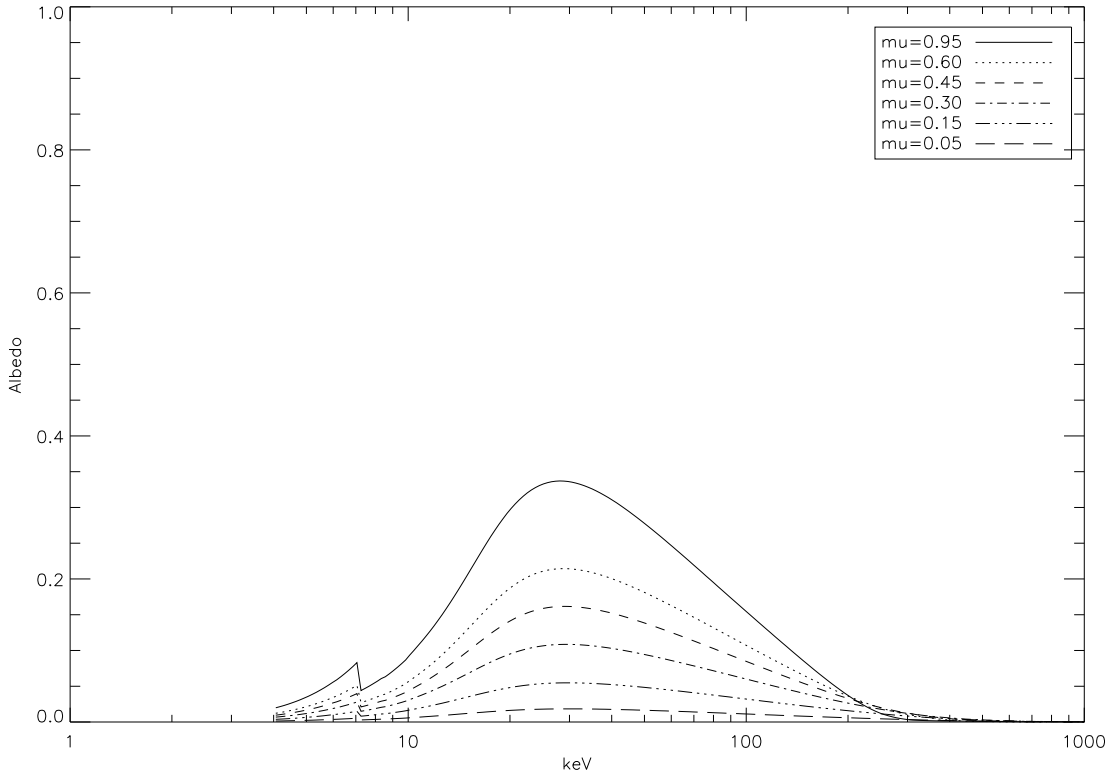

b. Reflection spectrum for $\gamma = 3$ (anisotropic)

Figure 5.15: Anisotropic albedo using a radiative transfer solution at spectral indexes $\gamma = 2, 3$ for various observer angles μ (n=6)

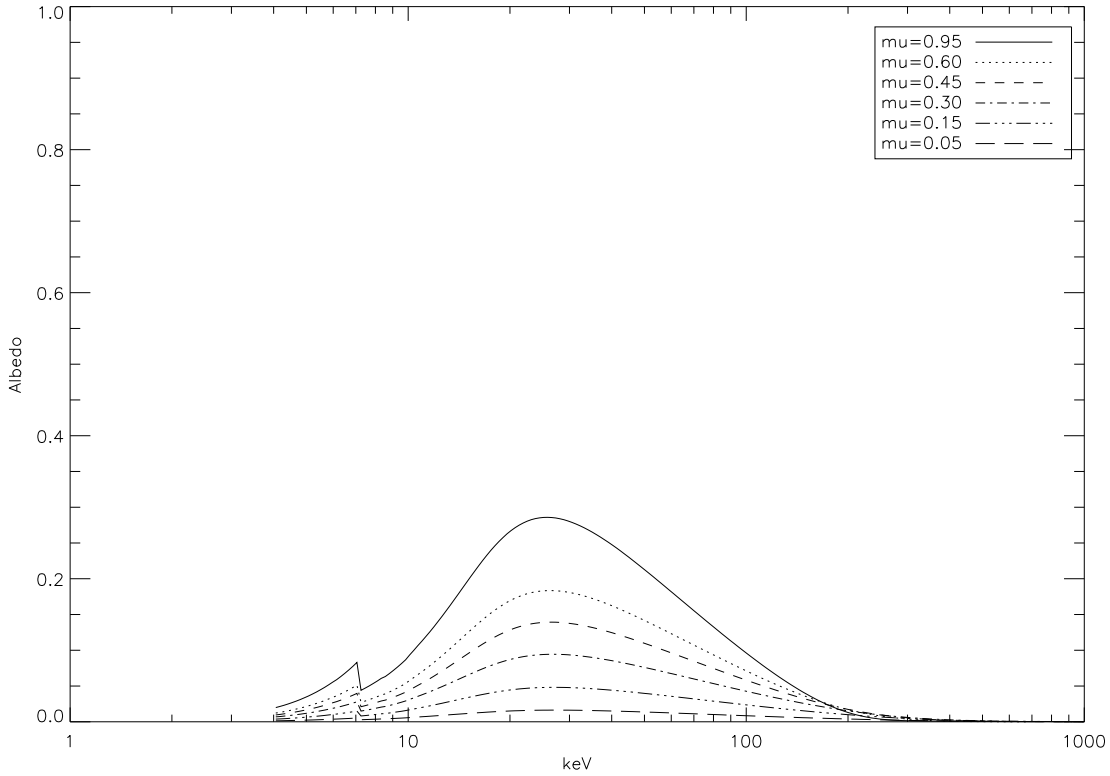

a. Reflection spectrum for $\gamma = 4$ (anisotropic)

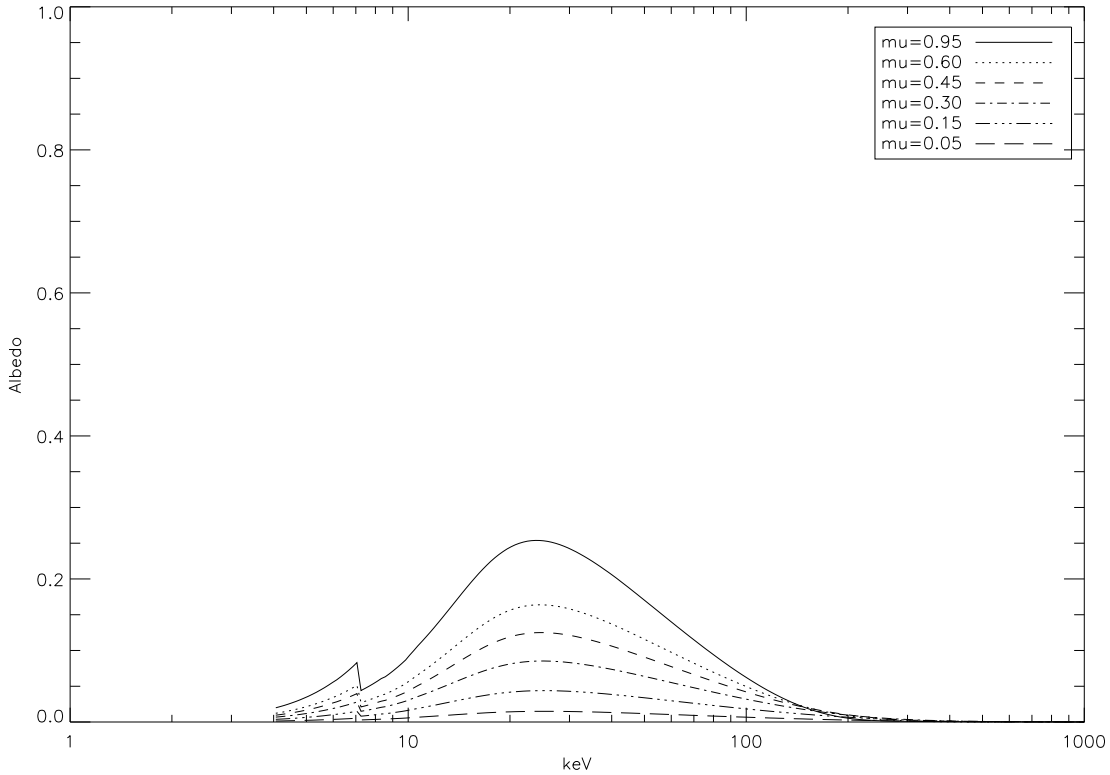

b. Reflection spectrum for $\gamma = 5$ (anisotropic)

Figure 5.16: Anisotropic albedo using a radiative transfer solution at spectral indexes $\gamma = 4, 5$ for various observer angles μ (n=6

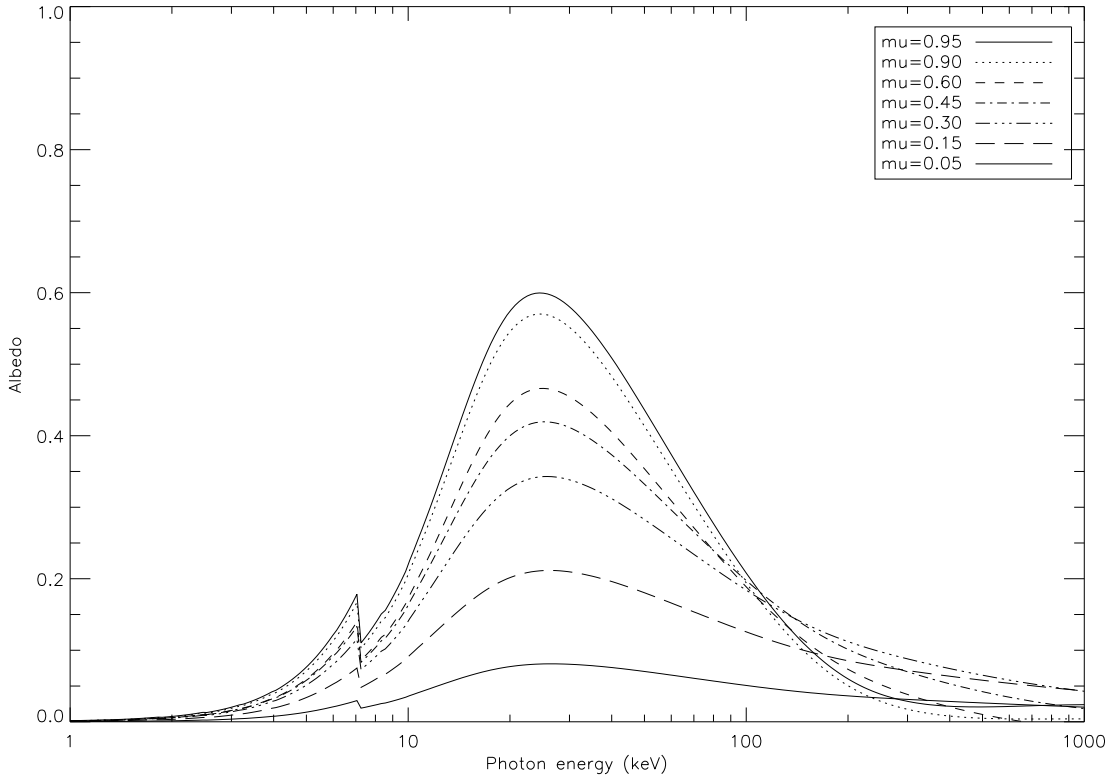

c. Reflection spectrum for $\gamma = 4$ (isotropic)

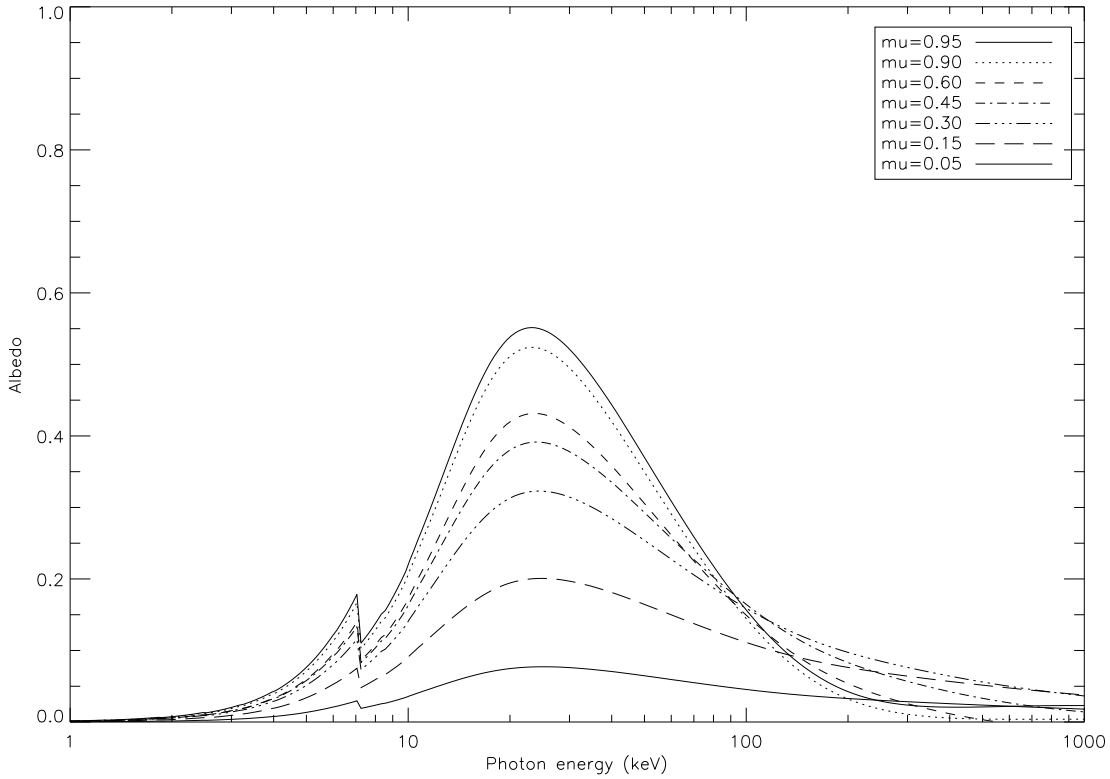

d. Reflection spectrum for $\gamma = 5$ (isotropic)

Figure 5.3: Isotropic albedo using a radiative solution

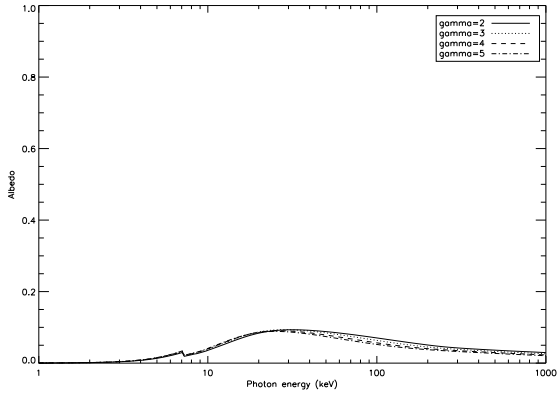

a. $\mu = 0.05$

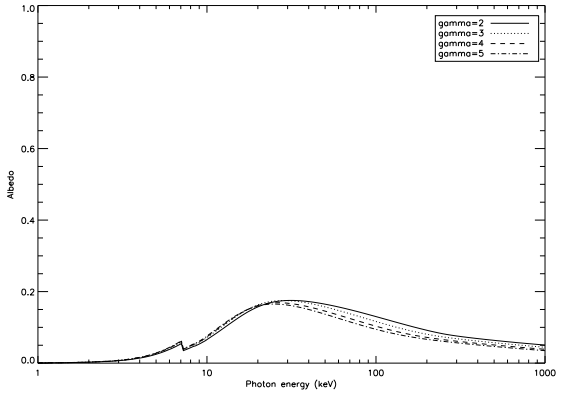

b. $\mu = 0.10$

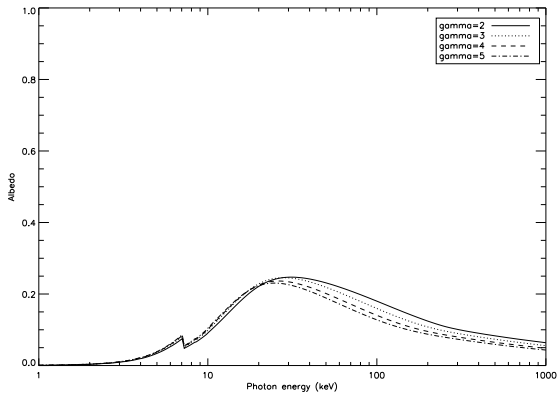

c. $\mu = 0.15$

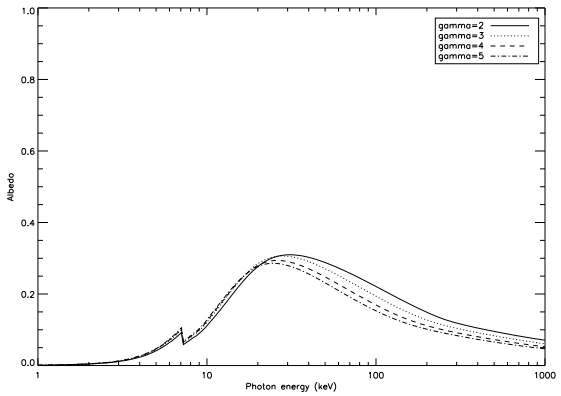

d. $\mu = 0.20$

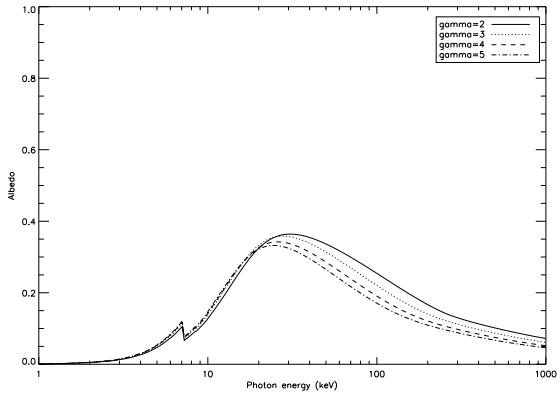

e. $\mu = 0.25$

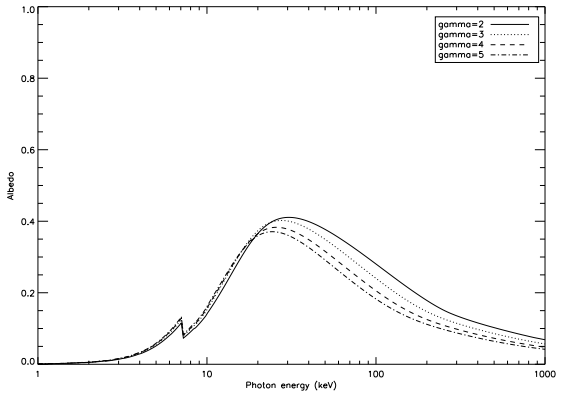

f. $\mu = 0.30$

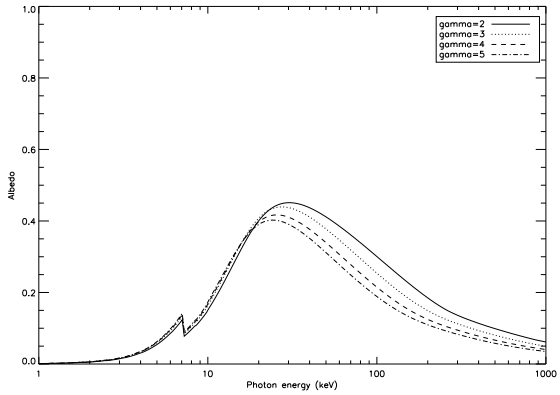

g. $\mu = 0.35$

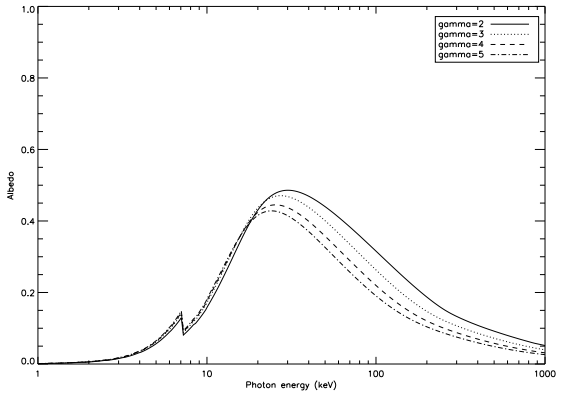

h. $\mu = 0.40$

Figure 5.4: Albedo spectrum for $\gamma = 2 - 5$ for various viewing angles μ

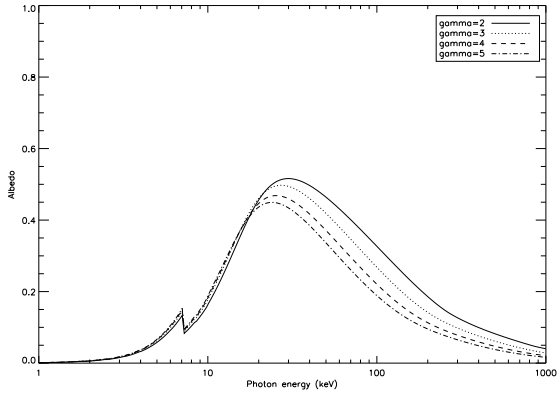

a. $\mu = 0.45$

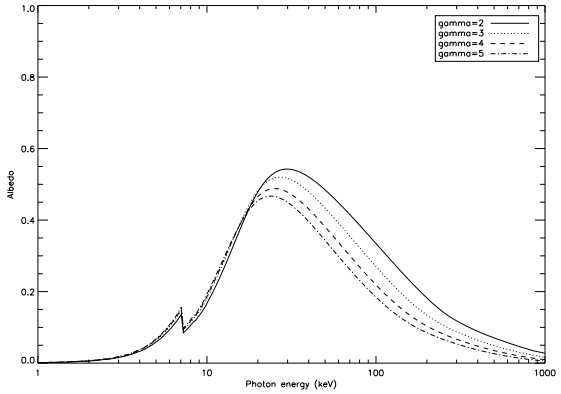

b. $\mu = 0.50$

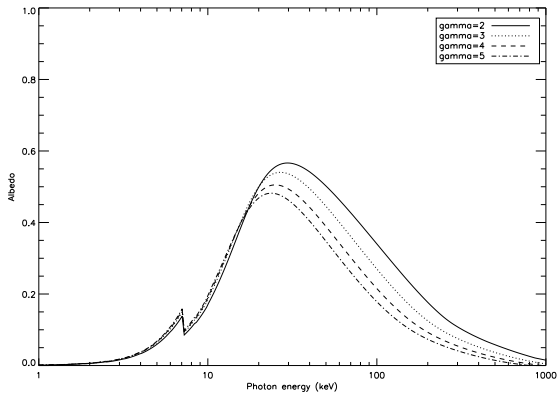

c. $\mu = 0.55$

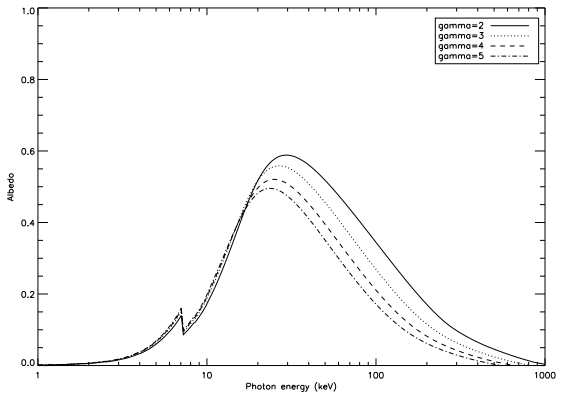

d. $\mu = 0.60$

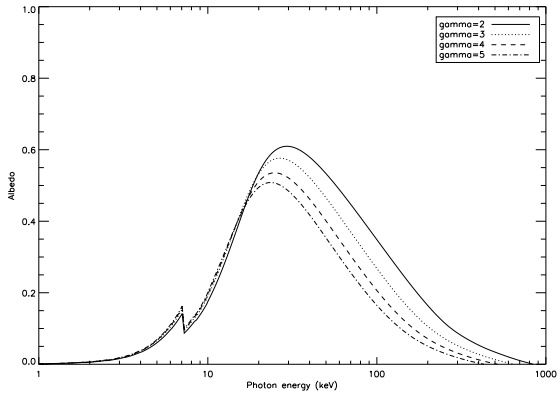

e. $\mu = 0.65$

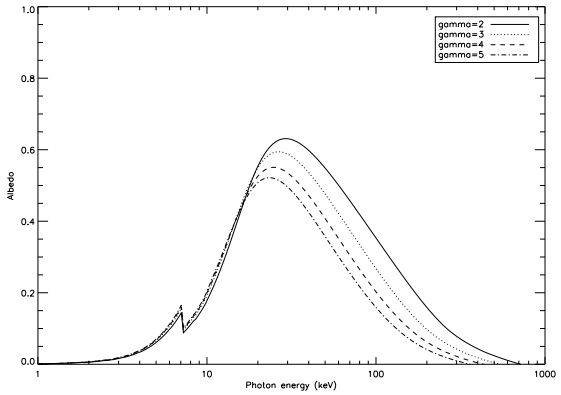

f. $\mu = 0.70$

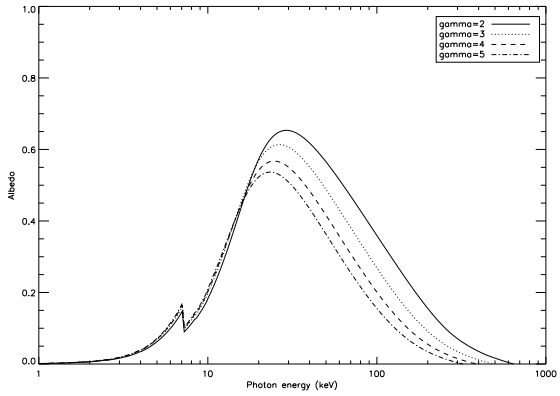

g. $\mu = 0.75$

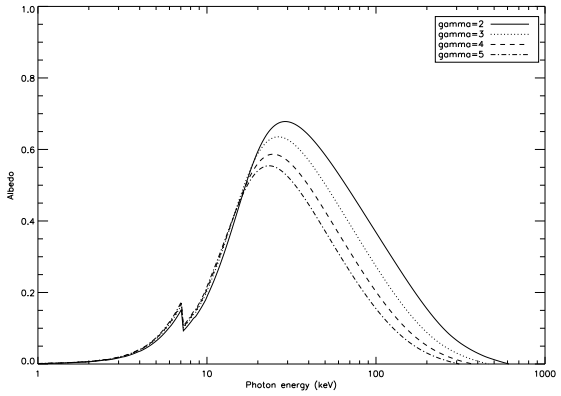

h. $\mu = 0.80$

Figure 5.5: Albedo spectrum for $\gamma = 2 - 5$ for various viewing angles μ

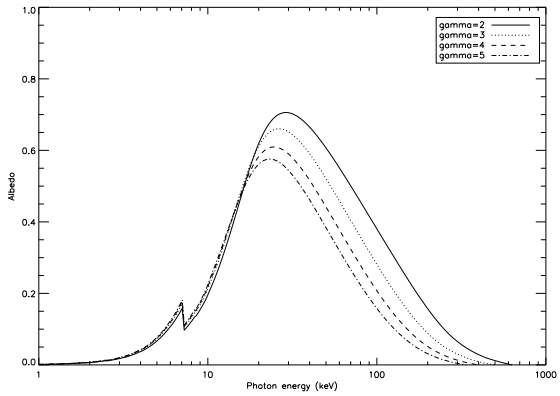

a. $\mu = 0.85$

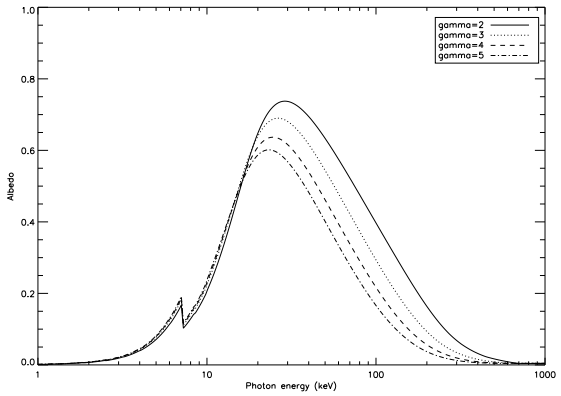

b. $\mu = 0.90$

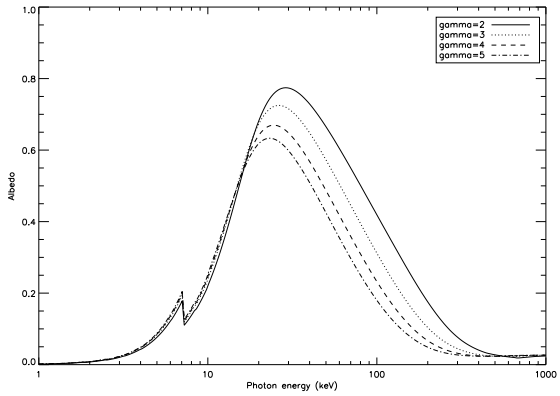

c. $\mu = 0.95$

Figure 5.6: Albedo spectrum for $\gamma = 2 - 5$ for various viewing angles μ

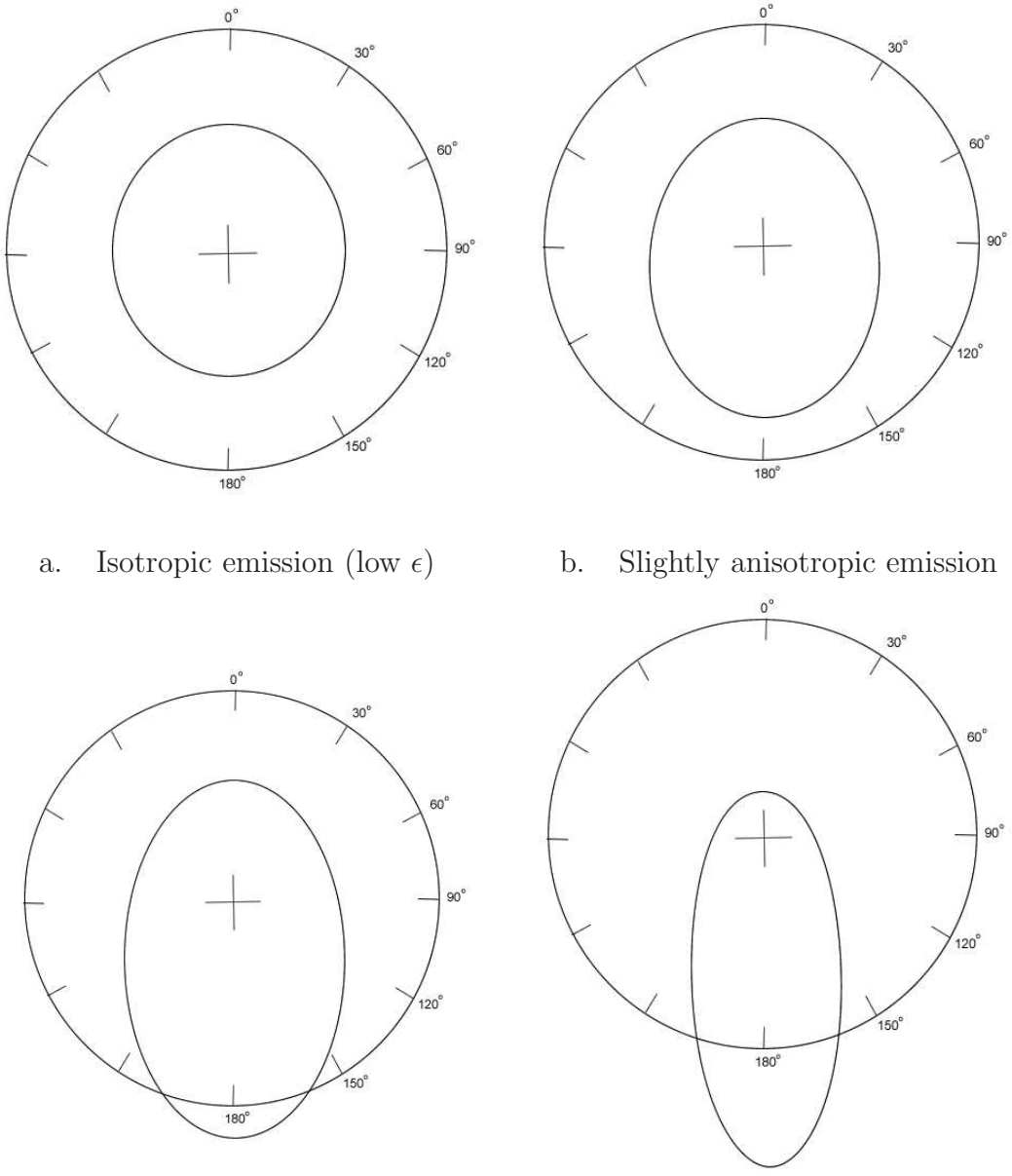

a. Isotropic emission (low ϵ)

b. Slightly anisotropic emission

c. anisotropic emission

d. Highly anisotropic emission (high ϵ)

Figure 5.8: Fully angular anisotropic primary emission

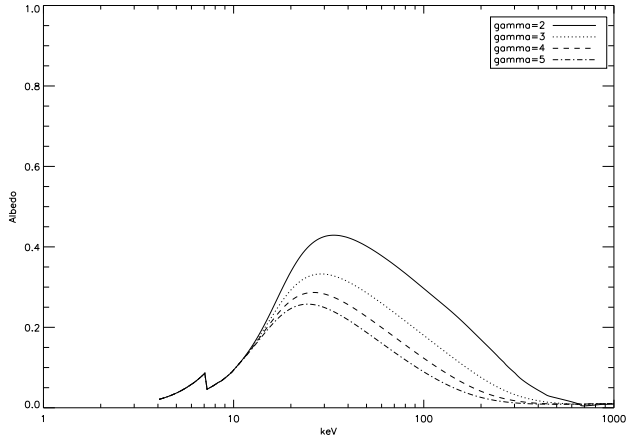

a. $\mu = 0.95$

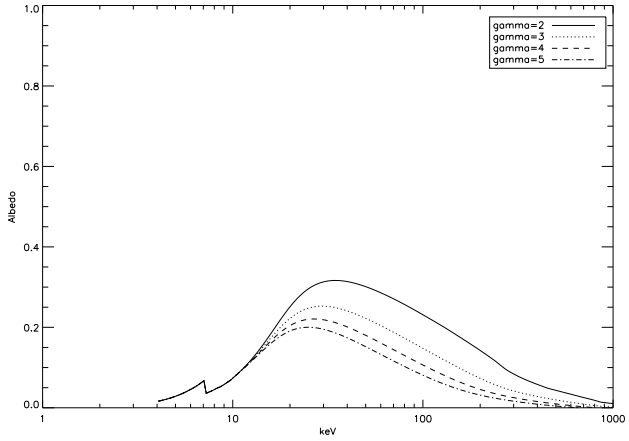

b. $\mu = 0.60$

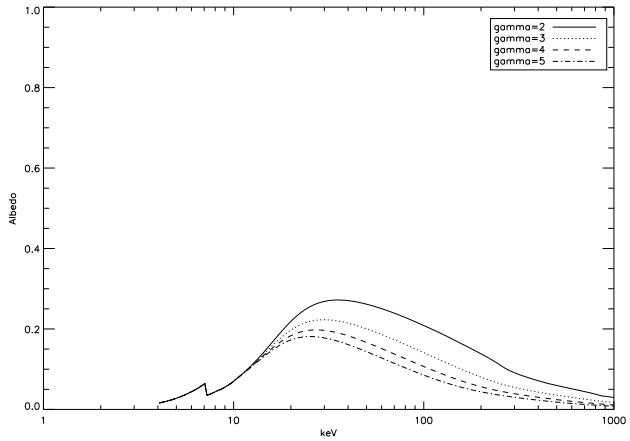

c. $\mu = 0.45$

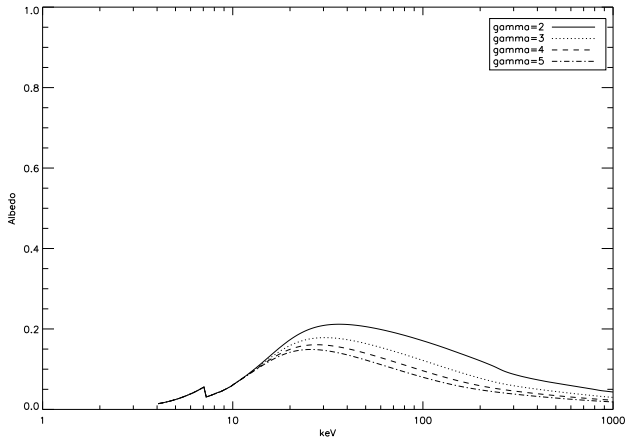

d. $\mu = 0.30$

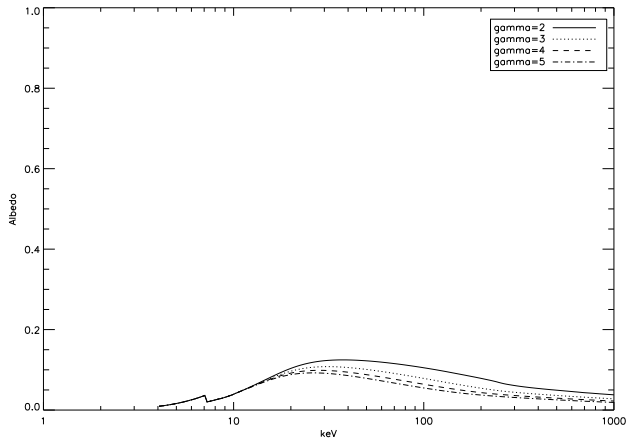

e. $\mu = 0.15$

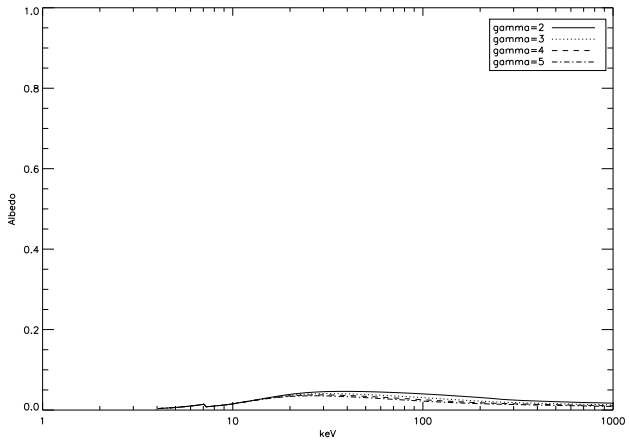

f. $\mu = 0.05$

Figure 5.17: Anisotropic albedo using a radiative transfer solution at various observer angles μ for spectral indexes $\gamma = 2 - 5$ (n=0).

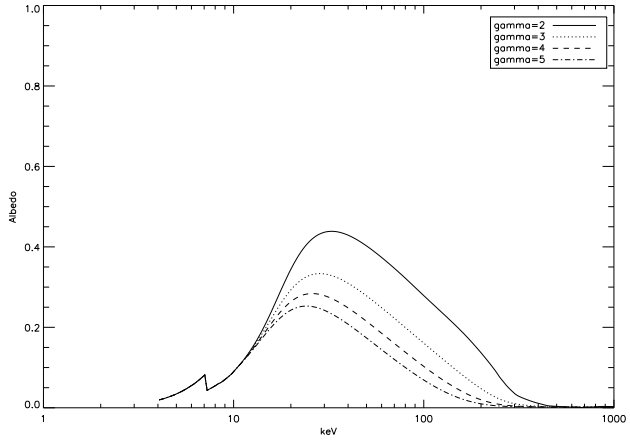

a. $\mu = 0.95$

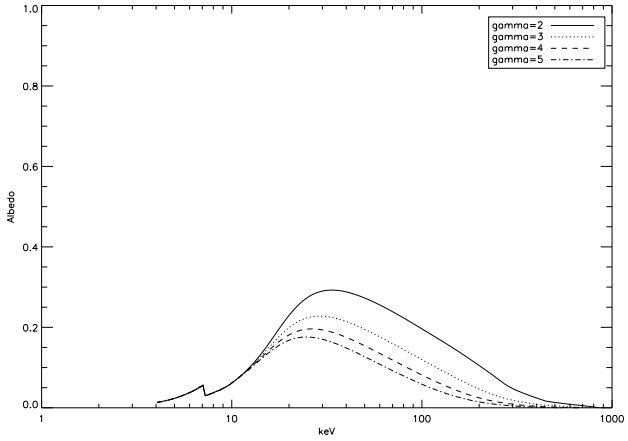

b. $\mu = 0.60$

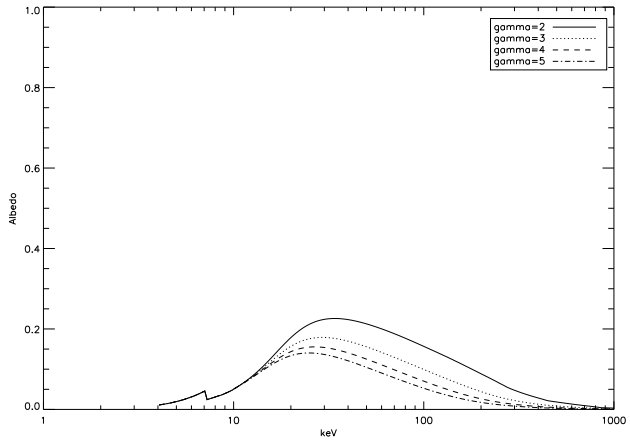

c. $\mu = 0.45$

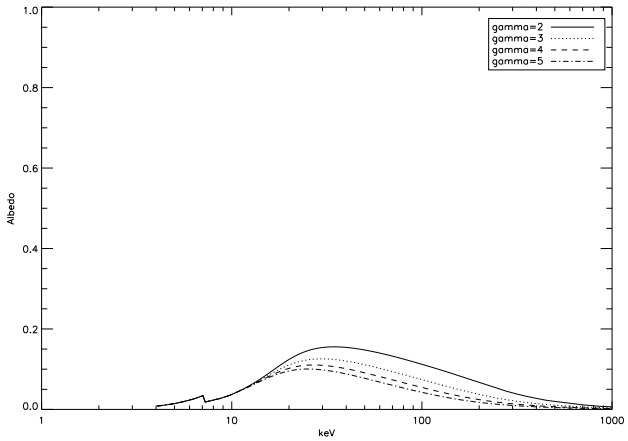

d. $\mu = 0.30$

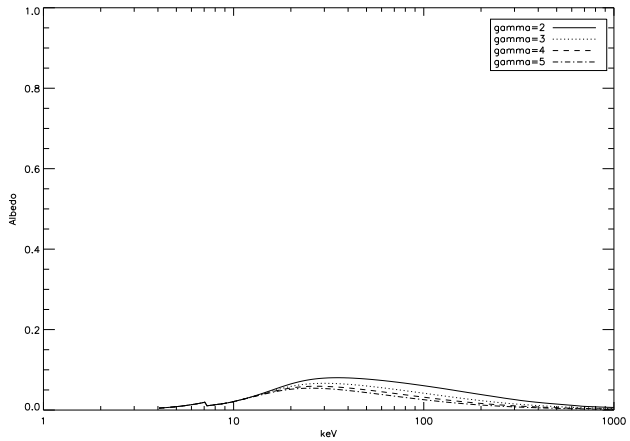

e. $\mu = 0.15$

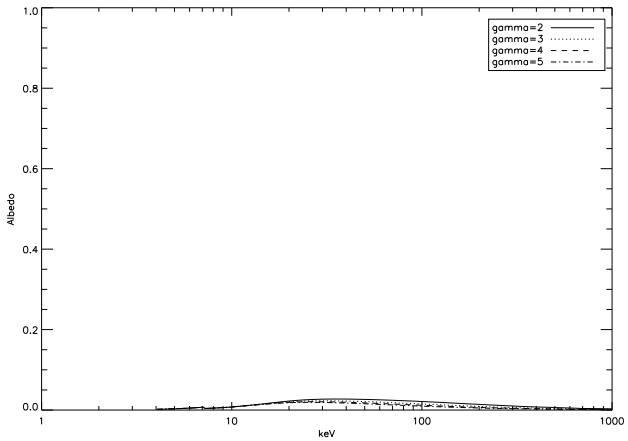

f. $\mu = 0.05$

Figure 5.18: Anisotropic albedo using a radiative transfer solution at various observer angles μ for spectral indexes $\gamma = 2 - 5$ (n=2).

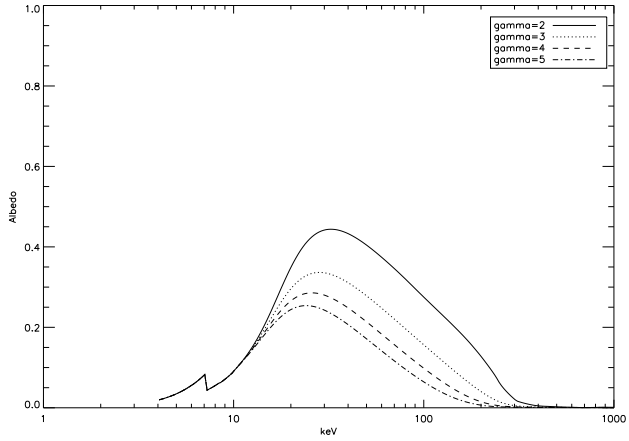

a. $\mu = 0.95$

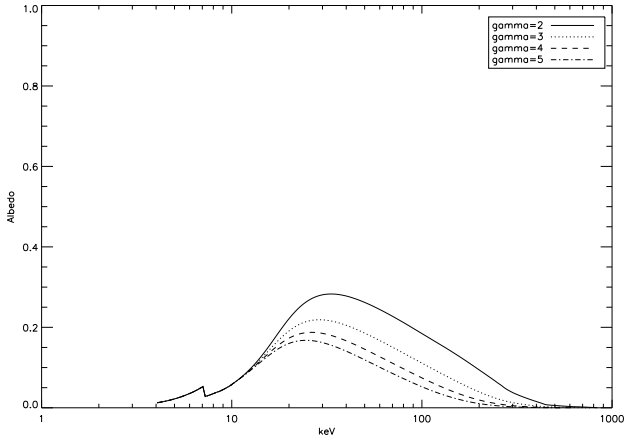

b. $\mu = 0.60$

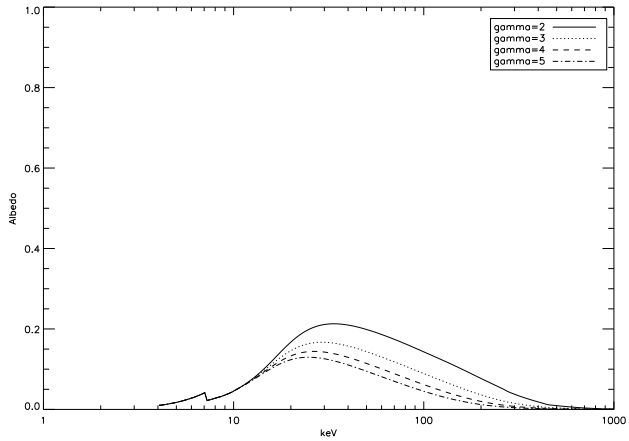

c. $\mu = 0.45$

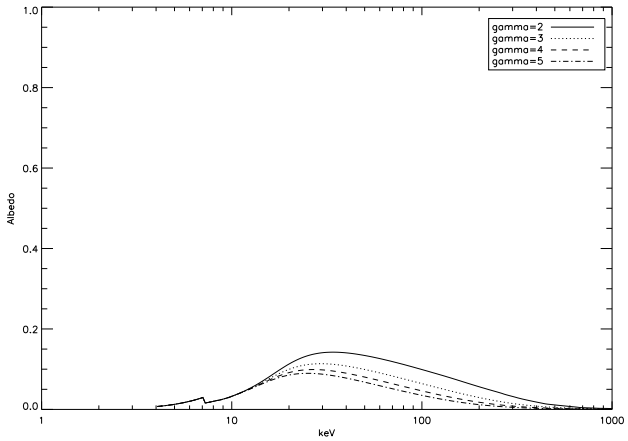

d. $\mu = 0.30$

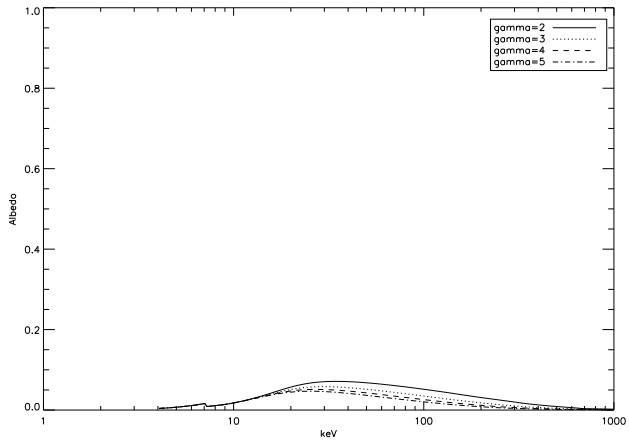

e. $\mu = 0.15$

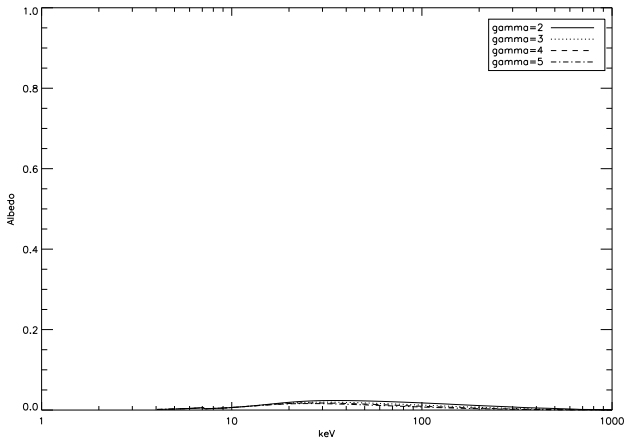

f. $\mu = 0.05$

Figure 5.19: Anisotropic albedo using a radiative transfer solution at various observer angles μ for spectral indexes $\gamma = 2 - 5$ (n=4).

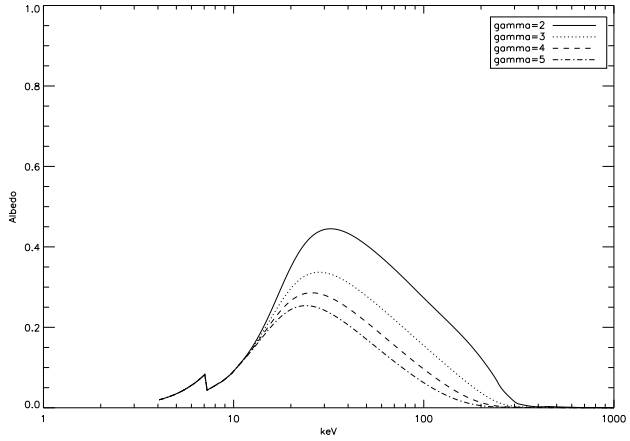

a. $\mu = 0.95$

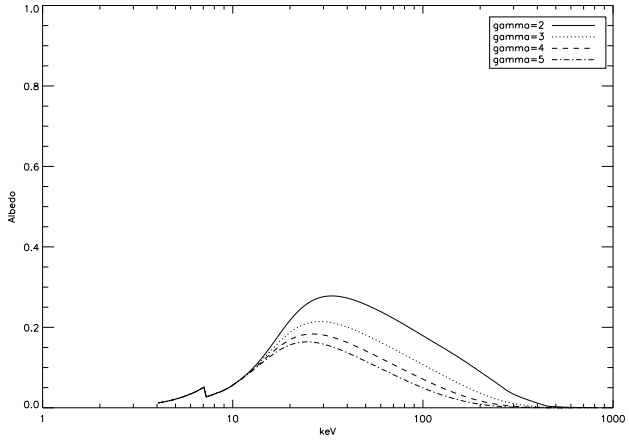

b. $\mu = 0.60$

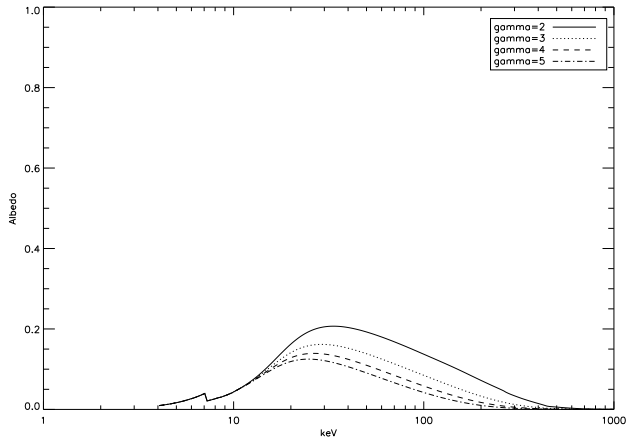

c. $\mu = 0.45$

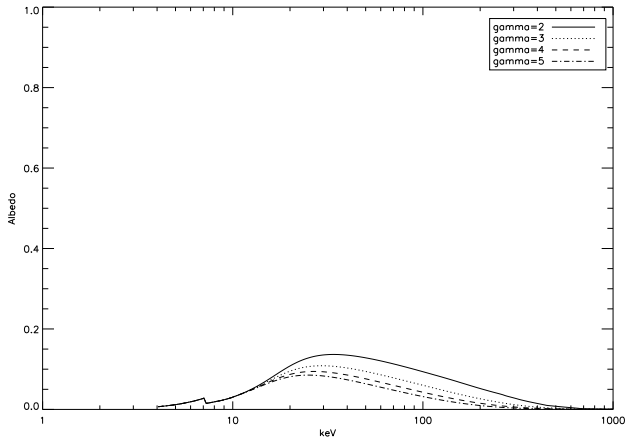

d. $\mu = 0.30$

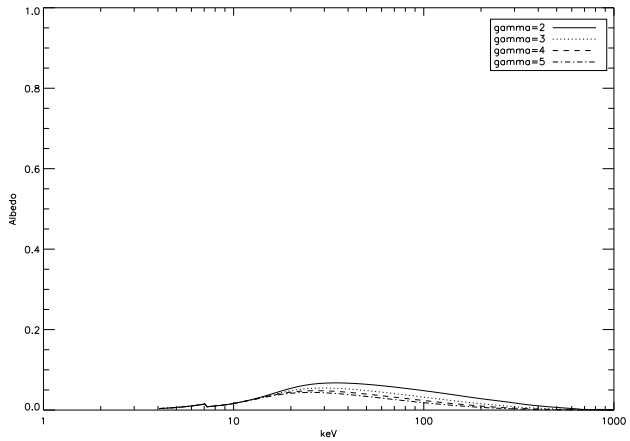

e. $\mu = 0.15$

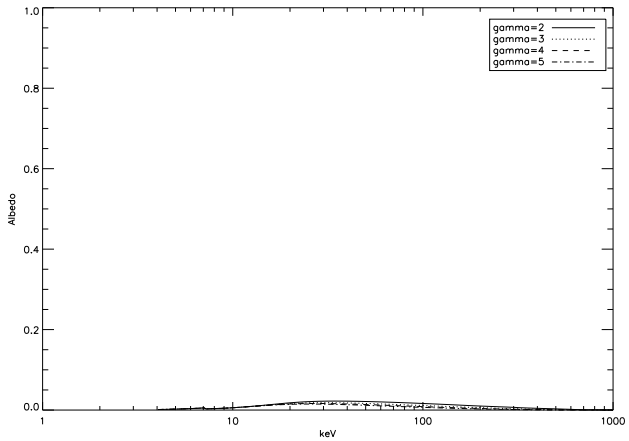

f. $\mu = 0.05$

Figure 5.20: Anisotropic albedo using a radiative transfer solution at various observer angles μ for spectral indexes $\gamma = 2 - 5$ (n=6).

Figures (5.9) - (5.16) and (5.17) - (5.20) show the plots of the albedo spectrum for various degrees of anisotropy (n) and for a chosen functional form of photon emission.

These figures are similar to the isotropic reflection spectra (section 5.3.1) but the influence of the anisotropy can be seen as a flattening of the slope of the reflection spectra $R(\epsilon)$ in the $50keV - 200keV$ energy range.

5.5 Empirical Fit to Leach & Petrosian Data

In this section we describe an empirical fit to data published on the primary HXR anisotropic spectra emitted by an electron beam within Leach & Petrosian (1983). Although we applied an analogous technique for the Eddington approximation in Section 4.7, the fully angular Green's solution requires a slightly modified approach.
We do this as a 2 stage process:

1. A 3 parameter empirical fit to the angular data given in figure 4 in reference Leach and Petrosian at the two data points (22keV and 210 keV respectively). This is achieved using a least squares fit on the angular data given in table 5.1 below.

2. A linear interpolation of these angular parameters between the data points in energy to give an energy dependent angular anisotropic fit.

5.5.1 The Anisotropic Emission Model

We introduce a 3 parameter fit or model here as

$$I(\theta)_\epsilon = (a_\epsilon + b_\epsilon cos(\theta))^{\zeta_\epsilon} \tag{5.3}$$

at photon energies ϵ where

1. a - the value of the emission at $\theta = 0$

2. b and ζ fit the anisotropy of the emission

θ	$22(keV)$	$210(keV)$
0	0.50	0.095
30	0.55	0.12
60	0.60	0.30
90	0.80	0.55
120	1.10	1.15
150	1.15	1.50
180	1.20	1.60

Table 5.1: Data points digitised from Leach & Petrosian (1983, Figure 4)

5.5.2 The Least Squares Fit

We can use a least squares fit to obtain values for a, b and ζ for the given model in equation 5.3. The fitting algorithm is implemented as an IDL routine (Appendix D) using the curve fitting and optimisation routine *CURVEFIT* (IDL Online Help (March 06(2007)) and this routine supplied a value for the χ^2 fit for the given least squares fit.
Here we present an algorithm which can be summarised by the following:

1. choose an initial minimum and maximum value, along with the size of the step increment for parameters

2. scan the parameter space for these parameters from a minimum to the maximum

3. evaluate equation 5.3 at each of the values and test the model against the data points from figure 4, Leach and Petrosian using a least squares fit

4. at the end of the scan of all of the parameter spaces we will obtain a value for a, b and ζ at which the χ^2 test is a global minimum[10].

The above algorithm is repeated at both energies ($22keV$ and $210keV$) which gives the energy independent form of the fit.

Using the data plot extraction application, Dexter (Demleitner et al. (2001)), the data points for $I(\theta)$ were extracted from figure 4 (Leach and Petrosian figure 4). These are given in Table 5.1 below.

Using these 2 data points in Table 5.1 as a reference point for the scan of the parameter space in the the least square fit routine (Appendix D) the following fit

[10]As any minimum value obtained may be a local minimum all of the parameter space must be scanned to ensure that we have a global maximum

ϵ/keV	a	b	ζ
22	0.9	-0.2	1.95
210	0.8	-0.5	1.95

Table 5.2: Least squares fit parameters

was obtained for the fit parameters a_ϵ, b_ϵ and ζ_ϵ at 22keV and 210 keV respectively, for the given model in equation (5.3).

The resulting best fit parameters are given below in table 5.2

5.5.3 Extending the Empirical Fit to be Energy Dependent

In order to extend our anisotropic emission model to be energy dependent we apply a linear interpolation between the empirically fitted parameters from the least squares fit[11].

Thus we express the three parameters above, in the form of a straight line $y = mx + c$, in an energy dependent form as

$$a(\epsilon) = -\frac{0.1}{188}\epsilon + 0.912 \tag{5.4}$$

$$b(\epsilon) = -\frac{0.3}{188}\epsilon - 0.165 \tag{5.5}$$

$$\zeta(\epsilon) = 1.95 \tag{5.6}$$

It is noted that ζ is constant however for consistency with the other fitted parameters we will continure to refer to $\zeta(\epsilon)$. Thus we can re-express equation 5.3 in an energy dependent, empirical fitted, anisotropic form as

$$I(\epsilon, \theta) = A_o \epsilon^{-\gamma} \times (a(\epsilon) + b(\epsilon) cos(\theta))^{\zeta(\epsilon)} \tag{5.7}$$

Equation (5.7) can therefore be implemented within a new version of the external routine and used within the Poutanen 'black box' algorithm.

[11] A linear fit for energy dependence between the two data points (22keV and 210 keV) given by Leach & Petrosian (1983) could be viewed as simplistic however this approach allows the model to be updated upon the publication of more comprehensive data.

5.5.4 Results - Empirically Fitted Angular Dependent Anisotropic Green's Function (Radiative Transfer) Solution

We can use the energy dependent anisotropic emission model defined in equation (5.7) within the algorithm of Poutanen et al. (1996).

The following figures 5.21(a)–(b) and 5.22 (a)–(b) give the intrinsic reflection spectrum $R(\epsilon)$ for $\gamma = 2 - 5$ for various values of μ.

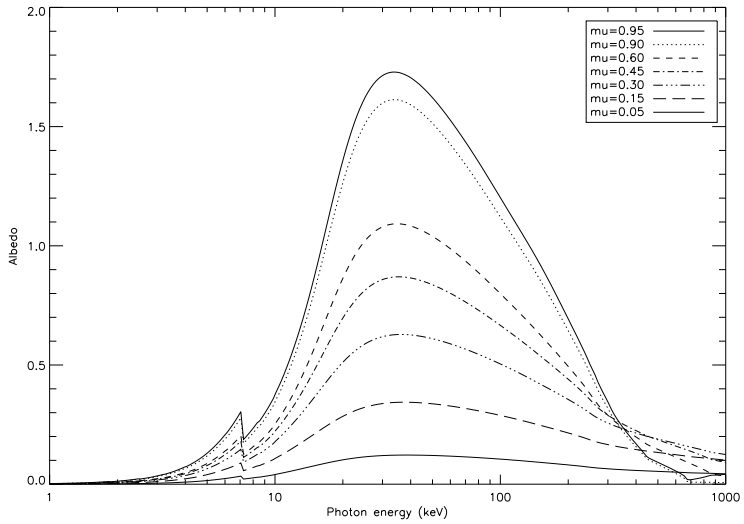

a. Reflection spectrum for $\gamma = 2$ (isotropic)

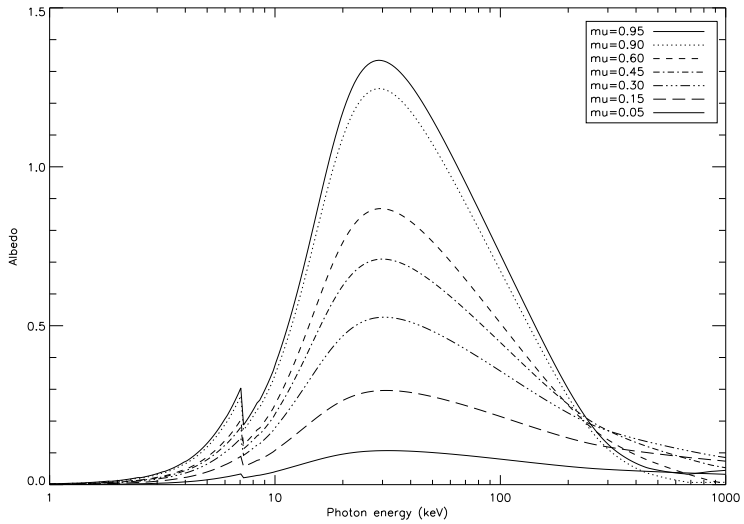

b. Reflection spectrum for $\gamma = 3$ (isotropic)

Figure 5.21: Radiative transfer solution: anisotropic albedo for an empirical fit to Leach and Petrosian data

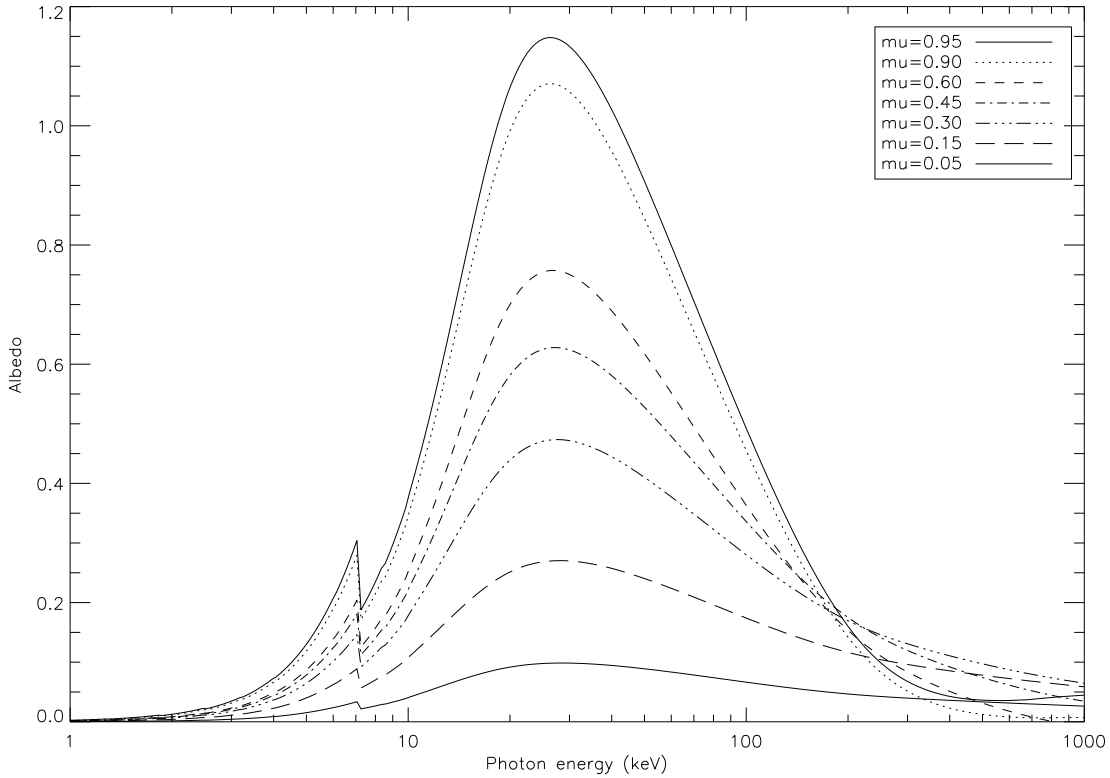

c. Reflection spectrum for $\gamma = 4$ (isotropic)

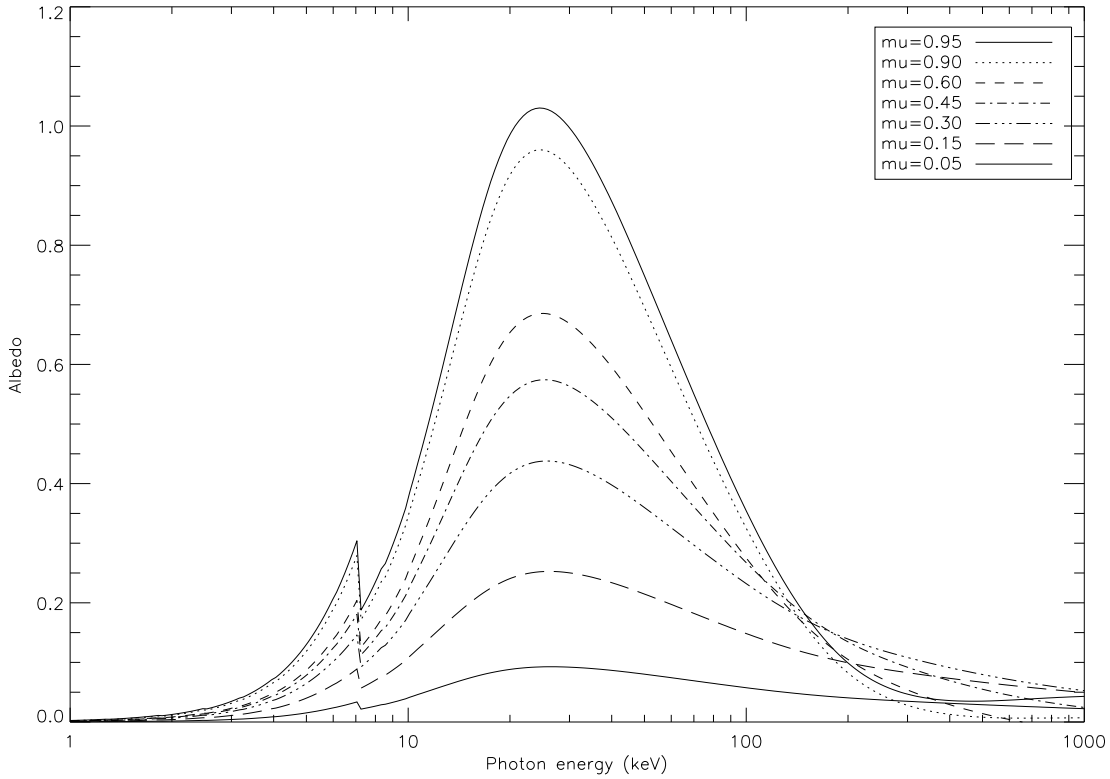

d. Reflection spectrum for $\gamma = 5$ (isotropic)

Figure 5.22: Radiative transfer solution: anisotropic albedo for an empirical fit to Leach and Petrosian data

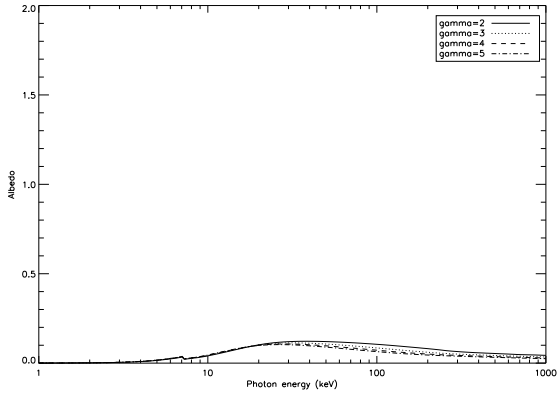

a. $\mu = 0.05$

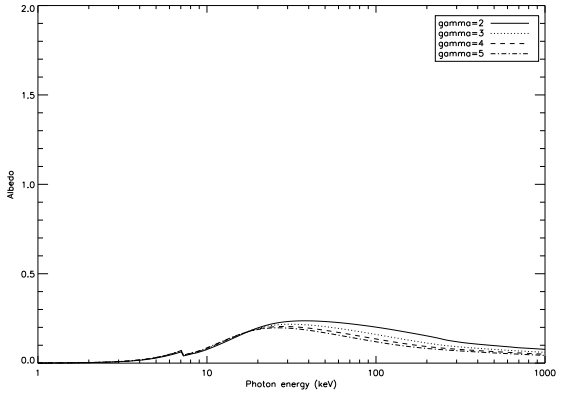

b. $\mu = 0.10$

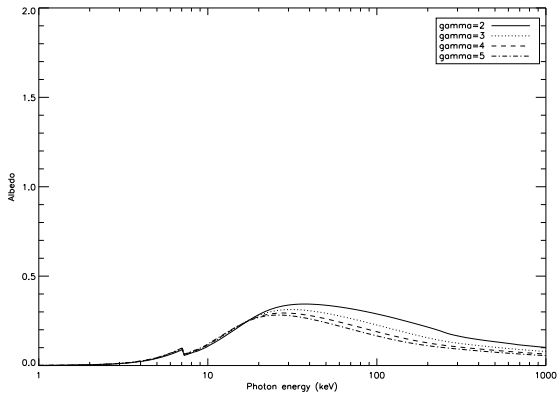

c. $\mu = 0.15$

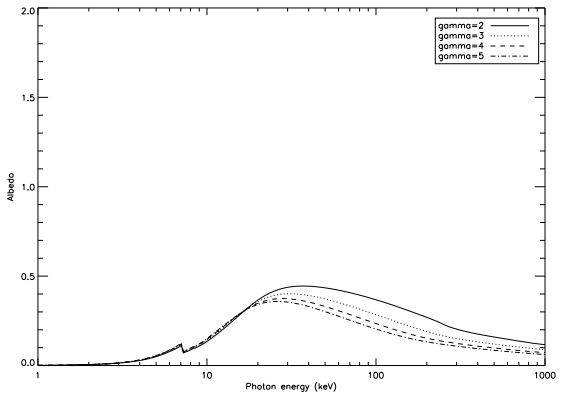

d. $\mu = 0.20$

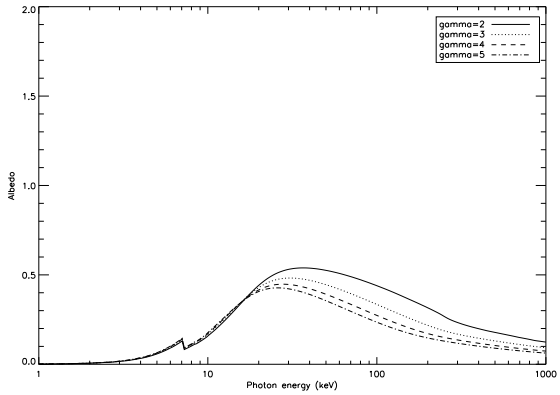

e. $\mu = 0.25$

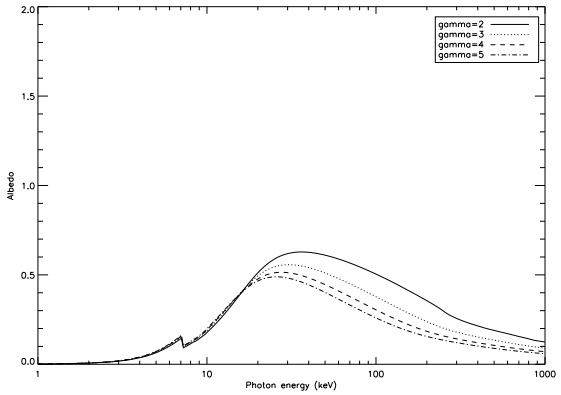

f. $\mu = 0.30$

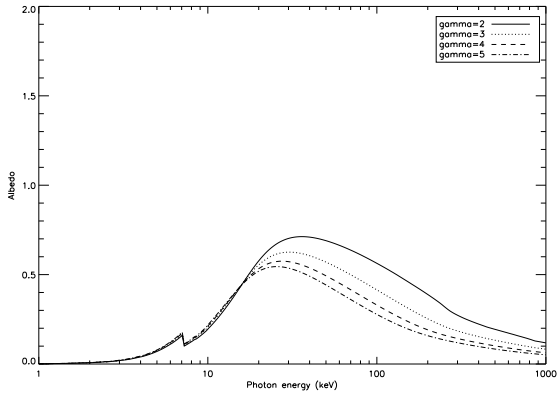

g. $\mu = 0.35$

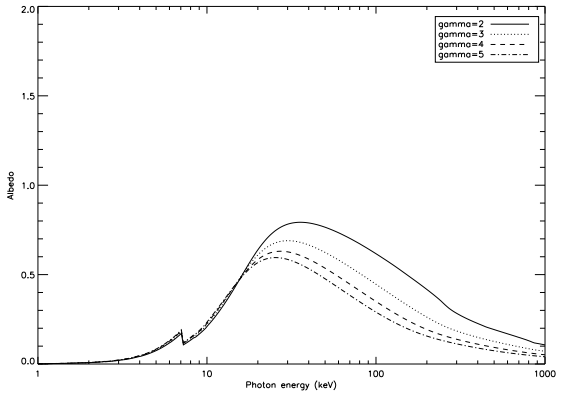

h. $\mu = 0.40$

Figure 5.23: Plots of albedo spectrum for $\gamma = 2 - 5$ for various viewing angles μ

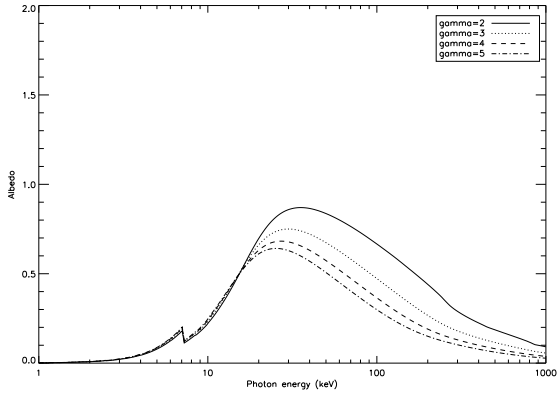

a. $\mu = 0.45$

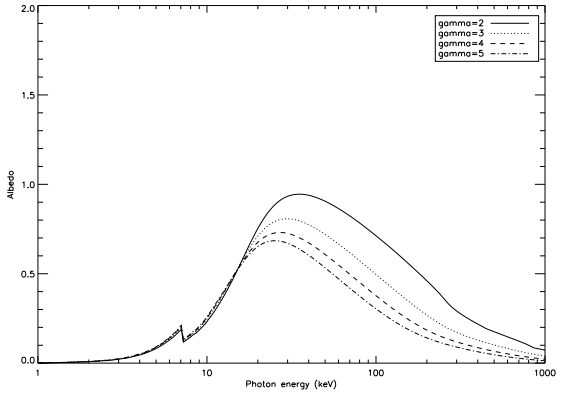

b. $\mu = 0.50$

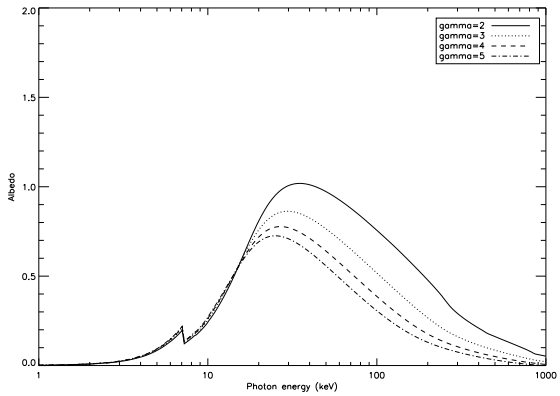

c. $\mu = 0.55$

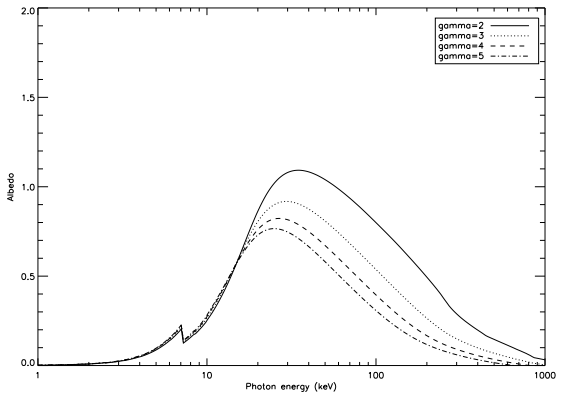

d. $\mu = 0.60$

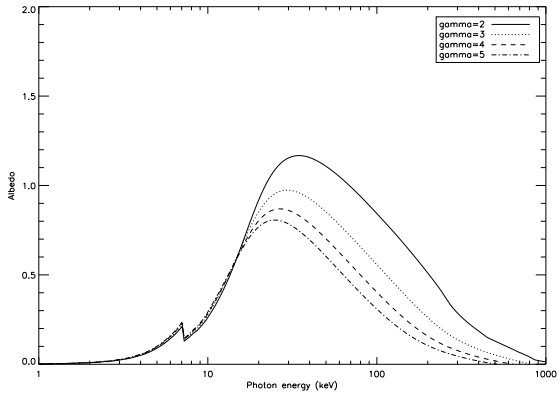

e. $\mu = 0.65$

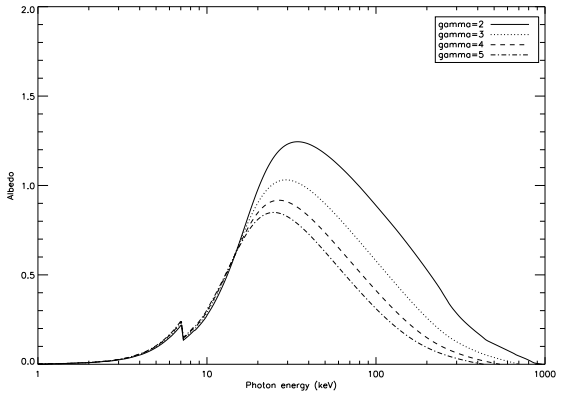

f. $\mu = 0.70$

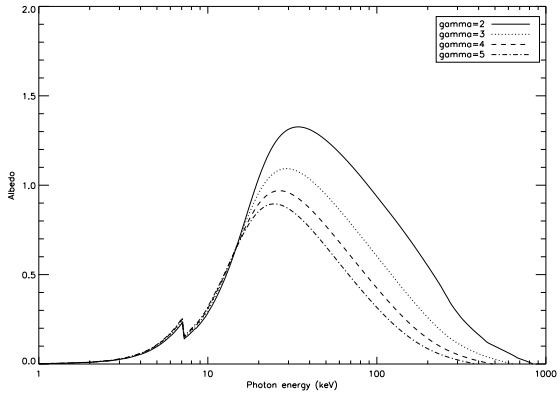

g. $\mu = 0.75$

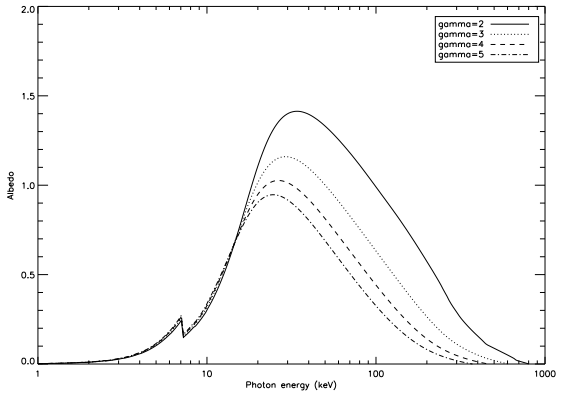

h. $\mu = 0.80$

Figure 5.24: Plots of albedo spectrum for $\gamma = 2 - 5$ for various viewing angles μ

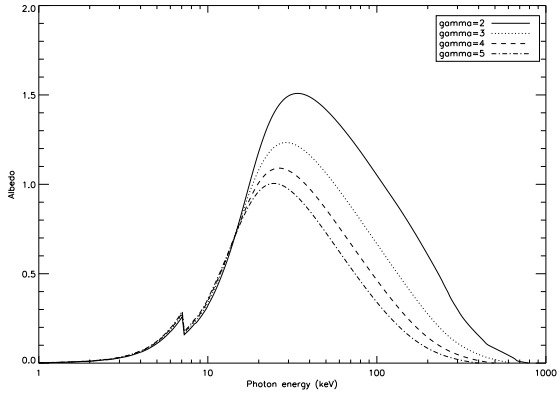

a. $\mu = 0.85$

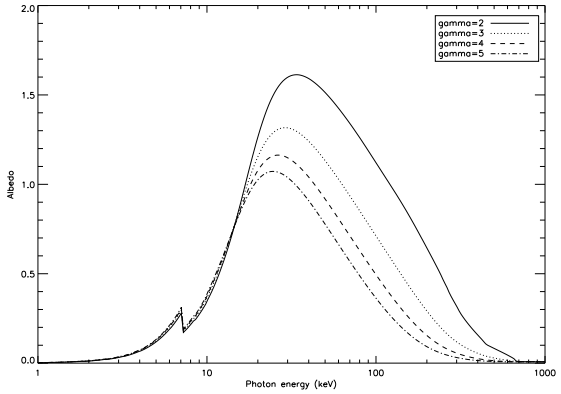

b. $\mu = 0.90$

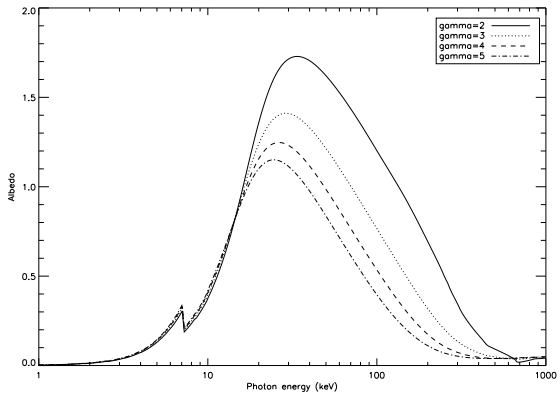

c. $\mu = 0.95$

Figure 5.25: Plots of albedo spectrum for $\gamma = 2 - 5$ for various viewing angles μ

Figures 5.23.(a)–(h), 5.24.(a)–(h), and 5.25.(a)–(c) show the plots of the albedo spectrum for $\gamma = 2 - 5$ for various viewing angles μ. The figures show the usual form of the Compton reflection spectrum and the peak at 7keV which is due to Iron line (K-edge) absorption.

5.5.5 Analysis & Discussion

As can be seen from Figure (5.7) a comparison of the fully angular Green's function of Poutanen et al and the Eddington hemisphere averaged Green's function of Kontar et al shows that they are similar both in shape and scale for an isotropic primary photon spectrum. Given that Magdziarz & Zdziarski (1995) is the scientific basis for both methods, it was important to verify that both methods agree in the isotropic limit (Poutanen found that both methods agreed to within 6 percent of each other).

We extended the radiative transfer method using a simple anisotropic func-

tional form. This tested that the differences in the observed photon spectrum between the Eddington, hemisphere averaged Green's function and the fully angular dependent Green's function correction, in essence, depend upon how the anisotropic radiation field in the fully angular (Poutanen) case is redistributed into the equivalent representation in the hemisphere averaged case.

From Figures (5.21), (5.22), (5.23.(a)–(h)), (5.24.(a)–(h)) and (5.25.(a)–(c)) it can be seen that the anisotropic emission appears to have an effect on both the scale and form of the reflection spectrum $R(\epsilon)$. This was apparent for primary photon spectra with a hard spectral index ($\gamma = 2$) but progressively decreased for spectra with higher spectral indices.

Clearly the effects of using a linear interpolation (in energy ϵ) within the empirical fit to the Leach and Petrosian data can be seen in the results of figures (5.21) and (5.22). This results in a 'straight line bulge' in the Compton reflection spectra for hard photon spectra ($\gamma = 2, 3$) in the 50 and 300keV energy range.

However a simplistic model of the energy dependence is being used here[12] and this is illustrated at relativistic energies $> 500keV$ which would result in a different energy dependence from the emission, for the same functional form, at non relativistic energies. This is the best model that we have at present, and it is hoped that as and when more data points become available then a linear interpolation can be improved upon.

One property of the spectra is that those produced using the radiative transfer solution do not fall to zero (say above 200keV) as quickly as in the hemisphere averaged method. This is evident from figures (5.9), (5.10), (5.2), (5.3), (5.21) and (5.22) for spectra away from the disk centre *i.e.* $\mu \leq 0.40$. This is more evident towards the limb.

[12]it is accepted that the empirical anisotropic model of the primary photon emission becomes unphysical above 400keV due to the linear fit in energy between the two data points - 22keV and 210keV.

Chapter 6

Inference of Electron Spectrum Anisotropy from Photon Spectra - Effect of Albedo Approximation

6.1 Introduction

In chapters (4) and (5) we investigated how isotropic and anisotropic primary photon emission altered the photospheric albedo and its effect on observed photon spectra. We initially used a hemisphere averaged approach which we referred to as the Eddington approximation (chapter 4) and subsequently we looked at a radiative transfer solution approach provided by Juri Poutanen (chapter 5).

In this chapter we use these results to investigate how the full anisotropic analysis affects the recovery of anisotropic mean electron spectra when using the *Stereoscopic electron spectroscopy* technique of Kontar & Brown (2006). This technique known more familiarly as the *Dentist Mirror*[1] allows the recovery of angle dependent $\bar{F}(E,\mu)$ from observed photon spectra. Here we are using synthetic anisotropic observed photon spectra to see how the conclusion of that paper are changed when we use the full anisotropic albedo rather than the Eddington approach. Specifically does the fully anisotropic albedo treatment confirm or conflict with their assertion that the electron distribution $\bar{F}(E,\mu)$ must be nearly isotropic.

Clearly this is an important test as the conclusion of Kontar and Brown casts doubt on models such as the collisional thick target that involve beamed (or

[1]Here the solar surface is being used as a mirror to reflect downward emitted primary HXR photons back into the direction of the observer in an analogous way to a dentist using a small mirror to view a patients teeth.

anisotropic) photon emission.

6.2 "Stereoscopic" Electron Spectroscopy and Photospheric Backscatter

In Kontar & Brown (2006) the authors emphasise that the albedo spectral component within the observed photon spectrum offers valuable insight into the anisotropy of the flare fast electron distribution. in particular to constrain the directivity of the flare electrons so strongly that the conventional models such as the collisional thick target (Brown 1972) with downward beaming or collimated beaming may be excluded.

6.2.1 An Overview of the Two Directional Spectroscopic Inversion

Kontar and Brown represent the photon flux observed at earth, $I(\epsilon)$, in terms of a direct upward and backscattered downwards component at the flare source. Therefore the flux towards an observer $I_o(\epsilon, \theta)$ can be written as

$$I_o(\epsilon) = \frac{\bar{n}V}{4\pi R^2} \int_\epsilon^\infty \left[Q_F(\epsilon, E)\bar{F}_u(E) + Q_B(\epsilon, E)\bar{F}_d(E) \right] dE \tag{6.1}$$

where $\bar{F}_{u,d} = (\bar{n}V)^{-1} \int F_{u,d}(E, r)n(r)dV$

The electron spectrum $F(E, \theta)$ is described in a two directional approximation where $F_u(E)$ and $F_d(E)$ are the density weighted volumetric mean flux spectra of electrons directed towards the observer upwards and downwards, averaged over $\delta\theta \approx 45^o$.

As previously demonstrated in chapters (2) to (5) X-Ray photons directed downwards towards the solar surface undergo backscattering and absorption in the dense photosphere. This can be represented as a convolution of the downward photon emission with a Green's function for Compton reflection. Kontar and Brown use the Magdziarz and Zdziarski Green's function for angle-dependent Compton reflection (Magdziarz & Zdziarski 1995) given in chapter 4 as

$$I_r(\epsilon, \mu) = \int_\epsilon^\infty G(\mu, \epsilon, \epsilon^{'}) I_d(\epsilon^{'}) d\epsilon^{'} \tag{6.2}$$

where $I_d(\epsilon)$ is the downward directed flux and $G(\mu, \epsilon, \epsilon^{'})$ is the Magdziarz and Zdziarski Green's function for Compton reflection.

Thus the reflected photon flux can be written as

$$I_r(\epsilon, \mu) = \frac{\bar{n}V}{4\pi R^2} \int_{\epsilon}^{\infty} G(\mu, \epsilon, \epsilon^{'}) d\epsilon^{'} \int_{\epsilon^{'}}^{\infty} \left[Q_F(\epsilon^{'}, E) \bar{F}_u(E) + Q_B(\epsilon^{'}, E) \bar{F}_d(E) \right] dE \tag{6.3}$$

The total observed flux as seen by an observer at earth (Chapter 4) is given by the sum of the upwards and downward component as $I_u(\epsilon) + I_r(\epsilon)$. By regularized inversion of 6.3 Kontar and Brown were able to find $\bar{F}_u(E)$ and $\bar{F}_d(E)$ essentially because the forms of $\mathcal{Q}_F$ and $\mathcal{Q}_B$ are different.

Kontar and Brown found that the ratio $\frac{\bar{F}_u(E)}{\bar{F}_d(E)}$ was close to unity. They concluded that the electron distribution was so close to isotropic that it would rule out the models that relied on anisotropic emission such as the collisional thick target (Brown 1972). The Kontar and Brown work was based on an Eddington approximation treatment of the albedo radiative transfer. Here we investigate whether the Kontar and Brown conclusions are changed if one instead uses a full anisotropic treatment of the scattering process. In short the absence of a strong albedo feature precludes the basic models that involve beaming.

6.2.2 The Technique

In Chapters 4 and 5 we studied how anisotropy affects the albedo by using an empirical fit to published data. We did this by using an Eddington hemispheric approach (chapter 4) and a radiative transfer approach (chapter 5). A comparison between the two approaches showed that whilst they agreed for isotropic emission differences appeared when the emission became anisotropic and was very apparent using the empirical fit.

The two directional spectroscopic inversion presented in Kontar & Brown (2006) was implemented in the form of a IDL algorithm (4.2). Again (as in chapter (5)) we use the algorithm as a 'black box' and we are not concerned with the internal workings of the algorithm which we assume to be correct. However as we provide a synthetic observed photon spectrum to the algorithm instead of a raw RHESSI data file (as originally implemented) we must modify the IDL algorithm slightly however we do so in such a way as to preserve the integrity of the science implemented in it and to ensure we do not add errors.

We now use the results in Chapters 4 and 5 to test the findings of Kontar and Brown:

1. We use the results from section 4.7.2 (the empirical fit to the Green's hemispheric approach in chapter (4)) as input to the spectroscopic inversion algorithm.

2. We similarly use the results from section 5.5.4 (the empirical fit to the radiative transfer approach in chapter 5) as input to the algorithm.

3. By comparing the differences between the two sets of results from the inversion we can determine if a full anisotropic radiative transfer approach alters the conclusion of Kontar and Brown.

The full listing of the stereoscopic inversion algorithm used in this chapter is extensive and it is not feasible to list it here. Instead the listing of the algorithm can be found in Appendix E - The fit2d routine.

6.2.3 The Inversion Routine

We use the inversion routine developed by Kontar and Brown as a black box, as such we are not concerned with the inner workings of the algorithm but only with the inputs (the photon spectra) and the outputs (the electron spectra).

The electron spectra that are recovered from the Hemispheric Eddington Green's function results and the full radiative transfer results are given in Figures (6.1) - (6.4) and Figures (6.5) - (6.8) below.

6.2.4 Stereoscopic Electron Spectroscopy from Anisotropic Photon Spectra - Eddington Hemisphere Averaged Approximation

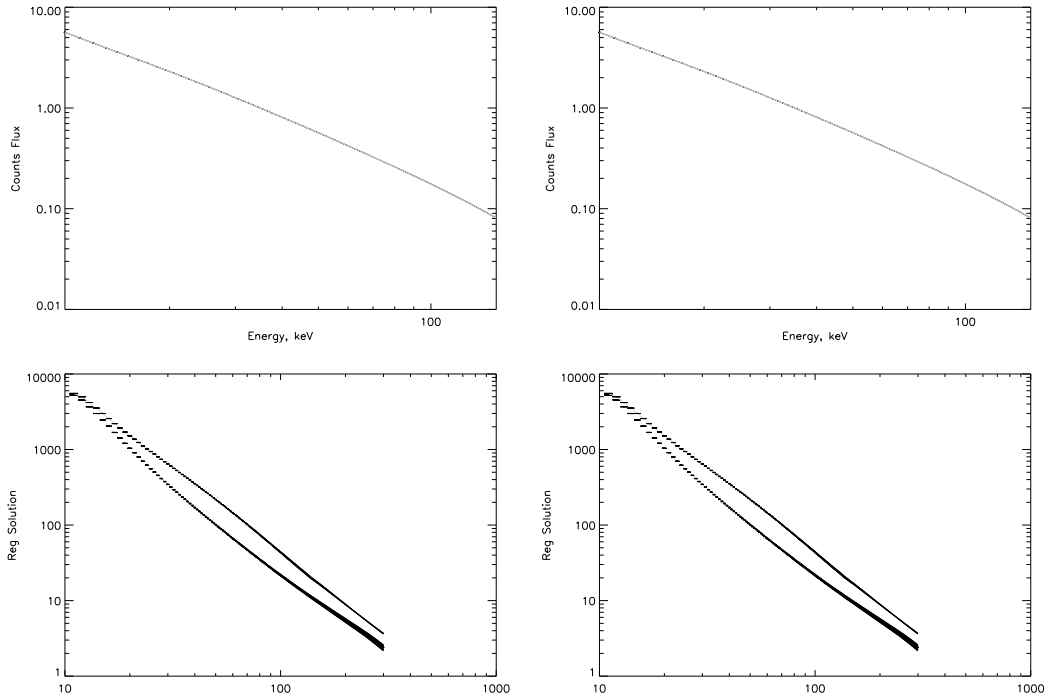

a. $\mu = 0.95$ b. $\mu = 0.90$

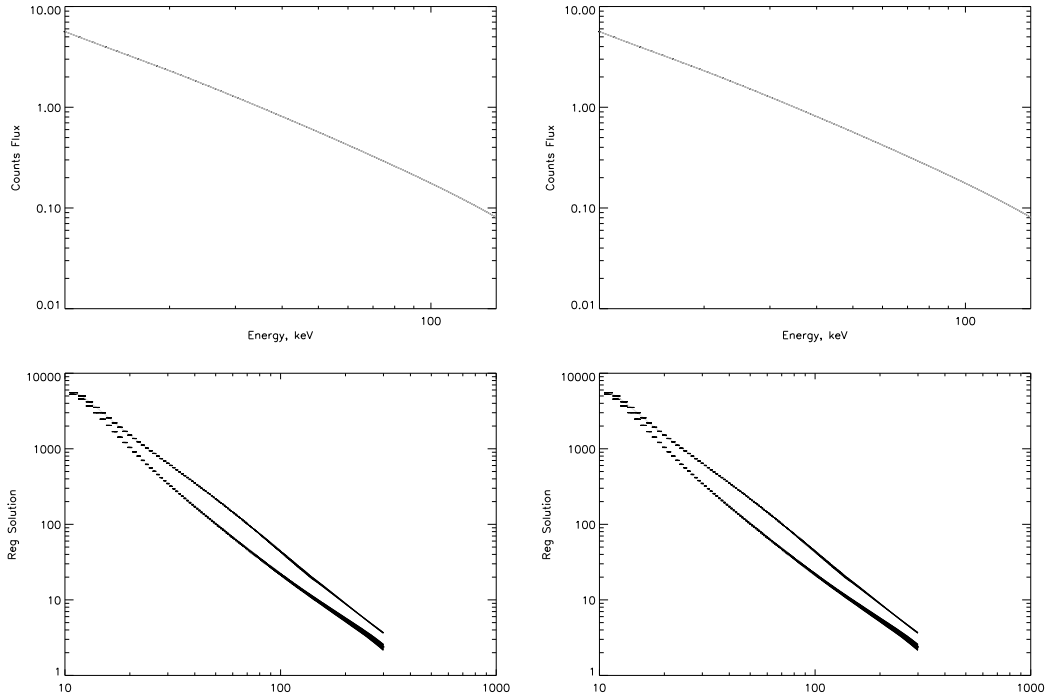

c. $\mu = 0.60$ d. $\mu = 0.45$

Figure 6.1: The recovered electron spectra (**bottom plot**) and the forward fitted photon spectra (**top plot**) from the hemispheric Eddington Green's function results for a spectral index of $\gamma = 2$

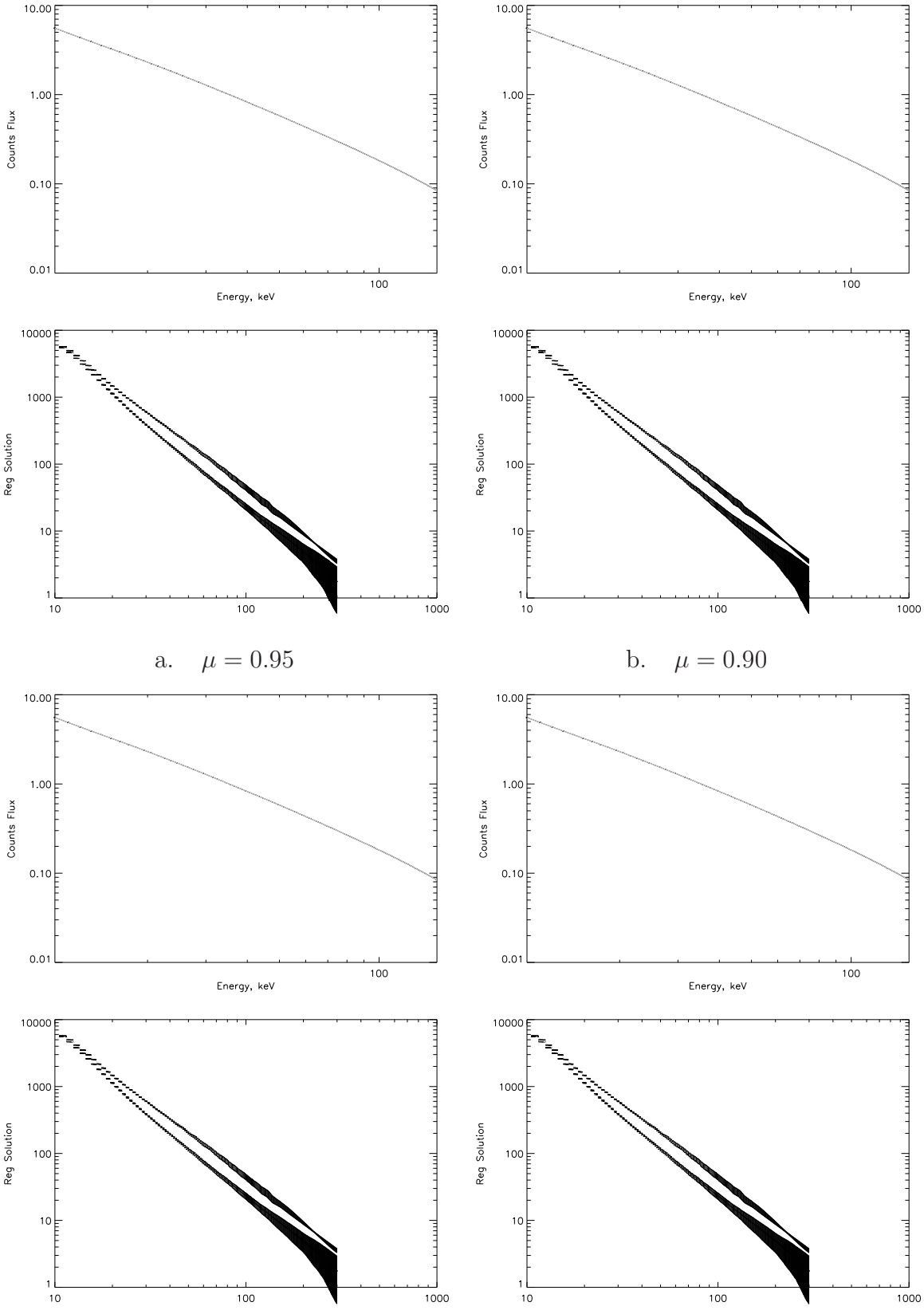

a. $\mu = 0.95$

b. $\mu = 0.90$

c. $\mu = 0.60$

d. $\mu = 0.45$

Figure 6.2: The recovered electron spectra (**bottom plot**) and the forward fitted photon spectra (**top plot**) from the hemispheric Eddington Green's function results for a spectral index of $\gamma = 3$

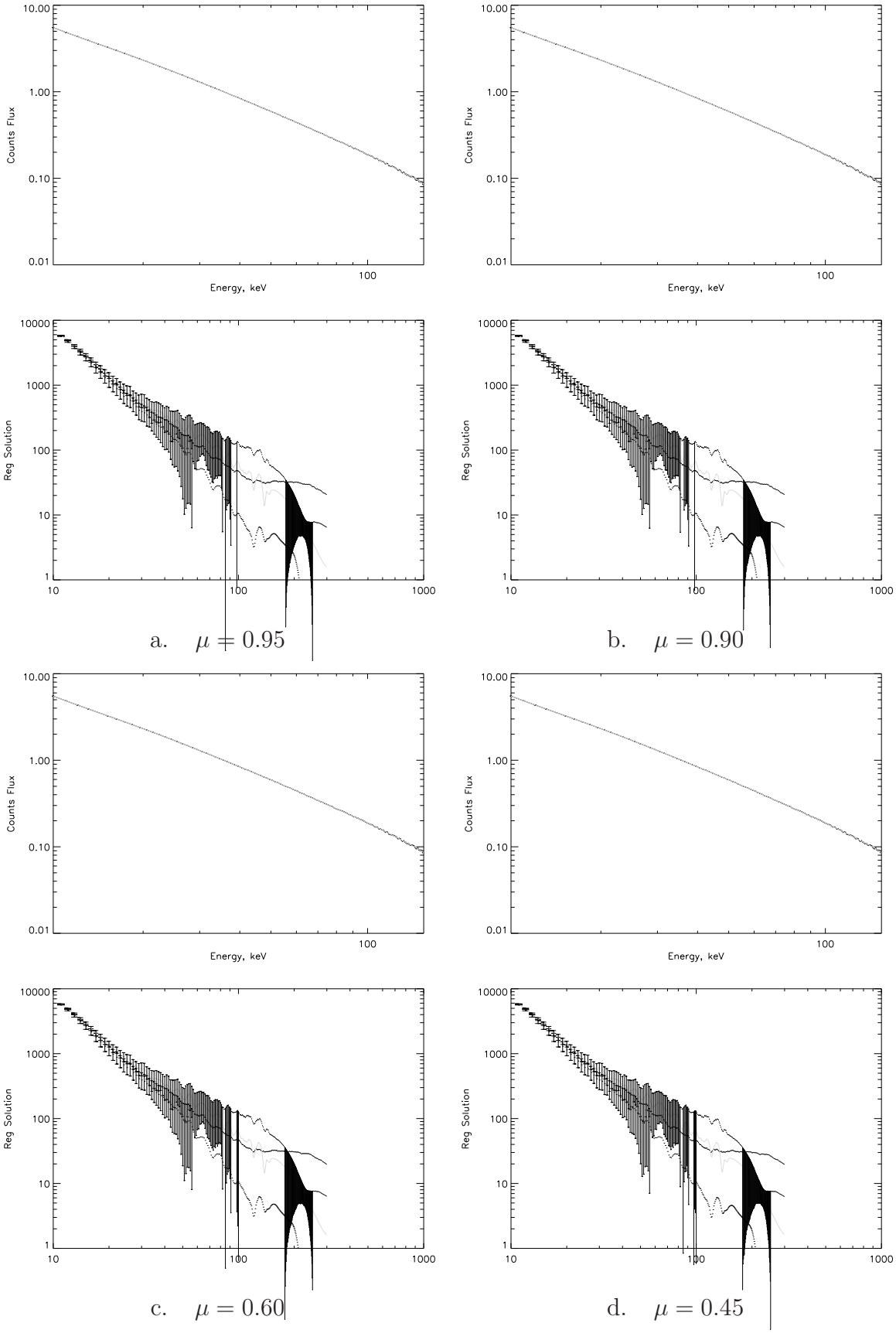

Figure 6.3: The recovered electron spectra (**bottom plot**) and the forward fitted photon spectra (**top plot**) from the hemispheric Eddington Green's function results for a spectral index of $\gamma = 4$

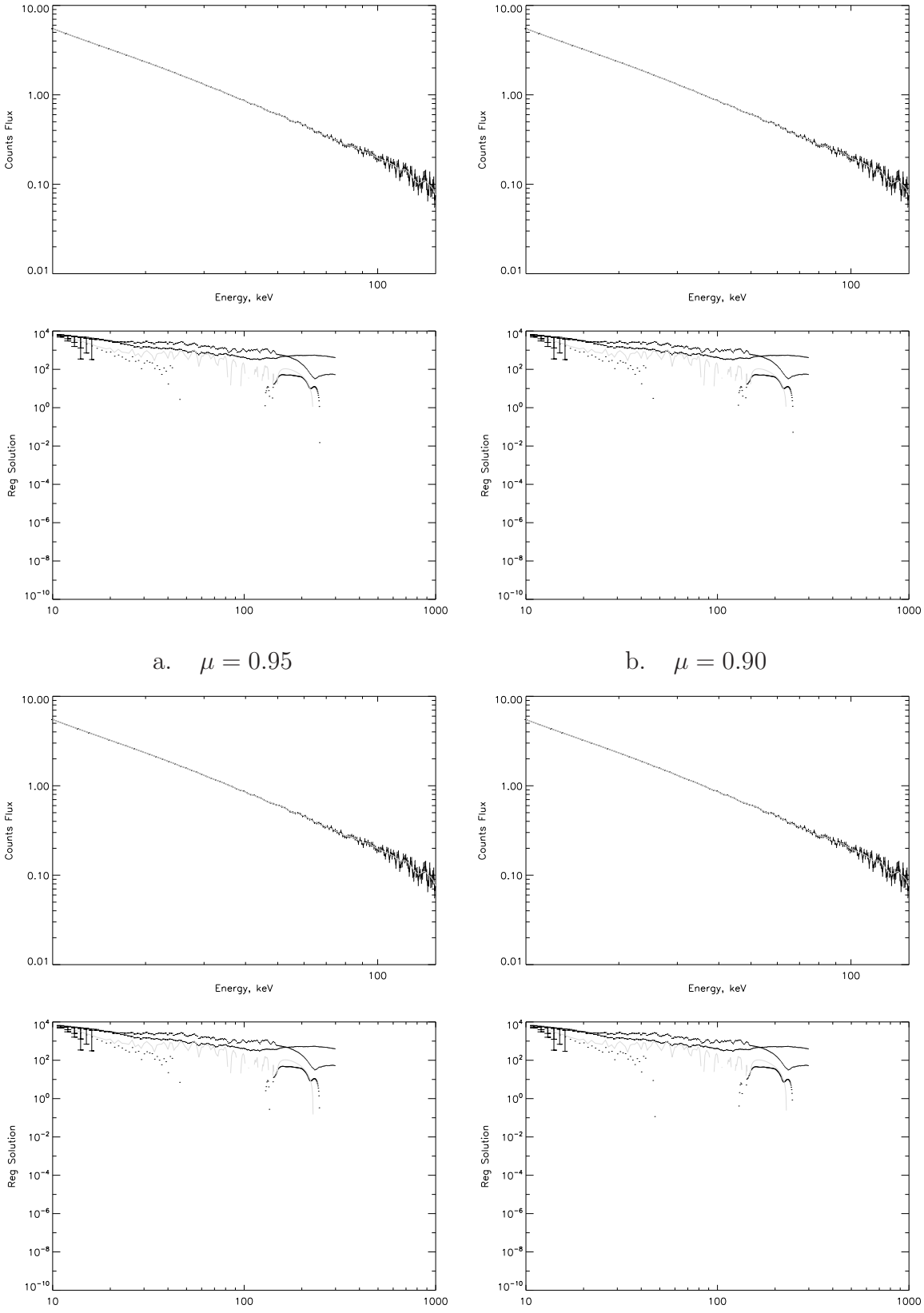

a. $\mu = 0.95$

b. $\mu = 0.90$

c. $\mu = 0.60$

d. $\mu = 0.45$

Figure 6.4: The recovered electron spectra (**bottom plot**) and the forward fitted photon spectra (**top plot**) from the hemispheric Eddington Green's function results for a spectral index of $\gamma = 5$

6.2.5 Stereoscopic Electron Spectroscopy from Anisotropic Photon Spectra - Radiative Transfer Solution Approach

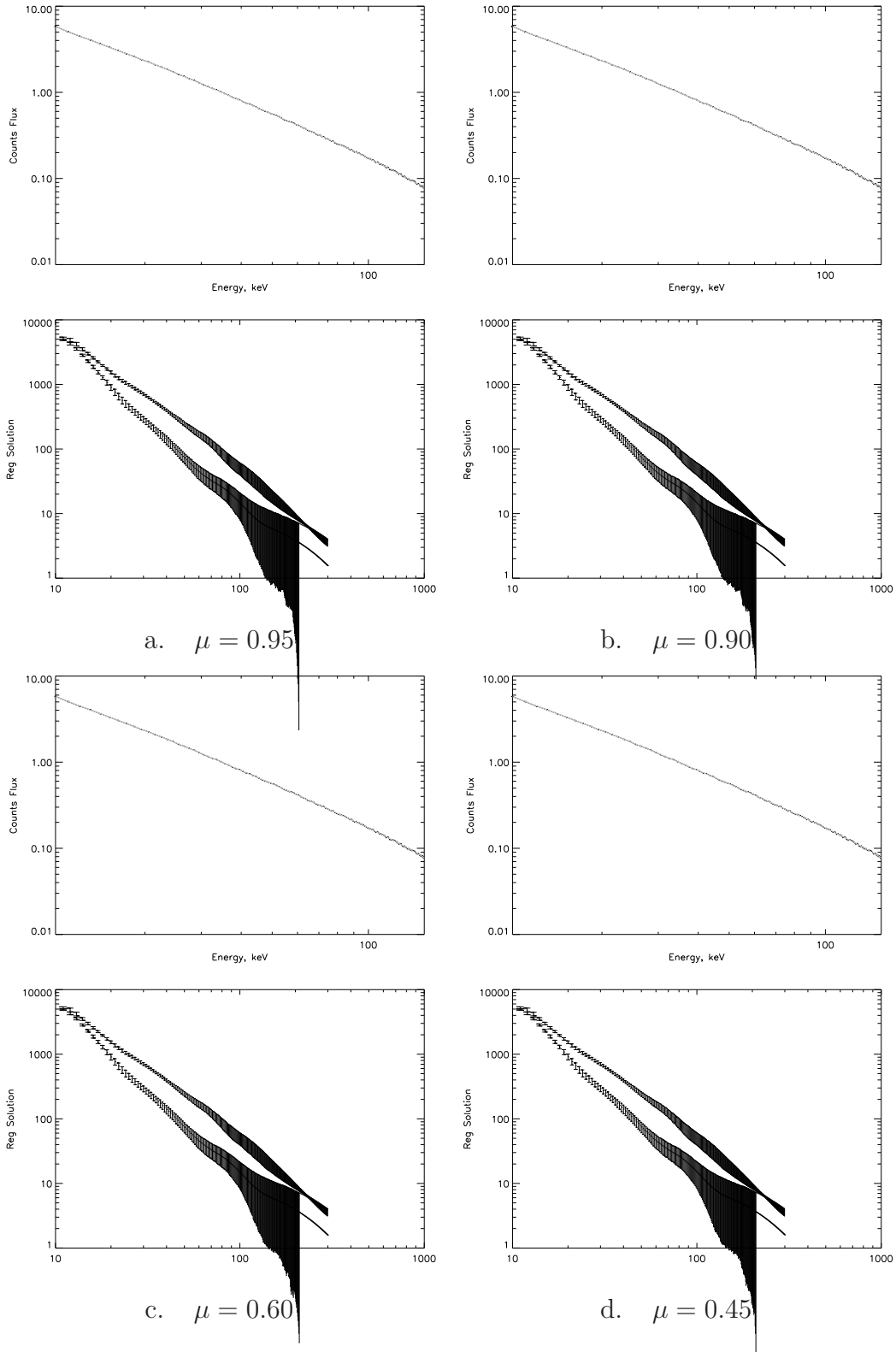

Figure 6.5: The recovered electron spectra (**bottom plot**) and the forward fitted photon spectra (**top plot**) from the radiative transfer solution results for a spectral index of $\gamma = 2$

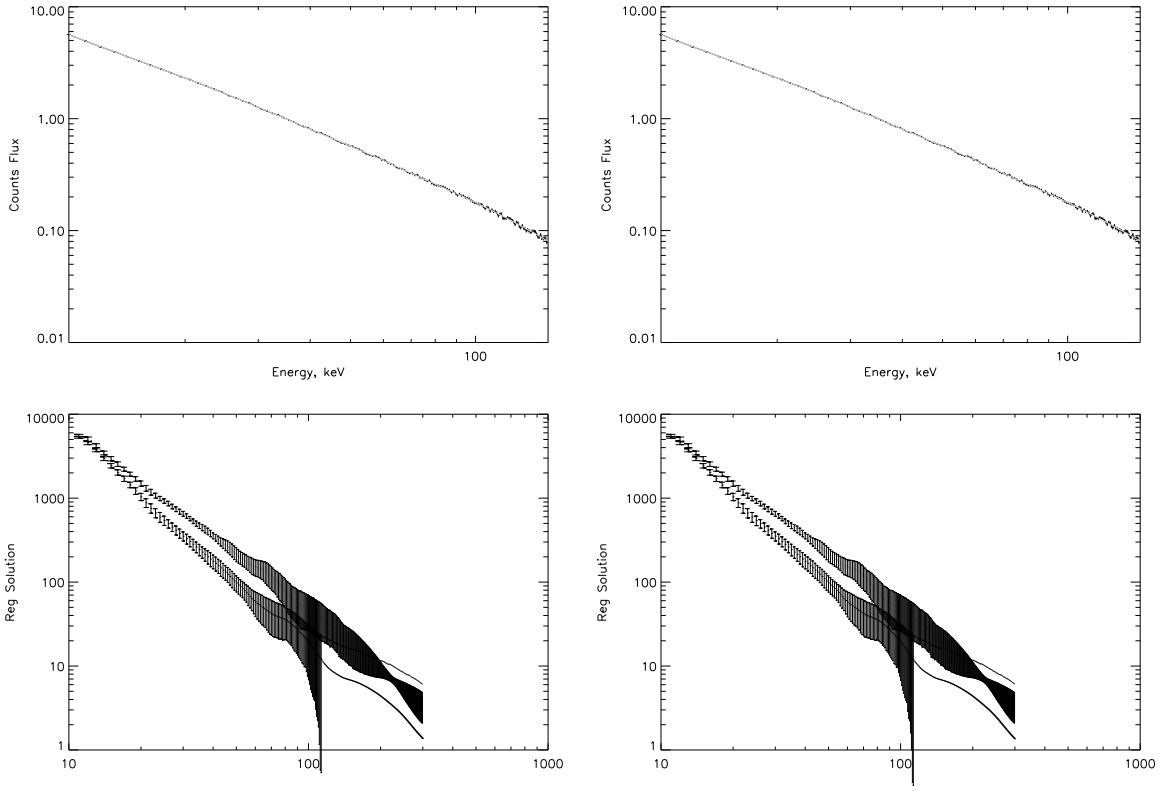

a. $\mu = 0.95$ b. $\mu = 0.90$

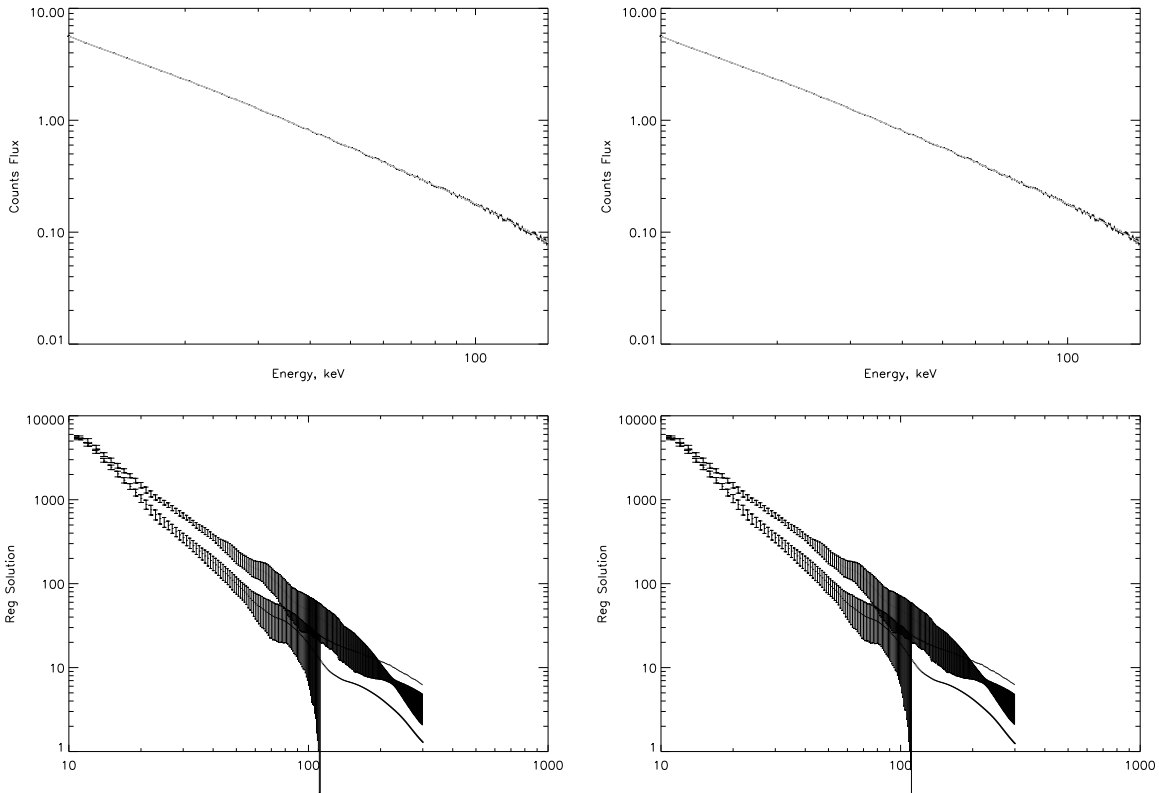

c. $\mu = 0.60$ d. $\mu = 0.45$

Figure 6.6: The recovered electron spectra (**bottom plot**) and the forward fitted photon spectra (**top plot**) from the radiative transfer solution results for a spectral index of $\gamma = 3$

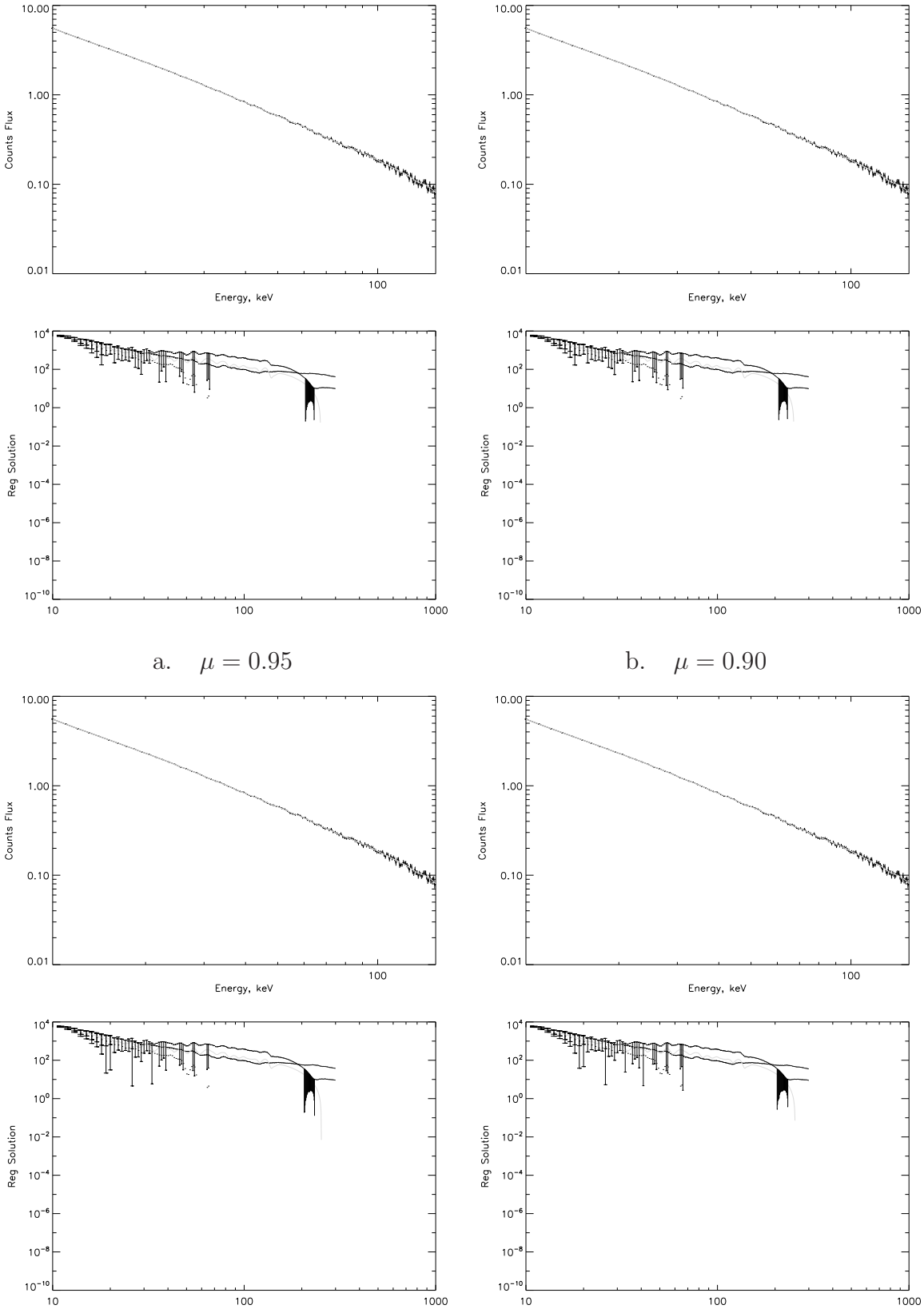

a. $\mu = 0.95$

b. $\mu = 0.90$

c. $\mu = 0.60$

d. $\mu = 0.45$

Figure 6.7: The recovered electron spectra (**bottom plot**) and the forward fitted photon spectra (**top plot**) from the radiative transfer solution results for a spectral index of $\gamma = 4$

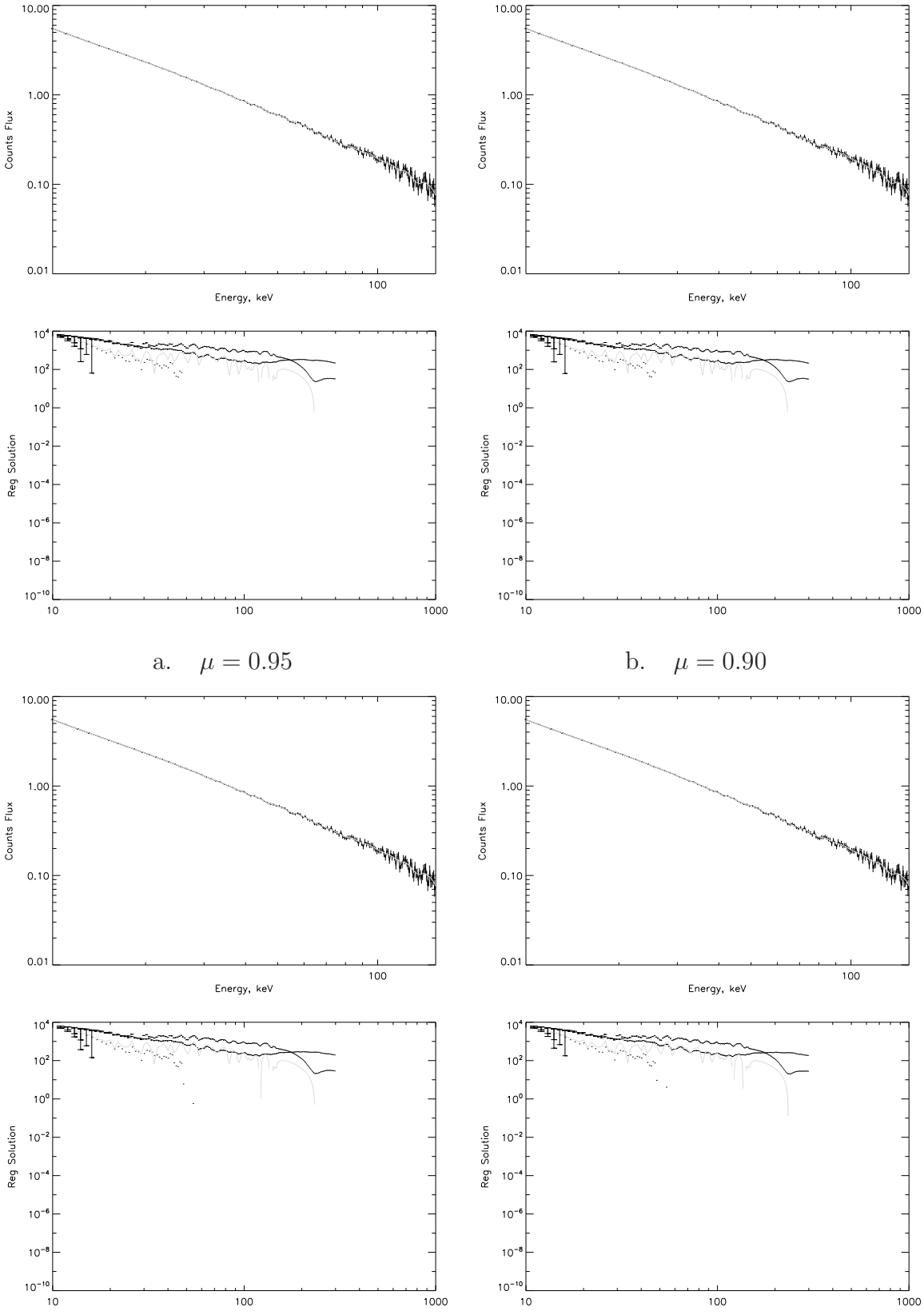

a. $\mu = 0.95$

b. $\mu = 0.90$

c. $\mu = 0.60$

d. $\mu = 0.45$

Figure 6.8: The recovered electron spectra (**bottom plot**) and the forward fitted photon spectra (**top plot**) from the radiative transfer solution results for a spectral index of $\gamma = 5$

1. The lower plot in figures 6.1 – 6.4 show the two mean electron spectra $\bar{F}(E,\mu)$ ($\bar{F}_u$ (upper line) and $\bar{F}_d$ (lower line)) for the hemisphere averaged, empirically fitted, Green's function (Eddington) approach to albedo prediction. The upper plot shows the photon count flux along with the forward fit.

2. The lower plot in figures 6.5 – 6.8 show the two mean electron spectra $\bar{F}(E,\mu)$ ($\bar{F}_u$ (upper line) and $\bar{F}_d$ (lower line)) for full radiative transfer anisotropic (Poutanen) treatment of albedo. Again the upper plot shows the photon count flux along with the forward fit.

6.3 Analysis & Discussion

The mean results for $\bar{F}_u(E)$ and $\bar{F}_d(E)$ for the two approaches to albedo are very similar for $\mu = 0.95$ (close to the disk centre) but it is clear that the error bars in the results from the Poutanen approach are considerably worse than in the equivalent Eddington results. For both approaches for $\gamma = 2$ the error bars are tiny on both $\bar{F}_u$ (up) and $\bar{F}_d$ (down) but get progressively worse with increasing γ. Given that the criteria for an acceptable solution (lower plot in each subfigure) using the stereoscopic technique is a continuous regularised solution for $\bar{F}_u(E)$ and $\bar{F}_d(E)$ it appears that the hemisphere averaged approach yields acceptable solutions for $\gamma = 2, 3, 4$ but only $\gamma = 2, 3$ gives positive results for the Poutanen approach.

In fact the results given here are consistent with the sort of instability expected when the model used becomes more complex than the information content of the data can justify (section 4.1.4) and this manifests itself as gaps in the regularised solution and as the high frequency oscillations (at higher energies) in the Count flux of Figures 6.1 – 6.4 and 6.5 – 6.8. We can therefore maintain that the Poutanen results are "less invertable" for larger γ than the hemispheric approach using the stereoscopic technique given the instability in the regularised solution and the oscillations in the Count flux.

However, one important caveat is that Kontar and Brown's algorithm internally uses averaging such that the electron spectrum is approximated by beams in two directions averaged over angle. This is similar to the Eddington approach studied in Chapter 4 and the hemisphere average, empirically fitted, anisotropic photon spectra used in this chapter to verify their results. Indeed the similar-

ity to the Eddington approach may be a source of the larger error bars within the Poutanen regularised solution as the differences between the hemispheric and Poutanen Green's function approaches will be amplified upon inversion. Whilst this does not affect the conclusion of the work presented here we should be mindful that this averaging in the stereoscopic routine may "wash out" some of the anisotropic detail present in the input photon spectra and therefore lead us to conclude that the electron distribution is more isotropic that it actually is.

It therefore appears that the Kontar and Brown conclusions that $\bar{F}(E)$ is near isotropic holds up even when albedo is treated fully rather than in the Eddington approximation.

6.3.1 Conclusion

Using synthetic anisotropic 'observed' photon spectra generated from a hemisphere averaged, empirically fitted, Green's function approach (Chapter 4) and a full radiative transfer solution approach (Chapter 5) we have confirmed the findings published by Kontar & Brown (2006) using the Stereoscopic electron spectroscopy technique.

To conclude, given the results in figures 6.1 – 6.4 and 6.5 – 6.8 above, doing a full anisotropic scattering properly does not fundamentally change the findings that the electron distribution ($\bar{F}(E, \mu)$) is nearly isotropic to such a degree of confidence that it casts doubt on models which are based upon beaming such as the collisional thick target (Brown 1972).

Chapter 7

Conclusion and Future Work

7.1 Conclusion

In Chapter 2 we have explored the effect of photospheric albedo on observations of global flare hard X-ray spectra and derived an expression to allow approximate correction for this in the case of primary power-law photon spectra. We also examined, for the Kramers cross-section, the consequences of ignoring the albedo correction in using observed spectra to infer flare source electron spectra for thin and thick target interpretations and shown that the effects are very significant in terms of inferred spectral shape, especially for hard spectra. We extended the analysis to other cross sections such as Bethe Heitler and found that the effects of the albedo were enhanced when compared with the Kramers case. This is consistent with the effects of albedo on deriving electron spectra which is expected to be even larger for more realistic smoother cross-section approximations, because they filter the electron spectral features even more. We also emphasised that the effects of albedo should be considered alongside other corrections such as that of nonuniform target ionisation in the case of the thick target beam model as discussed by Kontar et al. (2002) and Kontar et al. (2003).

In Chapter 3 we extended the work presented in Chapter 2 to investigate, for the Kramers cross-section, the consequences of ignoring the *anisotropic* albedo correction in using observed spectra to infer flare source electron spectra for thin and thick target interpretations. We evaluated expressions for the thin and thick target electron spectra by introducing an energy dependent anisotropy into the observed photon spectrum in the form of a hemisphere average fraction. This again demonstrated that the effects, in the case of an energy dependent anistropy, are very significant in terms of inferred spectral shape, especially for hard spectra.

In Chapter 4 we demonstrated a Hemispheric Eddington Green's function approach to the Albedo and the influence on the Hard X-Ray photon spectrum. We also extended the discrete Compton Green's operator approach developed by Kontar to examine energy dependent anisotropic effects in the photospheric albedo by introducing this by using a Hemispheric Eddington approximation to represent the anisotropy. We investigated this for both a simple energy dependent anisotropic relationship and an empirical fit derived from published solar data by Leach and Petrosian. We show that energy dependent anisotropic effects have a significant effect upon the spectral shape of the observed photon spectrum this is most noticeable with in increasing photon energy. Finally we found that in assuming an isotropic power law primary photon spectrum we underestimate the reflection spectrum $R(\epsilon)$ and therefore the observed photon spectrum within the 30keV to 200keV energy range.

In Chapter 5 we used a full radiative transfer green function approach, developed by Poutanen, for studying the effect of full angular dependent photon emission on the observed photon spectrum. We examined the consequence of this on the photospheric albedo for isotropic photon emission and extended this technique to a fully angular anisotropic analysis using an energy dependent empirical fit derived from published solar data by Leach and Petrosian. We then compared the observed photon spectra produced by the radiative transfer and hemisphere average green function approaches and found that both methods agree well in the isotropic limit but for anisotropic emission the full radiative solution approach appears to have an effect upon both the scale and form of the albedo.

In Chapter 6 using synthetic anisotropic observed photon spectra generated from a hemisphere averaged, empirically fitted, Green's function approach and a full radiative transfer solution approach we have confirmed the findings published by Kontar & Brown (2006) using the Stereoscopic electron spectroscopy technique. To conclude, we found that doing full anisotropic scattering properly does not fundamentally change the findings that the electron distribution ($\bar{F}(E,\mu)$) is nearly isotropic to such a degree of confidence that it casts doubt on models which are based upon beaming such as the collisional thick target.

7.2 Future Work

The full radiative transfer solution (Chapter 5) is currently implemented as a Fortran application however it is hoped to provide this functionality to the wider solar community using IDL. This can be achieved by providing the functionality as a library which can be accessed from RHESSI software or related modules. Clearly this preserved the algorithms at the expense of having to use an external library from within IDL. It would also be possible to re-engineer the algorithms from Fortran 77 into IDL which would provide a great consistency with the existing RHESSI software.

The Solar Orbiter mission (7.1) is part of the ESA Cosmic Vision 2015-2025 Science programme and is ESAs contribution to the International Living with a Star (ILWS) programme. The primary goal of this 6 year mission is to produce images of the Sun at an unprecedented resolution and perform closest ever in-situ measurements in the visible, extreme ultra-violet and X-rays energies. One of the payloads of the Solar Orbiter is the X-ray Imager (STIX): it provides imaging spectroscopy of solar thermal and non-thermal X-ray emission and quantitative information on the timing, location, intensity, and spectra of accelerated electrons as well as of high temperature thermal plasmas, mostly associated with flares and/or microflares.

Clearly this will provide an important opportunity for obtaining high quality data. It will also provide data which can help improve the empirical fit used within this thesis. In particular the Leach and Petrosian data used (two data points in energy) allowed only a linear fit. STIX will hopefully provide the directivity of primary HXR photons for a range of energies and allow a more complex empirical fit.

The "Stereoscopic" electron spectroscopy technique developed by Kontar and Brown 2006 (The dentist mirror approach) uses averaging such that the electron spectrum is approximated by beams in two directions averaged over angle. Although the Eddington approximation is consistent with this assumption, the results of the radiative transfer approach of Chapter 5 assume the electron emission would have a full angular distribution. Clearly there is some inconsistency between the assumptions in the forward modeling that produced the photon spectra and the inversion used within the dentist mirror technique. Whilst this does not invalidate the work presented in this thesis a dentist mirror approach assuming a full angular distribution for the electron emission would allow a more

accurate comparison.

Finally as noted by Kontar & Brown (2006), the directly emitted solar HXR photons and those that are Compton reflected have distinct signals. One idea is to exploit this difference in the detection of extra solar planet by using the direct signal from the star and the albedo signal from an extrasolar planet. Initial calculations indicate that to detect extra solar planets by this technique would require 3 to 4 orders of magnitude of improvement in the sensitivity of current spacecraft detector. However by exploring this idea it is hoped that the work may inform some design aspects of the design of detectors in future spacecraft.

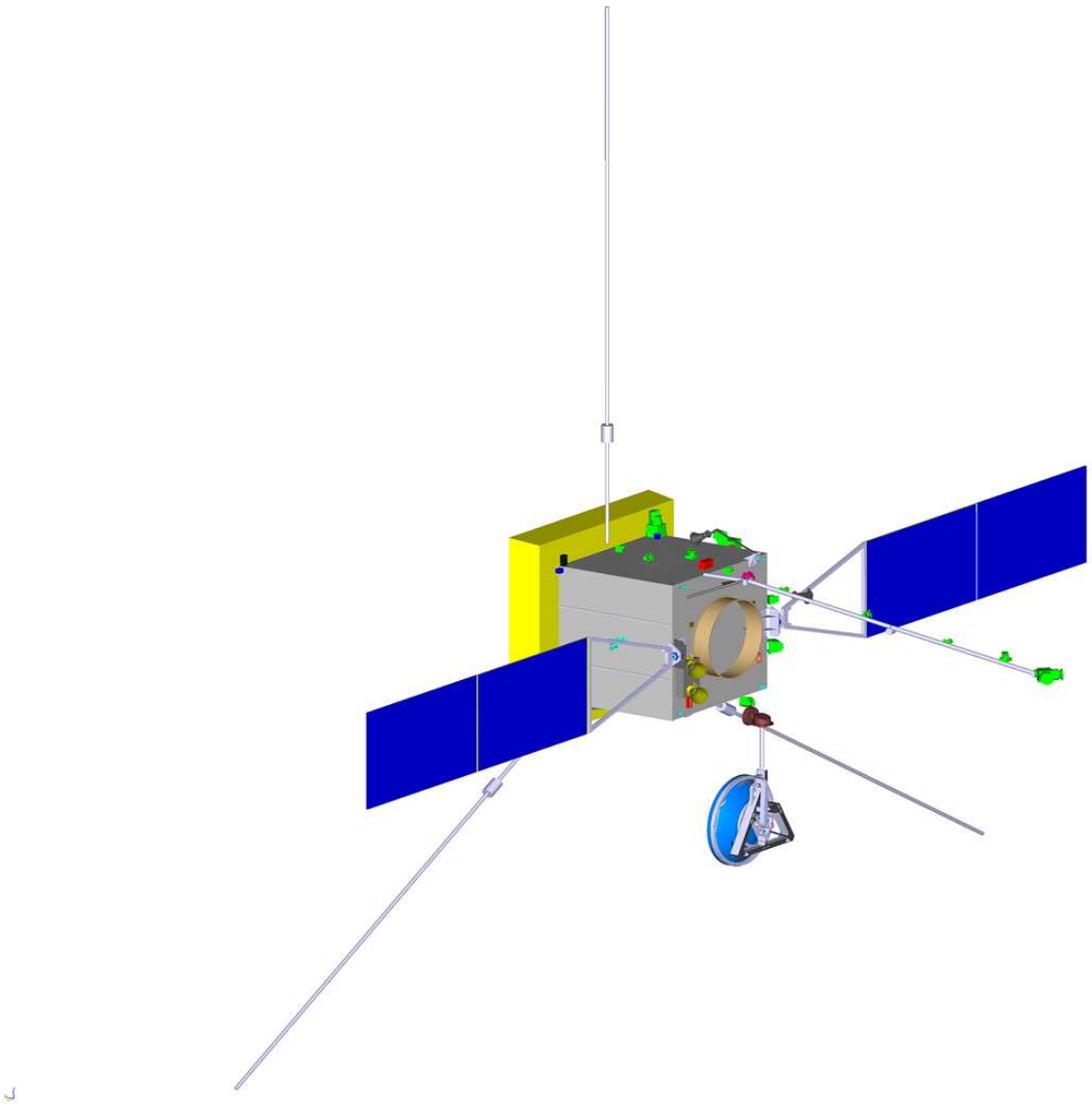

Figure 7.1: An illustration of the ESA Solar Orbiter spacecraft

Bibliography

Alexander, R. C. & Brown, J. C. 2002, Solar Physics, 210, 407

Aschwanden, M. J. 2004, Physics of the Solar Corona. An Introduction, ed. Aschwanden, M. J. (Praxis Publishing Ltd)

Aschwanden, M. J. 2005, Physics of the Solar Corona. An Introduction with Problems and Solutions (2nd edition), ed. Aschwanden, M. J.

Bai, T. 1978, Solar Physics, 59, 141

Bai, T. & Ramaty, R. 1978, Astrophysical Journal, 219, 705

Brown, J. C. 1971, Solar Physics, 18, 489

Brown, J. C. 1972, Solar Physics, 26, 441

Brown, J. C. 1973, Solar Physics, 28, 151

Brown, J. C. & Emslie, A. G. 1988, Astrophysical Journal, 331, 554

Carrington, R. C. 1859, Monthly Notices of the Royal Astronomical Society, 20, 13

Christensen-Dalsgaard, J., Dappen, W., Ajukov, S. V., et al. 1996, Science, 272, 1286

Craig, I. J. D. & Brown, J. C. 1986, Inverse problems in astronomy: A guide to inversion strategies for remotely sensed data, ed. I. J. D. Craig & J. C. Brown

Craig, I. J. D. & McClymont, A. N. 1976, Solar Physics, 50, 133

Demleitner, M., Accomazzi, A., Eichhorn, G., et al. 2001, in Astronomical Society of the Pacific Conference Series, Vol. 238, Astronomical Data Analysis Software and Systems X, ed. F. R. Harnden, Jr., F. A. Primini, & H. E. Payne, 321–+

Elwert, G. & Haug, E. 1970, Solar Physics, 15, 234

Emslie, A. G. 1978, Astrophysical Journal, 224, 241

Emslie, A. G. 1996, PhD thesis, D Sc thesis, University of Glasgow, (1996)

Golub, L. & Pasachoff, J. M. 2001, Nearest Star, ed. N/A

Grant, I. P. & Hunt, G. E. 1969a, Royal Society of London Proceedings Series A, 313, 183

Grant, I. P. & Hunt, G. E. 1969b, Royal Society of London Proceedings Series A, 313, 199

Hecht, J. . 2006, Solar Flares will disrupt GPS in 2011, Tech. rep., published on 29th September 2006

IDL Online Help (March 06, . 2007, IDL Reference Guide: Procedures and Functions CURVEFIT, Tech. rep.

Koch, H. W. & Motz, J. W. 1959, Rev. Mod. Phys., 31, 920

Kontar, E. P. & Brown, J. C. 2006, Astrophysical Journal, Letters, 653, L149

Kontar, E. P., Brown, J. C., Emslie, A. G., et al. 2003, Astrophysical Journal, Letters, 595, L123

Kontar, E. P., Brown, J. C., & McArthur, G. K. 2002, Solar Physics, 210, 419

Kontar, E. P., MacKinnon, A. L., Schwartz, R. A., & Brown, J. C. 2006, Astronomy and Astrophysics, 446, 1157

Kramers, H. A. 1923, Phil. Mag., 46, 836

Leach, J. & Petrosian, V. 1983, Astrophysical Journal, 269, 715

Lin, R. P., Dennis, B. R., Hurford, G. J., et al. 2002, Solar Physics, 210, 3

Magdziarz, P. & Zdziarski, A. A. 1995, Monthly Notices of the Royal Astronomical Society, 273, 837

Poutanen, J., Nagendra, K. N., & Svensson, R. 1996, Monthly Notices of the Royal Astronomical Society, 283, 892

Priest, E. R. 1984, Solar magneto-hydrodynamics, ed. Priest, E. R.

Ramaty, R. 1987, Solar Physics, 113, 203

Ridpath, I. 1997, Oxford Dictionary of Astronomy, ed. I. Ridpath

Santangelo, N., Horstman, H., & Horstman-Moretti, E. 1973, Solar Physics, 29, 143

Schmahl, E. J., Hurford, G. J., & RHESSI Team. 2004, in Bulletin of the American Astronomical Society, Vol. 36, Bulletin of the American Astronomical Society, 759–+

Tandberg-Hanssen, E. & Emslie, A. G. 1988, The physics of Solar Flares, ed. N/A

Tomblin, F. F. 1972, Astrophysical Journal, 171, 377

White, T. R., Lightman, A. P., & Zdziarski, A. A. 1988, Astrophysical Journal, 331, 939

Woan, G. 2000, Cambridge Handbook of Physics, ed. G. Woan

Appendix A

Greens Function Correction to a Power Law Spectrum

A.1 Isotropic Simulation Algorithm

```
;+
; PROJECT: P.hD.
; NAME:   simple_greens_correction
;
;
; PURPOSE:  To calculate the green's corrected albedo
;           for a given primary photon spectrum
;
;
; CATEGORY:
;
;
; CALLING SEQUENCE:
;
;   simple_acorrect , anisotropy=X (X-variable)
;
;
; INPUTS:
;    anisotropy      - a coeficient showing the ratio of the flux in
;                      observer direction to the flux downwards
;
;                      if anisotropy=1 (default) the source is
```

```
;                       isotropic
;
;    outfile          - the root name for the output files
;
; USES precomputed green functions from files
; green_compton_mu***.dat, where *** is cos(theta)
;
; OUTPUTS:
; files containing the primary, observered, and albedo spectrum.
;
; SIDE EFFECTS:
; none
;
; RESTRICTIONS:
; None
;
; PROCEDURE:
; none
;
; MODIFICATION HISTORY:
; calum@astro.gla.ac.uk, 8-feb-2005

;-
function normal_spec, x, gamma, e_o
;
return, (1/(2*!PI*e_o))*(gamma-1)*((x/e_o)^(-gamma))
;
END
pro simple_greens_correction, anisotropy, outfile
;
; global variables
;
e_o=30.0
gamma=4.0
flux_scale=1.0
;
```

```
if n_elements(anisotropy) EQ 0 then begin
  print,'Setting the value for the anisotropy to its default value (=1).'
  return;
endif;

print,'Calculating the Greens corrected albedo for: ' + $
strtrim(anisotropy,2)

if n_elements(outfile) EQ 0 then begin
    print, 'You must supply a root filename for the output spectra.'
    return;
endif;

primary_photon_file=outfile + '.' + strtrim(anisotropy,2) + '.primary.dat'
total_photon_file=outfile + '.' + strtrim(anisotropy,2) + '.total.dat'
albedo_photon_file=outfile + '.' + strtrim(anisotropy,2) + '.albedo.dat'

; get the greens compton file - these should be stored within the
;                               calling directory
restore,'compton_data/green_compton_mu095.dat'

;
; this part loads the greens correction
;
aa=p.albedo
ee =p.edges

ee2=(ee-3.)^2/max(ee-3.5)+3.

;
; e1 if the photon energy
;
e1 =(ee(0,*)+ee(1,*))/2.
de1=(ee(1,*)-ee(0,*))

;
```

```
; define the primary spectrum
;

flux=fltarr(n_elements(e1))

for i=0,n_elements(e1)-1 do begin
  flux(i)=normal_spec(e1(i), gamma, e_o)
endfor

; scale up the flux
flux = flux_scale*flux;

;
; calculate the reflected spectrum here.
;
; note that the anisotropy is just a constant multiplier
; so can be applied after the matrix multiplication
;
a1=(aa##(anisotropy*flux)) ; anisotropy constant here

;
; the albedo is the ratio of the reflected to the incident spectrum
; so just divide
;
albedo=a1/flux

;
; The observed spectrum is just the sum of the primary and the
; reflected spectrum
;
total_flux=flux+a1

;
; The rest of the procedure plots/saves the data
; in various formats
;
```

```
window,0, retain=2
!P.Multi=[0,1,2]

plot,e1,albedo,/xlog,yrange=[0,1], PSYM=3

plot_oo,e1,flux
oplot,e1,a1,line=1
oplot,e1,total_flux,line=2

!P.Multi=0

print,'Completed .....................................OK'
;stop

tstamp=timestamp()

set_plot, 'PS'

device, filename='simple_isotropic_refl_spec_'+strtrim(tstamp,2) + $
'.albedo.ps', xsize=24,ysize=17,xoffset=2,yoffset=2,ENCAPSULATED=0

plot,e1,albedo,/xlog,yrange=[0,1], line=3, xtitle='keV', $
ytitle='Normalised Units'

device, /close
set_plot, 'X'

set_plot, 'PS'
device, filename='simple_isotropic_refl_spec_'+strtrim(tstamp,2)+$
'.spectrum.ps', xsize=24,ysize=17,xoffset=2,yoffset=2,ENCAPSULATED=0

plot_oo,e1,flux, xtitle='keV', ytitle='Normalised Units',yrange=[1e-7,1]
oplot,e1,a1,line=1
oplot,e1,total_flux,line=2
```

```
device, /close
set_plot, 'X'

openw,11,primary_photon_file
for i=0, n_elements(e1)-1 do begin

if e1(i) GT 298.000 then break;

printf,11, e1(i)-0.5, e1(i)+de1(i)-0.5, flux(i), sqrt(flux(i))
endfor
close,11

openw,11,total_photon_file
for i=0, n_elements(e1)-1 do begin
if e1(i) GT 298.000 then break;
printf,11,  e1(i)-0.5, e1(i)+de1(i)-.5, total_flux(i), sqrt(flux(i))
endfor;

close,11

openw,11,albedo_photon_file
for i=0, n_elements(e1)-1 do begin
if e1(i) GT 298.000 then break;
printf,11, e1(i)-0.5,e1(i)+de1(i)-.5,albedo(i), sqrt(flux(i))

endfor
close,11

end
```

A.2 The Energy Independent Greens Anisotropic Correction - Simulation Algorithm

We implement Equation (4.17) detailed page 87 within the IDL routine given below.

```
;+
; PROJECT:
;   PhD
;
; NAME:
;   aniso_ang_correct_norm.pro
;
;
; PURPOSE:
;   Calculates the simple anisotropic greens reflection for a given
;   Spectral Ind & Ang
;
; CATEGORY:
;   Spectra, Modeling, inversion, regularisation
;
; CALLING SEQUENCE:
;
; CALLS:
;
; INPUTS:
;  spec_idx - spectral index
;  ang - angle of observer
;
; OPTIONAL INPUTS:
;
; OUTPUTS:
;
;
; OPTIONAL OUTPUTS:
;   none
```

```
;
; KEYWORDS:
;   none
;
; COMMON BLOCKS:
;   none
;
; SIDE EFFECTS:
;
;
; RESTRICTIONS:
; angle must be a multiple of 5 in the interval 005 <= cos(theta) <= 0.95
;
; PROCEDURE:
;
; MODIFICATION HISTORY:
;   Version 1, calum@astro.gla.ac.uk, 3 Jul 2006
;   IDL version:
;
;-----------------------------------------------
; supporting functions section
;-----------------------------------------------
function comp_spec, x, gamma,  e_o
;
; The emission has been integrated over mu
;
; this is for a mu=0, gamma=4
;
;gamma=4
;mu=0
;e_o=30.0; keV
;
return, (1/(2*!PI*e_o))*(gamma-1)*((x/e_o)^(-gamma))
;
END
;
```

```
pro aniso_ang_correct_norm, anisotropy, spec_idx, ang

data_path='./compton_data'
results_path='results/normalised_angular'
;greens_file='green_compton_mu0'

if not keyword_set(anisotropy) then begin
print, 'Defaulting Anisotropic Coefficient to 1';
anisotropy=1.0;
endif;

if not keyword_set(spec_idx) then begin
print, 'Defaulting Gamma to 2.0';
anisotropy=1.0;
endif;

if ang mod 5 ne 0 then begin
print, 'Angle must be a multiple of 5';
return;
endif else begin
  if ang eq 5 then begin
    greens_file='green_compton_mu0'+'05'+'.dat'
  endif else begin
    greens_file='green_compton_mu0'+strcompress(ang+0,/remove_all)+'.dat'
  endelse;
print, greens_file;
endelse;

restore, data_path +'/' + greens_file

aa=p.albedo
ee =p.edges

output_filename='anicorr.'+strn(anisotropy)+'.'+strn(spec_idx) + $
'.' + strcompress(strtrim(ang),/remove_all)
```

```
ee2=(ee-3.)^2/max(ee-3.5)+3.

e1 =(ee(0,*)+ee(1,*))/2.
de1=(ee(1,*)-ee(0,*))

; thermal
;flux=exp(-e1/2.)+1./e1^(5)
;simple power law
;flux=1./e1^(spec_idx)

flux=fltarr(n_elements(e1))

eps_o=30.0 ; keV
for i=0,n_elements(e1)-1 do begin
   flux(i)=comp_spec( e1(i), spec_idx,  eps_o )
endfor

; normalise the flux
; pre multiply the upwards primary flux by
; (1-anisotropy)
flux=(1-anisotropy)*flux

;pout_flux=rd_tfile('mc_g2.isotropic.dat',2,/auto,/convert)

;flux=pout_comp_spec(e1)
a1=fltarr(n_elements(aa(*,0)))

; anisotropy constant here
a1=(aa##(anisotropy*flux*e1))/e1

;stop

Set_plot, 'PS'
Device, filename=output_filename+'.ps', xsize=17,ysize=24,$
xoffset=2,yoffset=2,ENCAPSULATED=0
```

```
!P.multi=[0,1,2]
plot,e1,a1/flux,/xlog,yrange=[0,1],PSYM=3, xtitle='energy, $
kev',ytitle='Normalised Units', title='Reflection Spectrum'

plot_oo,e1,flux, xtitle='energy, kev',ytitle='Counts', $
title='Primary, Reflected, & Observed Spectrum'

oplot,e1,a1,line=1
oplot,e1,flux+a1,line=2

DEVICE, /CLOSE

SET_PLOT, 'X'

window,0
!P.Multi=[0,1,2]
plot,e1,a1/flux,/xlog,yrange=[0,1],PSYM=3, xtitle='energy, kev',$
ytitle='Normalised Units', title='Reflection Spectrum'

plot_oo,e1,flux, xtitle='energy, kev',ytitle='Counts', $
title='Primary, Reflected, & Observed Spectrum'

oplot,e1,a1,line=1
oplot,e1,flux+a1,line=2

!P.Multi=0

; write out the data to the file

openw, lun, output_filename+'.dat', /get_lun
for j=0, n_elements(e1)-1 do begin
  printf, lun, e1(j), flux(j), a1(j)
endfor
free_lun, lun

;cmd='ps2pdf output_filename+'.ps'
```

```
;spawn, cmd

cmd='mv '+ output_filename+'.ps'+' '+ results_path
print, cmd
spawn, cmd

cmd='mv '+ output_filename+'.dat'+' '+ results_path
print, cmd
spawn, cmd

print,'Completed ................................OK'
;stop

end
```

A.3 The Energy Dependent Greens Anisotropic Correction - Empirical Fit Algorithm

```
;+
; PROJECT:
;   PhD
;
; NAME:
;   var_aniso_ang_cmp_lp.pro
;
;
; PURPOSE:
;   Calculates the simple anisotropic greens reflection for a given
;   Spectral Ind & Ang
;
; CATEGORY:
;   Spectra, Modeling, inversion, regularisation
;
; CALLING SEQUENCE:
;
; CALLS:
;
; INPUTS:
;  spec_idx - spectral index
;  ang - angle of observer
;
; OPTIONAL INPUTS:
;
; OUTPUTS:
;
;
; OPTIONAL OUTPUTS:
;   none
;
; KEYWORDS:
;   none
```

```
;
; COMMON BLOCKS:
;   none
;
; SIDE EFFECTS:
;
;
; RESTRICTIONS:
; ang must be a multiple of 5 in the interval 005 <= cos(theta) <= 0.95
;
; PROCEDURE:
;
; MODIFICATION HISTORY:
;   Version 1, calum@astro.gla.ac.uk, 16 Jul 2006
;   Version 1.1, calum@astro.gla.ac.uk, 9  Aug 2006 (clean up)
;   Version 2.0, calum@astro.gla.ac.uk, 10 Aug 2006 (added integration
;                                                    into routine)
;   Version 2.1, calum@astro.gla.ac.uk, 28 Aug 2006 (clean up)
;   IDL version:
;
;-----------------------------------------------
; supporting functions section
;-----------------------------------------------

pro var_aniso_ang_cmp_lp, spec_idx, ang

; Program Initialisation

; set up the results path information
data_path='./compton_data'
results_path='results/lp_anisotropy'

if not keyword_set(spec_idx) then begin
print, 'Defaulting Gamma to 2.0';
spec_idx=2.0;
endif;
```

```
if ang mod 5 ne 0 then begin
print, 'Angle must be a multiple of 5';
return;
endif else begin
  if ang eq 5 then begin
    greens_file='green_compton_mu0'+'05'+'.dat'
  endif else begin
    greens_file='green_compton_mu0'+$
    strcompress(ang+0,/remove_all)+$
    '.dat'

  endelse;
print, greens_file;
endelse;

; this loads the greens correction matrix
; from the raw datafile into the idl data structure
restore, data_path +'/' + greens_file

; data structure assignment
aa=p.albedo
ee=p.edges ; the energy(s) are the edges of the data bins

output_filename='anicorr'+'.'+strn(spec_idx) + '.' + $
 strcompress(strtrim(ang),/remove_all)

ee2=(ee-3.)^2/max(ee-3.5)+3.
e1 =(ee(0,*)+ee(1,*))/2.
de1=(ee(1,*)-ee(0,*))

; allocate the memory for the photon spectrum
flux=findgen(n_elements(e1)) ; should be photon spectrum
flux_down=fltarr(n_elements(flux))

; the input parameters here represent a
```

```
; power law primary spectrum of spectral index spec_idx
a=[0.0, 1.0, 10000000, spec_idx, 0.0, 0.0, 0.0]
flux=spectral_model( e1, a)

for k=0, n_elements(flux)-1 $
do flux_down(k)=fractional_downwards_emission(e1(k))*flux(k)

;stop

a1=fltarr(n_elements(aa(*,0)))

a1_intrinsic=fltarr(n_elements(aa(*,0)))
; we have to create a unit matrix such that
; the matrix albebra provides a cross section of the
; correct dimension
unit_matrix = fltarr(n_elements(aa(*,0)),n_elements(aa(*,0)))

print, 'stage 2'
;stop
for i=1, n_elements(aa(*,0))-1 do begin
unit_matrix[i,i]=1.0
endfor

; create the matrices to represent the emission into the
; upward and the downward hemisphere -- eddington approximation
up_emission_matrix = fltarr(n_elements(aa(*,0)),n_elements(aa(*,0)))
down_emission_matrix = fltarr(n_elements(aa(*,0)),n_elements(aa(*,0)))

; now loop through the energies and calculate the
; directivity from leach & petrosian (83)
; this will be used in the cross section (matrix)
for i=1, n_elements(e1)-1 do begin
;       ; if eph(i) GT upper_lim then break;

; reset the emission (matrices) to be zero apart
; from the current ith value
```

```
for j=1, n_elements(aa(*,0))-1 do begin
  up_emission_matrix[j,j]=0.0
  down_emission_matrix[j,j]=0.0
endfor

; to represent our mono-energetic experiment for the ith value
; we need to ensure the correct matrix algebra - The emission matrix
; needs to be a diagonal of the nxn matrix
;up_emission_matrix[i,i]=1.0
;down_emission_matrix[i,i]=1.0
;up_emission_matrix[i,i]=0.5
;down_emission_matrix[i,i]=0.5

; Emission vectors:
;
; The upwards:downwards ratio is based upon the results of
; leach and petrosian 1983ApJ...269...713 Figure 4
; The results are only really 2 data points in photon energy - the
; directivity varies depending upon the model specified in the paper
; (9 in total).
; Assumption:
; Directivity does vary with theta (theta=0 is vertically upward).
; I have taken theta=0 and theta=180 for the "absolute" directivity
; d(theta=0)=0.1 and d(theta=180)=2.0 would give a Directivity D=20
; for 220KeV. Also D should be normalised to avoid the problem of
; adding extra photon spectra with increasing photon energy eps.
; Therefore if D=1 (isotropic) 1/2 goes into the upwards hemisphere
; (2 parts) if D=2 twice the emission is downward to upwards (3 parts)
; so 1/3 of the emission is upwards, in general D=X=> 1/(X+1) is emitted
; upwards; downwards emission is 1-upwards emission.

; commented out for poutanen comparison

; up_emission_matrix(i,i) = 1/(directivity(flux(i))+1)
; down_emission_matrix(i,i) = 1-up_emission_matrix(i,i)
```

```
;
; Changed to be consistant with poutanen
;

down_emission_matrix(i,i)=fractional_downwards_emission(e1(i))
up_emission_matrix(i,i) = 1-down_emission_matrix(i,i)

print, i,  up_emission_matrix(i,i),down_emission_matrix(i,i)

; stop


; main calculation algorithm

; the unit_matrix is added for clarity
cross_section=(aa##down_emission_matrix);+(up_emission_matrix##unit_matrix)

; anisotropy constant here for each mono energetic input/experiement energy
; but varies with energy (c.f. leach & petrosian)
; what we end with is the (greens method) resulting spectra for a series
; of mono-energetic 'experiments'. When these experiements are added
; together/integrated across the photon energy range we get the
; resulting observed spectrum a1 from the input primary spectrum containing
; the albedo 'correction'

a1=a1+(cross_section##(flux))
a1_intrinsic=a1_intrinsic+(cross_section##(flux_down))

;a1=(cross_section##(flux))
endfor

;stop

scaled=a1/flux

openw, lun, output_filename+'.dat', /get_lun
```

```
for j=0, n_elements(e1)-1 do begin
  printf, lun, e1(j), flux(j), a1(j)
endfor
close, lun, /all

openw, lun, output_filename+'.intrinsic.dat', /get_lun
for j=0, n_elements(e1)-1 do begin
  printf, lun, e1(j), flux_down(j), a1_intrinsic(j)
endfor
close, lun, /all


Set_plot, 'PS'
Device, filename=output_filename+'scaled_lp.ps', xsize=17,ysize=24,$
xoffset=2,yoffset=2,ENCAPSULATED=0

!P.multi=[0,1,2]
plot,e1,a1/flux,/xlog,yrange=[0,2],PSYM=3, xtitle='energy, kev',$
ytitle='Normalised Units', title='Reflection Spectrum'+' ('+$
output_filename+')'

plot_oo,e1,flux, xtitle='energy, kev',ytitle='Counts', $
title='Primary, Reflected, & Observed Spectrum'+' ('+$
output_filename+')'

oplot,e1,a1,line=1
oplot,e1,flux+a1,line=2

DEVICE, /CLOSE

SET_PLOT, 'X'

Set_plot, 'PS'
Device, filename=output_filename+'.albedo.ps', xsize=17,ysize=24,$
xoffset=2,yoffset=2,ENCAPSULATED=0
```

```
plot,e1,a1/flux,/xlog,yrange=[0,2],PSYM=3, xtitle='energy, kev',$
ytitle='Normalised Units', title='Reflection Spectrum'+' ('+$
output_filename+')'

DEVICE, /CLOSE

SET_PLOT, 'X'

Set_plot, 'PS'
Device, filename=output_filename+'.spectrum.ps', xsize=17,ysize=24,$
xoffset=2,yoffset=2,ENCAPSULATED=0

plot,e1,flux, xtitle='energy, kev',ytitle='Counts', $
title='Primary, Reflected, & Observed Spectrum'+' ('+output_filename+')'

oplot,e1,a1,line=1
oplot,e1,flux+a1,line=2

DEVICE, /CLOSE

SET_PLOT, 'X'

window,0
!P.Multi=[0,1,2]
plot,e1,a1/flux,/xlog,yrange=[0,2],PSYM=3, xtitle='energy, kev',$
ytitle='Normalised Units', title='Reflection Spectrum'+' ('+$
output_filename+')'

plot_oo,e1,flux, xtitle='energy, kev',ytitle='Counts', $
title='Primary, Reflected, & Observed Spectrum'+' ('+$
output_filename+')'

oplot,e1,a1,line=1
oplot,e1,flux+a1,line=2
!P.Multi=0
```

```
window,3
plot_oo,e1,flux, xtitle='energy, kev',ytitle='Counts', $
title='Primary Spectrum'+' ('+output_filename+')'

;
; move the generated files to the output directory
;
cmd='mv '+ output_filename+'*.ps'+' '+ results_path
print, cmd
spawn, cmd

cmd='mv '+ output_filename+'*.dat'+' '+ results_path
print, cmd
spawn, cmd

print, 'Calculation complete';
;stop

return

end
```

Appendix B

An Explanation for Non-Power-law Behavior in the Hard X-ray Spectrum of the July 23, 2002 Solar Flare

The following paper was published in Astrophysical Journal Letters, Issue 2 (2003 October 1).

AN EXPLANATION FOR NON–POWER-LAW BEHAVIOR IN THE HARD X-RAY SPECTRUM OF THE 2002 JULY 23 SOLAR FLARE

Eduard P. Kontar,[1] John C. Brown,[1,2] A. Gordon Emslie,[2] Richard A. Schwartz,[3]
David M. Smith,[4,5] and R. Calum Alexander[1]

Received 2003 March 17; accepted 2003 March 26; published 2003 September 8

ABSTRACT

High-resolution *Reuven Ramaty High Energy Solar Spectroscopic Imager* (*RHESSI*) data reveal that solar flare hard X-ray spectra show systematic deviations from power-law behavior. Even for injection of a power-law electron spectrum, such deviations are expected because of a number of effects, including nonuniform target ionization and solar albedo backscattering of the primary hard X-ray flux. In this Letter, we examine 1 keV resolution hard X-ray spectra for the intense 2002 July 23 event, corrected for the effects of decimation, pulse pileup, and background. We find that the observed spectra indeed deviate from a power-law behavior in a manner consistent with the effects of nonuniform target ionization. Further, this interpretation of the observed deviations requires that the amount of coronal material increases during the initial phase of the flare. The implications of this discovery for models of atmospheric response to flare heating are discussed.

Subject headings: Sun: flares — Sun: transition region — Sun: X-rays, gamma rays

1. INTRODUCTION

Solar flare hard X-ray spectra may contain non–power-law features, i.e., changes in the local power-law spectral index $\gamma(\epsilon)$ (e.g., Johns & Lin 1992; Thompson et al. 1992; Piana, Brown, & Thompson 1995). It is tempting to attribute such features to corresponding features in the accelerated electron distribution. However, there are important physical processes that produce non–power-law photon spectra even if the injected electron spectrum is a power law. Among these processes are (1) photospheric albedo (Hénoux 1975; Langer & Petrosian 1977; Bai & Ramaty 1978; Alexander & Brown 2002), which produces an enhancement in the 30–100 keV range, and (2) nonuniform ionization of the flare target (Brown 1973a; Brown et al. 1998), which produces a local spectral hardening around photon energy $\epsilon = E_*$, the minimum electron energy required to reach the near-neutral chromospheric layers of the flare (Kontar, Brown, & McArthur 2002; Brown, Emslie, & Kontar 2003). In this Letter, we present evidence for the latter feature in the *Reuven Ramaty High Energy Solar Spectroscopic Imager* (*RHESSI*) high-resolution photon spectra for the intense 2002 July 23 solar flare. We also discuss the evolution of E_* with time and the implications for models of atmospheric response to flare heating.

2. DATA REDUCTION AND ANALYSIS

The unprecedented sensitivity and spectral resolution of *RHESSI* produces very high quality count rate spectra. However, it also creates several instrumental issues (see Smith et al. 2002) that must be addressed in the deduction of the corresponding photon spectra, which we now discuss.

First, to conserve onboard memory space during the recording of large events, the count rate is "decimated," a procedure wherein only 1 out of every N counts (where N is a variable, but known, number) is actually recorded. Allowance for decimation to reproduce actual count spectra is straightforward.

Second, the onboard electronics requires a finite time ($\simeq 8 \times 10^{-7}$ s) to detect a photon event. Multiple photons that arrive at a detector within this interval are therefore recorded as a single count with an energy equal to the sum of the individual photons involved. This "pulse pileup" effect can be substantial for intense flares such as the July 23 event and must be corrected for (Smith et al. 2002). The number of events wrongly recorded because of pileup is proportional to the square of the observed count rate. This is a function of time due not only to temporal variation in the flare itself but also to modulation of the incoming flux by the rotating grids.

Use of discrete time intervals and corresponding average count rates generally leads to an underestimation of the pileup correction. To see this, divide a given time interval into n equal subintervals, with C_i counts in each subinterval. Then the average count rate for the interval is $\langle C \rangle = \Sigma\, C_i/n$ and the applied pileup correction would be $\sim\langle C \rangle^2$. However, the *correct* pileup correction is $\sim\langle C^2 \rangle$, which is always greater than $\langle C \rangle^2$ (since, because of modulation by the imaging grids, the C_i are never equal, even for a constant source with negligible statistical noise). For a given photon energy, *RHESSI*'s finer grids produce a relatively small modulation amplitude but a relatively high modulation frequency. Conversely, the coarser grids result in a high modulation amplitude (i.e., large variation in C) at a relatively low frequency. Figure 1 compares the spectra corrected for pileup with various time binnings for the detector corresponding to the coarsest grid (grid 9); significant spectral features in the energy range below 50 keV are caused by pulse pileup. The error introduced by using time-averaged pileup can be up to 20 times the statistical error in the case of the 2002 July 23 flare.

Third, the detector response in a matrix form must be used to convert count rates to photon fluxes. During periods of intense count rate, the instrument deploys additional attenuator

[1] Department of Physics and Astronomy, University of Glasgow, The Kelvin Building, Glasgow G12 8QQ, UK; eduard@astro.gla.ac.uk, john@astro.gla.ac.uk, calum@astro.gla.ac.uk.

[2] Department of Physics, The University of Alabama in Huntsville, Huntsville, AL 35899; emslieg@uah.edu.

[3] Science Systems and Applications, Inc., Laboratory for Astronomy and Solar Physics, Code 682, NASA Goddard Space Flight Center, Greenbelt, MD 20771; richard.schwartz@gsfc.nasa.gov.

[4] Space Sciences Laboratory, University of California at Berkeley, Grizzly Peak at Centennial Drive, Berkeley, CA 94720; dsmith@ssl.berkeley.edu.

[5] Now at the Department of Physics and Santa Cruz Institute for Particle Physics, University of California at Santa Cruz, 1156 High Street, Santa Cruz, CA 95064.

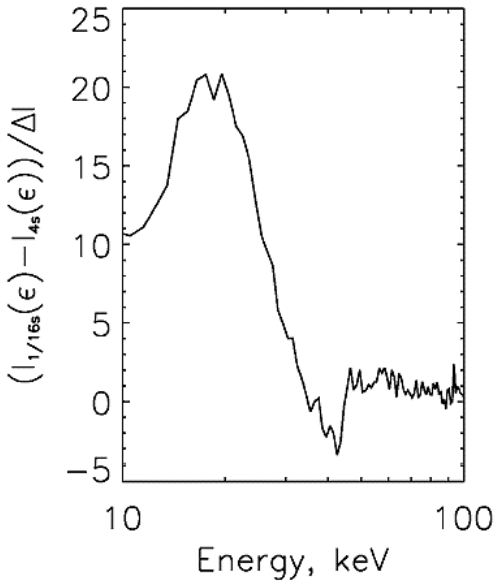

FIG. 1.—Difference (normalized to the statistical error in the data points) between the *RHESSI* detector 9 spectrum corrected for pileup with a 0.0625 s accumulation interval and that with 4 s accumulation interval, for the time interval 00:30:00–00:30:20 UT.

plates in the photon path. The response matrix (Smith et al. 2002) takes into account the presence of these attenuators, along with Compton scattering, K-shell fluorescent escape from the detector surface, attenuation in materials within the cryostat, resolution broadening, and the photoelectric effect. We are confident in our modeling of these effects, even with the full attenuation deployed, at energies above 15 keV.

Fourth, the background must in general be accurately evaluated and subtracted to obtain the true solar photon spectrum. However, for the intense July 23 event, the exact determination of the (relatively weak) background flux is not crucial to the analysis.

For our analysis we used 1 keV binned data collected over 20 s time intervals from 00:27:00 to 00:38:00 UT and corrected for decimation, pileup, detector response, and background. The spectra were summed over seven front segment detectors from detectors 1–9, excluding detectors 2 and 7 because of their limited energy resolution. The data were processed using release version 8 of the *RHESSI* software and the SPEX software available on the Solar Software Tree.

3. SPECTRAL FEATURES ASSOCIATED WITH NONUNIFORM TARGET IONIZATION

As shown by Kontar et al. (2002), a power-law electron spectrum injected from a coronal source toward a neutral chromosphere produces (for Kramers' cross section) a photon spectrum

$$I(\epsilon) = \frac{I_0}{(\lambda+1)\epsilon}\left\{\frac{\epsilon^{2-\delta}}{\delta-2} + \frac{E_*^{2-\delta}}{2\lambda} B\left[\frac{1}{1+(\epsilon/E_*)^2}, \frac{\delta}{2}-1, \frac{1}{2}\right]\right\}, \quad (1)$$

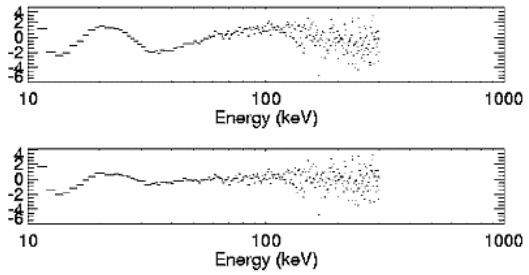

FIG. 2.—Photon spectrum residuals, normalized by the statistical error for the spectral fit, for the time interval 00:30:00–00:30:20 UT for (*top panel*) an isothermal Maxwellian plus power law and (*bottom panel*) an isothermal Maxwellian plus the nonuniform ionization spectrum given by eq. (1) with $\delta = 4.24$ and $E_* = 53$ keV.

where $\lambda = 0.55$ is a factor related to the ratio of collisional energy-loss cross sections in ionized and neutral targets, I_0 is an electron flux scale factor, δ is the spectral index of the injected electron spectrum, $B(x; a, b)$ is the incomplete beta function, and E_* (keV) $\simeq (10^{-17} N_*)^{1/2}$ is the minimum electron energy required to reach the chromospheric layers at column density N_* (cm^{-2}), where the ionization fraction of the ambient target drops sharply below unity. (We recognize that the Kramers cross section, and hence eq. [1], is only a first approximation but believe it is adequate for the present purpose, namely, a comparison of the goodness of different model fits.)

For $E_* \to 0$ or $E_* \to \infty$, $I(\epsilon)$ assumes the power-law form $I(\epsilon) \sim \epsilon^{-\gamma}$, with $\gamma = \delta - 1$. However, for $\epsilon \simeq E_*$, the spectrum (1) flattens, with a local power-law slope $\gamma < \delta - 1$ (Brown et al. 2003). We therefore seek evidence for such local spectral flattenings and the corresponding values of E_* for the photon spectra observed in the 2002 July 23 event.

Following Holman et al. (2003), we first fit the photon spectra obtained in § 2 to the sum of a thermal Maxwellian at a single temperature T plus a power law of index γ. We here limit ourselves to the issue of deviations from a power law in the "nonthermal" component of the spectrum above ~40 keV. The top panel of Figure 2 shows an example of such deviations, which represent significant deviations from the power-law fit at energies above ~40 keV. These deviations are much reduced by replacing the power law by equation (1), with the minimum rms residual obtained for values of $\delta = 4.24$ and $E_* = 53$ keV (Fig. 2, *bottom panel*). The χ^2 for the fit over the 10–300 keV range is 0.8, compared to the χ^2 for a thermal plus power-law fit of 1.4. There are still significant residuals present in the range from ~10 to 30 keV; these are most probably due to the assumption of a single-temperature thermal component. Consideration of additional thermal emission from plasma at temperatures in the range ~3–10 keV should account for these residuals (Piana et al. 2003) but will not significantly affect the spectrum at energies above ~40 keV and so the conclusions of this Letter.

4. TEMPORAL VARIATIONS OF THE FIT PARAMETERS

Allowance for nonuniform target ionization offers an elegant direct explanation for the shape of the observed hard X-ray spectrum. It also allows the values of the fit parameters kT (keV), δ, and E_* to be estimated as functions of time, as shown in Figure 3, together with the corresponding value of N_* (cm^{-2}) $\simeq 10^{17} E_*$ (keV)^2.

The thermal plasma temperature rises quickly to a value of

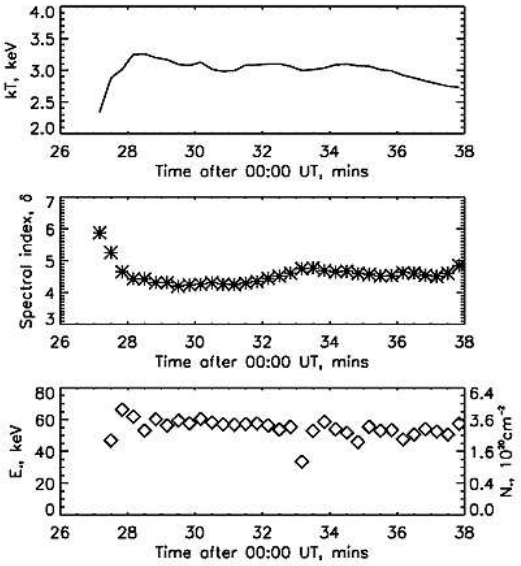

FIG. 3.—Variation of kT, δ, E_*, and N_* throughout the event. The variation of other parameters, such as emission measure, can be found in Holman et al. (2003).

≃3 keV and decreases fairly slowly thereafter. The injected electron flux spectral index δ follows a general "soft-hard-soft" trend (Fletcher & Hudson 2002) and qualitatively agrees with the time history of the simple best-fit power-law index γ (Holman et al. 2003). E_* rises quickly during the first minute or so from ~40 to ~70 keV near the flare peak and thereafter declines rather slowly. The corresponding values of N_* are $\sim 2 \times 10^{20}$ to 5×10^{20} cm^{-2}.

5. DISCUSSION AND CONCLUSIONS

The essential results of this study are that (1) for a power-law electron injection spectrum, the expression for bremsstrahlung emission from a nonuniformly ionized target is a better fit to observed spectra than the expression for a uniform target for energies above 40 keV, and (2) the value of E_* (and correspondingly N_*) varies with time.

The time for the increase in E_* to occur is of the order of a minute, much larger than the timescale to reach ionization equilibrium at the relevant number densities $n \sim 10^{12}$ cm^{-3}, yet consistent with hydrodynamic timescales (an approximate scale height/sound speed) for coronal density increase due to chromospheric evaporation in impulsive electron-heated scenarios (e.g., Mariska, Emslie, & Li 1989). For the event in question, however, this timescale is also comparable to the rise time in the injected electron flux (see light curves in Holman et al. 2003). In such cases, the atmosphere evolves through a series of quasi-static density profiles, the amount of coronal material being dependent on the instantaneous electron flux (e.g., Brown 1973c). In a closed loop, the increase in N_* creates a growing coronal overpressure that in turn causes the rate of chromospheric evaporation to drop *below* the injected electron flux profile (and so the hard X-ray intensity; Brown et al. 2000). Figure 3 shows some evidence for just such a gradual decline in E_* from 00:28 to 00:38 UT.

It is of interest to consider also the absolute values of E_* and N_* from a theoretical point of view. N_* can be roughly defined as the depth at which the hydrogen ionization fraction x falls to 0.5. While this can occur over a wide range of densities, depending on the flare model adopted, the temperature at this level is always close to $T_x \simeq 8500$ K (e.g., Brown 1973b; Machado et al. 1980). For empirical models of large flares (e.g., model F2 of Machado et al. 1980), appropriate to the 2002 July 23 event, this temperature occurs at $N_* \simeq 1 \times 10^{19}$ cm^{-2}.

This value of N_* can be compared with the value of $N_{\rm tr}$, the column density at the top of the radiatively stable chromosphere, where the temperature is equal to the peak in the optically thin radiative loss curve $f_{\rm rad}(T)$, viz., $T = T_c \simeq 60{,}000$ K (e.g., Raymond, Cox, & Smith 1976). Neglecting ambient heating and assuming ionization equilibrium (see above), the variation of temperature with depth in a beam-heated chromosphere is obtained by balancing beam heating ($\sim n \mathcal{F}_{20} N^{-\delta/2}$) and radiative cooling [$= n^2 f_{\rm rad}(T)$], where n is the local number density (cm^{-3}) and $\mathcal{F}_{20}$ is the electron energy flux (ergs cm^{-2} s^{-1} above [arbitrary] reference energy $E = 20$ keV). Hydrostatic pressure balance requires that $nT \sim N$, so that setting $f_{\rm rad} \sim T^3$ (Raymond et al. 1976), the energy balance relation becomes

$$N \sim \mathcal{F}^{(2/\delta+2)} T^{(-4/\delta+2)}. \tag{2}$$

With $\delta = 4$ (see Fig. 3), we obtain

$$\frac{N_*}{N_{\rm tr}} = \left(\frac{8500}{60{,}000}\right)^{-2/3} \simeq 3.7; \quad \frac{E_*}{E_{\rm tr}} \simeq 1.9, \tag{3}$$

where $E_{\rm tr}$ is the energy required to reach depth $N_{\rm tr}$. The absolute value of $N_{\rm tr}$ is obtained by setting $T = T_c$ in equation (2) and applying the scale factor from equation (7) of Doyle et al. (1985, correcting errors in Brown 1973c). For $\delta = 4$ this gives

$$N_{\rm tr} = 3.3 \times 10^{18} T_1^{1/3} \left(\frac{\mathcal{F}_{20}}{10^{11}}\right)^{1/3}. \tag{4}$$

The quantity T_1 appears in the above through the hydrostatic relation between the gas pressure $2nkT_1$ and the overlying column weight $\simeq N_{\rm tr} m_{\rm H} g$ (where k is Boltzmann's constant, $m_{\rm H}$ the hydrogen mass, and g the solar gravity); its value depends on whether the flare-heated matter has yet expanded to a new hydrostatic state. There are two extreme cases. In the first, considered by Doyle et al. (1985), the heating is so impulsive that T_1 reflects the temperature (and so the scale height) of the preheated chromosphere, viz., $T_1 \simeq 5000$ K. In the other extreme (Brown 1973c), the heating is considered quasi-steady, so that the chromosphere maintains a hydrostatic (open-top) loop equilibrium. In this case, the appropriate value of T_1 is $T_1 = T_c = \simeq 60{,}000$ K. The gradual rise in hard X-ray flux for the 2002 July 23 event implies that the latter case is more appropriate, so that

$$N_{\rm tr} = 1.3 \times 10^{20} \left(\frac{\mathcal{F}_{20}}{10^{11}}\right)^{1/3}, \quad E_{\rm tr}\,({\rm keV}) = 32 \left(\frac{\mathcal{F}_{20}}{10^{11}}\right)^{1/6}. \tag{5}$$

By equation (3), the corresponding values of N_* and E_* are

$$N_* = 4.9 \times 10^{20} \left(\frac{\mathcal{F}_{20}}{10^{11}}\right)^{1/3}, \quad E_*\,({\rm keV}) = 62 \left(\frac{\mathcal{F}_{20}}{10^{11}}\right)^{1/6} \tag{6}$$

or somewhat lower if allowance is made for the effects of overpressure in a closed flux tube (Brown et al. 2000).

Note that these are relatively weak scalings with $\mathcal{F}_{20}$. Even for an order of magnitude increase in $\mathcal{F}_{20}$ over the main phase of the flare (see Holman et al. 2003), E_* increases by only a factor of $10^{1/6} \simeq 1.5$. The value of E_* in equation (6) agrees with the values in Figure 3 for $\mathcal{F}_{20} \simeq 10^{11}$ ergs cm^{-2} s^{-1}.

Holman et al. (2003) estimate, from the spatially integrated hard X-ray flux, that the peak injected power $P_{20} \simeq 10^{29}$ ergs s^{-1}; a beam energy flux $\mathcal{F}_{20} \simeq 10^{11}$ ergs cm^{-2} s^{-1} thus corresponds to a beam area $\simeq 10^{18}$ cm^2. This is comparable to the footpoint area found through hard X-ray imaging for this event (Emslie et al. 2003).

In addition to the correction for target ionization structure, the hard X-ray spectrum is modified by the photospheric albedo contribution, mainly in the 30–60 keV energy range and serendipitously in the same range as the values of E_* found above. Using the Bai & Ramaty (1978) results, we have found (R. C. Alexander et al. 2003, in preparation) that adding albedo corrections alone to a pure power-law spectrum reduces the χ^2 of the fit from 1.4 to 0.8, while combining the albedo and nonuniform target ionization factors reduces it somewhat further (to 0.6). We conclude that the data are consistent with the presence of *both* effects, although a detailed comparison will require more work on albedo modeling, taking into account the effect of flare heliocentric distance and relaxing some of the more restrictive model assumptions used to date (e.g., Bai & Ramaty 1978), such as the geometry of the primary hard X-ray source and the angular distribution of the primary photon distribution.

As a final remark, our analysis here has been based entirely on a power-law electron injection spectrum. However, even for other injected spectral forms, the effect of ionization structure would introduce comparable features in the photon spectrum at energies $\simeq E_*$. In other words, incorporation of nonuniform ionization structure is clearly a key factor to be considered in the reconstruction of *any* observed photon spectrum due to a thick target beam.

This work was supported by NASA's Office of Space Science through grant NAG5-98033 and by a Particle Physics and Astronomy Research Council *RHESSI* Mission Grant.

REFERENCES

Alexander, R. C., & Brown, J. C. 2002, Sol. Phys., 210, 407
Bai, T., & Ramaty, R. 1978, ApJ, 219, 705
Brown, J. C. 1973a, Sol. Phys., 28, 151
———. 1973b, Sol. Phys., 29, 421
———. 1973c, Sol. Phys., 31, 143
Brown, J. C., Emslie, A. G., & Kontar, E. P. 2003, ApJ, 595, L115
Brown, J. C., Krucker, S., Güdel, M., & Benz, A. O. 2000, A&A, 359, 1185
Brown, J. C., McArthur, G. K., Barrett, R. K., McIntosh, S. W., & Emslie, A. G. 1998, Sol. Phys., 179, 379
Doyle, J. G., Byrne, P. B., Dennis, B. R., Emslie, A. G., Poland, A. I., & Simnett, G. M. 1985, Sol. Phys., 98, 141
Emslie, A. G., Kontar, E. P., Krucker, S., & Lin, R. P. 2003, ApJ, 595, L107
Fletcher, L., & Hudson, H. S. 2002, Sol. Phys., 210, 307
Hénoux, J.-C. 1975, Sol. Phys., 42, 219
Holman, G. D., Sui, L., Schwartz, R. A., & Emslie, A. G. 2003, ApJ, 595, L97
Johns, C., & Lin, R. P. 1992, Sol. Phys., 137, 121
Kontar, E. P., Brown, J. C., & McArthur, G. K. 2002, Sol. Phys., 210, 419
Langer, S. H., & Petrosian, V. 1977, ApJ, 215, 666
Machado, M. E., Avrett, E. H., Vernazza, J. E., & Noyes, R. W. 1980, ApJ, 242, 336
Mariska, J. T., Emslie, A. G., & Li, P. 1989, ApJ, 341, 1067
Piana, M., Brown, J. C., & Thompson, A. M. 1995, Sol. Phys., 156, 315
Piana, M., Massone, A. M., Kontar, E. P., Emslie, A. G., Brown, J. C., & Schwartz, R. A. 2003, ApJ, 595, L127
Raymond, J. C., Cox, D. P., & Smith, B. W. 1976, ApJ, 204, 290
Smith, D. M., et al. 2002, Sol. Phys., 210, 33
Thompson, A. M., Brown, J. C., Craig, I. J. D., & Fulber, C. 1992, A&A, 265, 278

Appendix C

Full Radiative Transfer, Greens Function, Solution

C.1 Original, Isotropic Algorithm

```
      program reflection
      IMPLICIT REAL*8(A-H,O-Z)
      parameter(nr=400,nco=2,kko=nco*nr,nrefl=2)
      PARAMETER(MAXFRE=71,MAXANG=3,MAXSC=25)
      PARAMETER(II=MAXFRE,NC=MAXANG,ND=1,KK=II*NC,LL=ND*KK)
      PARAMETER(NEX=II+II*(II-1)/2,NCX=NC+NC*(NC-1)/2)
      COMMON/QQCM2/A(II),UANG(NC),AANG(NC),AC(LL),AINT(LL),CINT(LL)
      COMMON/WFRE/XX(II),XLOG(II),XKEV(II),EXXY(NEX),S0(II)
      real*8 direct_out(kko),compsp(kk),xr(nr),frefl(kko),angout(nco)
      real*8 aout(nco)
C    reflected spectrum (scaled)
      real*8 frefl_2
C
      real*4 par_refl(nrefl)
C     placeholder for processing command line arguments
      CHARACTER*40 argument
      INTEGER*4 option
c     debug switch
      INTEGER*4 debug
C     end of command line processing
      ioniz=0
      irefl=0
```

```
c     count the number of arguements passed from the command line
      n=iargc()


      if(n.ne.1) then
         write(*,*) 'Invalid number of Arguments'
         write(*,*) 'Usage: <program_name> <option>.'
         write(*,*) 'Exiting...'
         return
      endif

C     use a test routine to check the comand line
      do i=1,n
         call getarg(i,argument)
C         print *, argument
         READ(UNIT=argument, FMT='(I5)') OPTION
C         print *, option
      end do

      if(option.lt.1) then
         write(*,*) 'Invalid Option'
         write(*,*) 'Usage: <program_name> <option>.'
         write(*,*) 'Exiting...'
         return
      endif

      if(option.gt.3) then
         write(*,*) 'Invalid Option'
         write(*,*) 'Usage: <program_name> <option>.'
         write(*,*) 'Exiting...'
         return
      endif

c compute angular nodes (cos of angles) and weight
c (Gaussian quadrature)
```

```
      CALL QDRGSDO(UANG,AANG,NC)
      DO 20 L=1,NC
         UANG(L)=0.5D0*(1D0+UANG(L))
         AANG(L)=AANG(L)*5D-1
c         write(*,*) UANG(L)
c         write(*,*) AANG(L)
         write(*,*) 'UANG:', acos(UANG(L))*360/(2*3.14)
         write(*,*) 'AANG:', acos(AANG(L))*360/(2*3.14)
   20 CONTINUE

      read * , debug
c       return

c (cosine of) angles where reflected spectrum is computed
c (here we also use the Gaussian quadrature, but one can use
c  anything you like)
c      CALL QDRGSDO(ANGOUT,AOUT,NCO)
      DO 30 L=0,NCO-1
         ANGOUT(L)=cos((180.0*L/(NCO-1))*(3.1415926536/180))
 AOUT=1/(NCO-1)
c  write(*,*) 'Refl ang:', 180.0*L/(NCO-1), ANGOUT(L)
   30 CONTINUE

      L=0
      ANGOUT(L)=cos(0.0)*(3.1415926536/180)
      L=1
      ANGOUT(L)=cos(180.0)*(3.1415926536/180)

      read *, debug

c      CALL QDRGSDO(ANGOUT,AOUT,NCO)
c      DO 30 L=0,NCO-1
c         ANGOUT(L)=0.95
c  AOUT=1/(NCO-1)
c  write(*,*) 180.0*L/(NCO-1), ANGOUT(L)
c   30 CONTINUE
```

```
c      return


c      DO 50 text=0,NCO-1
c  write(*,*) acos(angout(text))*(180/3.1415926536)
c   50 CONTINUE

c      return


c photon energies (in units of m_e c**2) where reflected spectrum
c is computed
      do i=1,nr
c      x=10**(-1d0+.05d0*i)
      x=10**(-3d0+.012d0*i)
      xr(i)=x
      enddo
c*****************************************************************
c INPUT PARAMETERS
c FOR  THE DIRECT RADIATION
c spectral energy index of the direct radiation
c for thermal bremsstrahlung alpha=0d0
c for typical spectra from black holes in Seyferts alpha=-1d0
      alpha=0d0

c cutoff energy in m_e c**2
c for solar flares ecut is ~ 100 keV, i.e. =0.2
c for black holes in Seyferts ecut ~ 100 keV, i.e. =0.2
       ecut= 0.2d0
c        ecut= 2.0d0
C        ecut= 20000.0d0
c*****************************************************************

c IMPORTANT! - THIS IS THE DIRECT RADIATION
c total escaping flux in a given direction
```

```
c of the direct radiation
c here: for isotropic source
      do i=1,nr
        x=xr(i)
        do j=1,nco
        k=j+(i-1)*nco
C        direct_out(k)=x**alpha*dexp(-x/ecut)
C        direct_out(k)=x**(-4.0)
c generally this can be a function of angles and energy
C        direct_out(k)=direct_ang(x,angout(j))
C call the external wrapper function for calculate for the
c desired model
direct_out(k)=spectral_model(x,angout(j),option)
c write(*,*) x, direct_out(k)
       enddo
c write(*,*) x, direct_out(k)
      enddo


c THIS HAS TO BE MODIFIED TO INCLUDE THE ANISOTROPIC RADIATION
c EMITTED IN THE DOWNWARDS HEMISPHERE
      open(26,file='output.reflected.debug.dat')
c      write(26,1000) (angout(j),j=1,nco)
c incoming photon spectrum
c specific intensity of radiation
c as a function of photon energy and angles
c
c watch out for the resolution of the floats 1e-8
c
      do i=1,ii
c photon energies in mc**2
      x=10**(-5.d0+.10d0*i)
      xx(i)=x
      xlog(i)=dlog10(x)
      do j=1,nc
      k=j+(i-1)*nc
```

```
c this is the log of the values not the values themselves
c      compsp(k)=x**alpha/UANG(j)*dexp(-x/ecut)
c      compsp(k)=x**alpha/UANG(j)*dexp(-x/ecut)*angout(j)/UANG(j)
c generally this is a function of angles and energy
c     compsp(k)=direct(x,-UANG(j)) /UANG(j)
c      compsp(k)=spectral_model(x,angout(j)/UANG(j),option)*dexp(-x/ecut)
C      compsp(k)=log10(100000000*spectral_model(x,UANG(j),option))

c
c We have to premultiply the spectral model values by a constant
c to avoid infinities in log space
      compsp(k)=dlog10(10000*spectral_model(x,UANG(j),option))
c      compsp(k)=compsp(k)-4
      compsp(k)=compsp(k)*dexp(-x/ecut)
      write(*,*) x, compsp(k), i, j,
      spectral_model(x,UANG(j),option), uang(j)
c factor 1/UANG(j) appears because we need here specific intensity
c minus sign in the argument, because the radiation is going down

      write(26,1030) xx(i),compsp(k), spectral_model(x,UANG(j),option)

      enddo
      enddo

      close(26)

c log of Fe abundance
      par_refl(1)=0.
c log of "metal" abundance
      par_refl(2)=0.


C*****************************************************
C PRINTING RESULTS OF CALCULATIONS
C*****************************************************
```

```
      open(20,file='output.angles.dat')
      open(22,file='output.direct.dat')
      open(24,file='output.reflected.dat')

      call PNSrefl(compsp,xr,frefl,angout,
     + par_refl,nrefl,nr,kko,nco,ioniz,irefl)
c print outgoing angles
C      write(*,*) nco
      write(20,1000) (angout(j),j=1,nco)
c      write(20,1010)
      write(22,1000) (angout(j),j=1,nco)
c print direct radiation intensity going to the observer
      do i=1,nr
      write(22,1030) xr(i),(direct_out(J+(I-1)*NCO),J=1,nco)
c      write(22,1030) xr(i),(compsp(J+(I-1)*NCO),J=1,nco)
      enddo
c print reflected  radiation FLUX going to the observer
c      write(20,1020)
      write(24,1000) (angout(j),j=1,nco)
      do i=1,nr
      frefl_2=frefl(J+(I-1)*NCO)/4
c      write(24,1030) xr(i),(frefl(J+(I-1)*NCO)*angout(j),J=1,nco)
      write(24,1030) xr(i),(frefl_2*abs(angout(j)),J=1,nco)
      enddo

      close(20)
      close(22)
      close(24)

C end of printing
C the number of arrays write to the file is determined here
C*****************************************************
      stop
 1000 format(' cos of outgoing angles',/ 40d13.5)
 1010 format('   energy          flux of direct radiation')
 1020 format('   energy          flux of reflected radiation')
```

```
 1030 format( 40d13.5)
      end
```

C.2 External C Library - Empirical Fit

The following C code is the external library used in Section 5.5 of Chapter 5.

```
/*
   R.C. Alexander (PhD.) 01.11.2006
   Ammeded after Alec M discussion 11.09.2007
   Ammeded after debugging 01.12.2007

   Externally called poutanen function:

   This will calculate I(eps,mu) for a given functional form
   to allow comparison with the Greens approach.


*/
/* external rountine called from fortran */
#include <math.h>
#include <stdio.h>
#include <stdlib.h>
#include "ext_proc.h"

static const double eps_o=30.0;  // (keV)
static const double emass=511.0; // (m_e c^{2} in keV)
// (introduced due to low photon counts)
static const double photoncount=1.0;

static float a=0.0,b=1.0; // 0.0 < mu <= 1.0

static double A_const=1.0;

/* these are need for the integration routine parameter passing */
```

```
double g_gamma=3.0,g_eps=1.0;
int g_nth_order=0;

/*
 * These are the declaration of the parameter
 * interpolation functions.
 */
double a_param(double eps);

double b_param(double eps);

double eta_param(double eps);

/*
 * function forward declarations
 */
double PrimaryIntensity(double *eps,
double *theta,
double *gamma,
int nth_order);

double Normalise(double *eps,
 double *theta,
 double *gamma,
 int nth_order);


// new part

// should really use a macro
// but I want to see it work in the debugger
inline float mu(float theta) {

  //  return cos(theta);
  return theta;
```

```
}

/*++

The functional form of Intensity:

Refer to Ph.D. thesis, chapter 5

--*/

double PrimaryIntensity(double *eps,
double *theta,
double *gamma,
int    nth_order)
{

  double v_rtn=0.0;
  float  v_temp=0.0;
  double v_theta;

  A_const=(photoncount/(2*M_PI*(eps_o/emass)));

  //#ifdef __DEBUG_
  fprintf(stdout, "eps:%lf\ttheta:%lf\tgamma:%lf\tnth_order:%d",
                    *eps,*theta,*gamma, nth_order);
  //#endif

  g_eps=(*eps)*emass; // convert to Mec^2
  g_gamma=*gamma;
  g_nth_order=nth_order;

  v_theta=*theta;

    /* Important
     * Angular, energy dependant function
     * using the empirical fit to Leach and Petrosian
```

```
     * data
     */

  v_temp=A_const* \
    pow((g_eps/eps_o),-(g_gamma))* \
    pow((a_param(g_eps/eps_o)+ \
    b_param(g_eps/eps_o)*v_theta),eta_param(g_eps/eps_o));

  fprintf(stdout," return from func %f for %f (%f) \n",
            v_temp,(g_eps),(g_eps/(eps_o+g_eps)));

  v_temp*=*eps;

#ifdef __DEBUG_
  fprintf(stdout,"return from func %f for %f \n",v_temp,(*eps));
#endif
  v_rtn=(double)v_temp;

  //v_rtn*=*eps;

#ifdef __DEBUG_
  fprintf(stdout, "\t%f\n",v_rtn);
#endif

  return v_rtn;
}

/*++

The functional form of Intensity:

Refer to Ph.D. thesis, chapter 5

--*/

double Normalise(double *eps,
```

```
 double *theta,
 double *gamma,
 int    nth_order)
{

  double v_rtn=0.0;

  float v_temp=0.0;

  A_const=(photoncount/(2*M_PI*(eps_o/emass)));

#ifdef __DEBUG_
  fprintf(stdout, "eps:%lf\ttheta:%lf\tgamma:%lf\tnth_order:%d",
        *eps,*theta,*gamma, nth_order);
#endif

  g_eps=(*eps)*emass; // convert to Mec^2
  g_gamma=*gamma;
  g_nth_order=nth_order;
  g_nth_order=0.0;


  v_temp=((g_nth_order)+1)*A_const*(g_gamma-1)* \
    pow((g_eps/eps_o),-(g_gamma))* \
    pow(2,(((g_eps/(eps_o+g_eps))*g_nth_order)+1))/ \
    ((((g_eps/(eps_o+g_eps))*g_nth_order)+1));

#ifdef __DEBUG_
  fprintf(stdout, "Normalise \t%f\n",v_temp);
#endif

  v_temp*=*eps;
  v_rtn=v_temp;

#ifdef __DEBUG_
  fprintf(stdout, "Normalise \t%lf\n",v_rtn);
```

```
#endif

  return v_rtn;
}

/*++

This function is a wrapper for the spectal model function simply to
provide a consistant interface for the fortran module and to allow the
spectral mode to be changed undernith.

--*/

/*
underscore is for fortran compatibility
use __NOUNDERSCORE__ of the compiler allow it
*/
double spectral_model__(double *eps,
double *theta,
double *gamma,
double *nth_order)
{
  double v_rtn=0;

  int v_nth_order=(int)(*nth_order);

  fprintf(stdout,"nth_order %d\n",v_nth_order);

  v_rtn=PrimaryIntensity(eps,
theta,
gamma,
v_nth_order);

#ifdef __DEBUG_
  fprintf(stdout,"Spectral Model Return:\t%d\n", v_rtn);
#endif
```

```
  return v_rtn;
}

/*
underscore is for fortran compatibility
use __NOUNDERSCORE__ of the compiler allow it
*/
double spectral_normalisation__(double *eps,
double *theta,
double *gamma,
double *nth_order)
{
  double v_rtn=0;

  int v_nth_order=(int)*nth_order;

  v_rtn=Normalise(eps,
  theta,
  gamma,
  v_nth_order);

#ifdef _DEBUG_
  fprintf(stdout,"PrimaryIntensity Return:\t%f\t%f\n",
  (*eps)*511.0, v_rtn);
#endif

  return v_rtn;
}


/*
 * Empirical fit parameter function for a supplied
 * energy (Chapter 5, thesis)
 */
```

```
double a_param(double eps) {
  return (double) ((-0.1*eps)/188) + 0.912;
}

double b_param(double eps) {
  return (double) ((-0.3*eps)/188) -0.165;
}

double eta_param(double eps) {
  return (double) 1.95;
}



/*
 * Leach and Petrosian model fits
 * & eddington approximation functionality
 *
 */
double directivity(double eps)
{
  return (double) 0.78+((19.0*(eps))/188.0);
}

double fraction_up__(double* eps) {

  double alpha=(1/(directivity(*eps)+1));

  return alpha;
}

double fraction_down__(double* eps)
{

  double alpha=1-(1/(directivity(*eps)+1));

  return alpha;
```

```
}


/*
underscore is for fortran and C compatibility
use __NOUNDERSCORE__ if the compiler allow it
*/

double str2num_dbl__(char *numnchr)
{
  double v_rtn;

  v_rtn = (double)strtod(numnchr,NULL);

#ifdef _DEBUG_
  fprintf(stdout,"Return:\t%lf\n", v_rtn);
#endif

  return v_rtn;
}

float str2num_flt__(char *numnchr)
{
  double v_rtn;

  v_rtn = strtod(numnchr,NULL);

#ifdef _DEBUG_
  fprintf(stdout,"Return:\t%lf\n", v_rtn);
#endif

  return (float)v_rtn;
}

float str2num_int__(char *numnchr)
{
```

```
  int v_rtn;

  v_rtn = atoi(numnchr);

#ifdef _DEBUG_
  fprintf(stdout,"Return:\t%d\n", v_rtn);
#endif

  return v_rtn;
}

inline double fround(double n, unsigned int d)
{
  return floor(n*pow(10.,d)+0.5 )/pow(10.,d);
}

void form_ext__(double *gamma, double *nth_order, double *angle, char* ext)
{
  int v_order=(int)*nth_order, v_angle=(int)(fround((*angle)*100,0));

  //  fprintf(stdout,"%lf\n",*gamma);

  sprintf(ext,"g%1.0lfn%dmu0%d",*gamma, v_order,v_angle);

  return;
}

/*
 * Driver routine: only used to test the external functions
 *
 */

#ifdef _DEBUG_DRIVER_

/*
  This is purely for debugging the integration routines (22.11.2006)
```

```
*/

int main(int argc, char** argv)
{
  int idx=0;
  double v_total=0.0;

  double eps=1.0, *p_eps=&eps;
  double theta=0.0, *p_theta=&theta;
  double gamma=3.0, *p_gamma=&gamma;

  int nth_order=2, *p_nth_order=&nth_order;

  /*
  for(idx=0;idx<360;idx++)
    {
      fprintf(stdout,"%d\t%lf\t%lf\t%lf\t%lf\n",idx
      , AngularCmpt(idx,2)
      , AngularCmpt(idx,3)
      , AngularCmpt(idx,4)
      , AngularCmpt(idx,5)
      );
    }
  */

  theta=0.0;
  nth_order=2;

  for(eps=1.0;eps<511;eps++)
    {

      fprintf(stdout,"%lf\t", *p_eps);

      for(theta=0.0;theta<180.0;theta+=60)
{
  for(nth_order=2;nth_order<8;nth_order+=2)
```

```
    {

      fprintf(stdout,"%lf\t", PrimaryIntensity(p_eps,
       p_theta,
       p_gamma,
       p_nth_order));
    }
}

      fprintf(stdout,"\n", *p_eps);

    }

  return 0;
}

#endif
```

Appendix D

A Least Squares Empirical Fit

D.1 The Algorithm

```
;
; Fitting Routine
;
pro gfunct, x, a, f, pder       ; Function + partials
  bx = exp(a(1) * x)
  f=(a[0]+a[1]*cos((!PI/180)*x))^a(2)           ;Evaluate the function
  IF N_PARAMS() ge 4 THEN $     ;Return partials?
     pder= [[bx], [a(0) * x * bx], [replicate(1.0, N_ELEMENTS(f))]]
end

;
; Driver Routine
;
pro main

i=0.0
i_min=0.0
i_max=1.0
i_iter=0.05

j=0.0
j_min=0.0
j_max=1.0
```

```
j_iter=0.05

k=0.0
k_min=-2.0
k_max=2.0
k_iter=0.05

x=[0,30,60,90,120,150,180]                    ;Define indep & dep variables.
y=[0.5,0.55,0.6,0.8,1.1,1.15,1.2]; 22keV data
;y=[0.095,0.12,0.3,0.55,1.15,1.5,1.6]; 210keV data
Weights=0.25/y                    ;Weights

openw,lun,'chi_results.dat',/get_lun, width=300

a=[0.25,-0.9,0.3]                ;Initial guess
yfit=curvefit(x,y,Weights,a,sigma,function_name='gfunct',ITER=100)

printf, lun, ''
printf, lun, 'Function parameters: ',a,yfit
printf, lun, '', i

i=i_min;
j=j_min;
k=k_min;

while i lt i_max do begin
   while j lt j_max do begin
      while k lt k_max do begin

         a[0]=i
         a[1]=j
         a[2]=k

         yfit=curvefit(x,y,Weights,a,sigma,function_name='gfunct',ITER=100)

         if total(abs(y-yfit)) lt 0.3 then begin
```

```
            printf, lun, ''
            printf, lun, 'Function parameters: ',a,yfit
            printf, lun, y
            printf, lun, y-yfit
            printf, lun, 'Fit',total(abs(y-yfit))

            printf, lun, 'GOOD FIT'
         end

         k=k+k_iter
      endwhile
      j=j+j_iter
      k=k_min
   endwhile
   i=i+i_iter
   j=j_min                      ;
endwhile

close, /all

end
```

Appendix E

The Fit2d Routine

The fit2d listing has been formatted for printing. The symbol $ denotes where a line has been split to allow the line to fit on the page.

```
function fbar, x,a

  IF a[0] LT 0. THEN a[0] =0.

;a[5]=a[3]
;IF (a[5] LT -1.) THEN a[5]=-1.

 ; fbar1=a[0]*exp(-x/a[1])/sqrt(a[1])+((x LT a[4]) AND $
 (x GT 3.))*a[2]*(a[4]/x)^a[3]+(x GE a[4])*a[2]*(a[4]/x)^a[5]

fbar1=(x GT 10.)*a[0]*(50./x)^a[1]
;fbar2=(x GT 10.)*a[2]*(50./x)^a[3]

;fbar1=a[0]*exp(-x/a[1])/sqrt(a[1])+(x GT 10.)*a[2]*(50./x)^a[3]

;EB=50.
;Fbar1=a[0]*exp(-x/a[1])/sqrt(a[1])+ $
(x LT a[4])*a[2]*(a[4]/x)^a[3]+(x GE a[4])*a[2]*(a[4]/x)^a[5]
;Fbar2=a[0]*exp(-x/a[1])/sqrt(a[1])+ $
(x LT a[8])*a[6]*(a[8]/x)^a[7]+(x GE a[8])*a[6]*(a[8]/x)^a[9]

  fbar2=fbar1
```

```
;Fbar=[(2.-1.97*exp(-sqrt(x/100.)))*a[2]*Fbar1,Fbar2]
;fbar=a[0]*(50./x)^a[1]

;fbar=fbar*x

  Fbar=[Fbar1,Fbar2]
  return, fbar

end


PRO fit_function, X, A, F
;thermal + powerlaw
  COMMON SHARE1,CrossSection,ee_long,const,drm,de,matrix,bg,Msun,Mup

;f0=fltarr(n_elements(ee_long))
;for i=0, n_elements(ee_long)-1 do f0(i)=fbar(ee_long(i),a)
  f0=fbar(ee_long,a)
;f1=(CrossSection##(f0*de))
;f=drm#transpose(f1)

;f=MATRIX#(f0*[de,de])
  f=transpose(MATRIX##f0)
;f=(Mup+4.*Msun)#(f0*de)+bg
;*******************************************************

END

pro fit2d, ph_fname

  COMMON SHARE1,cs_long,ee,R2pi4,drm,de,matrix,bg,Msun,Mup

;inversion using SVD method + regularisation
;method by Piana, 1994

  z=1.2                         ;z- Mean atomic number of the target plasma.
```

```
  R=1.496e+13                    ; 1AU distance in cm

  R2pi4=((4.*!PI*R^2)/1e+28)
  EE_max=400

; upper limit for electrons
; SIMULATION OF MAX ENERGY

; we need to get the edges data from the cross section
  ;restore, 'brm_cross_poutanen_ee.3.00000.95.0.00000.dat'
  restore, 'ang_brm_cross.dat'
; we want to import the observed photon spectrum file here
; not a spex file
;  ph_spectr_file='data/Poutanen/Poutanen.g4n6mu095.data.rhessi_data'

; poutanen
;  ph_spectr_file=$
;'thesis_work/poutanen/anisotropic/empirical/empirical_results/'+ ph_fname

; poutanen isotropic check
  ph_spectr_file='thesis_work/poutanen/isotropic_check/isotropic/'+ ph_fname

; eddington
;   ph_spectr_file=$
;'thesis_work/forward_greens_conv/results/lp_anisotropy_working/'+ ph_fname

; eddington isotropic check
;   ph_spectr_file=$
;'thesis_work/forward_greens_conv/results/lp_isotropic_check/'+ ph_fname

  ph_data=rd_tfile(ph_spectr_file, 5, /auto, /convert)

; we need 100 datapoints

  tweak=0.01
```

```
;  restore, ph_spectr_file
;  stop
;  bg=fltarr(n_elements(eps_data))

  eps=fltarr(2,n_elements(ph_data[0,*]))
  eps[0,*]=ph_data[0,*]
  eps[1,*]=ph_data[1,*]

;  obsi=ph_data[2,*]

; primary spectrum
;  obsi=ph_data[3,*]*10000*(1+ph_data[4,*])

; observed spectrum
  obsi=ph_data[3,*]*10000*(1+ph_data[4,*])
  eobsi=fltarr(n_elements(ph_data[0,*]))

  ebacki=fltarr(n_elements(ph_data[0,*]))

  print, 'Photon file loaded.'

;  stop



  set_plot, 'PS'
  device, filename=ph_spectr_file+$
  '.test.ps', xsize=24,ysize=17,xoffset=2,yoffset=2,ENCAPSULATED=0

  plot, eps[0,*]+eps[1,*]/2, obsi, /xlog, /ylog, title=ph_fname

  device, /close
  set_plot, 'X'

; return
```

```
;  stop

  backi=fltarr(n_elements(ph_data[0,*]))
  for i=0,n_elements(backi)-1 do backi[i]=0.0

  bg=backi

;  stop

  counts =obsi-bg
  ecounts=sqrt((eobsi)^2+(ebacki)^2)
  ecounts=(ecounts LT counts*tweak)*counts*tweak+$
  (ecounts GT counts*tweak)*ecounts
  e_in=p.e_in

  ecounts=sqrt(obsi)

;  edges=p.edges
  edges=p.e2n

;  drm=p.drm
; the drm is just a unit matrix
  ;drm=fltarr(n_elements(ph_data[0,*]),n_elements(ph_data[0,*]))
  drm=fltarr(400,400)
;
; we dont want the rhessi drm here but will replace it with
; a square unit matrix diag(99) with the rest of the 99x109 elements 0
;

;  stop

  for i=0, n_elements(drm[*,0])-1 do begin
     ; print, i
     for j=0, n_elements(drm[0,*])-1 do begin
        drm[i,j]=0.0
     endfor
```

```
  endfor

;  stop

  for i=0, n_elements(drm[*,0])-1 do begin
    ; print, 'Unit: '+string(i)
     drm[i,i]=1.0
  endfor

;  stop

; photon_data=rd_tfile('data/mc_anicorr.3.00000.95.2.00000.dat', 3, /auto, /co
; plot, photon_data[0,*], photon_data[2,*]/photon_data[1,*], /xlog, yrange=[0,
; data_interp=interp(photon_data[1,*], photon_data[0,*], e_c)

  e_c =transpose(edges(1,*)+edges(0,*))/2.
  de_c=edges(1,*)-edges(0,*)
  ee=transpose(e_in(1,*)+e_in(0,*))/2.
  de_in=transpose(e_in(1,*)-e_in(0,*))

;  stop

;  ph_spectr_file='jcb_test.dat'


  for i=0, N_elements(drm(0,*))-1 do drm(*,i)=drm(*,i)/de_c ;(i)

  output_file =STRMID(ph_spectr_file, 0, STRPOS(ph_spectr_file, '.dat'))+$
               '_00sol.dat'
  output_file2=STRMID(ph_spectr_file, 0, STRPOS(ph_spectr_file, '.dat'))+$
               '_00log.dat'
  Foo_file=STRMID(ph_spectr_file, 0, STRPOS(ph_spectr_file, '.dat'))+$
               '_00F0.dat'
  ps_file =STRMID(ph_spectr_file, 0, STRPOS(ph_spectr_file, '.dat'))+$
               '_00sol.ps'
  ps_file_err=STRMID(ph_spectr_file, 0, STRPOS(ph_spectr_file, '.dat'))+$
```

```
                '_00err.ps'
  errors_file=STRMID(ph_spectr_file, 0, STRPOS(ph_spectr_file, '.dat'))+$
                '_00err.dat'
  ps_file_fit=STRMID(ph_spectr_file, 0, STRPOS(ph_spectr_file, '.dat'))+$
                '_00fit.ps'

;reader,starte,ende,photon,ephoton,ph_spectr_file
;reads the data from data file

;restore,'jan17F/brm_cross_logbins.dat'
;restore,'jan17F/ang_brm_cross.dat'

;restore,'brm_cross_logbins.dat'
;restore, 'brm_cross_109_597log_ee.dat'

;  restore, 'brm_cross_greens_ee.dat'
;  restore, 'brm_cross_poutanen_ee.3.00000.95.0.00000.dat'
  restore, 'ang_brm_cross.dat'
;  stop
  print, 'Cross Section'
;  stop

;e2N    =p.energy
;cs_long=total(p.cross_section(0:5,*,*),1)/$
(1.-cos(60.*!PI/180.))
;cs_long2=total(p.cross_section(10:16,*,*),1)/$
(cos(110.*!PI/180.)-cos(170.*!PI/180.))

  e2N    =p.e2N
  cross_section=p.cs
  ;cross_section=p.cs[*,1:100]

  cs_long=total(cross_section(0:5,*,*),1)/$
  (1.-cos(60.*!PI/180.))
  cs_long2=total(cross_section(10:16,*,*),1)/$
  (cos(110.*!PI/180.)-cos(170.*!PI/180.))
```

```
  ThetaH=40.
;*********************************
  ss=0.
  ss2=0.
  fi= findgen (18)*10. +5.
  betta=fi
  i_theta0=3

  for i=i_theta0,i_theta0 do begin
     for j=0, 17 do begin

        cosTheta= cos(thetaH*!PI/180.)*cos(betta(i)*!PI/180.)+$
                  sin(thetaH*!PI/180.)*sin(betta(i)*!PI/180.)*$
                  cos(fi(j)*!PI/180.)
        theta = 180.- acos(cosTheta)*180./!PI

        cosTheta1= cos(0.*!PI/180.)*cos(betta(i)*!PI/180.)+$
                    sin(0.*!PI/180.)*$
                   sin(betta(i)*!PI/180.)*cos(fi(j)*!PI/180.)
        theta1 = acos(cosTheta1)*180./!PI

        ss=ss+2.*cross_section(round((theta-2.0)/10.),*,*)/$
            (1.-cos(180.*!PI/180.))*$
           sin(betta(i)*!PI/180.)/Sin(theta*!PI/180.)

        ss2=ss2+2.*cross_section(round((theta1-2.)/10.),*,*)/$
            (1.-cos(180.*!PI/180.))*$
            sin(betta(i)*!PI/180.)/Sin(theta1*!PI/180.)

        print,theta,theta1,betta(i),fi(j),round((theta-2.0)/10.)
     end
  end

  cs40  =transpose(ss)*1e22
  cs40_2=transpose(ss2)*1e22
```

```
;  stop

  cs_long =transpose(cs_long)
  cs_long2=transpose(cs_long2)

  csi=total(cross_section(0:8,*,*),1)/(1.-cos(90.*!PI/180.))
  csi=transpose(csi)*1e22

  ee=transpose(e2N(1,*)+e2N(1,*))/2.
  de=transpose(e2N(1,*)-e2N(0,*))

;restore,'brm_cross_logbins.dat'
;cs_long_ee=p.cs

  print, 'Cross section - End processing'

;  stop


;restore,'aug20F/green_compton_mu075.dat'
;restore,'jan17F/green_compton_mu080.dat'

;restore, 'green_compton_mu070.dat'
  restore, 'compton_data/400/green_compton_mu095.dat'

  GREEN1=p.albedo
  e2green=p.edges
  Neg=n_elements(e2green)/2
  Green=fltarr(n_elements(ee),n_elements(ee))
  ggg=interpolate(green1,ee,ee,/grid)
;GREEN(0:Neg-1,0:neg-1)=ggg

;for i=0,n_elements(edges)/2-1 do Green1(i,*)=Green1(i,*)*de(i)

;  stop
```

```
  cs =cs_long*1e22              ;(0:M-1,*)
  cs2=cs_long2*1e22             ;(0:M-1,*)

;for i=0, n_elements(cs(0,*)) do cs(*,i)=cs(*,i)

;  stop

  ;drm=rebin(drm,400,400)

  for i=0, n_elements(drm[*,0])-1 do begin
     ; print, i
     for j=0, n_elements(drm[0,*])-1 do begin
        drm[i,j]=0.0
     endfor
  endfor


  for i=0, n_elements(drm[*,0])-1 do begin
    ; print, 'Unit: '+string(i)
     drm[i,i]=1.0
  endfor

;  stop

  print, 'Matrix Debug'
;  stop

  Matrix=drm#transpose(cs) ;drm is required to dimension
;Matrix=transpose(cs)

;Matrix=rebin(matrix,400,400)

; turn the matrix into two dimensional
;for i=0,n_elements(drm(0,*))-1 do Matrix(i,I) = cs(0,i)
```

```
  print, 'Matrix Debug Matrix'
;  stop


  M1 =transpose(Green1)#transpose(csi)
;  M1w=m1
;  m1=rebin(m1,400,400)

 ; m1w=fltarr(400,400)
 ; m1w=drm
 ; for i=0,n_elements(drm(0,*))-1 do m1w(i,i) = m1(i)
 ; m1 = m1w

  print, 'Matrix Debug M1'
;  stop

  M2 =transpose(cs40)       +drm#transpose(cs)

  print, 'Matrix Debug'
;  stop

;M1 =transpose(Green1)#transpose(csi)
;M2 =transpose(cs40);+drm#transpose(cs)

  Msun =drm#(transpose(Green1)#transpose(cs)+transpose(cs2))
;Msun =(transpose(Green1)#transpose(cs))+transpose(cs2)

;Msun2=drm#(transpose(Green1)#transpose(cs2))
  Mup =drm#(transpose(cs)+(transpose(Green1)#transpose(cs2)))
;Mup  =transpose(cs)+(transpose(Green1)#transpose(cs2))

;Mup2 =drm#transpose(cs2)

;  stop

;  msun1=msun
```

```
;  msun=fltarr(400,400)
;  for i=0,n_elements(msun(*,0))-1 do msun(i,i)=msun1(i)

;  mup1=mup
;  mup=fltarr(400,400)
;  for i=0,n_elements(mup(*,0))-1 do mup(i,i)=mup1(i)

;  m21=m2
;  m2=fltarr(400,400)
;  for i=0,n_elements(m2(*,0))-1 do m2(i,i)=m21(i)


;  cfit_range=where((e_c GE 10.) AND (e_c LT 501.))
;  efit_range=where((ee GE 10.)  AND (ee LT 1000.))

  cfit_range=where((e_c GE 10.) AND (e_c LT 150.))
  efit_range=where((ee GE 11.)  AND (ee LT 300.))


  Matrix =Matrix(min(cfit_range):max(cfit_range),min(efit_range):max(efit_rang
;  stop

  Msun =Msun(min(cfit_range):max(cfit_range),min(efit_range):max(efit_range))
  Mup =Mup(min(cfit_range):max(cfit_range),min(efit_range):max(efit_range))

  M1 =M1(min(cfit_range):max(cfit_range),min(efit_range):max(efit_range))
  M2 =M2(min(cfit_range):max(cfit_range),min(efit_range):max(efit_range))

;Msun2 =Msun2(min(cfit_range):max(cfit_range),min(efit_range):max(efit_range))
;Mup2 =Mup2(min(cfit_range):max(cfit_range),min(efit_range):max(efit_range))
;  stop
  counts =counts(min(cfit_range):max(cfit_range))
  ecounts=ecounts(min(cfit_range):max(cfit_range))
  e_c    =e_c(min(cfit_range):max(cfit_range))
  bg     =bg(min(cfit_range):max(cfit_range))
  de_c   =de_c(min(cfit_range):max(cfit_range))
```

```
  ee     =ee(min(efit_range):max(efit_range))
  de     =de(min(efit_range):max(efit_range))

  Matrix=[[Msun],[Mup]]
;  stop
;Matrix=[[Msun],[Msun]]

  MT    =[[M1],[M2]]
;test remove for data

  Matrix=transpose(Matrix)
  MT=transpose(MT)

  for i=0,n_elements(ee)-1 do Matrix(i,*)=Matrix(i,*)*de(i)
  for i=N_elements(ee),2*n_elements(ee)-1 do Matrix(i,*)=Matrix(i,*)*$
        de(i-N_elements(ee))

  for i=0,n_elements(ee)-1 do MT(i,*)=MT(i,*)*de(i)
  for i=N_elements(ee),2*n_elements(ee)-1 do MT(i,*)=MT(i,*)*$
        de(i-N_elements(ee))

  print,'Forward fitting  ......................'

;Apar=[1e+8,3.,100.,2.1,100.,2.]

;  Apar=[8.e+006,1.20049, 17.2163, 2., 30.438, 2.]
;  Apar=[0.0,1.20049, 17.2163, 2., 30.438, 2.]

;  Apar=[1.3,3.1]
   Apar=[650,2.2]

;  stop
;Apar=[3e+5,4.3,26.8,1.,300.,-.5]
  rat=.2*ecounts/counts
  seed = 1001L                  ;for gaussian distribution of errors
```

```
  fbar0=fbar(ee,apar)
;fbar0(N_elements(ee):2*N_elements(ee)-1)=$
        fbar0(N_elements(ee):2*N_elements(ee)-1)
;/(1.+sqrt((ee-10.)/50.))^2
  counts=MT##fbar0
  ft=fbar0
  counts=counts+(randomu(seed,N_elements(counts))-0.5D0)*4.*counts*rat
  counts=transpose(counts)
  ecounts=rat*counts
;test starts here

  plot_oo,ee,fbar0(0:N_elements(ee)-1),ytitle='Electron flux',$
    xtitle='Energy,keV',xrange=[10,1000]
  oplot,ee,fbar0(N_elements(ee):2*N_elements(ee)-1),line=2

;  stop

  openw,1,'test_data_jcb.dat'
  for i=0, n_elements(ee)-1 do printf,1,ee(i),fbar0(i),$
        fbar0(N_elements(ee)+i)
  close,1

  openw,1,'test_data_counts_jcb.dat'
  for i=0, n_elements(e_c)-1 do printf,1,e_c(i),counts(i),ecounts(i)
  close,1

  ;Apar=[1e+7,1.33,10.8,1.,1800.,1.]

;Apar=[1e+7,1.33,20.8,1.]

  ;Apar=[9e+8,1.3,4.,2.1,100.,3.2]

  ;Apar=[1.3,3.1]

  weights=1./ecounts^2
  loadct,39
```

```
  window,3
  fbar0=fbar(ee,apar)
  plot_oo,ee,fbar0(0:N_elements(ee)-1),ytitle='Fit',xtitle='Energy,keV'
  oplot,ee,fbar0(N_elements(ee):2*N_elements(ee)-1),line=2,color=200
  oplot,ee,ft,line=2,color=500

  print, 'before fitting'

;  stop

;*********************************************************

For i=0, 10 do begin
fit = CURVEFIT(e_c,counts,weights,Apar, SIGMA, $
    FUNCTION_NAME='fit_function', ITMAX=100,/noderivative)

print,'Fit parameters are :', apar
end
fbar0=fbar(ee,apar)
oplot,ee,fbar0,line=1
print,'Fit parameters are :', apar
;*********************************************************

res=(counts-fit)/ecounts
;normilised residuals

res_sum=fltarr(N_elements(e_c))
for k=0,N_elements(e_c)-1 do res_sum(k)=total(res(0:k))/(float(k)+1.)

print,'CHI2=',total(res*res)/float(n_elements(E_c)-n_elements(apar))

window,1,xsize=600,ysize=700,title='Forward fit results'
!P.MULTI=[0,1,3]

plot_oo,e_c,counts, ytitle='Count Flux',xtitle='Energy, keV',$
    xstyle=1,xrange=[min(e_c),max(e_c)]
```

```
ERRplot,e_c,counts-ecounts,counts+ecounts
oplot,e_c,fit,line=0,color=220

plot,e_c,res,/xlog,psym=10,ytitle='Normilised Residuals',$
    xtitle='Energy, keV',xstyle=1,xrange=[min(e_c),max(e_c)]
oplot,e_c,e_c/e_c,line=1
oplot,e_c,-e_c/e_c,line=1

plot,e_c,res_sum,xrange=[min(e_c),max(e_c)],$
    ytitle='Cumulative residuals',/xlog,$

xstyle=1,xtitle='Energy, keV',yrange=[-1,1],PSYM=10
oplot,e_c, 1./sqrt(e_c-min(e_c)),line=1
oplot,e_c,-1./sqrt(e_c-min(e_c)),line=1
oplot,e_c, 3./sqrt(e_c-min(e_c)),line=1
oplot,e_c,-3./sqrt(e_c-min(e_c)),line=1


!P.Multi=0

; stop


window,3

plot_oo,ee,fbar0(0:N_elements(ee)-1),ytitle='Fit',xtitle='Energy,keV'
oplot,ee,fbar0(N_elements(ee):2*N_elements(ee)-1),line=1

; stop

Set_plot, 'PS'
Device,filename=ps_file_fit,xsize=12,ysize=18,ENCAPSULATED=1
!P.MULTI=[0,1,3]
!P.CHARSIZE=2
!P.thick=1.5
```

```
plot_oo,e_c,counts, ytitle='Count Flux',$
        xtitle='Energy, keV',xstyle=1,xrange=[min(e_c),max(e_c)]

ERRplot,e_c,counts-ecounts,counts+ecounts
oplot,e_c,fit,line=0,color=220

plot,e_c,res,/xlog,psym=10,ytitle='Normilised Residuals',$
        xtitle='Energy, keV',xstyle=1,xrange=[min(e_c),max(e_c)]

plot_oo,ee,fbar0(0:N_elements(ee)-1),$
        ytitle='Electron flux',xtitle='Energy,keV',xrange=[10,1000]
oplot,ee,fbar0(N_elements(ee):2*N_elements(ee)-1),line=2

;stop

!P.thick=1
!P.CHARSIZE=1
!P.Multi=0
DEVICE, /CLOSE
set_plot,'X'

print,'fitting completed ..................................... OK'

; stop

openw,1,'ff_residuals_jcb.dat'
for i=0, n_elements(e_c)-1 do printf,1,e_c(i),res(i),res_sum(i)
close,1

;stop

;fit=0.
;fbar0=fbar0*1e-8

; preconditioning of the cross-section
```

```
precond1=sqrt(fit)
for i=0,N_elements(fit)-1 do  Matrix(*,i)=Matrix(*,i)/precond1(i)
counts =counts/precond1
ecounts=ecounts/precond1

M=2*N_elements(ee)
N=N_elements(e_c)

precond2=sqrt([Msun#fbar0(0:M/2-1),Mup#fbar0(0:M/2-1)])


D0=fltarr(M,M)
For i=0,  M/2-1 do D0(i,i)=1./sqrt(fbar0(i))
;For i=M/2,M-1   do D0(i,i)=sqrt(ee(i-M/2))*sqrt(de(i-M/2))/$
        sqrt(fbar0(i-M/2));*sqrt(de(i-M/2));/sqrt(i-float(M)/2+1.)

For i=M/2,M-1   do D0(i,i)=1./sqrt(fbar0(i-M/2))

D1=fltarr(M,M)

for i=0, M/2-2 do D1(i,i+1)=1./sqrt(fbar0(i)/ee(i))
for i=0, M/2-1 do D1(i,i)  =-1./sqrt(fbar0(i)/ee(i))
for i=M/2, M-2 do D1(i,i+1)=1./sqrt(fbar0(i-M/2)/ee(i-M/2))
for i=M/2, M-1 do D1(i,i)  =-1./sqrt(fbar0(i-M/2)/ee(i-M/2))

L=D1

;L=D0+0.01*D1

Fbar0=fbar0;*1e-22

counts=counts-fit/precond1
;stop
;gsvdcsq,Matrix,L, alpha,betta,gamma,U,V,W
inv_gsvdcsq,Matrix,L,alpha,betta,U,V,W
inv_gsvdcsq,Matrix,L,alpha,betta,U,V,W
```

```
print,'Generalized SV decomposition  .... ................. OK '


;opt0=Trace(transpose(Matrix)##matrix)/Trace(transpose(L)##L)
opt0=1.;/total(ephoton*ephoton)

print,'Initial guess .... ',opt0

;reg_parameter,alpha,betta,U,W,counts,ecounts,ee,opt,opt0
;REG_PARAMETER,Alpha,Betta,u,w,counts,Fbar0,ecounts,ee,opt,opt0

reg_tweak=.95
inv_reg_parameter,Alpha,Betta,U,W,counts,ecounts,Fbar0*0.,reg_tweak,opt

print,'regularisation parameter ................. OK '
;regularization parameter


;reg_solution,Alpha,Betta,U,W,e_c,ee,counts,opt,n,m,reg_sol
;reg_solution,Alpha,Betta,U,W,starte,ee,counts,Fbar0,opt,n,m,reg_sol

inv_reg_solution,Alpha,Betta,U,W,counts,opt,fbar0*0.,reg_sol

;solving reg solution
print,'regularisation solution  ................. OK '

inv_reg_resolution,Alpha,Betta,opt,W,[ee,ee],[de,de],FWHM

reg_sol=reg_sol;+Fbar0

ph_reg=Matrix##(reg_sol)
counts=counts

;*********************************************************************
```

```
window,7
plot_oo,ee,reg_sol+Fbar0,xtitle='energy, kev',ytitle='Electron flux'
oplot,ee,reg_sol(M/2:M-1)+Fbar0(M/2:M-1),line=1
;oplot,ee,Fbar0,line=1,color=220

;stop


Set_plot, 'PS'
Device,filename=ph_spectr_file+'.electron_split.ps',$
         xsize=24,ysize=17,xoffset=2,yoffset=2,ENCAPSULATED=0

plot_oo,ee,reg_sol+Fbar0,xtitle='energy, kev',ytitle='Electron flux'
oplot,ee,reg_sol(M/2:M-1)+Fbar0(M/2:M-1),line=1
;oplot,ee,Fbar0,line=1,color=220

device, /close
set_plot, 'X'


loadct,39
window,0

plot_oo,e_c,counts+fit/precond1, xtitle='Photon Flux',ytitle='energy, keV'
ERRplot,e_c,counts+fit/precond1-ecounts,counts+fit/precond1+ecounts
oplot,e_c,ph_reg+fit/precond1,line=0,color=220

;*****************************************************************

;res=(counts-ph_reg)/ecounts

inv_residuals,ph_reg+fit/precond1,counts+fit/precond1,ecounts,e_c,'2dfit.ps'


; stop
```

```
;calculating confidence strip
Npass =300
; Init seed for a repeatable sequence:
seed = 1001L
seed = 5L ;for gaussian distribution of errors

Strip_array=fltarr(Npass,N_elements(reg_sol))

for i=0, Npass-1 do begin

;rand_arr=(randomu(seed,N_elements(reg_sol))-0.5D0)*6.*ecounts

rand_arr=(randomn(seed,N_elements(reg_sol)))*ecounts*3.

print,'pass # ',i,' out of ',Npass

photonX=counts+rand_arr

;photonX=(photonX LE 0)*1e-6 +(photonX GT 0)*photonX

optX=opt


;reg_solution,Alpha,Betta,U,W,ee,ee,photonX,optX,n,m,reg_solX
;reg_solution,Alpha,Betta,U,W,e_c,ee,photonX,fbar0,optX,n,m,reg_solX

inv_reg_solution,Alpha,Betta,U,W,photonX,opt,fbar0*0.,reg_solX

Strip_array(i,*)=reg_solX

end

nbins=9
;number of bins for error estimate
reg_sol_err=fltarr(N_elements(reg_sol))
```

```
Diff    = fltarr(Npass,N_elements(reg_sol))
Dist_err= fltarr(Nbins,N_elements(reg_sol))
ERR_fit = fltarr(3,N_elements(reg_sol))

For i=0, N_elements(reg_sol)-1 do begin
Diff(*,i)= strip_array(*,i)-reg_sol(i)
Dist= HISTOGRAM(Diff(*,i),NBINS=7,locations=X_err)
fit_gauss=GAUSSFIT(X_err,Dist,gauss_params,NTERMS=3)
ERR_fit(*,i)=gauss_params
end

for j=0, N_elements(reg_sol)-1 do reg_sol_err(j)=$
    max(abs(strip_array(*,j)-reg_sol(j)))

reg_sol_err=err_fit(2,*)

new_sol=total(Strip_array,1)/N_elements(strip_array(*,1))

print,'Confidence strip ..............................  OK'
;finished


counts=counts+fit/precond1
ph_reg=ph_reg+fit/precond1
Reg_sol=reg_sol+fbar0

;*****************************************
; converting to physical values
reg_sol    =(reg_sol)*R2pi4
reg_sol_err=reg_sol_err*R2pi4
;*****************************************

res=(ph_reg-counts)/ecounts

res_sum=fltarr(N_elements(e_c))
```

```
for k=0,N_elements(e_c)-1 do res_sum(k)=total(res(0:k))/(k+1.)

loadct,39
window,3,xsize=600,ysize=600
!P.Multi=[0,1,2]

plot_oo,e_c,counts, ytitle='Counts Flux',xtitle='Energy, keV',$
xrange=[min(e_c),max(e_c)],xstyle=1,yrange=[min(counts),max(counts)]
ERRplot,e_c,counts-ecounts,counts+ecounts
oplot,e_c,ph_reg,line=0,color=220

plot_oo,ee,reg_sol,xrange=[min(ee),max(e_c)],ytitle='Reg Solution',PSYM=3
ERRplot,ee,reg_sol-reg_sol_err,reg_sol+reg_sol_err
oplot,ee,reg_sol(M/2:M-1),line=0,color=220

ERRplot,ee,reg_sol(M/2:M-1)-reg_sol_err(M/2:M-1),$
        reg_sol(M/2:M-1)+reg_sol_err(M/2:M-1)

!P.Multi=0

;stop

print, ph_spectr_file

Set_plot, 'PS'
Device,filename=ph_spectr_file+'.electron_solution.ps',$
        xsize=17,ysize=24,xoffset=2,yoffset=2,ENCAPSULATED=0
!P.Multi=[0,1,2]

plot_oo,e_c,counts, ytitle='Counts Flux',xtitle='Energy, keV',$
xrange=[min(e_c),max(e_c)],xstyle=1,yrange=[min(counts),max(counts)]
ERRplot,e_c,counts-ecounts,counts+ecounts
oplot,e_c,ph_reg,line=0,color=220

plot_oo,ee,reg_sol,xrange=[min(ee),max(e_c)],ytitle='Reg Solution',PSYM=3
ERRplot,ee,reg_sol-reg_sol_err,reg_sol+reg_sol_err
```

```
oplot,ee,reg_sol(M/2:M-1),line=0,color=220
ERRplot,ee,reg_sol(M/2:M-1)-reg_sol_err(M/2:M-1),$
    reg_sol(M/2:M-1)+reg_sol_err(M/2:M-1)

!P.Multi=0
device, /close
set_plot, 'X'



window,4,xsize=600,ysize=600
!P.Multi=[0,1,2]

plot,e_c,res,xrange=[min(e_c),max(e_c)],$
    ytitle='Normilised residuals',/xlog,xstyle=1,xtitle='Energy, keV',Psym=10

plot,e_c,res_sum,xrange=[min(e_c),max(e_c)],ytitle='Cumulative residuals',$
    /xlog,xstyle=1,xtitle='Energy, keV',yrange=[-1,1],Psym=10

oplot,e_c, 1./sqrt(e_c-min(e_c)),line=2,color=170
oplot,e_c,-1./sqrt(e_c-min(e_c)),line=2,color=170

!p.multi=0

;plot_oo,ee(0:80),-dF, ytitle='d(F/E)',xtitle='energy, keV'
;m_coef=1e+50

openw,11,output_file
for i=0, n_elements(ee)-1 do printf,11,ee(i),reg_sol(i),reg_sol_err(i),$
    reg_sol(i+M/2),reg_sol_err(i+M/2)

close,11



openw,11,errors_file
for i=0, n_elements(e_c)-1 do printf,11,e_c(i),res(i),res_sum(i)
```

```
close,11



;*********************************************************************
;               plot PS files

Set_plot, 'PS'
Device,filename=ps_file, xsize=17,ysize=24,xoffset=2,$
    yoffset=2,ENCAPSULATED=0
!P.multi=[0,1,2]

plot,e_c,counts,ytitle='counts Flux ',xtitle='energy, keV',/YLOG,$
        /xlog,xrange=[min(e_c),max(e_c)]

ERRplot,e_c,counts-ecounts,counts+ecounts
oplot,e_c,ph_reg,line=2

plot,ee,reg_sol,xrange=[min(ee),max(ee)],yrange=[1,1e+7],$
ytitle='Regularized solution',/ylog,/xlog,xtitle='Energy,keV',xstyle=1

ERRplot,ee,reg_sol-reg_sol_err,reg_sol+reg_sol_err
;oplot,ee+FWHM,reg_sol,line=1
;oplot,ee-FWHM,reg_sol,line=1


;oplot,ee,Ftest*R2pi4,line=1

;For i=0,Npass-1 do oplot,ee,(Strip_array(i,*))*R2pi4


DEVICE, /CLOSE
SET_PLOT, 'X'


Set_plot, 'PS'
```

```
Device,filename=ps_file_err, xsize=17,ysize=24,xoffset=2,$
        yoffset=2,ENCAPSULATED=0
!P.multi=[0,1,2]

plot,e_c,res,xrange=[min(e_c),max(e_c)],ytitle='Normilised residuals',$
        xtitle='Energy,keV',/xlog,xstyle=1

plot,e_c,res_sum,xrange=[min(e_c),max(e_c)],ytitle='Cumulative residuals',$
        xtitle='Energy,keV',/xlog,xstyle=1

oplot,e_c, 1./sqrt(e_c-min(e_c)),line=2
oplot,e_c,-1./sqrt(e_c-min(e_c)),line=2

!P.multi=0

DEVICE, /CLOSE
SET_PLOT, 'X'

Print,'CHISQ =',total(Res*Res)/(N_elements(Res))
print,'All completed ..................................... OK '
;stop
close, /all

end
```